# NANOSCALE TITANIUM AND POLYCATECHOLAMINE SURFACE SCIENCE TO ENHANCE BONE AND UTERINE TISSUE ENGINEERING

Alexander Steeves[1,2]

[1] Faculty of Engineering, Department of Mechanical Engineering, University of Ottawa, Canada
[2] Ottawa-Carleton Institute for Biomedical Engineering, Ottawa, Canada

*Submitted to the University of Ottawa in partial fulfillment of the requirements for the degree of*

**Doctor of Philosophy**
Biomedical Engineering

Supervisor: Dr. Fabio Variola

Ottawa-Carleton Institute for Biomedical Engineering (OCIBME)

Faculty of Engineering
Department of Mechanical Engineering

uOttawa

# ABSTRACT

The interface between biomaterials and tissues is fundamental to the success of implantable devices, such as orthopedic implants, and those biomaterials designed for soft tissue engineering applications. The efficacy of biomaterials in directing cell-specific responses is intricately linked to their physical and chemical properties. Physical attributes, such as topography and stiffness, interact synergistically with chemical characteristics, including surface chemistry, to modulate cellular behaviour. Understanding the multifaceted influences of biomaterials on cellular responses is pivotal in their design and application. The precise tailoring of these materials enables the stimulation of cell-type-specific pathways to elicit desired cellular behaviours. This thesis advances the field by expanding upon previous research conducted during my Master's degree, which explored the bioactive properties of a polydopamine (pDA) coating on a nanoporous titanium substrate (NPTi). Motivated by a desire to dissect the influence of each constituent separately, the first two studies herein are related to modifying the underlying titanium substrate, with the following two focusing on pDA-inspired polymers.

Our first study, described in **Chapter 3**, focuses on generating titanium dioxide ($TiO_2$) nanotubes with varying sizes, architectures, and spatial organizations. This is followed by an investigation of the bioactive effects of these substrates on human mesenchymal stem cells (hMSCs) in the context of orthopedic biomaterials, including proliferation, adhesion, osteogenic marker expression, and bone mineral quality assessment via Raman spectroscopy. The second study is provided in **Chapter 4** and focuses on using Pulsed-Water Jet (PWJ) technology for contaminant-free surface preparation of Ti. Following the generation of a textured substrate using the PWJ, in vitro testing was performed to assess the substrate's performance in periodontal implants. Human mesenchymal stem cells (hMSCs) and Saos-2 cells were employed to represent bone, while NIH/3T3 fibroblasts were used to represent the gums. **Chapter 5** returns to polymer science and extends beyond Dopamine (DA) polymer chemistry to include additional catecholamine (CA) family members, specifically levodopa (LD) and norepinephrine (NE), for the generation of polycatecholamine (pCA) substrate. While DA is achiral, the chiral nature of NE requires particular focus on the potential effects of chirality on pNE. This led to considering both L-norepinephrine (L-NE) and racemic norepinephrine (rac-NE) as precursor conditions. Within this expanded study, we examine the influence of precursor chemistry and concentration on the kinetics of pCA formation and the synthesis of pCA nanoparticles using these CA precursors. This work aims to elucidate the impact of precursor chemistry, chirality, and concentration on pCA synthesis, thereby providing foundational insights that support the tailored design of pCA substrates for targeted biomedical applications. Lastly, shifting focus to soft tissue engineering, **Chapter 6** explores the application of pDA, poly-L-norepinephrine (pLNE), and polylevodopa (pLD) to address uterine injuries, including those from Cesarean sections and intrauterine adhesions, which pose significant challenges to female reproductive health. Tissue engineering strategies utilizing these bioadhesive pCAs are being investigated for their potential to enhance uterine healing. Given the diverse cellular responses

observed with different pCAs, this study focuses on understanding the interactions of pCA-based materials with both transformed human endometrial stromal cells (T-HESCs) and pregnant human myometrial (PHM1-41) cells in a multi-tissue context. This comprehensive study highlights the cell-specific responses to pCA, namely proliferation, adhesion, and migration. This research aims to elucidate the mechanisms underlying these interactions, ultimately paving the way for novel biomaterial-based treatments in female reproductive medicine.

This work offers new perspectives on employing pCAs as a functionalization strategy for advanced tissue engineering and regenerative medicine applications, particularly in organ systems like the uterus. By working to bridge the gaps between materials science and cell biology, a multifaceted investigation into the intricate relationship between pCA biomaterials and cellular behaviour is presented. The findings herein provide a strong foundation for the use and further development of next-generation biomaterial-based therapies for both hard and soft tissue regeneration, potentially contributing to regenerative medicine.

# ACKNOWLEDGEMENT

This PhD journey has been one of growth and challenges, made possible only through the unwavering support and encouragement of many exceptional individuals.

First and foremost, I would like to express my deepest gratitude to my supervisor, **Dr. Fabio Variola**, for his guidance, insight, and mentorship. His support allowed me the freedom to explore new ideas, follow my hunches, and make mistakes. His trust gave me the confidence to push boundaries and take intellectual risks that shaped the course of my research, which has been critical to my growth as a researcher.

I would also like to sincerely thank my thesis committee members and support: **Dr. Marianne Fenech**, **Dr. Andrew Harris, Dr. Leila Mostaço-Guidolin, Dr. Jean-Philippe St-Pierre, Dr. Erik Suuronen**, and **Dr. Malcolm Xing**. Your feedback and constructive criticism helped refine my research and I am grateful for your time and dedication.

To my partner, **Zahra Wells**, your endless patience, encouragement, and love have carried me through every challenge of this journey. I am excited to face the next chapter of our lives together. And to my faithful companion, **Pablo Bear**, your presence has been a comforting reminder to take a break and enjoy the small moments. Though, I suspect you were mostly in it for the duck treats.

I am forever grateful to my parents, **David** and **Carol Steeves**, whose love, support, and belief in me have been a constant source of strength. My mother's unwavering faith and prayers have comforted me throughout this journey. To my *brosif* **Ryan Steeves**, my sister-in-law **Samantha**, and my niece **Hailey**, thank you for always being there and cheering me on, even from afar. And to all those not present but watching over me, your presence has not been forgotten.

To those who kept me grounded and helped me stay sane: **Ashley Cameron, Jake Topic, Warsama Ahmed** and **Dilara Jakupovic**. And to my brother from another mother, **Jean-Michel Guay**, wife **Alena** and son **Phillip** your friendship has meant the world to me, and I could not have made it through without your support and BBQ.

I would also like to acknowledge my office and lab mates for their camaraderie and support: **Ryan Berthelot, Parisa Gohari, Graham Killaire, David Lomboni, Sara Martinelli, Alp Ozgun, Matteo Pavarini, Elena Rainone, Karim Saadé, Farzan Soleymani,** and **Jaspreet Walia**. Working alongside you made the long hours in the lab much more bearable, and I am grateful for all the conversations and collaborations, especially with AYCE sushi.

Lastly, I want to thank everyone else who contributed to this journey in one way or another. It takes a village.

# STATEMENT OF ORIGINALITY AND CONTRIBUTION

To the author's knowledge, this thesis and work are entirely original. Research and manuscripts were prepared under the supervision of Dr. Fabio Variola, Department of Mechanical Engineering at the University of Ottawa, while enrolled in a PhD program in biomedical engineering at the Ottawa-Carleton Institute for Biomedical Engineering.

This monograph thesis comprises work from two (2) original articles published in peer-reviewed scientific journals and two (2) manuscripts in preparation.

**Manuscripts included in this thesis:**

**PUBLISHED**

- **Steeves, A. J.**, Ho, W., Munisso, M. C., Lomboni, D. J., Larranaga, E., Omelon, S., Martinez, E., Spinello, D., & Variola, F. (2020). The implication of spatial statistics in human mesenchymal stem cell response to nanotubular architectures. *Int J Nanomedicine*, *15*, 2151-2169. doi.org/10.2147/IJN.S238280

  *Contributions from co-authors:*

  **William Ho**: Partial design of the study, protocol design of NT synthesis, NT substrate synthesis, SEM acquisition of NT substrate, proliferation and morphology experiments up to imaging.

  **Enara Larrañaga**: Acquired the image of the HC surface in **Figure 3-1G**.

  **Davide Spinello**: Coded the simulations that I designed and successively analyzed.

  **Sidney Omelon**: Acquired the Raman data of the bone nodules.

  **Maria Chiara Munisso**: Analyzed the Raman data of the bone nodules.

  **David Lomboni**: Assisted in editing the manuscript.

  **Fabio Variola**: Acquired the Raman data of the bone nodules and assisted in editing the manuscript.

- **Steeves, A. J.**, Lomboni, D. J., Vijay, M., Tieu, A., & Variola, F. (2021). Direct cueing by pulsed-waterjet treated titanium on fibroblast, osteoblastic and human stem cells for prospective use in dental implants. *Materials Letters*, *290*. doi.org/10.1016/j.matlet.2021.129437

  *Contributions from co-authors:*

  **Andrew Tieu**: Surface preparation of the Ti samples at VLN Advanced Technologies Inc. with the PWJ.

  **David Lomboni**: Carried out half of the hMSCs culture and imaging for OSX nuclear localization.

**IN PREPARATION**

- **Steeves, A. J.** & Variola, F. Unraveling the Complexities of Polycatecholamine Coatings: Kinetics and nanoparticle formation.
- **Steeves, A. J.** & Variola, F. Probing the bioactivity of polydopamine, polynorepinephrine and polylevodopa-based materials: insights from a uterine context with human endometrial stromal and uterine myometrial cells.

# OTHER CONTRIBUTIONS

During my PhD studies, I was privileged to participate in multiple collaborative studies with fellow researchers of the Variola Lab, the Department of Mechanical Engineering (Dr. Davide Spinello), the Ottawa Heart Research Institute (Dr. Emilio Alarcon) and the Politecnico di Milano (Dr. Lorenzo Bonetti and Sara Martinelli). I was fortunate to continue collaborating with Dr. Mohammed Vijay and Andrew Tieu at VLN Advanced Technologies (Ottawa, Ontario). These partnerships contributed to the following publications, conferences and competitions:

**Peer-reviewed Publications**

- Martinelli, S., Pavarini, M., Moscatelli, M., **Steeves, A. J.**, Chiesa, R., & Variola, F. (2023). Enhanced Embedding of Cations into Titanium Surfaces by AC Plasma Electrolytic Oxidation for Osteointegrated Implants. *Advanced Engineering Materials*. doi.org/10.1002/adem.202300642
- Lomboni, D. J., **Steeves, A. J.**, Schock, S., Bonetti, L., De Nardo, L., & Variola, F. (2021). Compounded topographical and physicochemical cueing by micro-engineered chitosan substrates on rat dorsal root ganglion neurons and human mesenchymal stem cells. *Soft Matter*, *17*(21), 5284-5302. doi.org/10.1039/d0sm02170a
- **Steeves, A. J.**, & Variola, F. (2020). Elucidating Structure-Function Relationships Governing the Interfacial Response of Human Mesenchymal Stem Cells to Polydopamine Coatings. *J Mater Chem B*, *8*(2), 199-215. doi.org/10.1039/c9tb02188d (**Front cover**)
- Jacques, E., Hosoyama, K., Biniam, B., Eren Cimenci, C., Sedlakova, V., **Steeves, A. J.**, Variola, F., Davis, D. R., Stewart, D. J., Suuronen, E. J., & Alarcon, E. I. (2020). Collagen-Based Microcapsules As Therapeutic Materials for Stem Cell Therapies in Infarcted Myocardium. *ACS Biomater Sci Eng*, *6*(8), 4614-4622. doi.org/10.1021/acsbiomaterials.0c00245
- Kanda, P., Benavente-Babace, A., Parent, S., Connor, M., Soucy, N., **Steeves, A. J.**, Lu, A., Cober, N. D., Courtman, D., Variola, F., Alarcon, E. I., Liang, W., Stewart, D. J., Godin, M., & Davis, D. R. (2020). Deterministic paracrine repair of injured myocardium using microfluidic-based cocooning of heart explant-derived cells. *Biomaterials*, *247*, 120010. doi.org/10.1016/j.biomaterials.2020.120010

**Conference Presentations & Competitions**

- **Steeves, A. J.** & Variola, F. "Polydopamine as a multifunctional orthopedic coating for Human mesenchymal stem cell tissue engineering" *11th World Biomaterials Congress*, Glasgow, Scotland, 2020.
- **Steeves, A. J.** & Variola, F. "Implication of spatial statistics in the human mesenchymal stem cells response to semi-ordered titanium nanotube architectures - from early adhesion to bone mineral deposition" *11th World Biomaterials Congress (WBC)*, Glasgow, Scotland, 2020.
- **Steeves, A. J.**, Ho, W., Munisso, M. C., Lomboni, D. J., Larranaga, E., Omelon, S., Martinez, E., Spinello, D., & Variola, F. "The implication of spatial statistics in human stem cell response to nanotubular architectures." *11th* uOttawa Engineering Graduate Research Competition. (**3rd Pl., IEEE Award**)
- **Steeves, A. J.** & Variola, F. "Human mesenchymal stem cell response to semi-ordered nanotubular architectures from adhesion to bone deposition" *Canadian Biomaterials Society (CBS) 35th* AGM, Quebec City, Canada, 2019.
- **Steeves, A. J.** & Variola, F. "Human mesenchymal stem cells response to polydopamine: evidence supporting its use as a multifunctional coating in bone tissue engineering" *Canadian Biomaterials Society (CBS) 35th* AGM, Quebec City, Canada, 2019. (**1st Pl., PhD Oral; 2nd Pl., Emerging Talent**)
- **Steeves, A. J.**, Lomboni, D. J., Vijay, M., Tieu, A., & Variola, F. "In vitro response of osteoblastic and human mesenchymal stem cells to water-jet treated titanium surfaces for prospective use in periodontal implant fabrication," *2019 WJTA-IMCA Conference*. New Orleans, USA, 2019. (**2nd Pl., Conference Paper**)
- **Steeves, A. J.**, & Variola, F. (2020). Elucidating Structure-Function Relationships Governing the Response of Human Mesenchymal Stem Cells to pDA Coatings. (**2nd Pl., Emerging Materials and Processes**)

# TABLE OF CONTENTS

# LIST OF FIGURES

## LIST OF TABLES

# LIST OF ABBREVIATIONS

## GENERAL

| | |
|---|---|
| **µP** | Microparticle |
| **AFM** | Atomic force microscopy |
| **ANOVA** | Analysis of variance |
| **ATR** | Attenuated total reflectance (FTIR) |
| **BSA** | Bovine serum albumin |
| **BSG** | Borosilicate glass |
| **CS** | Cesarian section |
| **D&C** | Dilation and curettage |
| **DLS** | Dynamic light scattering |
| **DPFM** | Digital pulsed force mode (AFM) |
| **ETP** | Equilibrium transition point |
| **FA** | Focal adhesion |
| **FAK** | Focal adhesion kinase |
| **FF** | Form factor |
| **FTIR** | Fourier transform infrared spectroscopy |
| **HC** | Honeycomb (NTs) |
| **IRC** | Intrinsic reaction coordinate energy |
| **IUA** | Intrauterine adhesion |
| **LFPI** | Linearity of forward progression index |
| **NC** | Non-contact (AFM) |
| **NND** | Nearest neighbour distance |
| **NP** | Nanoparticle |
| **NPA** | Not preadsorbed |
| **NPTi** | Nanoporous titanium |
| **NT** | Nanotube |
| **OSX** | Osterix |
| **PA** | Preadsorbed |
| **PDR** | Polymer dispersion ratio |
| **PWJ** | Pulsed water jet |
| **RMS** | Root mean square roughness (Sa) |
| **rPDA** | Rough pDA |
| **SA** | Surface area |
| **SAM** | Self-assembled monolayer |
| **SEM** | Scanning electron microscopy |
| **SEP** | Standard electrode potential |
| **SIC** | Serum independent component |
| **sPDA** | Smooth pDA |
| **TC** | Tissue culture plastic |
| **UTE** | Uterine tissue engineering |
| **VIN** | Vinculin |
| **WCA** | Water contact angle |
| **XPS** | X-ray photoelectron spectroscopy |

## PRECURSORS AND POLYMERS

| | |
|---|---|
| **CA** | Catecholamine |
| **DA** | Dopamine |
| **LD** | Levodopa |
| **L-NE** | L-norepinephrine |
| **NE** | Norepinephrine |
| **rac-NE / R-NE** | Racemic norepinephrine |
| **pCA** | Polycatecholamine |
| **pDA** | Polydopamine |
| **pLD** | Polylevodopa |
| **pLNE** | Poly-L-norepinephrine |
| **pNE** | Polynorepinephrine |
| **pRNE** | Poly-rac-norepinephrine |

## CELL MODELS

| | |
|---|---|
| **hMSC** | Human mesenchymal stem cell |
| **NIH/3T3** | Mouse fibroblast (*embryo*) |
| **PHM1-41** | Pregnant human myometrial cell |
| **Saos-2** | Human osteoblast-like cell (*osteosarcoma*) |
| **T-HESC** | Trans. human endometrial stromal cell |

## FUNCTIONAL GROUPS

| | |
|---|---|
| **–CH=O** | Aldehyde |
| **$–NH_2$** | Amino |
| **–C=O** | Carbonyl |
| **–COOH** | Carboxyl |
| **$–COO^-$** | Carboxylate |
| **–OH** | Hydroxyl |
| **Ph–OH** | Phenolic hydroxyl |
| **Si–OH** | Silanol |
| **$Si–O^-$** | Silanolate |

## MOLECULES & COMPOUNDS

| | |
|---|---|
| **DHBA** | 3,4-dihydroxybenzaldehyde |
| **DHI** | 5,6-dihydroxyindole |
| **DHICA** | 5,6-dihydroxyindole-carboxylic acid |
| **DOPA** | 3,4-dihydroxyphenylalanine |
| **$SiO_2$** | Silicon dioxide |
| **$TiO_2$** | Titanium dioxide |

# 1 INTRODUCTION AND OVERVIEW

## 1.1 GENERAL INTRODUCTION AND MOTIVATION

Cells can detect, integrate information, and respond to physical and chemical stimuli. Within the context of physical signalling, interfacial cueing can be provided through topotaxis,[1] the guidance through geometric attributes of the substrate (e.g., size and distribution of features), and durotaxis,[2] the processing of substrate mechanical cues, namely stiffness, is transduced by transmembrane integrin proteins linked to the cytoskeleton via focal adhesions. Juxtaposed to this is chemical signalling that guides haptotaxis,[3] which uses receptors to perceive and interact with surface-bound antigens, and chemotaxis, through which cell surface receptors will bind to chemicals in free solution, allowing for a perception of a gradient, whether it elicits an attractive (chemoattractant) or repulsive (chemorepellent).[4] Building on these foundational cellular signalling and response concepts, this thesis explores the interplay between substrate material modifications and cellular behaviour.

Previously in our lab, we have sought to improve MG-63 osteoblast-like cell response to a composite biomaterial, namely by furthering the benefits of nanoporous titanium ("NPTi") with the addition of polydopamine (pDA) as a bioadhesive coating that was first reported by Lee et al. (2007).[5,6] No significant differences were found in the amount of protein adsorbed between NPTi and NPTi+pDA for the top 10 most abundant proteins. However, despite this, the pDA coating was still shown to improve cell adhesion and proliferation. This outcome highlighted the potential of pDA as a beneficial bioactive coating while suggesting the cell response is impacted by intrinsic properties of the material that go beyond impacting haptotaxis, known to be significantly affected by substrate adhesiveness.[3] Building on this, we decided to investigate further by separating the effects of the bioadhesive coating from those of the underlying substrate. This thesis presents novel research studies that systematically analyze the individual and combined effects of substrate features, such as $TiO_2$ nanotubes, and the application of various bioadhesive coatings on cellular behaviour.

## 1.2 OVERVIEW, SPECIFIC OBJECTIVES AND SYNOPSIS

This Ph.D. thesis investigates the intricate interplay between cells and biomaterials, focusing on titanium nanotubes and polycatecholamine (pCA) polymers. The first objective examines how bone-derived human mesenchymal stem cells (hMSCs) respond to varying sizes of nanotubular architectures on titanium surfaces. The second objective examines using pulsed water jet (PWJ) technology to prepare titanium substrate for use in dental implants. The third objective investigates the concentration-influenced kinetics of pCA coatings, including polydopamine (pDA), polylevodopa (pLD), and polynorepinephrine in both L-enantiomer (pLNE) and racemic mix (pRNE) forms. Finally, the thesis compares the effects of pDA, pLNE, and pLD on human endometrial stromal cells and pregnant myometrial cells, highlighting the distinct cellular interactions with these biomaterials. An outline of the thesis and the objectives are outlined below:

- **Chapter 1 (Introduction):** Provides an overview and general information about the thesis.
- **Chapter 2 (Background):** Provides a literature review about cell structures and cues that govern cell-substrate interactions.
- **Chapter 3 (OBJ-1):** A research paper focused on how the morphology and spatial organization of $TiO_2$ nanotubes impact the cell response of human mesenchymal stem cells (hMSCs).
- **Chapter 4 (OBJ-2)**: A research paper focused on Pulsed-Water Jet (PWJ) technology to surface prepare titanium substrates, followed by in vitro testing with human mesenchymal stem cells (hMSCs), Saos-2 and NIH/3T3 cell lines to assess the surfaces within the context of periodontal implants.
- **Chapter 5 (OBJ-3):** A research study focused on how the precursor chemistry and concentration impact the resulting kinetics and nanoparticle formation of pDA, pLNE, pRNE and pLD.
- **Chapter 6 (OBJ-4):** A research study focused on the candidacy of pDA, pLNE and pLD substrate within the uterine context using human endometrial stromal cells (T-HESC) and pregnant human myometrial smooth muscle cells (PHM1-41).
- **Chapter 7 (Conclusions):** Summarizes results and future directions.

**OBJ-1** **CHAPTER 3: Implication of spatial statistics in human mesenchymal stem cell response to nanotubular architectures**

**BACKGROUND**: Titanium nanotubes (NTs) have emerged as a consequential material in engineering owing to their unique properties, tunable properties, and various potential applications in biomedical, sensors, and photocatalysis contexts. Within the context of cell biology, however, in addition to the ability to tune the morphology, the spatial organization of these NTs contributes to the entropy of potential adhesion sites and can impact cell response.

**AIMS**: The research focuses on three key objectives: firstly, conducting a detailed morphological and spatial analysis of nanotubular titanium dioxide surfaces; secondly, exploring how these surfaces with varying nanotopographies influence the adhesion and proliferation of human mesenchymal stem cells (hMSCs); and thirdly, examining the effect of these surfaces on the differentiation of hMSCs and the quality of bone mineral they deposit. This comprehensive approach aims to elucidate the intricate interactions between cells and nanotubular surfaces.

**SIGNIFICANCE**: This research paper is significant as it enhances understanding of how spatial statistics contribute to the interaction between human mesenchymal stem cells and nanotubular $TiO_2$ surfaces. The findings regarding the influence of surface morphology and spatial organization on stem cell adhesion, proliferation, and differentiation are vital for developing improved bone regeneration therapies, offering potential for innovative applications in regenerative medicine and orthopedics.

**OBJ-2** **CHAPTER 4: Direct cueing by Pulsed Water Jet treated titanium on fibroblast, osteoblastic and human stem cells for prospective use in dental implants**

**BACKGROUND**: The pulsed-water jet technology, developed by VLN Advanced Technologies Inc., harnesses the power of pulsed water jets that deliver high-velocity water slugs that interact with the surface, inducing micro-cavitation and impulsive forces. This method provides an avenue for environmentally friendly and cost-effective surface preparation of titanium surfaces for periodontal implants. Substrates of varying properties can be generated by tuning the transverse nozzle speed, impacting the dwell time of the PWJ.

**AIM**: To garner a better understanding of how the surfaces generated by varying the nozzle speed impact the cellular response, three (3) different prepared substrates are compared to untreated titanium. By assessing the bioactive impact on bone-derived hMSCs and osteoblast-like Saos-2 cell lines that represent the bone and NIH/3T3 fibroblast cells that represent gum/mucosa, this work aims to assess how the PWJ parameters translate to potential protocols for enhanced surface preparation within the context of periodontal implants.

**SIGNIFICANCE**: The PWJ (Pulsed-Water Jet) study's innovative approach to surface engineering for periodontal implants is significant. By utilizing PWJ technology, the research aims to create titanium surfaces with enhanced biocompatibility and osteoconductivity, potentially benefiting the fabrication of dental implants. This study advances our understanding of cell-material interactions and paves the way for developing safer, more efficient, environmentally friendly, and cost-effective dental implant technologies.

**OBJ-3** **CHAPTER 5: Characterization of kinetics and particle formation in polymers derived from dopamine, levodopa, L-norepinephrine, and racemic norepinephrine**

**BACKGROUND**: Polydopamine (pDA) is a bioactive and bioadhesive material of interest that is commonly fabricated via autoxidative polymerization from the dissolution of the catecholamine dopamine (DA) precursor in an alkaline solution. Within the same family of catecholamines, norepinephrine (NE) and levodopa (LD) are reported as being able to generate polymer surfaces similarly through discrete properties (e.g., morphology, functional groups). Although the process of fabricating pDA has been well studied, pLNE and pLD have yet to be explored in this context.

**AIM**: To better understand the polymerization process, the impact of precursor concentration, a consequential aspect established in the research of pDA, on the kinetics of polymerization and the resulting properties of the substrate will be studied. Furthermore, the impact of chirality on

the polymerization process will be approached using NE precursor, whether as an L-enantiomer or a racemic mix.

**SIGNIFICANCE**: This study is significant as it extends our understanding of the polymerization of catecholamine-based materials beyond pDA. By focusing on how precursor concentration affects the polymerization kinetics and properties of pLNE, pRNE and pLD, the research aims to identify distinct characteristics of these biomaterials. The findings could biomaterials development with specific properties for targeted biomedical applications, improving our knowledge of how fabrication parameters influence the functionalities of CA-derived polymers.

**OBJ-4** **CHAPTER 6: Endometrial stromal and myometrial bioactivity analysis of polydopamine, poly-L-norepinephrine and polylevodopa coatings: from proliferation to migration**

**BACKGROUND**: Uterine injury is a prolific cause of distress for women worldwide, with the associated growth of scar tissue, fibroids, and intrauterine adhesions (IUAs). Particularly for IUAs, symptoms can include fertility concerns, including ectopic pregnancies, miscarriage, and infertility. In addition, women with symptomatic IUAs are diagnosed with Asherman's syndrome (AS). Although there are procedures to separate the uterine walls and resolve these ailments, namely dilation and curettage (D&C), they are met with re-adhesion rates between 30 and 62.5%. However, following the D&C, an opportunity exists to apply a treatment to the injured endometrium.

**AIM**: Considering the distinct properties of these surfaces (e.g., morphology, immunogenicity), a first step to potentially using these materials within the context of restorative intrauterine therapeutics is assessing how the cell populations respond. For this work, two immortalized cell lines representing the endometrium and the myometrium are considered. Specifically, they are endometrial stromal (T-HESC) and pregnant myometrial (PHM1-41) cells. This work aims to provide for the first-time measures of biocompatibility by discerning the effects of pCAs on cell morphology, proliferation, and migration within a 2D culture system.

**SIGNIFICANCE**: Considering the particularities of each surface, this research develops an understanding of the interfacial phenomena between multiple types of uterine cell lines and the surfaces. The morphological analysis provides a gauge of direct cell-substrate suitability, and the work on proliferation and migration offers indicators for therapeutic potential. This research demonstrates where these polymers sit along the spectrum of suitable materials for inclusion in intrauterine biomaterial-based therapeutics.

# 2 BACKGROUND

Cell-substrate interactions are multifaceted and involve dynamic crosstalk between cells, neighbouring cells, and the surrounding extracellular matrix (ECM). This dynamic interplay guides fundamental processes, such as cell adhesion, migration, proliferation, and differentiation.[7-11] Elucidating the intricacies of cell-substrate interactions is pivotal as it lays the foundation for material design and engineering.

## 2.1 CELL STRUCTURES AND FUNCTIONS

### 2.1.1 ACTIN

Fundamental to the structure and function of eukaryotic cells, the actin cytoskeleton is a filamentous network that extends throughout most cell types and is integral in various primary cell functions that require structural and dynamic forces, including the proliferation, differentiation, mechanotransduction, and migration of cells.

Management of the actin cytoskeleton is mediated by GTPase proteins that possess a conserved switching mechanism with an activated state characterized by the binding of Guanine Triphosphate (GTP) and influence several cell processes that depend on cytoskeletal dynamics.[12] A well-studied subfamily is the Rho family of small GTPases, characterized by their involvement in intracellular processes, including cell morphology, development, and movement. The three most studied Rho GTPases are Rac1, Cdc42, and RhoA, which are not exclusively associated with lamellipodia, filopodia, and stress fibres, respectively.

Filopodia are structures of particular interest for environmental sensing. These thin, finger-like projections protrude from the cell edge, most notably the lamellipodium, and enable cells to interact with and probe their physicochemical surroundings. These structures possess specialized receptors, particularly at high densities in their periphery, and have been associated with various cellular processes. They are involved in several migratory-based functions, including cellular migration, wound healing, and cell-cell interactions. Integral to their ability to detect the physical environment, the spiral F-actin structure of filopodia interacting with myosin-V results in force transmission from the base of the structure.[13] These dynamics result in the use of filopodia in cellular responses, such as the influence of migratory behaviour, which can be based on chemical cues, such as surface-bound chemicals environmental (chemotaxis) or substrate-bound chemoattractant (haptotaxis), and physical cues, including substrate rigidity (durotaxis). Another structure related to filopodia is the nanoscale membrane projections termed nanopodia, which have been found to provide sensory information about features as small as 8 nm.[14]

### 2.1.2 FOCAL ADHESIONS

Interfacing with the environment is a complex process that requires the coordination of a multitude of transmembrane and intracellular proteins in response to environmental cues. Focal adhesions are microscale plasma membrane-associated multimeric structures that couple the extracellular matrix (ECM) to the

intracellular cytoskeleton, enabling the transduction of mechanical forces into intracellular signalling cascades. Integrin proteins are α-β heterodimeric transmembrane receptors that bind to extracellular matrix (ECM) ligands in the environment, and their specificity is dependent on the 24 known dimer combinations of the 18 α and 6 β subunits.[15] Integrin α5β1 is the primary receptor for fibronectin, an ECM protein essential for adhesion, migration, and differentiation.[16] When activated by binding extracellular ligands, integrins undergo conformational changes and promote the recruitment and clustering of additional integrin proteins. This clustering increases the receptor avidity of the ligands by allowing the receptors to translocate to high ligand concentrations and acts as the initiation step for FA formation. Upon clustering, integrins recruit proteins, including paxillin and talin, that initiate early cell-matrix contacts as small nascent adhesions (<0.25 μm).[17] Effective force loading rates of these adhesions trigger the talin-dependent formation of focal complexes (≈0.5 μm), which can undergo progressive reinforcement with additional proteins focal adhesions (1–5 μm) and fibrillar adhesions (>5 μm), shown in **Figure 2-1A**.[17-19] The structure of mature focal adhesions with the intracellular signalling layer, medial force-transduction layer, and uppermost actin-regulatory layer are provided in **Figure 2-1B**.[19]

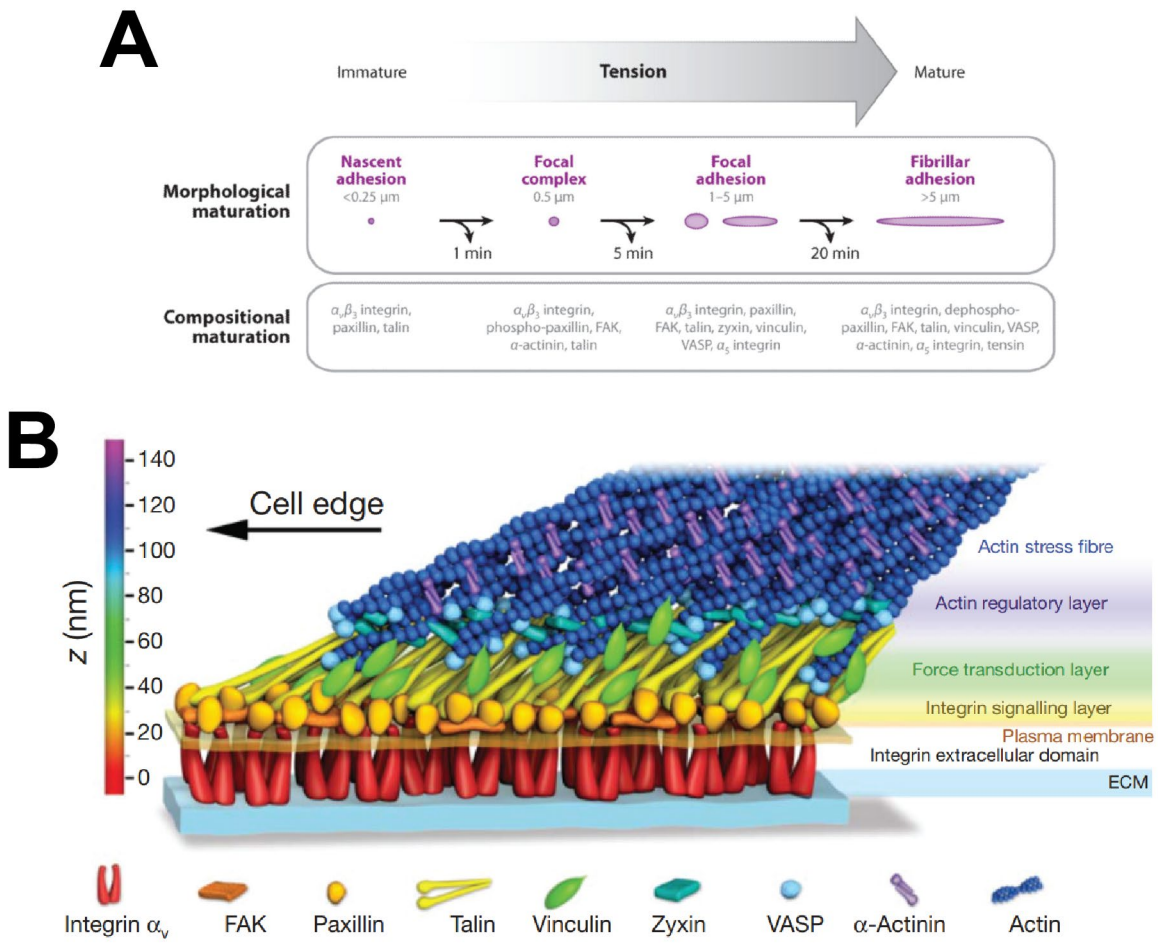


Figure 2-1: Focal adhesion maturation and nanoarchitecture

**(A)** Adhesion features represented by purple ovals; length scales indicate focal adhesion lengths. (*Below*) Compositional phases of adhesion maturation with protein components. At each step, adhesion turnover can occur (curved black arrows) after a specific time (the timescale below each arrow). AK, focal adhesion kinase; VASP, vasodilator-stimulated phosphoprotein. *Adapted from a study by Gardel et al. (2010)*. **(B)** Schematic focal adhesion molecular architecture model depicting the experimentally determined protein positions. Note that this model does not depict protein stoichiometry. *Reproduced by Schwartz et al. (2010) with permission from Elsevier. Licence number: 5703311383078.*

#### 2.1.2.1 *FORCE TRANSDUCTION LAYER*

This medial layer primarily comprises the proteins talin (TAL) and vinculin (VIN) that mediate the transmission of mechanotransduction signalling between the integrin and actin filaments.[19]

One of only two essential proteins for integrin activation,[20] talin (TAL), is a large multidomain protein with integrin-, vinculin-, and PIP5KIγ- binding domains that act as a mechanosensitive adapter protein to coordinate the assembly and maturation of focal adhesions.[21] As an integrin-actin bridge and the primary regulator of integrin activation,[22] TAL is responsive to mechanical forces and undergoes a structural change when subjected to low mechanical forces (5 pN).[23] This structural change increases the affinity for the binding of integrin, potentiating the conformational change that exposes vinculin binding sites (VBS).

VIN, the other primary component of the force transduction layer, contains four head domains (D1–4) bridged to its tail domain by a proline-rich linker (PRL).[24] While existing as an autoinhibited globular protein, VIN is rapidly recruited to FA sites. Successively, it undergoes a conformational change and relief of its inhibited form. However, the method of activating VIN is still under debate.[25] In its extended active state, the exposed D1 head domain of VIN binds the exposed VBS of TAL, whereas the tail domain binds actin.[26] Furthermore, VIN operates as a fundamental coordinator of FA fate owing to its many additional exposed binding sites to proteins, including α-actinin, VASP, vinexins, ponsin, Arp2/3, paxillin and PIP2. In addition to the stability of the talin-integrin complex facilitated by VIN activity, the ordered control of FA protein turnover plays a crucial role in coordinating cell polarization, as constitutively active VIN results in the loss of polarized cell migration.[24]

Cellular adhesion to the extracellular matrix is critical in various biological processes, including proliferation, cell spreading, and migration. Focal adhesion formation and the subsequent induction of FAK/RhoA are hypothesized to promote proliferation through topography-dependent modulation directly.[27,28] During the initial stages of cell spreading, integrin-containing filopodial projections are present around the periphery of a cell. They are crucial in the initial cell-ECM interaction and subsequent cell spreading.[29] These projections initiate cell-substrate adhesions that result in the lengthening of the filopodia, associated with the accumulation of additional integrin and focal adhesion components, resulting in the swelling of these projections into nascent focal complexes and subsequently into focal adhesions.[29] Subsequent focal adhesions formed around the periphery of the plasma membrane have shown to be highly dependent on the spacing of integrin ligands, exemplified by the differential evidence of spreading with productive tethers on nanopatterns of 8 nm Au particles spaced 108 nm apart versus patterns with 58 nm spacings.[30] These 108 nm spacings were also critical during cellular migration and dynamic behaviour. Curiously, research has shown that in 3D substrate, confinement is sufficient for cell-substrate interaction and enables the cell to proceed with focal adhesion-independent cell migration.[31]

## 2.2 CELL-SUBSTRATE INTERACTIONS

The intricate interplay between cells and their surrounding extracellular matrix (ECM) underpins the foundational aspects of cellular behaviour, guiding processes such as adhesion, proliferation, migration, and differentiation. This interfacial dialogue is facilitated by the surface properties of the substrate, where an array of physical and chemical cues is deciphered by the cell and translated into a cascade of intracellular activities.[32-34] Understanding cell-substrate interactions is critical in tissue engineering and regenerative medicine. It can inform the design of biomaterials that mimic a particular microenvironment (e.g., natural ECM), promoting the desired cellular responses and productive tissue formation. The synergistic interplay of these cues operates multifactorial, orchestrating a concerted cellular response and guiding the development of next-generation biomaterials to promote tissue regeneration and function.

### 2.2.1 PHYSICAL

In the investigation of cell-substrate interactions, the physical characteristics of the substrate surface play a pivotal role in modulating cellular behaviour. Physical properties such as surface topography and stiffness actively influence crucial cellular functions.

#### 2.2.1.1 *TOPOGRAPHY*

Topographical features at the heart of these cell-substrate interactions, ranging from the nano- to micro-scale, exist as patterns within the ECM of all tissue types for cell interface and instruction. In addition, their size, shape, geometry, and spatial organization properties have been shown to influence cell response.[35-38] Minute topographical features, as small as 8 nm, can influence filopodial dynamics and cellular responses. [14] Surface characteristics such as increased porosity and roughness enhance adhesion, filopodial activity, and migration.[39,40] The feature size, whether nanoislands, pillars, nanotube arrays, or pores, can influence cellular responses, with specific feature-dependent dimensions that play a critical role.[41] For example, the optimal diameter of nanotubes for cell adhesion and differentiation of stem cells into the osteogenic lineage has been reported to be 15 nm.[42,43] However, there appear to be inconsistencies as human adipose-derived stem cells were reported to benefit most from NTs of approximately 30-45 nm in diameter but may also benefit from 65-85 nm tubes,[44,45] whereas hMSCs and mice MSCs benefited most from 70-100 nm NTs.[46,47] Regardless, these discrepancies suggest that intricacies between cell types and the structural aspect of the surface are yet to be determined.

Another impact of topography is the spatially organized cues that influence the cellular response, which relies on two key attributes: alignment and distribution. Alignment, referring to the orientation of topographical features on a surface, is particularly relevant in tissues where the structural organization is critical for function, such as in muscle fibres, where aligned chitosan-based nanofibres promote myogenic gene expression in C2C12 myoblast cells and promote their fusion into myotubes.[48] In neural tissues, structural elements (e.g., actin stress

fibres and microtubules) align to the features and influence neurite outgrowth and branching.[49,50] Distribution, on the other hand, encompasses the density, depth, and uniformity of cue spacing across a 2-2.5D substrate or throughout a 3D material and can influence the local density of cell attachment sites and the accessibility of these sites to cells.[51] Moreover, the organization of these features, namely in the context of orderliness and entropy, has indicated that increasing disorder and larger structures can have unique influences on cell behaviour.[52,53]

#### 2.2.1.2 *STIFFNESS*

Stiffness is a fundamental physical property of biomaterials that influences cell behaviour through mechanotransduction, in which cells convert mechanical stimuli into biochemical signals. The rigidity of a substrate can dictate stem cell fate, guide the proliferation of cells, or support the maturation of differentiated tissues.[7,54,55] Softer materials often mimic the stiffness of brain tissue, promoting neural growth, whereas stiffer substrates can enhance osteogenic differentiation of stem cells, aligning with the mechanical properties of bone.[56] For example, substrate stiffness critically influences the lineage specification of hMSCs, with soft (<1 kPa), medium (8-17 kPa), and stiff (25-40 kPa) substrates guiding the multipotent cells toward neuronal, muscular, and osteoblastic differentiation, respectively,[56,57] Moreover, the material's stiffness has been shown to impact the formation of FAs, affecting their migratory behaviour.[58] Specifically, the size of FAs exhibits a biphasic correlation with cell migration speed across different rigidities. On softer substrates, cells typically form more minor FAs that facilitate faster movement, whereas, on stiffer substrates, more significant FAs are formed that initially enhance motility up to a critical size. Beyond this vital point, further increases in FA size result in impeded movement, which underscores the mechanosensitive nature of cell-substrate interactions and how the modulation of FA dynamics impacts processes, including migration. These dynamics are especially important for collective migration, a phenomenon critical in wound healing, where increased substrate stiffness amplifies friction at the cell-substrate interface.[59] In turn, it modulates the velocity and persistence of cell movements, thereby influencing the mechanical equilibrium between cell-generated forces and the resistance provided by the ECM. This control over cell migration through substrate stiffness is crucial for designing effective tissue scaffolds that facilitate specific regeneration pathways and optimize healing and tissue functionality.[56] By tailoring the mechanical properties of substrates, tissue engineers can direct cellular behaviours essential for forming and integrating functional tissues.

### 2.2.2 CHEMICAL

The chemical composition of a substrate significantly dictates the dynamics of cell-substrate interactions by contributing to the establishment of a biochemical milieu that affects cellular adhesion, proliferation, and differentiation.[60,61] Surface charge on biomaterials, defined as the net electric charge distributed over the

material's surface, is pivotal in mediating interactions between the biomaterial and cells.[62] Positive surface charges generally enhance cell attachment and proliferation by promoting protein adsorption, facilitating these processes, and promoting the differentiation of MSCs toward an osteoblast-like phenotype.[63,64] Conversely, negative charges can sometimes inhibit cell attachment by repelling specific proteins.[62,65] In this context, tailored surface charges on scaffolds can mimic the natural cellular environment, enhancing tissue repair and functionality.

Fundamentally, the surface charge can be modulated by the inclusion of several functional groups, including hydroxyl (–OH), carboxyl (–COOH), amino ($–NH_2$), and methyl ($–CH_3$) groups, which differ based on their charge and wettability and, therefore, their impact on cell function.[66-68] The wetting order of these vital functional groups has been determined to be –COOH > –OH > $–NH_2$ > $–CH_3$.[69] At physiological pH (7.4), ionization of the functional groups plays a crucial role in their interactions with biological systems.[62] For example, $–NH_2$ undergoes protonation into an amino group ($–NH_3^+$), which imparts a positive charge on the surface and attracts negatively charged ions and residues. Conversely, –COOH undergoes deprotonation to form a carboxylate group ($–COO^-$), which imparts a negative charge on the surface and attracts cationic ions and residues.

This modulation of surface charge alters the local electrochemical environment, influencing protein adsorption based on the residues within the protein and the pattern of charges on the surface.[70] However, the net charge of a protein does not necessarily dictate its adsorption behaviour, as the orientation and charge distribution across the entire protein, combined with the local conditions at the substrate interface, play a combinatory role.[71] Surface chemistry can drastically influence the adsorption conformation of fibronectin (FN), specifically around its central cell-binding domain, which can, in turn, impact the accessibility and affinity of particular integrin isoforms (e.g., α5β1) to specific sequences in FN (e.g., RGD).[72] Therefore, understanding and predicting the conformational changes induced by surface charge and its effects are integral in designing and manufacturing effective biomaterials with the intent to direct the cell response to improve tissue regeneration and function.[73]

## 2.3 TITANIUM MATERIALS

### 2.3.1 NANOTUBES (NTS)

Titanium nanotubes (NTs) have emerged as a consequential material in engineering owing to their unique properties, tunable properties (e.g., geometry and spatial organization), and various potential applications, including biomedical, sensors, and photocatalysis.[43,53,74,75] At their core, NTs are characterized by their nanoscale tubular structure, predominantly composed of titanium dioxide ($TiO_2$), a compound renowned for its robustness and biocompatibility.[76] The development of NTs marks a significant advancement in the field, particularly in enhancing material-tissue interactions. Their high surface-area-to-volume ratio, coupled with the inherent properties of $TiO_2$, make them ideal candidates for applications such as drug delivery systems, implants, and tissue engineering scaffolds.[77-79] Therefore, NTs represent a significant nanotechnology and biomedical engineering innovation, offering promising avenues for future medical advancements.

#### 2.3.1.1 *SYNTHESIS*

This multifaceted applicability of NTs is intrinsically linked to their synthesis method, which allows tailoring their physical and chemical characteristics to meet specific requirements. These fabrication techniques influence morphological attributes such as tube diameter, length, and wall thickness and impact their functional properties, including chemical reactivity and mechanical strength.[74,80-83] Several methods of NT synthesis include hydrothermal methods, which involve reacting precursors under high temperature and pressure in a water-based solvent,[84] sol-gel, where titanium alkoxides are hydrolyzed and condensed to form a gel,[85] and, most notably, within the context of this study, electrochemical anodization.[53] This latter method utilizes an electrolyte solution, often containing fluoride ions from hydrofluoric acid (HF) or ammonium fluoride ($NH_4F$), to facilitate the growth of an oxide layer on the titanium surface as it is juxtaposed against an inert counter electrode such as platinum (Pt).[53] When a voltage is applied, fluoride ions from the electrolyte penetrate this oxide layer, leading to localized dissolution and the formation of nanopores, which expand and deepen over time under an electrical field to form tubes. By controlling variables such as voltage, duration, electrolyte composition, aging, and distance between electrodes, the characteristics of the nanotubes, such as diameter, length, and wall thickness, can be precisely tailored.[81,86-88] Furthermore, the quality of the surface and the spatial organization of the NTs can be influenced and improved using multiple rounds of anodization.[53,89,90] This is because of the well-defined nucleation sites generated from the initial anodization stage and exposed by stripping the $TiO_2$ layer. This methodology enables a more controlled growth of better-aligned NTs.

#### 2.3.1.2 *CHEMICAL PROPERTIES*

The predominant feature of NT chemistry is that it is composed of $TiO_2$. This material is naturally produced through passivation when titanium is exposed to an oxygen-containing environment such as air or water. Being

inherently bioinert and non-toxic, the chemical stability of $TiO_2$ reduces the risk of inflammatory responses, ensuring that titanium nanotubes are well tolerated in biological environments, which is a crucial factor for their application in biomedical devices. The crystalline structure of $TiO_2$, which exists mainly in the anatase and rutile forms, plays a pivotal role in its chemical properties. Anatase $TiO_2$, known for its superior photocatalytic activity owing to its larger surface area, impacts the interaction with light and substances.[91] Rutile $TiO_2$, on the other hand, is valued for its stability, influencing its use in durability-critical applications. Anatase transforms into rutile during annealing, and the use of vacuum has been shown to slow this transformation and enable stable anatase structures at temperatures up to 900 °C.[92] Notably, within the context of $TiO_2$ nanoparticles (NPs), the uptake of anatase NPs was dramatically higher than that of rutile NPs, contributing to its significantly higher cytotoxic effect.[93] A critical factor in its chemistry and reactivity is the hydroxyl content of the $TiO_2$ layer, which has been shown to drastically impact the ability of peptides to adsorb on the surface. A computational study by Sampath et al. (2020) highlights the critical role of $TiO_2$ surface chemistry, particularly hydroxyl group distribution, in influencing the peptide binding mechanisms through the specific interactions of amino acids like arginine, lysine and aspartate.[94] Protein adsorption on nanotubes, shown to occur on the inter-pit spaces and within the nanopits,[60] facilitates cell-substrate interactions, including adhesion and migration,[61] and bactericidal performance.[95]

#### 2.3.1.3 *PHYSICAL PROPERTIES*

NTs are distinguished by their unique nanoscale tubular structure. Morphology, including diameter, length, and wall thickness, is critical in determining their suitability for various applications. Fundamentally, voltage control is used to achieve specific sizes. Although the dimensions achieved by voltage modulation are affected by the setup parameters (e.g., electrode distance and electrolyte composition), it is established that applying a voltage, commonly between 20–100V, is aligned with nanotubes of increasing diameter and length.[96,97] Subsequently, these aspects influence the surface area and porosity of the NT surface, which are instrumental parameters in biomedical applications. For instance, this translates to improved drug loading and release efficiency, as a large surface area allows for a higher drug adsorption capacity. Furthermore, porosity can influence the stability of adjunct coatings, including dissolving calcium phosphate (CaP) thin films.[98] Similarly, in catalysis, the increased surface area provides more active sites, thereby improving the efficiency of catalytic reactions.[99] Within nanomechanical properties, increasing the length of the NTs by increasing the voltage leads to a stark reduction in hardness and elastic moduli.[80] However, annealing can improve the elastic moduli linearly at temperatures up to 600 °C.[100] Another method to modify these properties is the use of an autoclave. Notably, Radtke et al. (2019) determined that titania nanotube coatings formed at lower voltage potentials (>15V) were not affected by autoclaving.[101] In contrast, structures formed at higher potentials were abolished, likely due to residual water-generating vapour. Precise control over these morphological and surface properties, afforded by precise

synthesis techniques such as electrochemical anodization, enables fine-tuning NTs for specific applications. By adjusting parameters such as the voltage and electrolyte composition during synthesis, the surface roughness, pore size, and tube diameter can be tailored, directly influencing these nanotubes' reactivity and interaction potential.

#### 2.3.1.4 *BIOMEDICAL APPLICATIONS*

Titanium nanotubes (NTs) have promising applications in biomedical engineering, including bone tissue engineering, intravascular stents, and biosensors. NTs have been incorporated into bone scaffolds for bone tissue engineering, enhancing osteoblast activity owing to their biocompatibility and surface properties.[102,103] This facilitates improved bone tissue regeneration. In the context of intravascular stents, the biocompatible nature of NTs and their ability to promote endothelial cell growth make them suitable for vascular implants, aiding in the rapid healing of vascular tissues.[104,105] Beyond their structural and cellular growth support roles in biomedical engineering, NTs exhibit crucial antibacterial properties, making them exceptionally versatile in medical applications.

The antibacterial properties of titanium nanotubes are another critical aspect and are vital for applications such as dental and orthopedic implants to reduce postoperative infections. Tailoring their nanoscale topography to increase roughness and surface energy has reduced bacterial growth.[106] Furthermore, the crystalline structure is crucial, with anatase phase nanotubes displaying more excellent antibacterial activity than rutile and amorphous phases, likely due to the unique electronic structure of anatase.[107] Larger diameter nanotubes also demonstrate enhanced antibacterial characteristics, possibly attributed to improved photocatalytic activity.

Additionally, antibacterial activity can be amplified by functionalizing the surface with particles such as silver nanoparticles or through implementation methods that allow for controlled elution.[108] Variably sized NT surfaces enable diverse porosity and surface area characteristics, influencing the elution of molecules; this technique has been well explored in the osteoinduction of stem cells, osteoblast differentiation, and hemocompatibility enhancement through the release of nanoparticles (e.g., copper, strontium) and drugs (e.g., naringin).[77,109-112] The loading and tuning of elution profiles are facilitated by polymeric coatings (e.g., chitosan, dopamine, polyaniline), either applied as a top layer or penetrating inside the nanotubes.

### 2.3.2 PULSED WATER-JET (PWJ) TECHNOLOGY

Pulsed Water-Jet (PWJ) technology was developed by VLN Advanced Technologies Inc. (Ottawa, Canada),[113] represents a groundbreaking method for precise material processing and surface modification. At its core, the technology harnesses the power of high-velocity pulsed water jets that deliver high-velocity water slugs that interact with the surface, inducing micro-cavitation and impulsive forces.[114] These forces effectively disrupt the surface layer, leading to the precise removal of material or contaminants without compromising the integrity of

the underlying substrate, and do so with minimal thermal or mechanical stress to the substrate. **Figure 2-2A** depicts the structural design of the PWJ apparatus, including the ultrasonic transducer, high-pressure chamber, and nozzle chamber paired with an oscillating core mechanism. **Figure 2-2B** provides a high-speed photographic capture of the water jet propagation, demonstrating the coherency and dispersion pattern of the jet under the specified steady-state parameters, which include the nozzle diameter, pressure, pulse frequency, and standoff distance. **Figure 2-2C** shows the integration of a robotic arm equipped with a pulsed-water jet attachment, safely housed within a containment unit, to ensure operational safety and mitigate any risks associated with high-pressure water jetting.

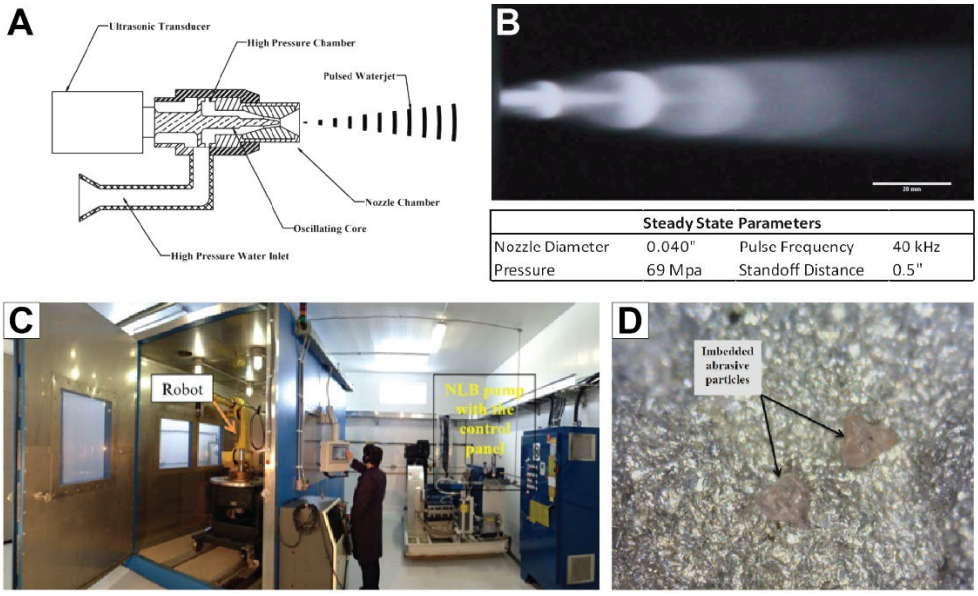


Figure 2-2: Pulsed-Water Jet (PWJ) technology

**(A)** Schematic of the PWJ and **(B)** high-speed image showing the water jet propagation during the steady state. **(C)** Typical setup with the encased robotic system. **(D) E**xample of abrasive contamination from sandblasted surface preparation.

This approach allows versatile and targeted surface alteration, enabling applications across various industries, from the aerospace and automotive industries to energy and infrastructure. Furthermore, the technique is environmentally friendly because it avoids the need for abrasive materials, as depicted in **Figure 2-2D,** or hazardous chemicals, thus positioning it as a sustainable alternative for surface cleaning, cutting, and preparation tasks.

## 2.4 POLYCATECHOLAMINE MATERIALS

The field of biomaterials benefits from the continued development of future generations that improve upon existing approaches to account for and conceivably tailor complex biological responses. In this effort, advances

have been underpinned by the discovery of naturally occurring surfaces and structures that have inspired the development of biomimetic surfaces that attempt to translate their functional properties within the context of biomaterials engineering.[115] One such material lauded for its diverse attributes, including as a bioactive surface and drug delivery platform, is polydopamine (pDA),[116,117] which is generated from the autoxidative polymerization of dopamine (DA) under alkaline conditions.

Fundamental to the polymerization, adhesive, and bioactive abilities, DA is a member of the catecholamine family of molecules, whose base structure is comprised of a catechol group (1,2-dihydroxybenzene) bridged to a terminal amine group ($–NH_2$) by an intermediate ethyl chain. The catechol group is fascinating as it can displace water molecules in place of bonding under aqueous conditions, underpinning its potential as a wet adhesive.[118,119] Naturally, the existence of similar catecholamines can lead to the potential for similar methodologies to produce surfaces based on the identity of the precursor chosen. Consequently, particular interest has been levied toward levodopa (LD), the naturally occurring precursor to DA, and norepinephrine (NE), a potential derivative of DA. Despite their significant homology, these precursors have been shown to produce polymers (i.e., polylevodopa [pLD] and polynorepinephrine [pNE]) with distinct morphological and bioactive characteristics.[120] Details of these precursors are provided in **Table 2-1**.

Table 2-1: Catecholamine precursor employed in this study

| Criterion | Dopamine (DA) | Norepinephrine (NE) | Levodopa (LD) |
|---|---|---|---|
| Formula | $C_8H_{11}NO_2$ | $C_8H_{11}NO_3$ | $C_9H_{11}NO_4$ |
| Mol. Weight (g/mol) | 153.18 | 169.19 | 197.19 |
| Structure | 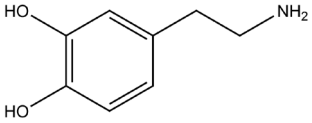 | 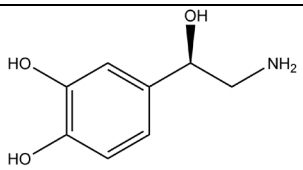 (*L-enantiomer*) | 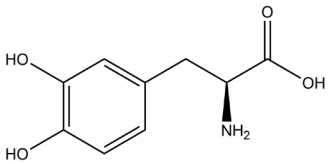 |
| Supplier *Code* | Sigma Aldrich *H8502* | **<u>Levo Enantiomer</u>** Cedarlane (Medchemexpress) *HY-13715A* **<u>Racemic mix</u>** Sigma Aldrich *A7256* | VWR (TCI America) *D06005G* |
| Notes | Supplied as DA•HCl (189.64 g/mol) | Formulated as NE•HCl (205.64 g/mol) | L-enantiomer (L-DOPA) |

### 2.4.1 POLYDOPAMINE (PDA)

Inspired by the wet adhesive abilities of common blue mussels (*Mytilus edulis*), researchers have investigated the molecular composition of their adhesive foot-like extensions ("byssus"). Analysis of the spatially distributed "*Mytilus edulis* foot proteins" (Mefp) identified a protein of interest, Mefp-5, at the plaque-substrate interface.[6,121] When sequenced, Mefp-5 contained an abundance of lysine (K) and nearly 30 mol% of DOPA (Y).[121] Taking into consideration the single molecule bonding potential of DOPA, which is a precursor of the neurotransmitter dopamine (DA),[122] Lee et al. (2007) found that reconstituting DA in an alkaline solution enabled autoxidative polymerization of DA into polydopamine (pDA).[6,120,123] This polymer coating, characterized by a nanoscale rough and globular morphology,[5] has been employed in various contexts, including as a functional biomaterial with intrinsic antibacterial properties,[124] a bioactive film for implant surface modification,[125] an immobilization coating for macromolecules (e.g., growth factors),[126] and as a versatile polymeric drug carrier platform.[127]

Typically, pDA synthesis involves 1–2 mg/mL DA in Tris-HCl (pH=8.5) as the alkaline solvent.[6,128] However, the reaction kinetics and surface characteristics are impacted by the precursor concentration, choice of solvent (e.g., PBS, $NaHCO_3$), exogenous oxidants, temperature and kinetic energy.[129-132] Materials generated are referred to as "polydopamines." However, the derivatives vary in reactivity (e.g., catechol in dopamine, o-quinone moieties in dopamine quinone).[128] The polymeric nature of pDA has been confirmed as being high molecular weight oligomers,[133], particularly trimers and tetramers.[134] Polymerization is proposed to begin with pH-induced auto-oxidation of dopamine to quinone, followed by crosslinking, oxidation and tautomerization (**Figure 2-3**).[135]

The involvement of several intermediates has been accepted.[134,136,137] In this context, the intermediate 5,6-Dihydroxyindole (DHI) is noteworthy.[128,137] Though DHI cannot generate a film, its incorporation with DA accelerates the synthesis rate beyond DA alone.[138] The DHI/DA interaction proposal pathways include DHI-DHI copolymerization, DA-DA dimer formation ahead of post-cyclization and DHI-DA dimerization ahead of DA cyclization. Lyu et al. (2019) suggested that DA readily sequesters DHI and plays a role in DA crosslinking, which is vital for pDA adhesion.[138] Conceivably, the early synthesized DHI may contribute to the high reported adhesion after depositing for 1 h, which is then sequestered DA monomers, explaining the significant drop after 2 h. Therefore, it is possible to combine DHBA with a limited DA monomer to act as an initiator, producing DHI-dense oligomers with tunable adhesion.

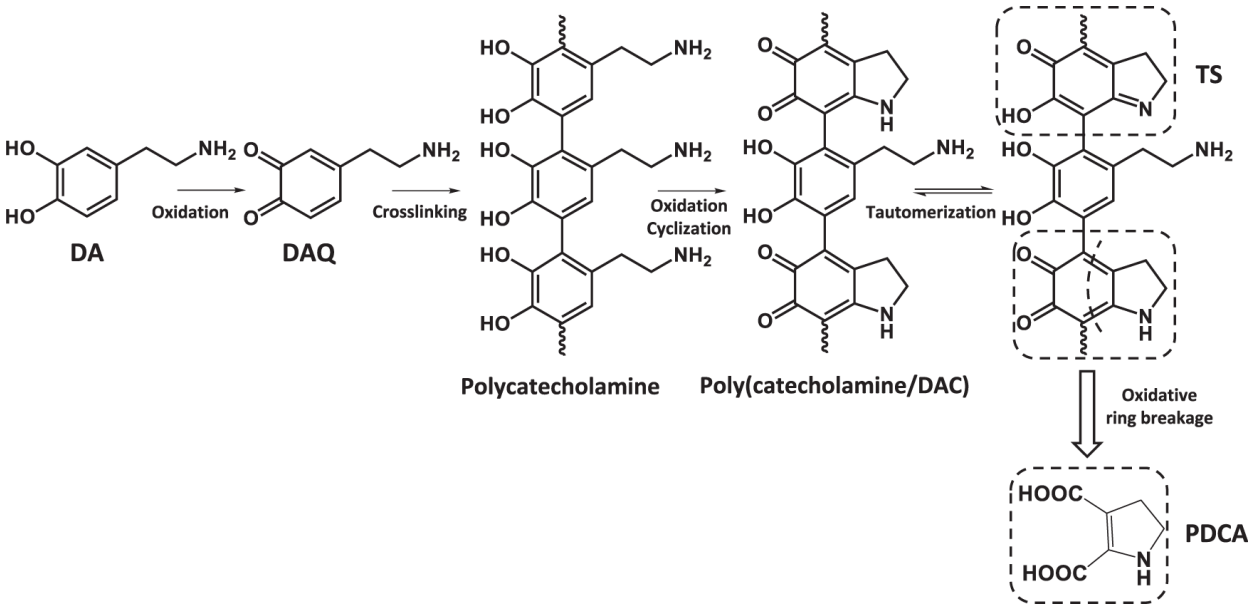


Figure 2-3: Proposed model for polydopamine film formation.

*This was reproduced by Hemmatpour et al. (2023) published by Springer Nature under Open Access (CC-BY).*

### 2.4.2 POLYNOREPINEPHRINE (PNE)

In pursuing biomimetic materials with previous work praising the versatility of dopamine-based materials, researchers have investigated the potential of structurally similar small-molecule catecholamine precursors.[118] Norepinephrine (NE) acts as a hormone and neurotransmitter. It is synthesized from the hydroxylation of dopamine by dopamine-*β*-hydroxylase (DBH) in noradrenergic neurones.[139] Under alkaline conditions, similar to those typically used for synthesizing pDA, NE undergoes an oxidative pathway for synthesizing a polynorepinephrine (pNE) material whose "ultrasmooth" and homogenous coating contrast.[120] This smooth morphology is reportedly due to the presence and inclusion of the 3,4-dihydroxybenzaldehyde (DHBA) intermediate. Applications of pNE as biocompatible surfaces have primarily focused on neuronal applications. In this context, pNE coatings on PTFE, PDMS, PS and glass substrate reported a 40–50% increase in the adhesion of human neural stem cells (hNSCs), with no significant effect on viability.[140] Furthermore, Chen et al. (2019) reported that PC12 cells on semi-patterned polycaprolactone (PCL) and polyethylene oxide (PEO) electrospun presented with a near 300% increase in average neurite length when compared to unfunctionalized microfibres.[141]

Although the mechanism for synthesizing pNE is not fully understood, the similarities in structure to pDA provide a foundation for generating several intermediates. NE may undergo cyclization and dehydration into DHI,[118] or tautomerization and non-melanogenic breakdown of O-quinone into DHBA (**Figure 2-4**), supported by the reduction in nitrogen ratio relative to the precursor.[120] The aldehyde group (–CH=O) of DHBA is believed to

interact with the amine group (–$NH_2$) of NE via a Schiff base condensation reaction, followed by reduction of the imide bond, thereby producing a DHBA-NE product whose protonated imine groups can undergo polyindolic crosslinking towards the final product of pNE.[118] Subsequently, an undetermined combination of the NE precursor, DHI and DHBA-NE polymerizes into pNE, resulting from polyindolic crosslinking contributing to π-π stacking.[118] Furthermore, while the polyindolic crosslinks of pNE may act as a π-group donor, the protonated amine groups of NE, pronated imine groups of DHBA-NE, and imine groups of DHI may contribute to cation-π interactions.

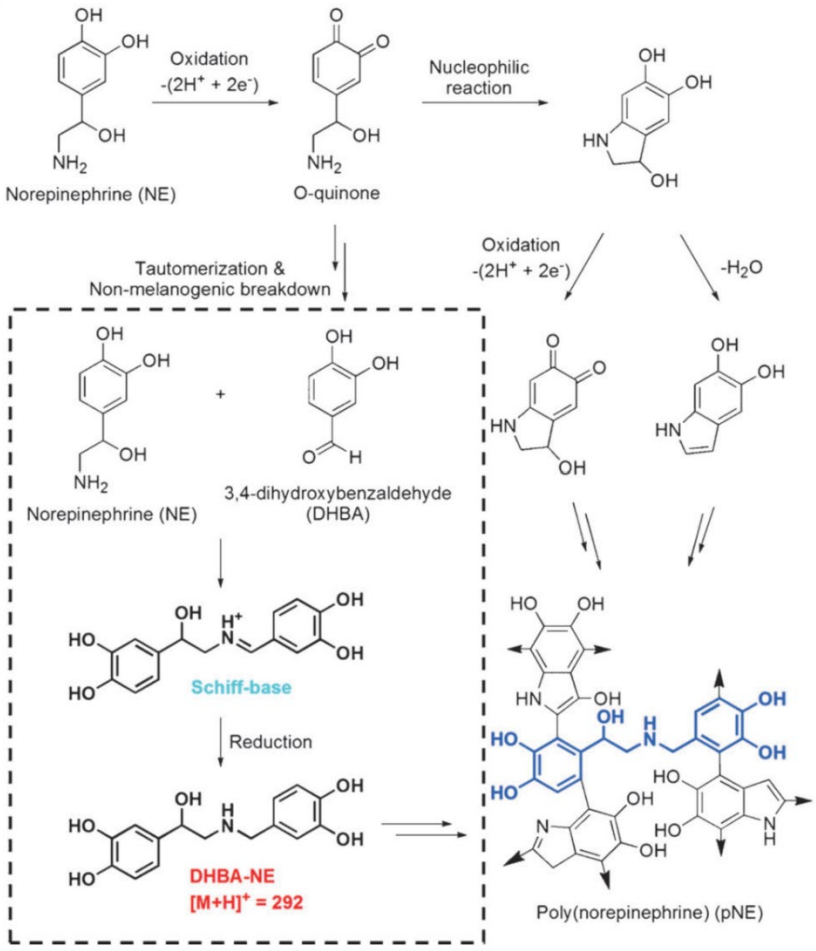


Figure 2-4: pNE polymerisation pathway.

*Adapted from Hong et al. (2013), with permission from Wiley. License ID 1434752-1.*

### 2.4.3 POLYLEVODOPA (PLD)

Levodopa (LD) is a catecholamine molecule that undergoes decarboxylation to form DA.[142] Consequently, the homology between these molecules has led to limited interest in using LD as a precursor to the formation of polylevodopa (pLD) coatings, presumably with potential as a viable biological platform similar to pDA and pNE. However, within the limited amount of literature, few articles employ pLD as a direct biomaterial platform with the lion's share capitalizing on the functional groups of pLD (–OH, –COOH, and $–NH_2$) to enhance the dispersion of AgNPs,[143] the coating of graphene to make water-processible conductive paints,[144] its use with $TiO_2$ nanoparticles to create a high affinity molecularly imprinted sensor for pesticides,[145] and the coating of capillaries for enhanced enantioseparation in open tubular electrochromatography (OT-CEC).[146]

Although the synthesis of pLD has not been investigated or described in detail as pDA or pNE, a suggested reaction mechanism by Tan et al. (2021) begins with the cyclization of LD (L-3,4-dihydroxyphenylalanine) into DHICA (5,6-dihydroxyindole-2-carboxylic acid) which is similar to the DHI (5,6-dihydroxyindole) seen in pDA and pNE synthesis, through a carboxylic acid group at the 2nd carbon of the pyrrole ring (**Figure 2-5**).[120] At this stage, DHICA may undergo decarboxylation into DHI, supported by the XPS elemental analysis indicating a significant 6% drop in the oxygen content in pLD compared to the LD precursor ($O\%_{LD}$≈29; $O\%_{pLD}$≈23). As approximately 80% of O is retained in pLD, it is suggested that the next step involves the oxidative mixed polymerization of DHICA, which did not undergo decarboxylation, and DHI, which did. However, in a reaction mechanism representing pLD nanoparticle formation, Bigdeli et al. (2017) suggested that oxidation of the–OH groups on the benzene ring occurs first, converting LD into L-dopaquinone.[147] The cyclization of dopaquinone follows this into dopachrome, which undergoes covalent polymerization, resulting in pLD solely comprising dopachrome subunits. The primary differences between these mechanisms are the intermediates generated and the sequence of oxidation and cyclization; however, neither mechanism has been confirmed. Of interest is that dopachrome in Hormozi-Nezhad et al. (2016) can tautomerize to form DHICA in Tan et al. (2021),[148] for which DHICA has shown to be a significant antioxidant and impacts the cross-talk between epidermal cells.[149]

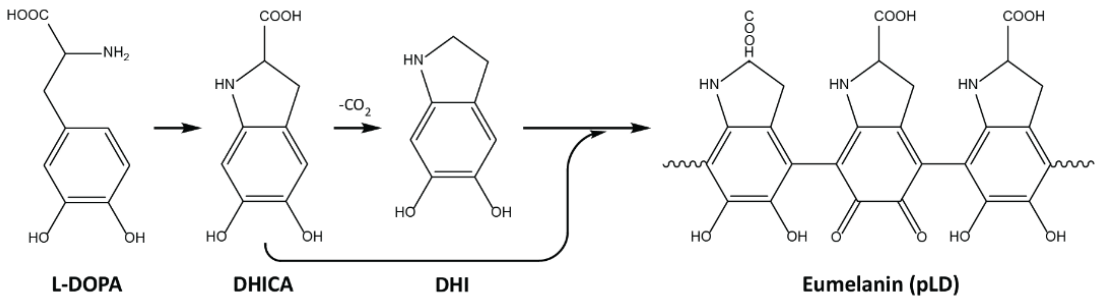


Figure 2-5: Polylevodopa synthesis pathway.

### 2.4.4 CHEMICAL PROPERTIES

These differences in material properties between these precursors indicate how tiny alterations in the catecholamine structure can drive significant chemical differences that influence surface formation. Summary tables for the chemical properties are provided in **Table 2-2**.

Table 2-2: Summary of the chemical properties of precursors and surfaces

| Parameter | Rank 1 | Rank 2 | Rank 3 | Notes |
|---|---|---|---|---|
| **Standard electrode potential (SEP)** | DA (0.829 eV) | LD (0.847 eV) | NE (0.851 eV) | Related to oxidation activity |
| **Intrinsic reaction coordinate energy (IRC)** | NE (49.5 kJ/mol) | DA (50.8 kJ/mol) | LD (56.3 kJ/mol) | Inversely related to cyclization activity |
| **Static water contact angle (WCA)** | pLD (29 ± 2°) | pNE (38 ± 3°) | pDA (45 ± 2°) | Ranked by hydrophilicity (lowest angle) |
| **Amine ($NH_2$) content** | pDA | pNE* (-39%) | pLD* (-45%) | Measured by Acid Orange II |
| | | * | | |
| **Phenolic Hydroxyl (Ph–OH) content** | pDA | pNE (-21%) | pLD (-70%) | Measured by micro-BSA |
| *Statistically similar values | | | | |

Shared in their respective syntheses is their reliance on two crucial stages: the precursors' oxidation and the intermediaries' cyclization. These are the rate-limiting steps to forming 5,6-Dihydroxyindole (DHI), an essential molecule in the proposed pDA, pNE, and pLD mechanisms. The propensity for precursor oxidation can be described by the standard electrode potential (E°) for the catechol-to-quinone transition. At standard deposition conditions (pH=8.6), Zhang et al. (2022) reported E° for DA ($E^{\circ}_{DA}$=0.829 eV), LD ($E^{\circ}_{LD}$=0.847 eV) and NE ($E^{\circ}_{NE}$=0.851).[150] Having the lowest E°, DA is the most likely to oxidize due to the absence of functional groups along its ethyl chain. However, the carboxyl group (–COOH) of LD and the hydroxyl group ($–OH^-$) of NE transform the intramolecular electron cloud and suppress the electron loss potential of phenolic hydroxyls. In a similar context, substituents of oxidized precursors can transform the electron density cloud again and impede cyclization between the phenol and amide moieties that generate the indolic structures.[118] Assessment of the intrinsic reaction coordinate energy (IRC) represents the energy barrier for cyclization. Therefore, it is inversely related to the cyclization potential. Accordingly, NE is reported as having the most significant cyclization potential ($IRC_{NE}$=49.5 kJ/mol), followed by DA ($IRC_{DA}$=50.8 kJ/mol) and LD ($IRC_{LD}$=56.3 kJ/mol).[150] When considering the rankings for oxidation activity (↑DA, LD, NE↓) and cyclization activity (↑NE, DA, LD↓) against the yield of DHI being highest for DA at 1 h, the oxidation step appears to be the primary rate-limited step, followed by cyclization.

In their polymer forms, each surface possesses distinct concentrations of phenolic hydroxyl (Ph–OH) groups that indicate the interfacial capability, measured by amine ($–NH_2$) groups that indicate functionalization potential.[120] Being polar functional groups, Ph–OH groups participate in intermolecular interactions, such as hydrogen bonding. The precursors possess two hydroxyl groups on their benzene ring, and non-canonical phenolic polymers reported peak adhesion with four $–OH^-$ groups, with little benefit from a fifth group.[151] However, the importance of the amine groups should not be overlooked—their substitution with a hydroxyl group results in materials with impaired adhesion and film formation.[152] The adhesion between pNE-pNE layers, representing pCAs, is approximately 30 times higher than that of polycatechol coatings.[118] This is suggested to be due to the interplay between amine groups and quinone moieties, which generate crosslinked oligomer structures responsible for the transient adhesion peak at early time points.[153] Furthermore, amine groups provide a significant opportunity for their functionalization owing to their positive charge at physiological pH. Micro-BSA protein analysis showed that pDA contains the most considerable component of Ph–OH, followed by pNE (-21%) and pLD (-70%) trailing in the back.[120] Acid Orange II analysis revealed that pDA possesses nearly twice the amine group content than pNE (-39%) or pLD (-45%). However, the use of these methods is questionable, and other methods for the assessment of Ph–OH groups (e.g., Folin–Ciocalteu assay) and amine content (e.g., ninhydrin assay) are preferred, ideally with a solution versus coatings of the molecules of interest.

Considering that the ranking of Ph–OH and $–NH_2$ functional groups is similar (↑DA, NE, LD↓), the roles and activities of these cell-facing moieties are essential for understanding the bioactivity of the surfaces. In this context, HUVEC adhesion was assessed on self-assembled monolayers (SAMs) with hydroxyl or amine group functionalization, indicating that compared to hydroxyls, the amine groups increased the fraction of adhered cells by 54%, and their area by 66%.[66] Notably, when carboxyl group (–COOH) functionalization was considered, researchers were reported to match the amine group condition for a fraction of adherent cells and even outperform it with a 17.6% greater interfacial area. However, this effect is not necessarily due to the direct interaction of the cell with the functional group.

Taken together, the chemical properties of these surfaces lead to drastic changes in their morphology and composition of resultant surfaces. For example, in surface chemistry, when compared to DA, additional hydroxyl groups (–OH) on NE and carboxyl groups (–COOH) on LD contribute to differences in their reaction mechanisms and, therefore, the presence and distribution of their respective intermediates.

### 2.4.5 MECHANICAL PROPERTIES

#### 2.4.5.1 *POLYDOPAMINE (PDA)*

The pDA possesses viscous and time-dependent elastic properties. In the context of Young's modulus, the high variability of reported values for pDA include 12.1 MPa, 92 MPa, 870 MPa, 6.3 GPa, 9 GPa and 4.3–10.5 GPa on gold, titanium, mica, polystyrene, glass and silica substrates, respectively.[5,132,154-157]

The adhesion component of pDA is valuable for understanding surface evolution. Through the prototypical methodology that uses a deposition period of 24 h,[53,132] literature suggests that adhesion is time-dependent and may peak at early time points (<3 h).[150,158] Specifically, Zhang et al. (2022) reported a 26% decrease in adhesiveness from 1 h ($F_{Adh\_1h}$=71.62 mN/m) to 2 h ($F_{Adh\_2h}$=52.82 mN/m). These results may be due to early adhesive species, particularly (DHI), whose π-conjugated electron densities enable cation-π interactions, undergoing sequestering by DA monomers or deprotonation of DHI, a suggested rate-limiting step at a rate inversely proportional to $H^+$ concentration.[134,159,160] This is supported by adding sodium persulfate to accelerate the kinetics, producing a >60% lower adhesion force at 1 h ($F_{Adh\_1h\_SP}$=27.66 mN/m), indicating a further along reaction.[150] Additionally, post-processing via annealing is an effective method to modulate mechanical properties and cellular responses.[161] However, considering that there are cell-specific optima of Young's modulus for spreading and migration,[57] a balance between adhesion and elasticity should be regarded as for interfacial phenomena (e.g., spreading and migration).

Lastly, an aspect of pDA that had previously been overlooked is the properties of discrete structures, namely, the difference between a deposited film and aggregates. Our lab previously performed an AFM-based nanomechanical analysis of pDA surfaces deposited with and without motion. This methodology resulted in a rough surface (rPDA) due to numerous, more significant aggregates than a typically smooth pDA (sPDA).[132] The bulk material was found to have several similar mechanical properties (e.g., stiffness), and structural discrimination led to the determination that aggregates required significantly less adhesion force (-80%) and detachment energy (-97.5%) to detach the AFM tip. Our results suggest that the presence of aggregates may significantly affect the practical application of pDA. For studies that intend to capitalize on material benefits for cell adhesion or particle capture (e.g., drug delivery),[117] the characteristics of the bulk material are not sufficient to model the capacity of the aggregates or nanoparticles.

#### 2.4.5.2 *POLY-L-NOREPINEPHRINE (PLNE) AND POLYLEVODOPA (PLD)*

The mechanical analysis of pNE and pLD surfaces is primarily sourced from Zhang et al. (2022), who reported a deposition period of 1h on the mica substrate, which is not congruent with typical deposition periods that span closer to 24 h at which the mass and thickness of coatings reach equilibrium.[6] Regardless, pDA was reported as having the greatest adhesion ($W_{ad}$=15.28 mN/m), followed distantly by pLNE ($W_{ad}$=3.89 mN/m) and pLD ($W_{ad}$=1.06 mN/m). The relationship between pDA and pLNE is interesting when consolidating water contact angle (WCA) results. Despite having a lower contact angle ($WCA_{pLNE}$=38 ± 3°; $WCA_{pDA}$=45 ± 2°), pLNE presented 78.7% lower adhesive strength than pDA after 1 h of polymerization.[150] Notably, Zhang et al. (2022) did not analyze pLNE surfaces deposited after 1 h, despite reporting that pDA experienced a 26% decrease in adhesiveness at 2 h ($pDA_{2h}$=52.82 mN $m^{-1}$). Nevertheless, these results may be attributed to the lower –OH and $–NH_2$ groups of pLNE and pLD compared to pDA, which appear misleading. For example, pLNE and pLD are reported as having

20% and 70% less phenolic hydroxyl (Ph–OH) groups,[120] but 75% and 93% lower adhesion, respectively.[150] However, essential to consider is the time difference for deposition between the adhesion analysis (1 h)[150] and the functional group analysis (24 h).[120]

### 2.4.6 CASE STUDY: ELUCIDATING STRUCTURE-FUNCTION RELATIONSHIPS GOVERNING THE INTERFACIAL RESPONSE OF HUMAN MESENCHYMAL STEM CELLS TO POLYDOPAMINE COATINGS

*Relevant manuscript*

**Elucidating structure-function relationships governing the interfacial response of human mesenchymal stem cells to polydopamine coatings**

Alexander J. Steeves[1,2], Fabio Variola[1-4#]

[1] Faculty of Engineering, Department of Mechanical Engineering, University of Ottawa, Ottawa, ON, Canada.
[2] Ottawa-Carleton Institute for Biomedical Engineering, Ottawa, Canada.
[3] Faculty of Medicine, Department of Cellular and Molecular Medicine, University of Ottawa, Ottawa, ON, Canada.
[4] Children's Hospital of Eastern Ontario (CHEO), Ottawa, ON, Canada.

**Submitted** on **2019–10–06** to the **Journal of Materials Chemistry B**

**Accepted** on **2019–11–10 | DOI:** 10.1039/C9TB02188D

***Front Cover Article***

*This section offers an overview of a closely related publication that originated during my MASc studies and was completed and published during my PhD. While most research was undertaken during the MASc phase, further analysis, experiments, figure generation, manuscript preparation, and publication were completed during the PhD stage. Although this article does not qualify as an independent contribution to this thesis, it was completed in my PhD and laid the foundation for refining the parameters of standalone polymer coatings. A summary of each section is provided below:*

#### *MOTIVATION*

Integrative biomaterials seek to capitalize on physical and chemical cues to direct cell behaviour. In 2016, we examined the response of pre-osteoblastic MG-63 cells to nanoporous titanium with and without the prototypical dip-coating of pDA, denoted as "statically deposited polydopamine" (sPDA).[5] This work highlighted the positive bioactive component of pDA, considering physical and chemical properties, which led to enhanced proliferation and adhesion compared to the modified nanoporous titanium substrate alone. In the same year, Su et al. (2016) provided evidence that if the unadulterated DA solution is subject to rotation during deposition, a unique surface is produced, termed "rotationally deposited polydopamine" (rPDA).[131] Although the rPDA surface showed enhanced antibacterial effects against gram-positive and gram-negative bacteria, its cellular impact was primarily assessed for cytotoxicity in HeLa cells. This lapse presents a research opportunity to explore the physicochemical properties of the substrate and the associated cellular response, particularly in bone-derived human mesenchymal stem cells (hMSCs). In this context, whereas Steeves et al. (2016) investigated the impact of an adjunct pDA coating to modify the interfacial substrate, this study examined the modification of coating properties.

### *OBJECTIVES AND HYPOTHESES*

Our primary objectives were twofold: first, to discern the mechanical and chemical distinctions between the novel rPDA surface and its sPDA counterpart, and second, to analyze their relative bioactive impacts. This study offers an in-depth physicochemical examination of both standard sPDA and rPDA and insights into how human mesenchymal stem cells differentially engage with these substrates. We hypothesized that while the substrates might share chemical and nanomechanical similarities, the pronounced presence of microscale aggregates and a more pronounced underlying globular and rough texture could enhance cellular interactions.

#### 2.4.6.1 *ABSTRACT*

The deposition of mussel-inspired polydopamine (pDA) has rapidly emerged as a simple yet effective strategy to functionalize the surfaces of biomaterials. The experimental simplicity of the deposition process, combined with its native bioactivity and bioadhesive properties, makes pDA an attractive solution for biomedical applications ranging from functional biomaterials for tissue engineering to antibacterial surfaces. Unveiling the interplay among deposition parameters, physicochemical properties of the resulting structures, and their functions is fundamental to unlocking more sophisticated knowledge of pDA biofunctionalization and its role in controlling critical biological events, such as stem cell response. Although the mechanism for the bio inductive capacity of pDA is not fully understood, the surface topography, chemistry, and adhesive properties are believed to play a critical role, individually or in combination. This study addresses the differential effects of these surface properties on pDA bioactivity. We achieved novel insights into the physicochemical makeup of two pDA coatings obtained by varying a critical parameter (i.e., solution agitation) during the deposition. We focused on the effects on human mesenchymal stem cells (hMSCs) under both standard and serum-free culture conditions. This study revealed serum-dependent and independent cueing in the bioactive induction caused by pDA.

#### 2.4.6.2 *INTRODUCTION*

Understanding how cells interact with natural (e.g., extracellular matrix) and synthetic (e.g., biomaterials) substrates remains challenging. Surface physicochemical properties can alter the cytoskeletal organization and cellular dynamics, influencing signalling pathways that dictate cell fate.[38] In bioengineering and regenerative medicine, the cellular response at the biomaterial-host tissue interface determines the success of an implanted device.[162,163] Research has investigated micro- and nano-structured surfaces to understand the relationship between surface features and cellular reactions, such as proliferation and differentiation.[32,164] This exploration aids in designing functional biomaterials and understanding cell biology, emphasizing the significance of pinpointing physical and chemical factors influencing cell activity.

Polydopamine (pDA), inspired by mussels, is a functional biomaterial that controls biological interfaces. Research into Mytilus edulis mussels showed that the essential adhesive protein Mefp5 contains L-DOPA,

dopamine's precursor.[6] This led to the generation of an adhesive pDA coating, which can coat various substrates and is frequently used to immobilize bioactive agents, bestowing novel properties like bacterial resistance and enhanced cellular functions.[165] In addition to many studies using pDA as a linker or in composites,[166,167] it also inherently has antibacterial capabilities.[168] A deposition rotation method produced a pDA surface with heightened antibacterial activity with no cytotoxic effects on HeLa cells.[131] It's believed that pDA's bio inductive properties might be linked to its interaction with serum proteins,[169] which are crucial for cell colonization.[170] However, our prior research indicated no direct correlation between pDA's effect on protein adsorption and enhanced osteoblastic cell growth.[5] To further understand pDA's bioactivity, we studied structure-function relationships in pDA coatings and observed human mesenchymal stem cell (hMSCs) responses, given their potential in future therapeutic applications.[171,172]

Our findings reveal that rotation during deposition creates a pDA surface with increased antibacterial properties and significantly boosts hMCS bioactivity. The surface interacts synergistically with serum proteins, indicating that pDA's unique physicochemical attributes of pDA complement those of the surrounding environment for beneficial outcomes. In conclusion, our study offers a deeper understanding of pDA's bio inductive mechanisms of pDA, supporting rPDA's potential of rPDA in bioengineering and regenerative medicine.

#### 2.4.6.3 *RESULTS AND DISCUSSION*

##### 2.4.6.3.1 MORPHOLOGY AND NANOMECHANICAL PROPERTIES

The topographical features of the r- and s-PDA coatings were examined by scanning electron microscopy (SEM) and Atomic Force Microscopy (AFM). SEM identified a granular pDA film and nano-to-micro surface aggregates following previous studies (**Figure 2-6A**).[5,131] The interaggregate regions of rPDA were found to be larger and more globular (**Figure 2-6B**). These aggregates were categorized as small (<300 nm) and large (>300 nm) based on their size. The small and large aggregates were larger on rPDA than on sPDA, with average sizes 70% and 131% larger, respectively (**Figure 2-6C**). The significant statistical deviation of these features on rPDA, based on the absolute values, suggests that the formation of aggregates on this surface is inherently stochastic and unpredictable. The mechanism of aggregate formation remains unclear, but Tris-HCl is linked to larger aggregate sizes than other common solvents.[130] Prior research indicates that the interplay between temperature and deposition methods (static, shaking, stirring) can rapidly influence pDA film kinetics.[173]

The mechanics of polymeric substrates affect cell behaviour. Using a digital pulsed force mode atomic force microscope (DPFM-AFM), we studied the nanomechanical properties, such as stiffness and adhesion force, along with the topography (**Figure 2-7A**). The values between substrates were relatively similar, and significant variances in the aggregate and inter-aggregate areas were found (**Figure 2-7B**).

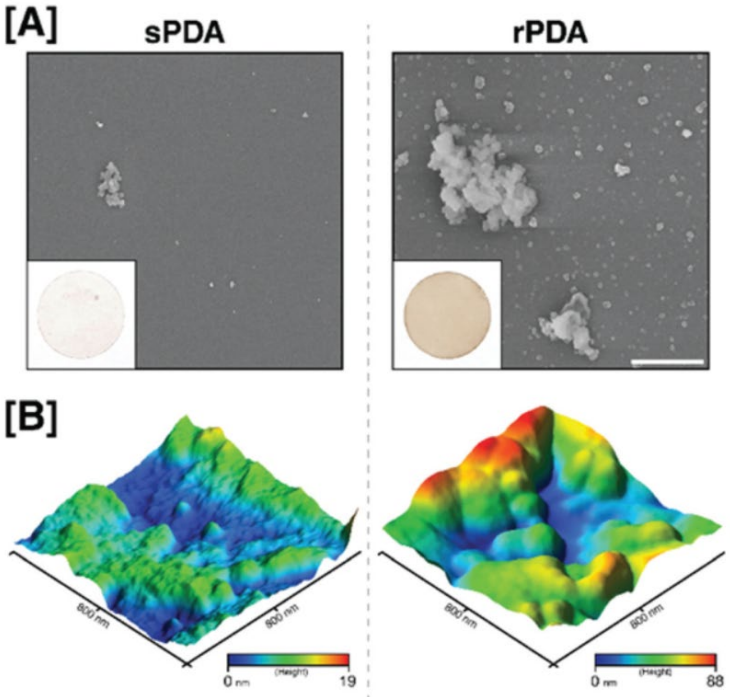


[C]

| Surface | Interaggregate Region (0.75 x0.75 µm) | | Global (6 x6 µm) | | | |
|---|---|---|---|---|---|---|
| | RMS[a] (nm) | Surface Area[a] (µm²) | RMS[b] (nm) | Surface Area[b] (µm²) | Aggregate Structure Dia. (nm) | Height (nm) |
| sPDA | 4.4 ± 1.4 | 0.57 ± 0.1 | 5.2 ± 2.1 | 36.4 ± 7.7 | 117 ± 57 | 9.6 ± 57 |
| rPDA | 20.1 ± 5.4 | 0.62 ± 0.2 | 95.6 ± 12.7 | 42.6 ± 8.3 | 901 ± 344 | 382 ± 116 |

*Abbreviations*: RMS, Root Mean Squared Roughness; Dia., Diameter
*a* Control RMS 0.4 nm and SA 0.56 µm²
*b* Control RMS 0.6 nm and SA 36 µm²

Figure 2-6: SEM and AFM visualization of sPDA and rPDA

**(A)** SEM and optical (*inset*) images of sPDA and rPDA. Scale bar = 3 µm. **(B)** AFM micrographs of the sPDA (*left*) and rPDA (*right*). **(C)** Quantification of the morphological parameters.

[A]

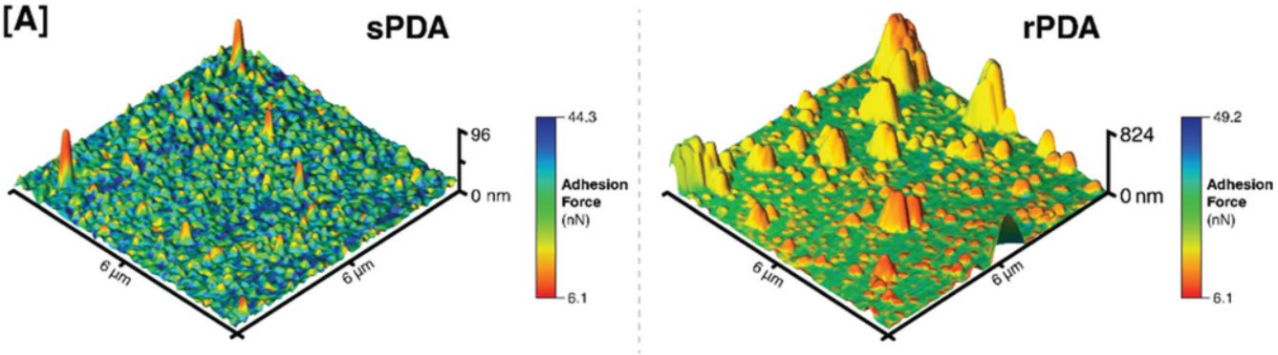


[B]

| Properties | sPDA | | | rPDA | | |
|---|---|---|---|---|---|---|
| | Interaggregate | Aggregate | Global | Interaggregate | Aggregate | Global |
| Stiffness (N/m) | 1.9 ± 0.1 | 1.9 ± 0.1 | 1.9 ± 0.19 | 2.0 ± 0.2 | 1.9 ± 0.1 | 2.0 ± 0.1 |
| Young's Modulus[a] (GPa) | 2.6 ± 3.1 | 8.4 ± 1.6 | 5.2 ± 3.7 | 3.5 ± 2.9 | 7.8 ± 2.3 | 6.7 ± 4.0 |
| Adhesion Force (nN) | 35.7 ± 6.5 | 7.6 ± 0.8 | 22.7 ± 15.3 | 37.4 ± 7.6 | 7.6 ± 0.8 | 24.6 ± 16.3 |
| Detachment Energy (nJ) | 1057 ± 354 | 57.0 ± 10.8 | 595 ± 576 | 1162 ± 445 | 56.9 ± 10.7 | 688 ± 655 |
| Hysteresis (nJ) | 5.8 ± 1.2 | 6.35 ± 1.4 | 5.9 ± 1.9 | 5.9 ± 1.3 | 6.6 ± 1.6 | 6.3 ± 2.7 |
| Compliance (N/m) | 0.53 ± 0.03 | 0.57 ± 0.02 | 0.54 ± 0.03 | 0.54 ± 0.03 | 0.57 ± 0.02 | 0.54 ± 0.03 |
| Hardness (MPa) | 22.4 ± 0.9 | 20.9 ± 0.7 | 21.7 ± 0.8 | 21.2 ± 0.6 | 20.9 ± 0.7 | 21.1 ± 0.6 |

*a* Measured using the DMT model which takes work of adhesion into consideration

Figure 2-7: Nanomechanical analysis of surfaces with DPFM-AFM

**(A)** DPFM-AFM micrographs of sPDA and rPDA showed variations in the adhesion force concerning topographical features. **(B)** Summary of quantified nanomechanical properties.

Notably, the force and energy required for detachment from the films were higher than those needed for the aggregates. Detaching from the film required an approximately 7-fold greater force and 40-fold greater energy. Concerning the Young's modulus, aggregates on both surfaces showed a higher elastic modulus (7.8–8.4 GPa) than the underlying film (2.6 to 3.5 GPa). Comparatively, the elastic modulus of the films is in the lower range of common polymers, similar to that of polymethylmethacrylate (PMMA, 2.4 GPa), while the aggregates are in the middle of the previously reported range of pDA surfaces (4.3–10.5 GPa).[5,123] Accordingly, the global Young's modulus of rPDA (6.7 GPa) was greater than that of sPDA (4.8 GPa), resulting from greater aggregates across the rPDA surface. Tuning the pDA surface through aggregate structure and prevalence may allow for better control of chemical cueing (e.g., targeted adsorption) or in generalized applications where pDA is used as a bioadhesive.

#### 2.4.6.3.2 SURFACE CHEMISTRY AND WETTABILITY

X-ray photoelectron spectroscopy (XPS) and Raman imaging were used to assess the chemical composition of the pDA coatings and determine whether stirring during deposition influenced the chemical properties, similar

to temperature variations.[173] High-resolution XPS spectra from C 1s, O 1s, and N 1s regions are depicted in **Figure 2-8A** with binding energies in **Figure 2-8B**. Although secondary amines remained dominant in the N 1s region, the increased tertiary amines in our samples might stem from the high Tris concentration (25 mM vs. 10 mM).[152,174] The O 1s region highlighted alcohol and carbonyl functional groups (C=O), with hydroxyl groups predominating, and is best explained by the conversion of intermediate quinone carbonyl groups to indole hydroxyl groups during the covalent binding of Tris amino groups (e.g., 5,6-indolequinone → 5,6-dihydroxyindole).[130]

In the case of Raman analysis (**Figure 2-8C**), spectral deconvolution allowed us to identify the specific bands that constitute the characteristic signature of pDA in the 900–1600 $cm^{-1}$ region (**Figure 2-8D**). Notably, the spectra collected on the rPDA substrates displayed an evident decrease in the relative intensity of the band at 1370 $cm^{-1}$, which is associated with C–N–C stretching in the indole aromatic ring. This signal may be due to an increased prevalence of the (DHI) intermediate in aggregate structures, which we showed to be considerably larger in size and number on rPDA surfaces. This hypothesis is supported by recent work by Lyu *et al.* (2019), which indicates that aggregates may result from the copolymerization of DHI and uncyclized dopamine intermediates.[138]

The surface topography and chemical makeup of a material impact the surface wettability.[175] XPS data revealed uniform chemistry across both surfaces. Using contact angle measurements, we found that sPDA surfaces had a much lower 52° static contact angle than the 78° static contact angle of bare glass coverslips (**Figure 2-8F**).[131,176] Notably, rPDA presented a significantly lower angle of 26°. Variations in the rotational deposition process could explain these discrepancies as larger nano- and micro-structures may enhance wetting by allowing better droplet immersion in surface asperities.[129]

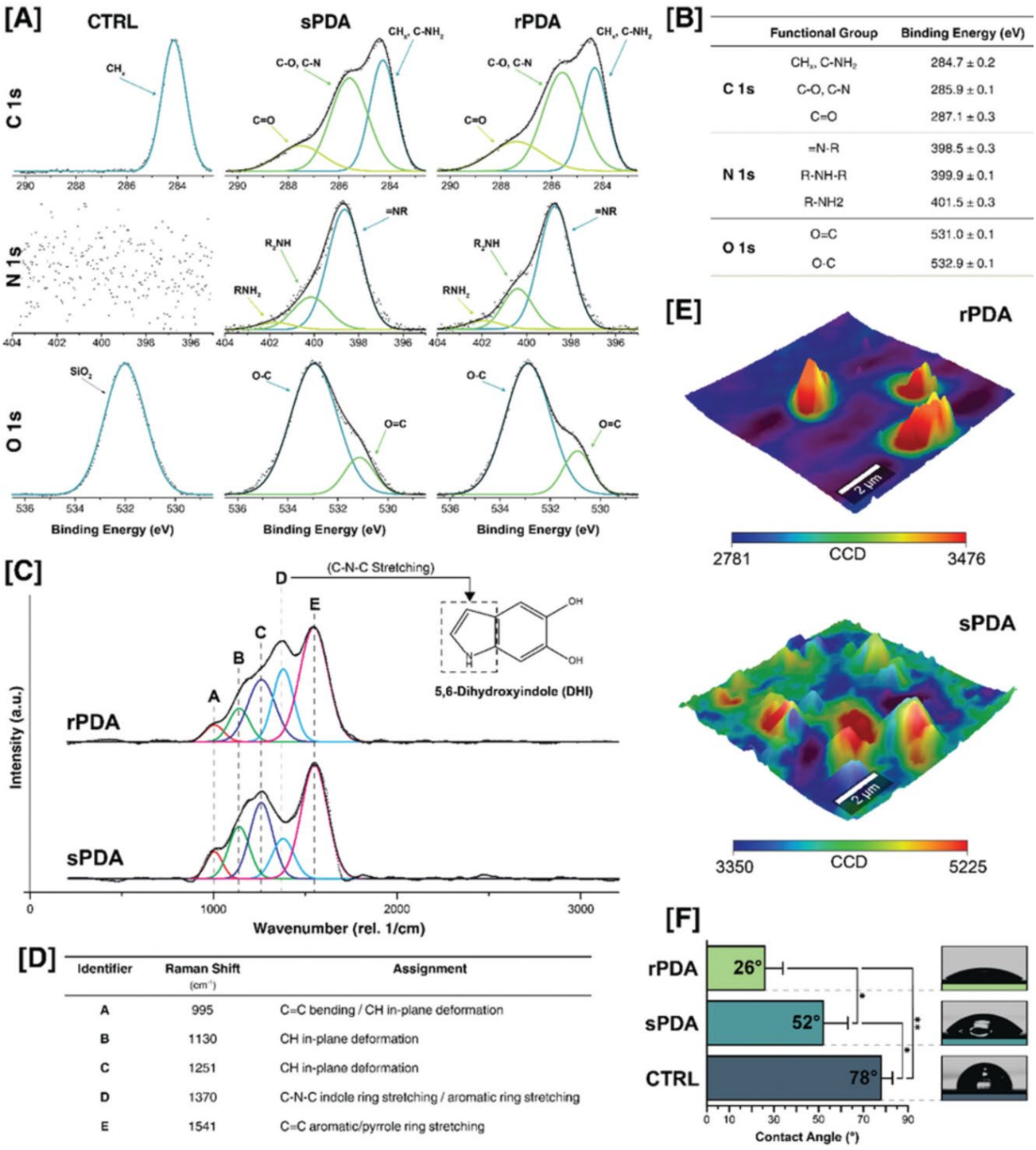


| | Functional Group | Binding Energy (eV) |
|---|---|---|
| C 1s | $CH_x$, C-$NH_2$ | 284.7 ± 0.2 |
| | C-O, C-N | 285.9 ± 0.1 |
| | C=O | 287.1 ± 0.3 |
| N 1s | =N-R | 398.5 ± 0.3 |
| | R-NH-R | 399.9 ± 0.1 |
| | R-NH2 | 401.5 ± 0.3 |
| O 1s | O=C | 531.0 ± 0.1 |
| | O-C | 532.9 ± 0.1 |

| Identifier | Raman Shift ($cm^{-1}$) | Assignment |
|---|---|---|
| A | 995 | C=C bending / CH in-plane deformation |
| B | 1130 | CH in-plane deformation |
| C | 1251 | CH in-plane deformation |
| D | 1370 | C-N-C indole ring stretching / aromatic ring stretching |
| E | 1541 | C=C aromatic/pyrrole ring stretching |

Figure 2-8: Surface chemistry and wettability analysis

**(A)** XPS spectra of the glass CTRL, sPDA, and rPDA. **(B)** XPS Binding Energy Assignment. **(C)** Representative Raman spectra of rPDA and sPDA. **(D)** Raman band assignments. **(E)** AFM-Raman overlay to display the correlation between variations in the benzene ring stretching modes (800–1800 $cm^{-1}$) and morphological features. **(F)** Contact angle goniometric measurement.

#### 2.4.6.3.3 CELLULAR RESULTS

**CELL MORPHOLOGY:** Like stiffness and micro-/nano-topography, biomaterial surface properties influence integrin-ECM binding group activation, impacting cell spreading and motility kinetics.[123,177] Using fluorescence microscopy images processed in a custom Cellprofiler pipeline, cell attributes like area, perimeter, form factor, and compactness were quantified. However, these metrics struggle to differentiate morphologies with jagged contours and irregular protrusions, such as protrusive, multipodal, and multipolar forms, which were manually classified (**Figure 2-9A**).

At 1 h (**Figure 2-9A,C**), hMSCs on sPDA and rPDA surfaces showed a significantly more spread morphology than controls, with 94% and 95% greater relative areas, respectively. While cell areas on sPDA and rPDA were similar, their perimeters differed, with enhancements of 34.1% and 77.6%, respectively, compared with controls. These results suggest more jagged contours on the pDA surfaces. The similarity in the cell areas was attributed to early-stage isotropic spreading. The difference in multipolar morphology between pDA samples was due to increased protrusive morphologies in rPDA, characterized by minimal area changes but significant perimeter variations.[35,178,179] By 4 h (**Figure 2-9A,D**), cell area and perimeter differences were less pronounced. However, the rPDA cells displayed greater compactness, suggesting a more irregular morphology. This outcome aligns with the multipolar morphologies and indicates mature focal adhesion, generating cell traction forces via actin stress fibres.[180] At 24 h (**Figure 2-9E**) rPDA cells were smaller by 19.3% compared to controls. This reduction in cell area on rPDA is attributed to the transition to late-stage morphologies, such as multipolar ones, which have a more contracted structure. The decrease in cell area and perimeter in the rPDA is believed to be due to cell body contraction, resulting in a uniform aspect ratio. Rac1-dependent recruitment and actinomyosin-mediated contraction during adherence indicate the onset of cell traction forces, leading to polarization and migratory behaviour.[181-184] In summary, rPDA surfaces promote advanced cell spreading more effectively than sPDA surfaces, facilitating integrin-mediated cell-substrate adhesion and earlier traction force generation via the actin cytoskeleton. This interaction might accelerate cell functions like cyclin D1 expression, influencing subsequent cell activities, including differentiation.[185]

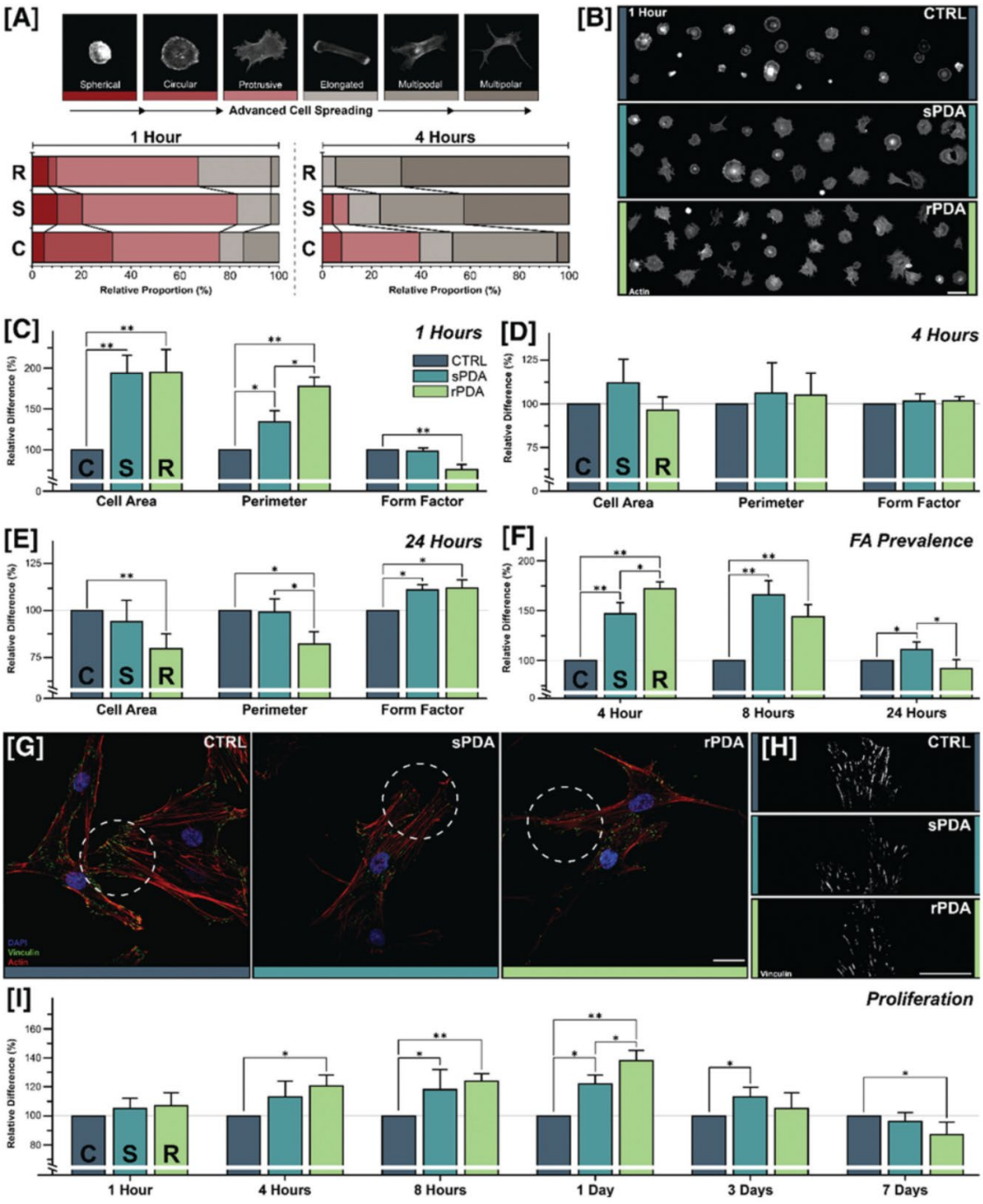


Figure 2-9: Morphology and proliferation analysis

**(A)** Morphology exhibited through the advancement of cell spreading, as visualized with phalloidin, with correlated colour bars (top). The relative proportions of morphologies were categorized from hMSCs incubated in serum-containing media and seeded on the CTRL (C), sPDA (S), and rPDA (R) surfaces. **(B)** Fluorescence images showing different morphologies of hMSCs adhering to their respective surfaces after 1 h. Scale bar = 100 µm. Quantitative morphological parameters at **(C)** 1 h, **(D)** 4 h and **(E)** 24 h. **(F)** Focal adhesion prevalence in the first 24 h. The results are expressed as a percentage increase/decrease in the untreated controls (C). ANOVA: *p < 0.05; **p < 0.01. **(G)** Confocal fluorescence images of focal adhesion complexes (vinculin), actin and nuclei. Scale bar = 25 µm. **(H)** Higher-magnification confocal fluorescence images of focal adhesions. Scale bar = 25 µm. **(I)** hMSCs proliferation is expressed as a percentage difference concerning untreated controls (C). ANOVA: *p < 0.05; **p < 0.01.

**FOCAL ADHESIONS**: To investigate focal adhesions in pDA bioactivity, we labelled the cells with vinculin, an early focal adhesion protein (**Figure 2-9F-H**). At 1 h, the contracted cell morphology made smaller focal complexes indiscernible on all surfaces; therefore, this time was excluded from the analysis. At 4 h, pDA surfaces exhibited significantly more focal adhesions than controls: sPDA by +47% and rPDA by +72%. At 8 h, sPDA and rPDA had +66% and +44% more focal adhesions than the controls. By 24 h, rPDA lagged behind sPDA by 17%, while sPDA maintained an +11% lead over the controls.

Cell adhesion to substrates is governed by integrin-mediated protein complexes, facilitating mechanotransduction.[30] Early focal complexes indicate initial integrin activation, potentially maturing into more extensive focal adhesions with adequate RhoA activity stimulation.[186] These structures, vital for cell-environment interactions, form in response to stimuli such as microtopography and surface stiffness. The formation of focal adhesions guides cell behaviour, which is crucial for studying cell-substrate interactions. The early pDA focal adhesion formation surges will likely result from integrin α5β1 activation and clustering.[5,187] Their abundance signifies effective cell-substrate interactions, which are driven by myosin-II forces and indicate superior stimuli.[181,188,189]

Considering the morphological data, the decline in focal adhesions on rPDA by 24 h suggests that cells transitioned to motility, characterized by a dynamic leading lamellipodium and a less active rear edge.[58,190] Thus, by 24 h, rPDA seems to support cells in advanced motility stages. The decrease in sPDA between 8 and 24 h also indicates a shift in motility. In contrast, control surfaces suggest cells are in earlier spreading stages or have reduced motility.

**CELL NUMBER:** To assess the bioactivity of the pDA surfaces, we examined the cell count, a key indicator of clinical potential (**Figure 2-9I**). Within 4 h, rPDA surfaces showed a 20.5% increase in proliferation compared to the controls, while sPDA remained comparable. By 8 h, rPDA and sPDA surpassed the controls by 23.7% and 18.2%, respectively. However, after 7 days, rPDA showed an 11% decrease compared to controls, while sPDA maintained a 13% elevation. pDA coatings enhance cellular viability and proliferation across various applications, from tissue engineering to stem cell therapy.[5,191,192] Variance in sPDA cell numbers at 4 and 8 h suggests varied cell cycle initiation, which our morphological analysis supports. After 24 h, distinct differences were observed between the surfaces. The exact reason for the enhancement of pDA proliferation remains inconclusive. Luo et al. (2013) linked endothelial cell proliferation to surface quinone content.[193] However, our XPS results showed no significant catechol difference between rPDA and sPDA. While some studies suggest that cell spreading and proliferation depend on surface chemistry, our findings indicate that topography and mechanical properties play essential roles.[187] Interestingly, rPDA surfaces showed reduced proliferation after 3 and 7 days. This result is in contrast with our previous MG63 proliferation results.[5] A could be attributed to rPDA's increased osteogenic

differentiation capacity. pDA's osteogenic potential is related to integrin clustering and PI3K signalling activation.[194] PI3K, enabled by FAK activity at focal adhesions, stimulates hMSC osteogenic differentiation via ERK pathways.[195] Thus, rPDA, which promotes cell spreading and focal adhesion, might enhance FAK/PI3K/ERK-mediated osteogenic differentiation, which counteracts cell proliferation.[196] Differentiation often leads to reduced cell cycle progression.

**FILOPODIAL PROJECTIONS:** SEM imaging showed that hMSCs had more filopodial projections on both pDA surfaces, interacting directly with the pDA aggregates (**Figure 2-10**). On the rPDA, these projections navigated around specific aggregate sizes before enveloping them, suggesting a preference for aggregates of particular sizes or properties. While rPDA had more projections, it was shorter than sPDA, possibly due to the polymeric features of the surface meeting the cellular interaction criteria. Most sPDA projections did not bind to aggregates. This observation indicates that cells preferentially interact with certain pDA features, reinforcing cell adhesion.

**SERUM INDEPENDENT COMPONENT (SIC):** pDA's interaction of pDA with serum protein stabilizes the adsorbed protein, preventing denaturation.[169] Tsai et al.'s (2011) study on serum-free pDA culturing introduced circulating serum protein, which influences cell stimulation and growth. Our study aimed to determine the adhesion properties of pDA by conducting cellular experiments under serum-free conditions. hMSCs were serum-starved and seeded on surfaces pretreated in serum-containing or serum-free media. ATR-FTIR measurements confirmed a protein adlayer on all surfaces, which is consistent with our previous findings.[5] We inferred similar protein adsorption due to the similar surface chemistry between sPDA and rPDA.

To detect a serum-independent component (SIC), we compared quantitative descriptors on pre-adsorbed (PA) and non-preadsorbed (NPA) surfaces (**Figure 2-11A-C**). After 1 and 4 h, hMSCs on NPA pDA surfaces showed advanced spreading morphologies, with rPDA surfaces displaying more advanced forms than sPDA. Pre-adsorption of serum proteins generally enhances cell spreading morphologies. After 4 h, the pDA surfaces continued to exhibit advanced morphologies. We determined the effects of serum on cellular morphology by comparing standard and serum-free cultures on PA substrates. At 1 h, the absence of serum increased the number of cells with a protrusive morphology. However, after 4 h, the pre-adsorbed protein adlayer offset this effect, consistent with previous work on the role of pre-adsorbed serum proteins.[197] Regarding spreading, within the first hour, serum protein pre-adsorption significantly enhanced cell spreading on all surfaces, with the control surfaces showing the greatest enhancement. At 24 h, the control surfaces showed the most significant enhancement, whereas sPDA and rPDA had similar effect sizes. These trends persisted throughout the first week.

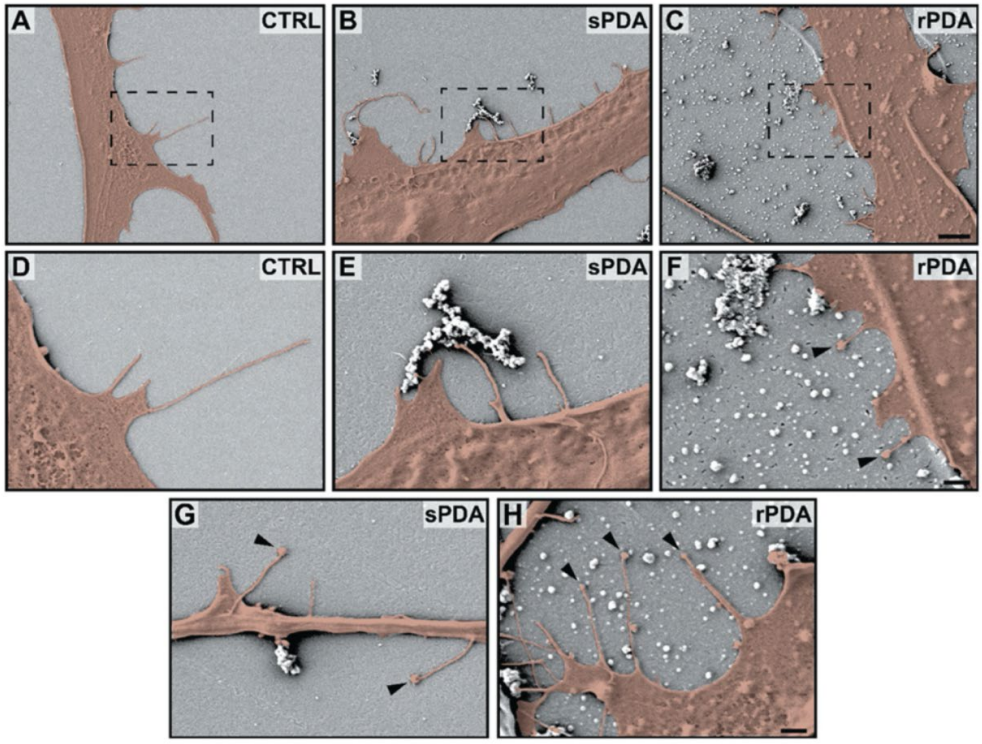


Figure 2-10: SEM of cells on studied surfaces

**(A-C)** Low-magnification SEM images of hMSCs seeded on the control and pDA surfaces. The lines visible in **(C)** are most likely defects (e.g., microcracks, polishing marks, scratches) in the underlying glass substrate, which yielded a localized accumulation of pDA, as previously reported for mechanically polished titanium. Scale bar = 1 µm. **(D-F)** High-magnification SEM images of hMSC projections. Scale bar = 4 µm. **(G, H)** Representative images of projections from hMSCs that interact with features on the sPDA and rPDA surfaces. Scale bar = 4 µm.

In terms of cell proliferation, after 24 h, all surfaces showed enhanced effects, with the control surfaces having the highest (**Figure 2-11D**). By day 7, these trends had persisted. In summary, rPDA surfaces consistently displayed advanced cell morphologies in serum-free cultures compared with sPDA and control surfaces. This observation confirms that pDA surfaces enhance cell spreading, even without serum. Unlike normal culturing, serum deprivation promotes isotropic spreading but does not delay transitions to later morphologies.[178] This observation suggests that pDA surfaces quickly initiate cell spreading and morphological transitions rather than relying on the stochastic environmental sensing of STEPs. While pDA bioactivity is often attributed to its adsorptive capacity,[5,191] our results indicate that rPDA, despite its chemical similarity to sPDA, offers additional features (e.g., topography) that support initial cell behaviour better than sPDA.

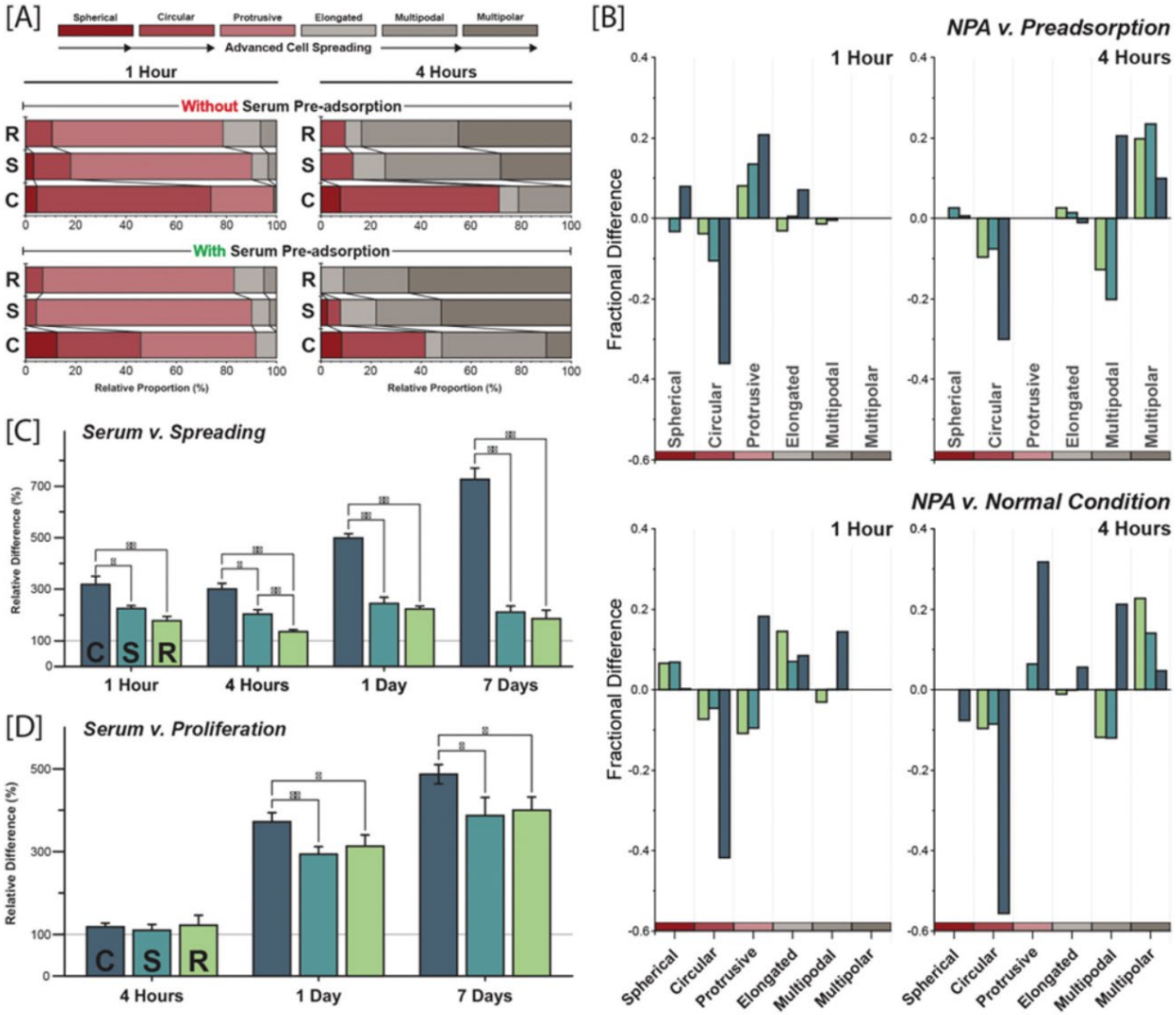


Figure 2-11: Analysis of the serum-independent component (SIC)

**(A)** The legend of morphologies is exhibited through the advancement of cell spreading with correlated colour bars (top). Relative proportions of hMSCs morphologies after incubation in serum-free media on control (C), sPDA (S), and rPDA (R) surface with and without pre-treatment in serum-containing media. **(B)** Comparative quantification of morphological differences associated with protein pre-adsorption (top) and presence of serum in the culture medium (bottom). The serum independent component (SIC) effect size for **(C)** cell spreading and **(D)** proliferation. The effect size was calculated as the ratio of the respective measures (e.g., proliferation) from pre-adsorbed samples to non-pre-adsorbed samples. ANOVA: *p < 0.05; **p < 0.01.

#### 2.4.6.3.4 CONCLUSION

This study investigated the physiochemical makeup of pDA surfaces, their influence on stem cell behaviour, and the Serum-Independent Component (SIC) of pDA. Many studies on pDA bioactivity have inconsistencies owing

to variable controls and limited surface analysis. Our detailed investigation revealed that rPDA surfaces, while chemically akin to sPDA, have enhanced wettability and roughness due to micro-/nano-scale particles. We found that more energy and force are needed to detach pDA films than aggregates, affecting cell adhesion dynamics during spreading and motility.

Despite their chemical similarities, rPDA surfaces induce more advanced cell spreading morphologies than sPDA surfaces. In addition, rPDA initially showed increased cell proliferation, suggesting potential differentiation. Owing to its established antibacterial activity, rPDA has emerged as a promising bioactive implant coating. We also confirmed SIC in pDA, which was previously overshadowed by the adsorption capacity of the polymer. SIC consistently promotes cell spreading over time but plays a diminished role in proliferation. The differences between sPDA and rPDA in regular cell culture were not solely due to their respective SICs, indicating other influential variables.

In conclusion, our study offers new insights into the physicochemical properties of sPDA and rPDA coatings and their bioactive effects. We have highlighted the significant role of pDA SIC in cellular adhesion. Our findings bolster rPDA's potential of rPDA as a biomaterial and enrich our understanding of pDA bioactivity, benefiting future pDA research.

## 2.5 UTERINE BIOLOGY

The uterus is a pear-shaped, hollow organ located in the pelvic cavity that is primarily responsible for enabling the implantation of a fertilized embryo and supporting gestation through labour and delivery.[198] At the lower end of the uterus, the cervix extends into the vagina. In addition to acting as a passage between the uterus and the vaginal cavity, the cervix also acts as a responsive barrier that regulates access to the uterine cavity and undergoes significant changes during the menstrual cycle and childbirth.[199] Within the uterine cavity, there are three primary layers: the endometrium, the innermost layer where implantation and menstruation occur; myometrium, the thick, smooth muscle layer that is responsible for contractile movements; and the perimetrium, the outermost layer which acts as a protective barrier.

### 2.5.1 ENDOMETRIUM

The endometrium consists of two main layers: the *stratum functionalis* (functional layer) and the *stratum basalis* (basal layer). The former is a dynamic component responsive to hormonal signalling and changes throughout the menstrual cycle.[200] The stratum functionalis primarily comprises two types of hormonally receptive cells: epithelial and stromal. On the other hand, in addition to being comprised of a dense array of cells and smaller numbers of glands, the basal layer acts as a reservoir of stem cells.[201] It facilitates the monthly regeneration of the *stratum functionalis*.

Endometrial Epithelial Cells (EECs) line the inner surface of the uterus and are highly responsive to estrogen and progesterone. Following menstruation and during the proliferative phase, these cells proliferate and form the glands that elongate and contribute to the thickening of the endometrium.[202]

Endometrial Stromal Cells (ESCs) are structural connective tissue cells that support the endometrial framework and play dynamic roles in response to the hormonal environment. ESCs exhibit a fibroblastic phenotype during the proliferative phase and increase in response to elevated estrogen.[203] As fibroblastic cells, they contribute to extracellular matrix (ECM) production and support the glandular epithelium. During the secretory phase, elevated progesterone levels trigger ESCs' decidualization of ESCs. Decidualized endometrial stromal cells (DECSs) are crucial for endometrial receptivity, as the local immunosuppressive effects enable the tolerance required to implant the semi-allogenic embryo, as it consists of genetic material from both the mother and father.[204] In the absence of an implanted embryo, decidualization of the DESCs is reversed, indicating the cyclic nature of the endometrial lining, and the cells are shed during menstruation.

### 2.5.2 MYOMETRIUM

The myometrium, the muscular layer of the uterus, is integral to organ function, particularly during menstruation and childbirth. The myometrium is structured into three indistinct layers: an outer longitudinal layer, which runs parallel to the long axis of the uterus; a thick middle layer, interlacing at oblique angles to the long axis of the uterus; and an inner layer, which has a circular organization and acts as a sphincter at the openings (cervix, fallopian tubes).[205] The myometrium's complex muscle fibre arrangement, rich vascularisation, and hormonal responsiveness facilitate powerful, coordinated contractions for menstrual blood expulsion and childbirth.

During the proliferative phase, the increase in estrogen promotes the thickening of the myometrium. In contrast, during the secretory phase, increased progesterone levels reduce myometrial contractility, creating an optimal environment for potential implantation.[206] Compared to estrogen, progesterone is the predominant hormone affecting the myometrium.[207] Progesterone receptor dynamics engage in complex signalling mechanisms that maintain the uterus's quiescent state, ensuring the relaxation of the myometrial walls to support fetal development. Further changes in receptor dynamics are associated with increased contractility and the onset of labour.[206] Additionally, disruptions in progesterone receptor signalling are implicated in increased myometrial contractility, contributing to the onset of pre-term labour.[207]

The primary component of the myometrium is myometrial smooth muscle cells (SMCs), which are responsible for the contractile properties of the uterus. Additionally, the myometrium contains fibroblasts, which produce the extracellular matrix (ECM), endothelial cells for vasculature, immune cells, including monocytes and macrophages, and myometrial interstitial Cajal-like cells telocytes (m-ICLC), which are interstitial cells that support tissue repair by acting as a scaffold and hormonal sensors that appear to coordinate growth and activity of the myometrium.[208,209]

### 2.5.3 PATHOPHYSIOLOGY

When damaged, wound healing of endometrial and myometrial tissues is essential for uterine fitness. This importance is especially true for the growing number of women in Canada who undergo delivery via Cesarean section (CS; 1997:18.7%, 2021:31.7%; Canadian Institute for Health Information). Following CS, improper wound healing can result in scar tissue formation that may compromise the integrity of the uterine wall, where biomechanical modelling suggests subsequent scar thinning and biomechanical changes may lead to higher regions of stress and, therefore, risk.[210,211] In this context, successful vaginal birth after Cesarean section (VBAC) occurs at rates between 50 and 85%, with risks including infection, failed trial of labour, and an approximate 0.3–1% risk of catastrophic uterine rupture.[212] Additionally, intrauterine adhesions (IUA) can form due to improper wound healing following trauma, potentially leading to the development of scar tissues that bond together. When symptomatic, the condition is known as Asherman syndrome (AS). AS is characterized by significant clinical manifestations, including infertility, reduced menstruation (hypomenorrhea), and the absence of menstruation (amenorrhoea).[213] However, treatment options have a considerable risk of re-adhesion. For example, hysteroscopic surgery has a reported re-adhesion rate of 30 to 62.5%.[214] Furthermore, these chances of recurrence are accompanied by a severity-related reduction in pregnancy rates (i.e., 53.3% for mild versus 9.5% for severe cases),[215] a nearly 30% lower birth weight, and complications including retained placenta (28.6%), placenta previa (7.1%), and fetal death (7.1%).[216] Consequently, biomaterial-based therapeutic interventions designed to minimize scarring and enhance the structural integrity of uterine defects are essential to ensure the safety of the mother and fetus.

### 2.5.4 UTERINE TISSUE ENGINEERING (UTE)

Uterine tissue engineering (UTE) is a pivotal domain in biomedical research that aims to offer solutions for uterine injury to support and sustain fertility. Integrating principles from biomaterials science, stem cell technology, and tissue engineering, an interdisciplinary approach seeks to address the critical challenges in regenerating or reconstructing functional uterine tissues.

Comprised of natural (e.g., collagen, gelatin, hyaluronic acid)[217-219] or synthetic (e.g., Pluronic F127, polyglycerol sebacate [PGS]),[220,221] and hydrogels are of particular interest owing to their biocompatibility and biodegradability. Underpinning their use in UTE is their capability to control and tune the gelation properties for optimal application and retention in vivo.372 Furthermore, they are capable[222] of intrinsic tuning of their mechanical properties. For example, methacrylate gelatin (GelMA) and sericin (SerMA) matrices were shown to have improved tunability of swelling mechanical and degradation properties by modulating the concentration of SerMA, which improved endometrial repair and receptivity in HUMSC-loaded constructs.[218] Advances in biomimetic endometrium interfaces include utilizing stem cell sheet engineering and surface-functionalized scaffolds to mimic the natural extracellular matrix (ECM) and its pivotal role in cellular behaviour and tissue

formation.[223,224] Decellularized biomimetic scaffolds have shown promise in replicating the essential biochemical and physical cues necessary for effective tissue regeneration.[208,225,226]

In addition to therapeutic approaches, in vitro models of the human endometrium have been used to elucidate the mechanisms of uterine function and pathology. These models, leveraging advanced biomaterials and 3D culture techniques, serve as invaluable platforms for drug screening, disease modelling, and investigating the complex interplay between various cell types within the uterine environment.[227-231]

Despite the significant advancements in UTE, several challenges remain. Replicating the hormonal and structural complexity continues to be a formidable obstacle.[222] Specifically, within myometrial tissue, the muscle layers' highly vascularised and complex arrangement may alter function during critical events (i.e., parturition).[208] Future research focuses on overcoming these challenges, enhancing scaffold functionality, refining cell-based therapies, and developing more sophisticated in vitro models that closely mimic the in vivo uterine environment.

## 2.6 CELL MODELS

This thesis explores the interactions between various biomaterials and cellular systems, focusing on different aspects of biomedical engineering, from bone regeneration to uterine tissue engineering. A range of cell models was employed to investigate these interactions comprehensively, each chosen for their relevance to specific research objectives. These models include bone-derived human mesenchymal stem cells (hMSCs) because of their multipotency and relevance to regenerative medicine, Saos-2 osteoblast-like cells, NIH/3T3 fibroblasts for dental implant applications, and uterine-specific cell lines T-HESCs and PHM1-41 to explore potential therapies for reproductive health. Each cell type offers unique insights into how engineered biomaterials interact with biological systems, providing a multi-faceted approach to understanding and optimizing cell-material interfaces for various biomedical applications. The details of each line are provided below:

### 2.6.1 BONE-DERIVED HUMAN MESENCHYMAL STEM CELLS

Discovered in 1970 by Friedenstein *et al.*,[232] human mesenchymal stem cells (hMSCs), derived from bone marrow, play a key role in regenerative medicine because of their ability to differentiate into various cell types such as bone, cartilage, and fat cells.[233] These multipotent cells, originating from the bone marrow stroma, are vital for tissue regeneration, possessing both self-renewal capability and diverse developmental potential.

The therapeutic potential of bone marrow-derived hMSCs in biomedical engineering and cell biology is gaining recognition, especially for bone regeneration and orthopedic treatment. Their capacity to form osteoblasts, essential for bone formation, is critical in treating conditions including osteoporosis.[234] Their immunomodulatory properties are crucial in autoimmune disease management and transplant success.[233,235] Biotechnology advances enhance their application in personalized medicine, particularly for patient-specific

bone-related therapies. This integration of cell biology with engineering underscores the versatility and significance of hMSCs in regenerative medicine, leading to further exploration of their differentiation abilities and interactions with engineered biomaterials such as titanium nanotubes in tissue engineering.

Additionally, the interactions between bone marrow-derived hMSCs and biomaterial surfaces, such as titanium nanotubes, are critical for understanding stem cell behaviour. These interactions involve complex signalling and physical contact that influence cell adhesion, growth, and differentiation. The substrate's properties, composition, texture, and stiffness are vital in directing the fate of hMSCs.[44,236,237] NTs have been shown to promote osteogenic differentiation by activating the mechanosensitive ion channel Piezo1, which, through calcium influx, triggers the downstream YAP pathway.[238] Furthermore, the underlying NT surface can influence the quality of bone nodules produced from differentiated hMSCs.[53] Understanding these interactions is crucial for optimizing biomaterial design in tissue engineering and regenerative medicine, ensuring the effective integration and functionality of implants.

### 2.6.2 SAOS-2 AND NIH/3T3 CELL MODELS

The Saos-2 cell line was first isolated from an 11-year-old Caucasian female by J. Fogh and G. Tempe in 1975 during the isolation of several human tumour lines for a greater understanding of cellular and molecular oncology and has been modified to derive new metastatic models of osteosarcoma.[239] While providing instructions for the general culture of these lines. Since then, various studies have exploited these cells over the following decades to model aspects of osteoblast activity. Although Saos-2 cells do not represent the entire scope of phenotypic attributes of human osteoblasts, their cytokine and growth factor expression profiles that reflect human osteoblasts well and their extensive mineralization make them a practical model with a phenotype similar to that of mature osteoblasts.[240] Within the context of periodontal implants, Saos-2 osteoblast-like cells allow for the evaluation of osseointegration and bone remodelling processes.

Originally derived from a 17- to 19-day-old Swiss mouse embryo,[241] the NIH/3T3 cell line has been a cornerstone of tissue engineering research because of its stability, ease of culture, and representativeness of fibroblast activity, which is crucial for wound healing and tissue regeneration. Historically, these cells have been instrumental in elucidating cellular behaviours, such as growth kinetics, differentiation, and extracellular matrix production, making them a preferred model for preliminary in vitro testing before proceeding to more complex in vivo models. Within the context of periodontal implants, the robustness and consistency of NIH/3T3 cells enables their use as an in vitro model to simulate the soft tissue environment surrounding implants (i.e., gums) while providing insight into fibroblast-implant interactions that are critical for the health of the peri-implant mucosa.[242]

When applied together, this dual-cell model approach enables multifaceted investigation of periodontal implants, addressing soft tissue integration and bone healing.

### 2.6.3 T-HESCS

Initially isolated in 2004 from tissues collected during the hysterectomy of a woman of reproductive age, these human endometrial stromal cells (HESCs) were transformed ("T") via the retroviral transfection of human telomerase reverse transcriptase (hTERT) with puromycin resistance.[2] Developed as an immortalized HESC model with a normal response to progesterone (P4) for decidualization studies, T-HESCs displayed similarities to primary HESCs in phenotype and karyotype.[2] — the latter being a previously limiting factor in immortalizing predating HESC models that employed a simian virus 40 (SV40) transformation.[3] Furthermore, comparative work investigating the cAMP and P4-mediated differentiation of T-HESCs versus first-trimester primary human decidual stromal cells (HDSC) has indicated that although T-HESCs present with a cAMP-induced phenotypical and gene response, a different response to P4 induction limits its use in progesterone-only protocols.[4]

### 2.6.4 PHM1-41 CELLS

Initially isolated in 1992 by a research group led by Dr. B.M. Sanborn, these cells were isolated from the uterus of a pregnant female (39 weeks).[243] Following immortalized by an "adenovirus vector pLXSN16E6E7…expressing E6/E7 proteins of…(HPV)-16," they are referred to as pregnant human myometrium 1-41 (PHM1-41). They are intended to provide a platform for better study of the smooth muscle layer of the uterus (myometrium). Consequently, PHM1-41s has provided an excellent platform to study aspects, including cross-talk with monocytes,[244] and calcium dynamics on the functioning of the myometrium.[245] Furthermore, PHM1 cells were found to have a transcriptome profile and calcium release dynamics similar to human primary myometrial cells.[246]

# 3 THE IMPLICATION OF SPATIAL STATISTICS IN HUMAN MESENCHYMAL STEM CELL RESPONSE TO NANOTUBULAR ARCHITECTURES

*Relevant manuscript*

**The implication of spatial statistics in human mesenchymal stem cell response to nanotubular architectures**

Alexander J Steeves[1,2], William Ho[#,1,2], Maria Chiara Munisso[#,3], David J Lomboni[1,2], Enara Larrañaga[4], Sidney Omelon[1,5], Elena Martínez[4,6,7], Davide Spinello[1], Fabio Variola[1,2,8,9]

[1] Faculty of Engineering, Department of Mechanical Engineering, University of Ottawa, Ottawa, ON, Canada.
[2] Ottawa-Carleton Institute for Biomedical Engineering, Ottawa, Canada.
[3] Department of Plastic and Reconstructive Surgery, Kansai Medical University, Moriguchi, Japan.
[4] Institute for Bioengineering of Catalonia (IBEC), The Barcelona Institute of Science and Technology (BIST), Barcelona, Spain.
[5] Faculty of Engineering, Department of Mining and Materials Engineering, McGill University, Montreal, QC, Canada.
[6] Centro de Investigación Biomédica en Red (CIBER), Madrid, Spain.
[7] Department of Electronics and Biomedical Engineering, University of Barcelona, Barcelona, Spain.
[8] Faculty of Medicine, Department of Cellular and Molecular Medicine, University of Ottawa, Ottawa, ON, Canada.
[9] Children's Hospital of Eastern Ontario (CHEO), Ottawa, ON, Canada.
[#] Contributed equally.

**Submitted** on **2019–11–12** to the **International Journal of Nanomedicine**

**Accepted** on **2020–02–16 | DOI:** 10.2147/IJN.S238280

## MOTIVATION

Exploring human mesenchymal stem cell (hMSC) interactions with nanotubular architectures is crucial for advancing tissue engineering and regenerative medicine. This study was motivated by the growing need to understand how the spatial arrangement of nanoscale features influences stem cell behaviour, which is a critical factor in designing effective biomaterials. The application of spatial statistics in this context offers a novel approach for quantitatively assessing and correlating the geometric properties of nanotubular structures with cellular responses. Such insights are crucial for optimizing the design of titanium-based nanotopographies to enhance their efficacy in clinical applications. Therefore, this study seeks to bridge a significant knowledge gap, paving the way for developing more sophisticated and biologically informed biomaterial designs.

## RATIONALE, HYPOTHESES AND OBJECTIVES

The study hypothesizes that the spatial characteristics and structural parameters of nanotubular titanium dioxide ($TiO_2$) surfaces, beyond simple diameter measurements, significantly influence human mesenchymal stem cells (hMSCs) behaviour and response. These spatial parameters include nanotube eccentricity, nearest-neighbour distance, and surface entropy.

## OBJECTIVES

1. **Synthesis of the substrate**: Capitalise on the established two-step anodization theory to generate an improved 3D-printed platform for both single and multi-hierarchical substrate fabrication.
2. **Characterisation of nanotubular surfaces**: To perform a comprehensive characterization of the nanotubular $TiO_2$ surfaces, the physical and chemical properties, including the tube diameter, wall thickness, various geometric parameters, and surface composition, were determined.
3. **Spatial statistical analysis of the substrate**: To conduct a spatial statistical analysis of the nanotubular surfaces, focusing on parameters including the nearest neighbour distance (NND) and entropy (S). The experimental results are also integrated and understood within entropy simulations that modulate crucial variables, including diameter and eccentricity.
4. **Assess the short-term response of hMSCs (0–7 d)**: To evaluate how hMSCs interact with nanotubular $TiO_2$ surfaces by assessing proliferation, adhesion, and morphological parameters. Furthermore, differentiation potential can be evaluated by determining osterix (OSX) expression.
5. **Assess the Long-term Impact by Mineral Analysis (28 D)**: To investigate the long-term effects of nanotubular surfaces on hMSCs, particularly their mineralization potential. Specifically, it employs Raman spectroscopy to analyze the mineral composition and assess its parameters, including crystallinity and mineral maturity.

## HYPOTHESES

1. The intricate spatial arrangement and geometric parameters of nanotubular $TiO_2$ surfaces, including the tube diameter, wall thickness, and surface entropy, significantly influence hMSC adhesion and proliferation. These effects will be quantitatively discernible through spatial statistical analysis, offering insights into optimal nanotopographic designs for tissue engineering applications.
2. The spatial organization and diameter of nanotubular $TiO_2$ surfaces significantly influence the osteogenic differentiation of hMSCs, as evidenced by the nuclear localization of osteogenic markers, including OSX, within a short-term interaction frame.
3. The long-term mineralization quality and maturity of the extracellular matrix produced by hMSCs on nanotubular $TiO_2$ surfaces are directly correlated with the specific surface characteristics, including the arrangement and physical properties of the nanotubes, as assessed by Raman spectroscopy after 28 d.

## MOTIVATION

Exploring human mesenchymal stem cell (hMSC) interactions with nanotubular architectures is pivotal in advancing tissue engineering and regenerative medicine. This study is motivated by the growing need to understand how the spatial arrangement of nanoscale features influences stem cell behaviour, a critical factor in designing effective biomaterials. The application of spatial statistics in this context offers a novel approach to quantitatively assess and correlate the geometric properties of nanotubular structures with cellular responses. Such insights are crucial for optimizing the design of titanium-based nanotopographies, aiming to enhance their efficacy in clinical applications. This research, therefore, seeks to bridge a significant knowledge gap, paving the way for the development of more sophisticated and biologically informed biomaterial design.

## RATIONALE, HYPOTHESES AND OBJECTIVES

The study hypothesizes that the spatial characteristics and structural parameters of nanotubular titanium dioxide ($TiO_2$) surfaces, beyond simple diameter measurements, significantly influence human mesenchymal stem cells (hMSCs) behaviour and response. These spatial parameters include nanotube eccentricity, nearest neighbour distance, and surface entropy.

### OBJECTIVES

6. **Synthesize the substrate**: To capitalize on the established two-step anodization theory to generate an improved 3D-printed platform for both single and multi-hierarchical substrate fabrication.
7. **Characterize the nanotubular surfaces**: To perform a comprehensive characterization of the nanotubular $TiO_2$ surfaces, examining physical and chemical properties, including tube diameter, wall thickness, various geometric parameters, and surface composition.
8. **Spatial statistics analysis of substrate**: To conduct a spatial statistical analysis of the nanotubular surfaces, focusing on parameters including nearest neighbour distance (NND) and entropy (S). Additionally, to integrate and understand experimental results within the context of entropy simulations that modulate crucial variables, including diameter and eccentricity.
9. **Assess the short-term response of hMSCs (0–7 D)**: To evaluate how hMSCs interact with the nanotubular $TiO_2$ surfaces by assessing proliferation, adhesion, and morphological parameters. Further, differentiation potential can be evaluated by determining Osterix (OSX) expression.
10. **Assess the Long-term Impact by Mineral Analysis (28 D)**: To investigate the long-term effects of the nanotubular surfaces on hMSCs, particularly their mineralization potential. Specifically, it employs Raman spectroscopy to analyze the mineral composition and assess parameters, including crystallinity and mineral maturity.

## HYPOTHESES

4. The intricate spatial arrangement and geometric parameters of nanotubular $TiO_2$ surfaces, including tube diameter, wall thickness, and surface entropy, will significantly influence hMSC adhesion and proliferation. These effects will be quantitatively discernible through spatial statistical analysis, offering insights into optimal nanotopography designs for tissue engineering applications.
5. The spatial organization and diameter of nanotubular $TiO_2$ surfaces will significantly influence the osteogenic differentiation of hMSCs, as evidenced by the nuclear localization of osteogenic markers, including OSX, within a short-term interaction frame.
6. The long-term mineralization quality and maturity of the extracellular matrix produced by hMSCs on nanotubular $TiO_2$ surfaces will be directly correlated with the specific surface characteristics, including the arrangement and physical properties of the nanotubes, as assessed by Raman spectroscopy after 28 d.

## 3.1 ABSTRACT

In recent years there has been ample interest in nanoscale modifications of synthetic biomaterials to understand fundamental aspects of cell-surface interactions towards improved biological outcomes. In this study, we aimed at closing in on the effects of nanotubular $TiO_2$ surfaces with variable nanotopography on the response on human mesenchymal stem cells (hMSCs). Although the influence of $TiO_2$ nanotubes on the cellular response, and on hMSC activity, has already been addressed in the past, previous studies overlooked critical morphological, structural and physical aspects that go beyond the simple nanotube diameter, such as spatial statistics. To bridge this gap, we implemented an extensive characterization of nanotubular surfaces with a focus on spatial structural variables including eccentricity, nearest neighbour distance (NND) and Voronoi entropy, and associated them to the hMSC response. In addition, we assessed the biological potential of a two-tiered honeycomb nanoarchitecture, which allowed the detection of combinatory effects that this hierarchical structure has on stem cells with respect to conventional nanotubular designs. To this end, we evaluated the cell response from early adhesion to bone mineral deposition, demonstrating substrate-induced differential biological cueing at both the short- and long-term. Ultimately, this work delineates a novel approach for the characterization of $TiO_2$ nanotubes which supports the incorporation of critical spatial structural aspects that have been overlooked in previous research. This is a crucial aspect to interpret cellular behaviour on nanotubular substrates. Consequently, we anticipate that this strategy will contribute to the unification of studies focused on the use of such powerful nanostructured surfaces not only for biomedical applications but also in other technology fields, such as catalysis.

## 3.2 INTRODUCTION

Elucidating the mechanisms that control how cells sense and respond to biomaterials surfaces has been the focus of a large body of literature in the past three decades.[33,247-252] Results from these studies have unequivocally established that physicochemical properties such as roughness, topography, surface chemistry, energy and stiffness, direct cell fate by affecting key phenomena including adhesion, proliferation, differentiation, gene and protein expression.[172,253-255] Among the factors known to control cellular events, nano-topographical features play a pivotal role by exerting direct cueing on adherent cells.[10,36,55,248,253,254,256-258] Based on this evidence, much effort has been invested in the design of synthetic nanostructured substrates to support the investigation of the interplay between nano-topographical cues and cellular functions.[10,248,254,257,259] Among the panoply of techniques developed to nanostructure biomaterials, anodization has rapidly emerged as a simple but effective electrochemical treatment to create bioactive nanostructures composed of arrays of aligned nanotubes on titanium, the gold standard in medicine.[74,78,259,260] The design of morphological parameters, mainly nanotube diameter, has been achieved through the modulation of experimental parameters (i.e., anodization voltage and

time, composition of the electrolytic solution), permitting to rationally engineer nano-topographical features and assess their influence on cellular events.[261,262] This allowed to determine, for example, that the inductive differentiation of hematopoietic stem cells into osteoclasts, as well as the proliferation of primary human osteoblast and rat mesenchymal stem cells, are enhanced on 15 nm wide nanotubes.[42,43] Conversely, nanotubes larger than 50 nm dramatically reduce rat mesenchymal stem cell activity and induced apoptotic programmed cell death.[43] More recently, human adipose-derived stem cells showed a diameter-dependent proliferation and differentiation elicited by nanotubes within a 30–45 nm diameter range.[44] Taken together, these studies indicate that smaller nanotube diameters provide beneficial effects on many stem cell functions when compared to larger nanotubes. However, the conclusive modelling of stem cell response to nanotubular surfaces is still a controversial subject as additional cellular processes critical in stem cell functions are favoured by larger nanotubes, thereby calling for further investigation to address these discrepancies.[263-265] In particular: (*i*) diameters ranging from 70 to 100 nm elicit a tenfold increase in human mesenchymal stem cell (hMSC) elongation and differentiation into osteoblast-like cells,[46] (*ii*) 100-nm diameter nanotubes promote greater differentiation of mice bone marrow mesenchymal stem cells (mMSCs) (when compared to 30 nm tubes),[47] (*iii*) 65–85 nm nanotubes provide the optimal substrate for the proliferation and osteogenic differentiation of human adipose-derived stem cells (hADSCs)[44,45] and (*iv*) mouse bone marrow stromal cells (mBMSCs) responded to 100-nm nanotubes with increased osteogenic differentiation compared to 30-nm nanotubes.[266] Although these inconsistencies may be due to the specific attributes of different cell lines employed in these studies (e.g., source tissue, species, donor-donor variation), there is undoubtedly morphology-dependent cueing exerted by nanotubes on cellular processes that warrant a more stringent investigation.

Notably, while seminal work has focused on nanotube diameter as the sole independent variable to explain the cell response to nanotubular surfaces, several yet potentially equally important morphological (e.g., inner-tube eccentricity and inter-tube spacing) and spatial parameters (e.g., geometric arrangement) were overlooked. The latter is especially critical for human mesenchymal stem cells as symmetry and disorder in circular nanopit arrays have been shown to influence hMSC functions.[267] In fact, it was shown that nanoscale disorder induces osteogenic differentiation and subsequent bone production in the absence of osteogenic supplements. Conversely, ordered nano-topographies limit cellular adhesion and osteoblastic differentiation. Accordingly, it could be conceived that prior contradicting results with nanotubular surfaces derive from lack of comprehensive characterization of nanostructures beyond the diameter and, more importantly, from the absence of stringent quantitative analysis of spatial statistics, given the principal role of symmetry and disorder.[268] Therefore, a cohesive protocol which comprehensively includes morphological and spatial analyses for stem cell-nanotube interactions is expected to provide the key to interpret cellular behaviour on anodized

titanium and to unify the approach for the investigation of not only nanotubular surfaces, but also of any substrate characterized by arrays of circular/oval pits.

Anodization has also proven to be a versatile and inexpensive method to generate complex self-assembled structures with the precise control over the surface features through modulation of key parameters and procedures (e.g., multistage protocols), permitting the distinctive advantage of fabricating hierarchical architectures (e.g., double-walled structures, nanorods, and nanowires).[74] Among these, morphologies such as lotus root-shaped/honeycomb structures[90,269-271] present a unique opportunity for a paradigm shift in the biomedical field, where synthetic multiscale architectures are increasingly explored to generate complex 3D-environments and geometries to support and regulate cellular activity.[272,273]

In this work, we aimed at bridging the gap in previous literature by introducing a series of morphological and spatial analyses for the characterization of nanotubular architectures, culminating in the descriptive analysis of nanotubular surfaces towards a cohesive investigation of cell-nanotube interactions. To this end, we investigated three nanotubular arrays with variable nanotube diameters and a two-tiered honeycomb structure. Successively, we carried out morphological and spatial analysis (e.g., Voronoi entropy) to quantify the tubular geometry, arrangement as well as degree of order for these architectures. Successively, our experimental data was validated by computational simulations to provide greater insight into the role of morphological parameters and spatial statistics. Subsequently, we evaluated the effects of the four surfaces on hMSC bioactivity (i.e., proliferative and morphological analyses) and osteogenic induction (e.g., bone mineral quality). Results from our study (*i*) highlight the importance of including additional morphological analyses and spatial statistics in the characterization of nanotubular surfaces for the purpose of enhancing the validity of cross-study comparisons, (*ii*) provide a comprehensive correlation between a multifactorial array of these parameters and hMSC activity extending from adhesion to bone mineral deposition, and lastly (*iii*) report the synergistic effects elicited by the HC architecture.

## 3.3 RESULTS AND DISCUSSION

### 3.3.1 SURFACE CHARACTERIZATION

**NT MORPHOLOGICAL ANALYSIS:** We have capitalized on the distinctive potential of anodization to engender self-ordered nanotubular substrates for the investigation of the interplay between differently sized nanotubes and bone-derived human mesenchymal stem cells. Specifically, using a 3D printed harness to maintain electrode distances (**Figure 3-1A**), a two-step anodization protocol was employed to generate arrays of titania nanotubes (**Figure 3-1B**), and rational variations in treatment parameters (i.e., time and voltage; **Table 3-1**) allowed us to modulate the resulting morphology. These surfaces were generated with matched voltages between each anodization step to enable the growth of aligned nanotubes with superior order from well-defined nucleation

sites formed during the first stage.[90,270] To investigate, for the first time, synergistic/antagonistic effects elicited by hierarchical nanotubular structures, we engineered a two-tiered surface characterized by clusters of smaller nanotube assemblies confined within larger domains. We first generated the first nanotubular layer with a voltage associated with the NT3 condition (60 V), to generate discrete regions for concentrated and clustered nanostructure growth in the subsequent stage. After removing the first stage oxide layer, which exposed the newly formed nucleation sites, the second stage nanotubular layer was generated with a voltage associated with the NT1 condition (20 V). The resulting two-tiered honeycomb architecture (HC) was successfully imaged by SEM (**Figure 3-1C**). It was found to be comprised of clusters of 5–7 smaller nanotubes (s-HC) contained within larger domains (L-HC).

Image analysis of the SEM micrographs confirmed the expected relationship between the applied voltage and nanotubes' lumen diameters,[270] with voltages of 20, 40 and 60 V resulting in mean diameters of 21 ± 5, 54 ± 10 and 92 ± 11 nm (labelled NT1, NT2 and NT3, respectively). A descriptive evaluation of the HC architecture established that s-HC domains (mean diameter of 21 nm) are enclosed within more significant L-HC boundaries (mean diameter of 108 nm). Therefore, while the s-HC nanotube array is identical, diameter-wise, to the NT1 surface, the L-HC was significantly larger than the NT3 nanotubes. To quantify these observations, we carried out Kolmogorov-Smirnov (K-S) testing on the diameter distributions (**Figure 3-1D**) and confirmed both the observed difference between the NT3 and L-HC domains (K-S, $p < 0.001$) and the similarity between NT1 and s-HC domains (K-S, $p=0.5842$). This allowed us to maintain consistency for at least one morphological variable to compare the NT1 surface and the HC architecture. This was particularly critical for the interpretation of cell behaviour the HC architecture. Ultimately, this has permitted us to single out variations in cellular response exclusively induced by other variables, including order and clustering of these ≈20 nm features and the presence of the overlaying L-HC array.

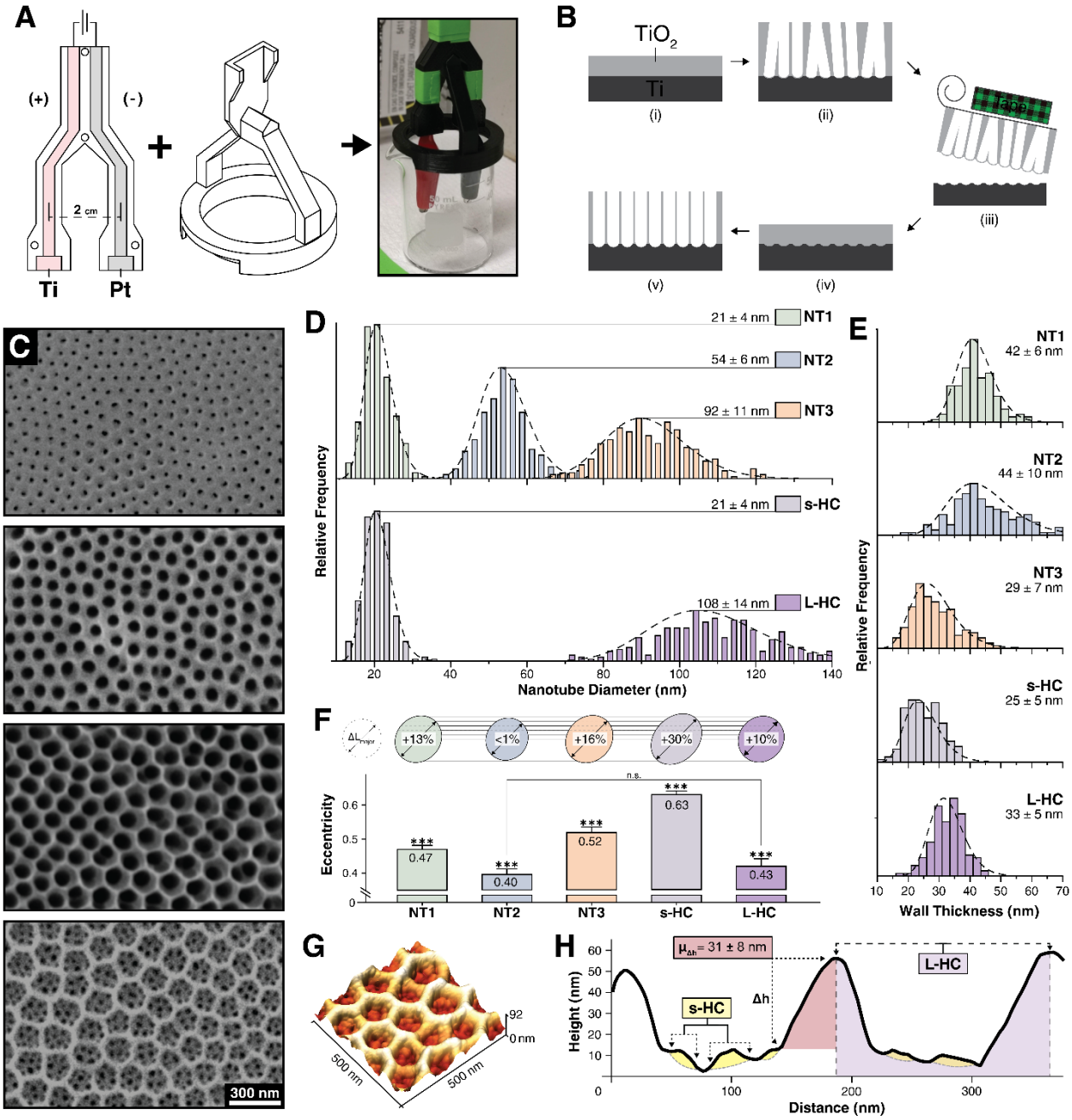


Figure 3-1: Nanotube generation, imaging, and structural analyses

**(A)** Custom-made setup for anodization. **(B)** Protocol of substrate generation via a two-step anodization process. **(C)** SEM images of the nanotube surfaces are categorized as NT1, NT2, NT3, and HC. **(D)** Diameter and **(E)** inter-tube wall thickness distributions. **(F)** Eccentricity analysis of nanotube morphology (bottom) with relative comparison across conditions (top). KW-ANOVA statistical comparison with †† = $p < 0.01$ against all other conditions. **(G)** 3D-AFM micrograph of the HC surface. **(H)** Representative line profile derived from AFM images to quantify the vertical gap (Δh). Statistical significance was defined as ***=$p < 0.001$. *Reproduced from Steeves et al. (2020), published by Dove Press under Open Access (CC-BY-NC).*

**SPATIAL ORGANIZATION OF NTS:** To complete the morphological characterization, we quantified the inter-tube spacing which, due to the continuous nature of our surface, can thereby be referred to as the shared wall widths between the nanotubes. This is opposed to common free-standing nanotubes where a gap, which is often disregarded, exists between the discrete walls of neighbouring tubes. Distributions of these widths are shown in **Figure 3-1E**. NT1 and NT2 displayed mean values of 42–44 nm, while NT3 was characterized by significantly narrower walls at ≈29 nm. In this context, Biggs *et al.* indicated that focal adhesion formation occurs in the interpit region.[267] In addition, it was shown that integrin clustering and the subsequent cellular adhesion improve as the interpit separation increases, identifying optimal effects for <70 nm.[274] This work conforms with our working hypothesis that, at the nanoscale, the order of interpit features (i.e., spacing) play an equally important role in the control of cellular adhesion and function. Further, introducing disorder and/or increasing the interpit spacing is suggested to facilitate focal adhesion formation which would then positively affect the process of cellular spreading.[274] Notably, similar optimal spacing values were found to apply to integrin-specific ligand nanopatterns.[275] Translated to our study, as our wall thicknesses are ≈43 nm, we expect integrin clustering, and thus focal adhesion formation, to occur readily on NT1 and NT2. However, as the intratube diameter on NT3 exceeds 70 nm (≈92 nm), coupled with the thinnest walls (≈29 nm), thus the lowest interpit area among the single-level architectures, and so we expect it to show the most detrimental effects on cell adhesion and spreading. In the case of the HC architecture, the available surface for FA establishment may be regarded as the sum between the walls of the L-HC layer and those pertaining to the s-HC arrays.

The morphological characterization of anodized surfaces was completed by assessing the eccentricity of nanotubes (**Figure 3-1F**), a parameter that assesses circular morphology which, until now, has been overlooked in the study of cell-nanotube interactions. Differences between conditions were confirmed by the nonparametric Kruskal-Wallis ANOVA test, due to the lack of normality in the data. For all NT surfaces, the nanotubes lumen displayed an elliptical outline (i.e., e>0) and was more marked in the NT3 surface. Conversely, the morphology closest to a perfect circle was displayed by NT2 substrate and L-HC domains. Notably, the s-HC condition showed the highest eccentricity, 30% greater than the one measured on the NT2 surface.

**ADDITIONAL HC NANOTUBE CHARACTERISTICS:** Given the 3D nature of the HC architecture, AFM analysis was necessary to determine the height difference between the outmost surface of the inner s-HC tubes and the outer surface of the L-HC domains (**Figure 3-1G**). This revealed a vertical step height difference ($\Delta h_{HC}$) of ≈31 nm (**Figure 3-1H**), crucial to the interpretation of our cellular results. In this context, it was shown that cells (C2C12 myoblasts) can sense, through integrins, adhesion proteins immobilized down to 100-nm-deep nanopits.[60] Considering the smaller vertical gap, we could thus expect that cells will be able to simultaneously sense both the L-HC and s-HC, thereby experiencing unique integrated cueing made possible by such two-tiered nanoarchitecture. Of note, depending on the point of reference, the L-HC array could be seen either as a planar

surface characterized by arrays of ≈30-nm-deep pits (point of reference: the outer surface of the L-HC) or as an array of ≈30-nm-high protrusions overlaying the s-HC layer (point of reference: the s-HC layer). In this context, a review by Biggs *et al.* analyzed previous literature on cellular interactions with arrays and nanopits and nanoprotrusions, concluding that:[274] (*i*) pit diameters greater than 70 nm perturb integrin clustering only when the z dimensions of the pits exceed ∼100 nm, (*ii*) cellular adhesion is decreased on structures measuring ∼70–100 nm in height and (*iii*) nanoprotrusion heights lower than 70 nm are insufficient to disrupt integrin formation and reinforcement (and, as a matter of fact, nanofeatures lower than 50 nm are comparable to planar substrates in terms of FA formation). Taken together, we can thus infer that, in either case, the vertical dimension of the L-HC layer is not expected to have any direct effect on FA clustering and, in turn, on the subsequent cellular spreading on the HC architecture.

**SPATIAL ANALYSES (EXPERIMENTAL):** After morphological characterization, we closed in on the spatial statistics to obtain information about the geometrical arrangement and spatial proximity between nanotubes. To this end, we first considered the nearest neighbour distance (NND) and assessed the average distance between the centroid individual nanotubes and that of their closest neighbours. This parameter complements the morphological description of nanotubular structures, and it results from the combination of the spatial distribution of the nucleation sites created during the first anodization step, the nanotube diameter and wall thickness. **Figure 3-2A** displays the NNDs for all conditions, showing the HC structure simultaneously comprises the smallest (s-HC array) and highest (L-HC array) NNDs. Of note, distances increased according to the diameter (e.g., $NND_{NT1}$=65 nm, $NND_{NT3}$=110 nm), which is consistent with the growth mechanism by which, as the nanotubes become larger, the centroids will diverge. We expanded our analysis to spatial statistics by generating Voronoi tessellations from the centroids of respective tubes, which allowed the subsequent assessment of surface entropy. Specifically, the Voronoi entropy was the lowest for the NT3 surface, indicating a more ordered arrangement when compared to the other NT conditions (**Figure 3-2B**); consistent with more marked constraining effects dictated by the larger size which limit their freedom to rearrange. In addition, the HC architecture displayed the highest values for the s-HC domains, denoting the smallest degree of order among all conditions analyzed. Such nanoscale semi-order is partly dictated by the spatial configuration of the initial nucleation sites created during the first anodization step, which affects the subsequent formation and growth of the nanotubes during the second step.[90,270,271] In addition, the degree of order intertwines with other morphological variables such as nanotube diameter, wall thickness, eccentricity and NND. A 2-way relationship between the degree of order and the morphological parameters can, in fact, be observed (**Figure 3-2C**).

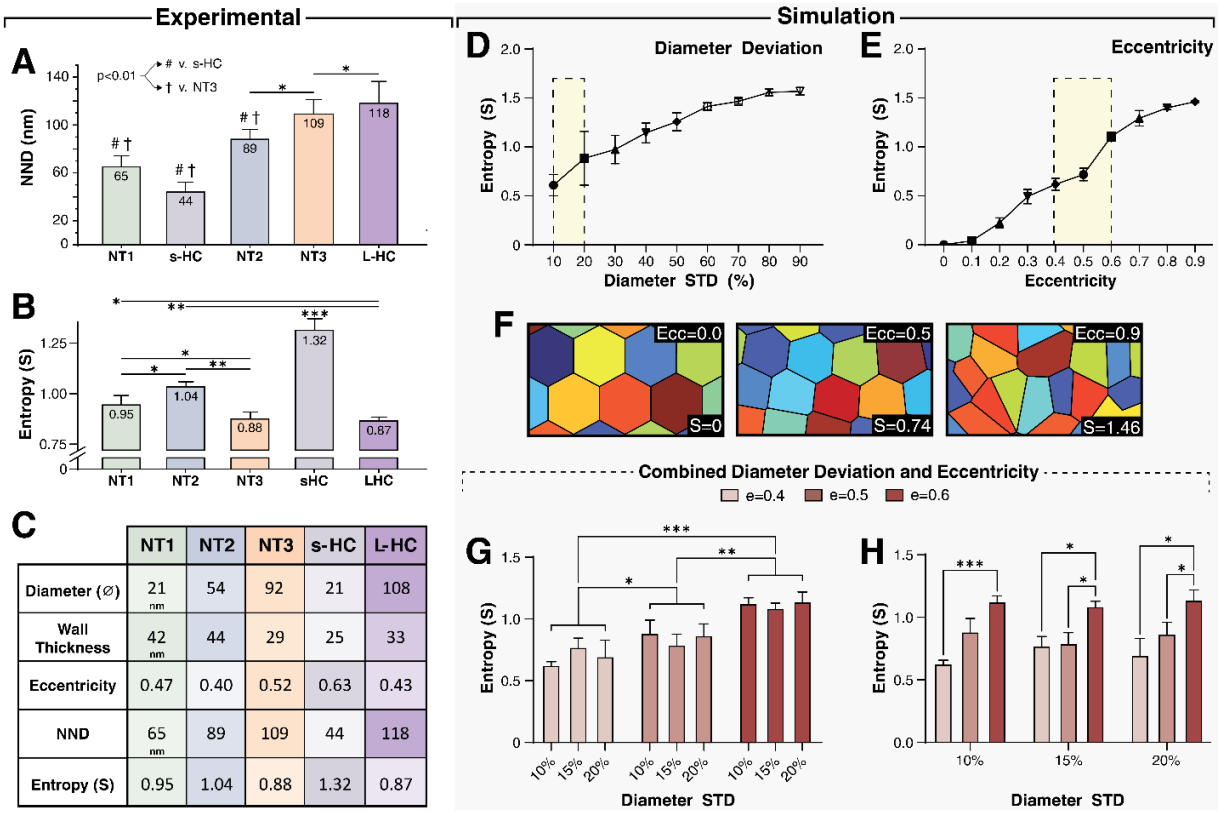


| | NT1 | NT2 | NT3 | s-HC | L-HC |
|---|---|---|---|---|---|
| Diameter (⌀) | 21 nm | 54 | 92 | 21 | 108 |
| Wall Thickness | 42 nm | 44 | 29 | 25 | 33 |
| Eccentricity | 0.47 | 0.40 | 0.52 | 0.63 | 0.43 |
| NND | 65 nm | 89 | 109 | 44 | 118 |
| Entropy (S) | 0.95 | 1.04 | 0.88 | 1.32 | 0.87 |

Figure 3-2: Spatial statistics analysis of nanotubular surfaces

**(A)** Experimental nearest neighbour distance (NND) and **(B)** Experimental Voronoi entropy. **(C)** Summary table of experimental data, showing (*i*) mean values of morphological parameters and (*ii*) ranking-based shading to visually compare properties across the different conditions tested. 20%, 40 %, 60%, 80% and 100% shading were used to rank morphological properties in ascending order based on their numerical values. Simulated effects of variations in **(D)** diameter and **(E)** eccentricity on entropy. **(F)** Examples of Voronoi tessellation on simulated ordered, semi-ordered and random patterns with entropy S equal to 0, 0.74 and 1.46, respectively. **(G-H)** Simulated combined effects of diameter and eccentricity deviation. Statistical significance was defined as *=p < 0.05, **=p < 0.01 and ***=p < 0.001. *Reproduced from Steeves et al. (2020), published by Dove Press under Open Access (CC-BY-NC).*

**SPATIAL ANALYSES (SIMULATIONS):** To demonstrate this hypothesis, we simulated nanotubular patterns with variable degrees of order which were subjected to the same Voronoi tessellation methods and analyses applied to the experimental surfaces. Our intention was to identify the individual and combinatory effects of these parameters, namely diameter and eccentricity, with respect to the resultant entropy which would then be drawn on to explain the experimental cellular response. As expected, our simulations demonstrated that the entropy increases as the variability of the diameter and/or of the eccentricity of elliptical nanotube-like features increase (**Figure 3-2D,E**), establishing a theoretical foundation to explain the observed relationship between nanotubular morphology and disorder. While these simulations spanned across a large range of variability (10–90% for diameter, 0–0.9 for eccentricity), the variations of these parameters were relatively confined with respect to our experimental data (10–20% for diameter, 0.4–06 for eccentricity), and are identified as the yellow fields within **Figure 3-2D,E**. Within these intervals, the entropy values are lower than those quantified experimentally (**Figure 3-2C**). This is likely since on NT and HC surfaces, the individual contributions of variations in diameter and eccentricity are compounded. To quantitatively demonstrate this aspect, we simulated the combined effects of variations in diameter and eccentricity within the ranges set out by our experimental data (**Figure 3-2G,H**). Our results show that while variations in diameter do not significantly affect the entropy, even small variations in eccentricity (i.e., 0.4–0.6) cause drastic changes in entropy. This finding cements the importance of including tubular eccentricity as a major contributor to the overall degree of order in the characterization of nanotubular arrays.

Notably, the higher disorder determined for the s-HC nanotubes may also derive from the clustering dictated by (*i*) the relative spatial arrangement of smaller tubes and/or (*ii*) the spatial constraints exerted by the larger L-HC domains. Computational simulations show in fact that by (*i*) decreasing the relative distance among s-HC tubes and/or (*ii*) increasing the confinement action by expanding the spacing of the L-HC domains, while keeping the arrangement of the s-HC tube constant, the entropy increases (**Figure 3-3**). It can thus be postulated that by rationally modulating the voltage of the two anodization steps, the spatial arrangement of the nucleation sites and/or the wall thickness of the L-HC domains could be controlled, thereby offering a strategy to design the degree of disorder of the s-HC clusters.

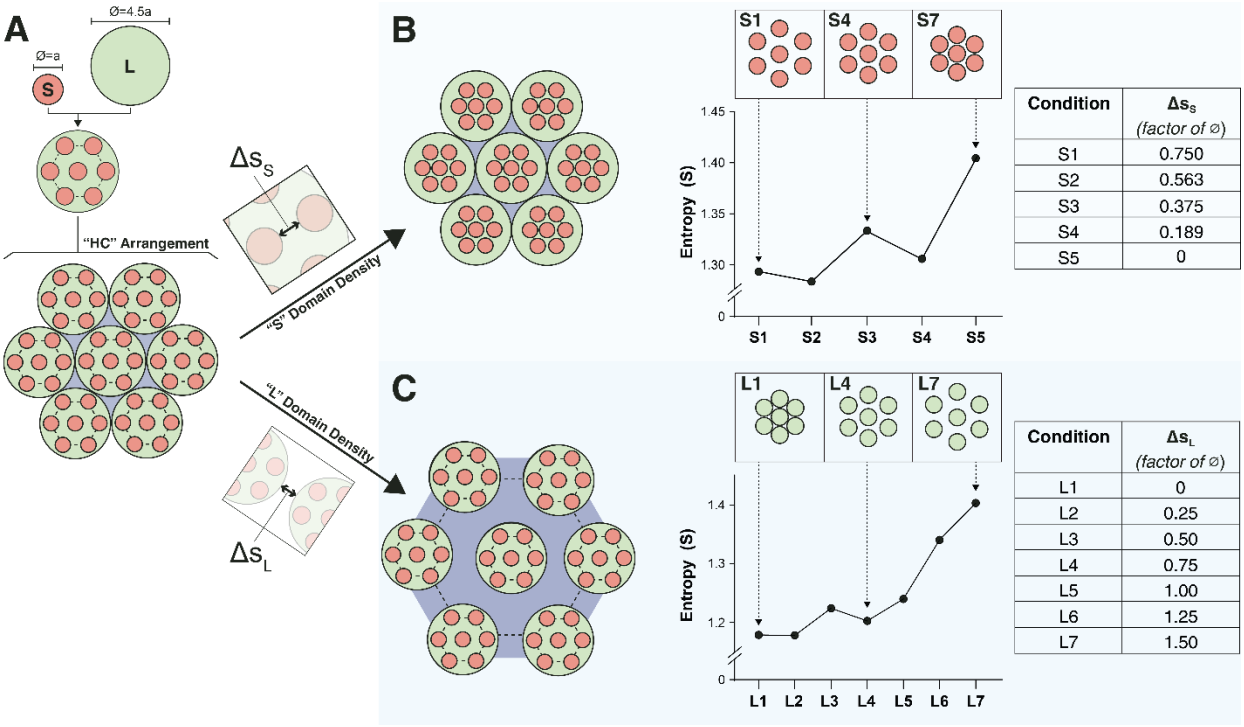


| Condition | $\Delta s_S$ (factor of ∅) |
|---|---|
| S1 | 0.750 |
| S2 | 0.563 |
| S3 | 0.375 |
| S4 | 0.189 |
| S5 | 0 |

| Condition | $\Delta s_L$ (factor of ∅) |
|---|---|
| L1 | 0 |
| L2 | 0.25 |
| L3 | 0.50 |
| L4 | 0.75 |
| L5 | 1.00 |
| L6 | 1.25 |
| L7 | 1.50 |

Figure 3-3: Simulated effects of domain spacing on entropy

**(A)** The setup is followed by simulation results from **(B)** tightening of small domain spacing and **(C)** expansion of large domain spacing. *Reproduced from Steeves et al. (2020), published by Dove Press under Open Access (CC-BY-NC).*

**ANALYSIS OF $TiO_2$ LAYER:** In addition to morphological analysis and spatial statistics, we applied Raman spectroscopy to assess the crystallinity of the nanotubular layers, a physical characteristic that plays an equally important role in controlling the response of adhering cells.[276,277] Although anodization is expected to produce mostly amorphous $TiO_2$ without post-annealing treatment, modification of time and water content in the electrolyte solution can nonetheless induce phase transformation to crystalline forms of titania (i.e., anatase, rutile).[278] As the crystal structure of the oxide layer has been shown to exert direct effects on cellular activity,[276,277] the degree of crystallinity of the nanotubular layer should be routinely assessed to standardize the evaluation of nanotube-controlled cellular events.[279] In this context, all surfaces investigated in this study displayed the distinctive spectrum of amorphous titania (**Figure 3-4A**), characterized by a broad band and by the absence of sharp peaks associated with the two crystalline phases (i.e., anatase and rutile).[280] This confirms that anodization did not alter the amorphous nature of the native $TiO_2$ layer.

Lastly, contact angle measurements assessed the wettability of surfaces (**Figure 3-4B**). Our data indicate that the contact angle decreased as the diameter of the NT substrates increased. Interestingly, the HC architecture displayed a contact angle value like that of the NT1 surface, suggesting that wettability is controlled by the s-HC layer given the similarities between these two conditions.

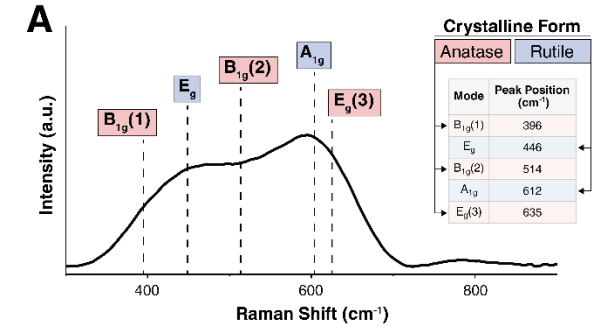


B

| Surface | NT1 | NT2 | NT3 | HC |
|---|---|---|---|---|
| Contact Angle(°) | 81 ± 4 | 58 ± 7 | 25 ± 3 | 85 ± 2 |

Figure 3-4: Raman spectroscopy of nanotube surfaces

**(A)** Representative Raman spectrum on nanotubular architectures and Raman peak assignment. **(B)** Contact angle values. *Reproduced from Steeves et al. (2020), published by Dove Press under Open Access (CC-BY-NC).*

### 3.3.2 CELLULAR RESULTS

**PROLIFERATION:** We successively evaluated the hMSC cell number at two different intervals to investigate topography-dependent effects on differential cellular proliferation. **Figure 3-5A** displays the cell number at 1 and 2 d of a culture determined by quantifying the number of DAPI-stained nuclei on each surface. At 24 h, the NT3

surface displayed the lowest count, indicating a negative effect on cell growth exerted by larger nanotubes. Conversely, the two surfaces with the highest entropy values, namely NT2 and HC, were also characterized by the highest proliferation at this timepoint. At 48 h, while cell count was statistically similar on the three NT surfaces, the HC architecture promoted cell growth, suggesting synergistic compounded effects since cells behave differently than on the respective nanotubular component counterparts (i.e., namely NT1 and NT3). Notably, we can ascribe the variations in CPI, especially significant for the NT1 and HC conditions, to their size distribution. Previous work has in fact shown that in the 15–20 nm diameter range, variations as small as 5 nm can yield a reduction of about 33% in cell proliferation.[42] In our case, NT1 and s-HC nanotube diameter varied within such a critical interval (i.e., from 17 nm to 25 nm) (**Figure 3-1D**) a factor that may have caused cells to experience compounded differential cueing resulting in a less homogenous overall behaviour. In addition, the NT3 substrate exhibited the lowest NSI (**Figure 3-5B**), thereby indicating a more marked nuclear deformation. This is most likely a result of cytoskeletal disorganization leading to the loss of structural integrity.[281] On NT3, cells may be in fact unable to generate large/reinforced focal adhesions leading to a more disorganized actin cytoskeleton which, in turn, hinders its ability to resist deformation from both internal and external forces.

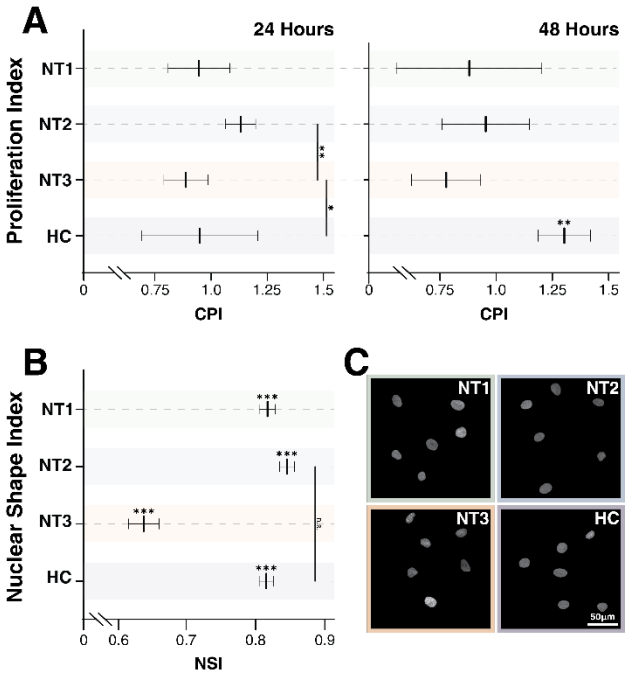


Figure 3-5: Proliferation and nuclear shape of hMSCs on titanium nanotubes

**(A)** Cell proliferation index (CPI) of hMSCs on nanotubular surfaces at 24h and 48h, **(B)** Nuclear shape index (NSI) at 24h, and **(C)** Representative images of hMSC nuclei at 24h. Statistical significance was defined as *=p < 0.05, **=p < 0.01 and ***=p < 0.001. *Reproduced from Steeves et al. (2020), published by Dove Press under Open Access (CC-BY-NC).*

**MORPHOLOGY**: We successively closed in on substrate-induced variations in cell morphology observed in immunofluorescence microscopy by quantifying cellular area, eccentricity, form factor (i.e., cellular shape) and protrusive index (**Figure 3-6A-D**). At 6 h, cells on the HC architecture displayed a marked spreading compared to those on NT substrates. In addition, eccentricity and reduced form factor similarly characterized cells adhering to NT1 and HC substrates. However, the HC elicited a significantly more protrusive morphology ($p < 0.01$). This suggests that while cells on the NT1 and HC surfaces display a more advanced spreading stage with respect to NT2 and NT3, characterized by the more elongated and protrusive cellular morphology, the HC architecture yielded greater cell spreading and abundance/length of protrusions. At 24 h, cells on the NT1 and HC surfaces displayed the highest cell area, indicating comparable cueing most likely due to the similarity between the NT1 and the s-HC nanotubes. At this interval, increasing the NT diameter yielded a reduction in the cell area, as previously reported for MC3T3 osteoblastic cells.[282] The same trend was also observed for the eccentricity: the HC showed the highest value, which gradually decreased from NT1 to NT3 surface (**Figure 3-6B**). The opposite tendency was observed for the cellular shape and protrusiveness (**Figure 3-6C,D**). At this time point, NT1 is the condition that elicits the most protrusive morphology (≈0.485), followed by HC/NT2 (≈0.525), suggesting that cells on the HC are more spread and into a migratory behaviour. At 48 h, the trend observed in the cell area at one day was consolidated. However, the following changes occurred: (*i*) eccentricity of cells on NT1 matched that on HC substrates, (*ii*) cells on NT2 substrates showed the smallest relative value and (*iii*) a reversed trend in the form factor was found for the HC substrates. In addition, cells on the HC/NT1 surfaces display the most protrusive morphology, with the lowest protrusion index of any timepoint (≈0.425). These morphological results can be summarized as follows: (*i*) cells on NT1/HC surfaces exhibit the highest spreading, in terms of cell area, when compared to the other conditions; (*ii*) while cells on NT1 maintain a protrusive morphology, cells on the HC surface appear to advance from protrusive (6h) to elongated (24h) and multipolar (48h) morphology as evidenced by considering the combined changes in eccentricity, form factor and protrusive index; (*iii*) cells on the NT3 surface (i.e., condition with the largest diameter and lowest entropy) exhibit the smallest surface area and a spherical morphology; (*iv*) cells on NT2 display intermediate features between such extremes. Taken together, our findings confirm the beneficial effects of topographies characterized by a combination of smaller diameters and higher entropy while demonstrating enhanced effects by the HC. This result is most likely associated with the greater disorder deriving from the higher eccentricity and clustering of the s-HC tubes, given that the L-HC array is not believed to exert direct cueing on FA clustering and cellular spreading because of its shallow nature. However, it may contribute to providing an extended surface for the establishment of FAs which makes up for the narrow wall thickness of the s-HC layer.

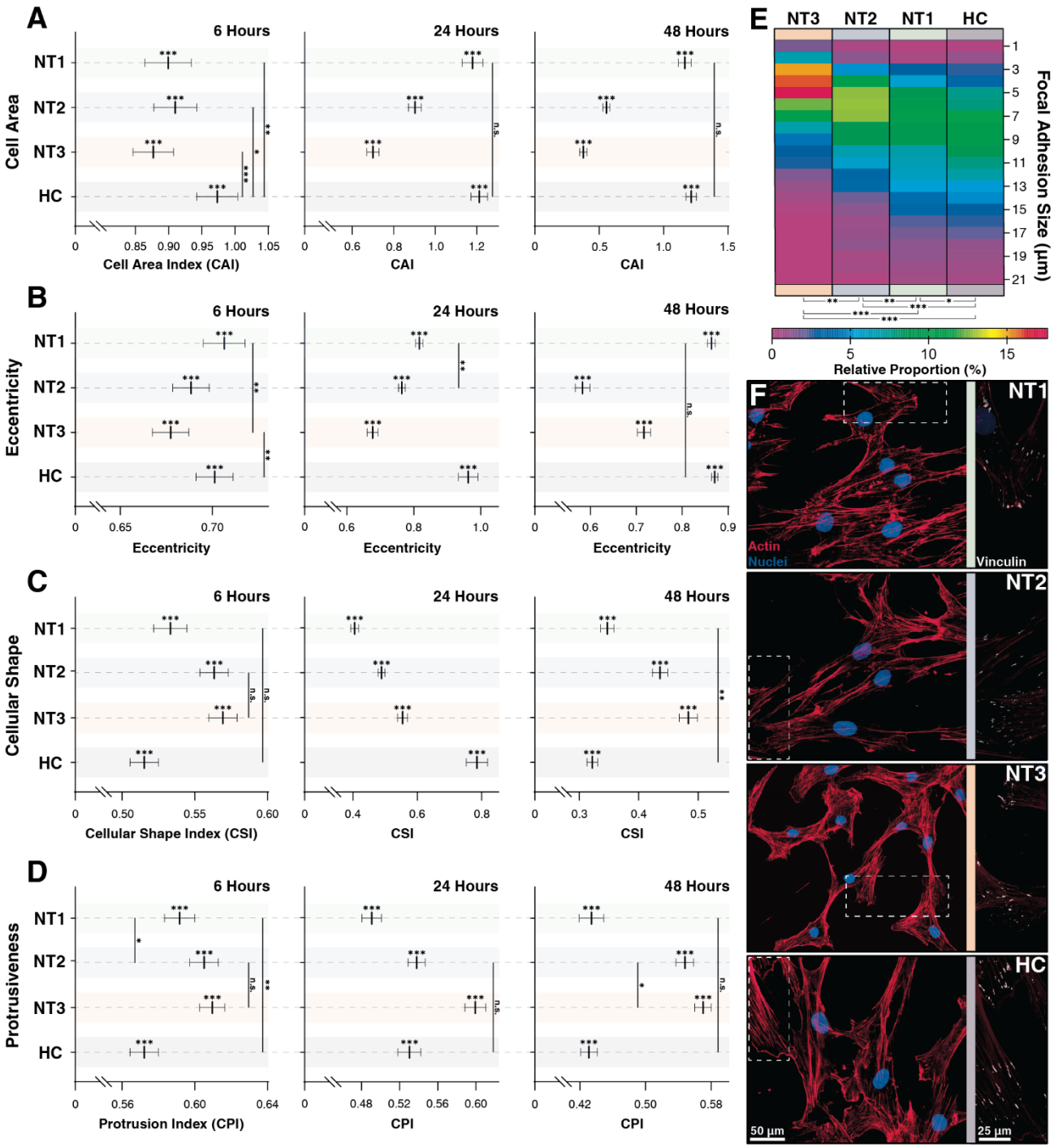


Figure 3-6: Morphological characterization of hMSCs

**(A)** cell area index, **(B)** eccentricity, **(C)** cell shape index and **(D)** protrusion index at 6h, 24h and 48h. **(E)** Distribution of focal adhesion length with respect to relative proportion. Cells on the NT3 surface have the lowest proportion of FAs above 11 µm in length. **(F)** representative fluorescence images. Statistical significance was defined as *=p < 0.05, **=p < 0.01, ***=p < 0.001 and n.s.=nonsignificant. *Reproduced from Steeves et al. (2020), published by Dove Press under Open Access (CC-BY-NC).*

**FOCAL ADHESIONS**: To link the morphological analyses to the intracellular response, we focused on focal adhesions (FAs), the multimeric clusters of adhesion molecules which are crucial assemblies in mechanobiology that link components of the extracellular matrix (ECM) to intracellular structures (i.e., cytoskeletal elements).[283] Importance of proper FA development and functioning of its constituents (e.g., focal adhesion kinase [FAK]) have been linked to several critical cell processes including migration, cell cycle progression and stem cell differentiation.[284,285] Subsequently, FAs are able to be used as direct and indirect indicators of cell-substrate interaction and so a concerted effort has been seen in the analyses of these structures with static (e.g., size) and dynamic (e.g., turnover kinetics) measures.[9,286,287] Of note, FA size have been indicated in key cell attributes including the prediction of cell migration,[58] mechanoresponse,[288] and stem cell biology[284,286] In this context, we measured the major axis length of the FAs at 24h using immunofluorescent labelling of Vinculin (**Figure 3-6F**) – one member of the multimeric complex that has even distribution across the FA[289] and acts as a key regulator of FA development as an adaptor protein to Talin and Actin.[290,291] To this end, size distributions were determined (**Figure 3-6E**) and, in a similar fashion to nanotube morphological distributions, comparisons were completed using the K-S statistical test. hMSCs seeded on NT2 ($\bar{\ell}_{NT2}$=3.65 µm) and NT3 ($\bar{\ell}_{NT3}$=2.53 µm) surfaces presented with FAs that were significantly smaller than on NT1 ($\bar{\ell}_{NT1}$=4.51 µm, $p < 0.001$). These results coincide with previous literature that noted a market decrease in focal adhesions on nanotubes with diameters approaching 100 nm (i.e., NT3),[42,292] and optimal spacing for normal FA development in the 58–72 nm range,[43,258] as seen with NT2 and NT3 surfaces. Notably, hMSCs seeded on the HC surface were characterized by slightly larger FAs ($\bar{\ell}_{HC}$=4.63 µm, $p < 0.05$) than those on the NT1 surface. Although the inter-tube spacing of the former (≈25 nm) is below the optimal range for the establishment of FAs, this interesting finding may be explained by postulating a beneficial contribution of the additional surface provided by the enveloping L-HC layer (≈33 nm), which would thus add extra area for the formation of FAs.

**OSTERIX (OSX):** In addition to the effects on cell adhesion and proliferation, surface nanotopography is capable of direct cueing for the differentiation of pluripotent stem cells towards their specific cell fates.[8,55,293] Topographical modification of titanium has shown to be effective in lineage guidance,[236,294-296] with $TiO_2$ nanotubes being capable of promoting variant strengths of osteogenic differentiation as a function of key physical properties of the tubular structures (e.g., diameter, length).[42,43,45,46] In this context, we investigated the osteoinductive capabilities of nanotubular architectures through the identification and distribution of the zinc-finger-containing Osterix/Sp7 (OSX) protein.[297] Regulation of the OSX gene by the osteoblastic RUNX2 transcription factor,[298] coupled with its control of downstream osteoblastic genes (e.g., Osteocalcin, Type I Collagen),[297] affirms its importance for the commitment of preosteoblastic cells toward mature osteoblasts. Specifically, the nuclear localization of OSX is an indication of the commitment to the osteogenic lineage.[297-299] Using a fluorescent reporter for OSX ($\lambda_{em}$=665 nm), and without the use of differentiation media, we were able

to detect the presence and localization of the OSX signal to the nuclear region as identified by a DAPI counterstain ($\lambda_{em}$=461 nm), shown in **Figure 3-7**. The confirmation of the osteoblastic commitment reaffirms that surface-driven osteogenic induction is taking place on all surfaces and thereby sets the groundwork for subsequent analyses (i.e., Raman) that asses the quality of the bone that is deposited by cells on their respective conditions.

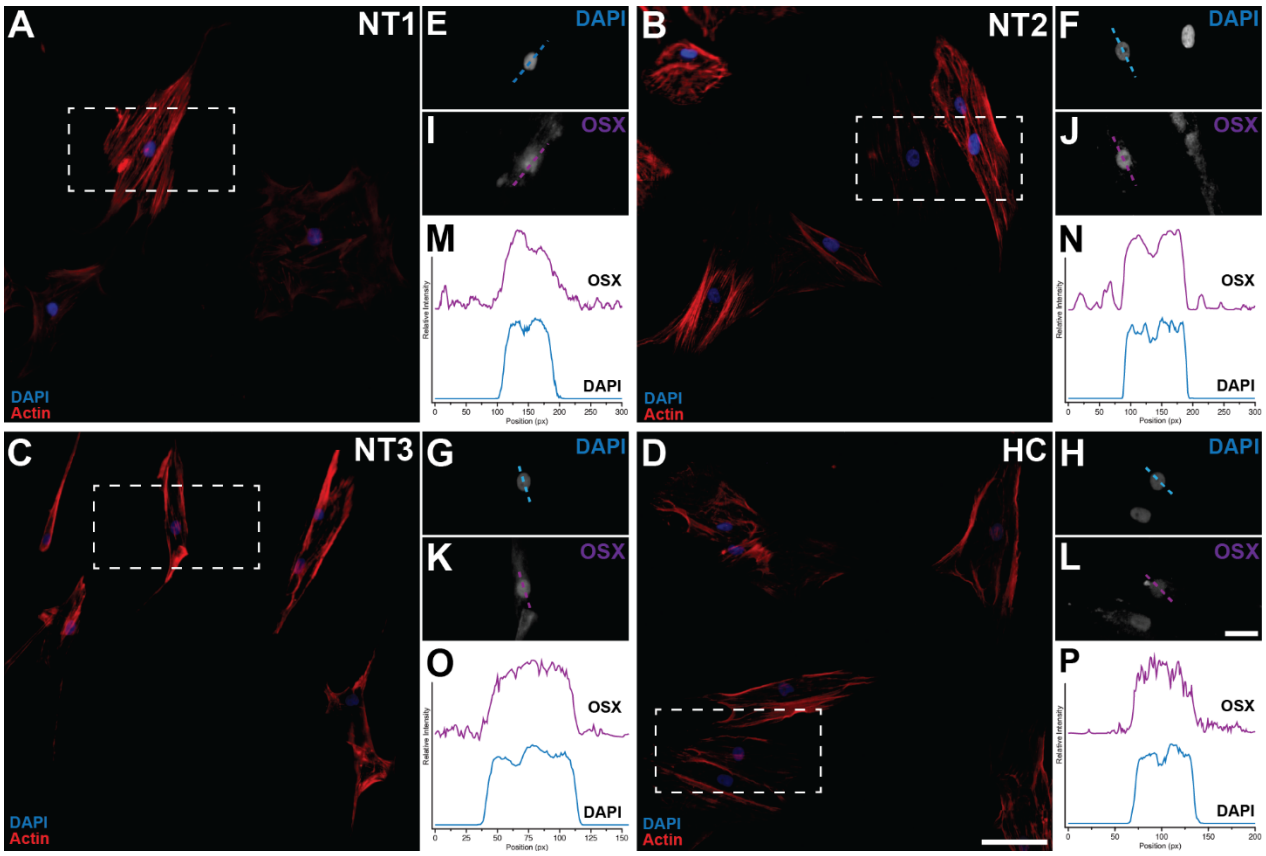


Figure 3-7: Nuclear localization of the osteogenic marker OSX at 7 d

Evidence of osteogenic differentiation through nuclear localization of Osterix (OSX / Sp7) at 7 d. Each set of 4 panels display immunofluorescence images of the cell body, 2D position and intensity profile of DAPI-stained nuclei and OSX signal for hMSCs on **(A-D)** NT1, **(E-H)** NT2, **(I-L)** NT3 and **(M-P)** HC surfaces, respectively. *Reproduced from Steeves et al. (2020), published by Dove Press under Open Access (CC-BY-NC).*

### 3.3.3 MINERAL ANALYSIS

To complete our analysis of hMSC response to nanotubular surfaces, we analyzed the properties of mineral nodules deposited *in situ* at 28 d of culture without the use of differentiation media by analyzing their Raman signature (**Figure 3-8A**). Four parameters were assessed as a way to gain insight into specific substrate-induced variations of bone quality.[300] The first parameter we considered was the mineral-to-matrix ratio (**Figure 3-8B**), which normalizes the amount of bone against the quantity of collagen, and has been shown to increase with bone tissue age.[300,301] In our case, the mineral nodules deposited on the HC architecture showed the highest ratio

with a marked difference with the NT1, while NT2 and NT3 did not show any statistical distinction between them. We successively assessed the carbonate-to-phosphate ratio (**Figure 3-8C**), which is indicative of regularly occurring carbonate substitutions in hydroxyapatite, a phenomenon was shown to increase with tissue age and to depend on the bone architecture and mineral crystallinity.[300,301] In these cases, the variability for the HC surface is greater than that for the other conditions, and this may be either due to chemical inhomogeneities and/or to the fact that the carbonate band partially overlaps another phosphate band at ≈1076 $cm^{-1}$, thereby reducing measurement precision especially for apatites with minimal carbonate content.[300,301] Considering that significant differences were nonetheless detected between nodules deposited on the HC substrates and those on the NT1 surface, and between nodules on NT3 surface and those on the NT1 substrate, by taking into context the mineral-to-matrix and phosphate-to-mineral ratios, we can conclude that among the conditions investigated, more advanced mineralization was found on the HC and NT3 substrates. The third parameter analyzed was the position of the $\nu_1PO_4^{3-}$ band within the 955–962 $cm^{-1}$ range. Previous work has demonstrated that the transition of the peak position from lower to higher wavenumbers, and a band shape change from a broad to narrow, are associated with the transformation of disordered amorphous calcium phosphate (ACP, 950 $cm^{-1}$) to mature crystalline hydroxyapatite (HAP, 960–962 $cm^{-1}$).[302,303] Raman data from all surfaces exhibit peaks in the neighbourhood of 958 $cm^{-1}$ (**Figure 3-8D**), indicating that the minerals are mainly composed of transformed HAP, with potential inclusions of its transitional intermediates (e.g., octacalciumphosphate [OCP])[304] in those conditions that exhibited the highest shift. In particular, nodules on NT1 and HC surfaces presented with a statistically similar peak position indicating a greater shared predominance of crystalline HAP when compared to the red-shifted bands exhibited on NT2 and NT3. Lastly, we assessed the inverse of full-width-at-half-maximum (1/FWHM) of the $\nu_1PO_4^{3-}$ band (**Figure 3-8E**) as a measure of crystallinity and crystalline homogeneity. The transition from disordered ACP to ordered HAP is observed with increased crystallite *c*-axis length and improvement in the stoichiometric organization of the crystal lattice.[300,305] Subsequently, reduction in short-range disorder and progressive homogeneity of the mineral constituents have shown to result in a narrowing of the bandwidth,[306] as observed for the HC architecture with respect to the NT conditions. Taken together, our Raman results show that the HC architecture induces more advanced mineralization of crystalline hydroxyapatite nodules when compared to the other conditions. Notably, the mineralization in the crystalline hydroxyapatite nodules on NT1 lags behind. Conversely, the hydroxyapatite on the NT3 surface is characterized by a degree of mineralization comparable to that of the HC substrate, but with a significantly lower degree of crystallinity and/or crystalline homogeneity. In this context, the correlation between early morphological signatures, namely MSC cell number and cell area at short intervals, with osteogenesis assessment was previously demonstrated, highlighting the power of immunofluorescence imaging to predict long-term mineralization.[307] It was shown that cell morphology, in particular, cell area, after 3 d was highly correlated with 35-day mineralization. We can thus

infer that the greater cell areas determined on the NT1 and HC surfaces at 48h may be responsible for the faster formation of crystalline HPA, with a more advanced maturation stage (in terms of crystalline homogeneity) for the latter. On the other hand, previous work has also reported that osteoblasts cultured on 100 nm diameter nanotubes experience increased nuclear elongation, a factor which was associated with increased alkaline phosphatase (ALP) and osteocalcin expression, as well as greater bone-forming ability *in vivo*,[282] and that, in part, could further explain the results obtained for the NT3 surface.

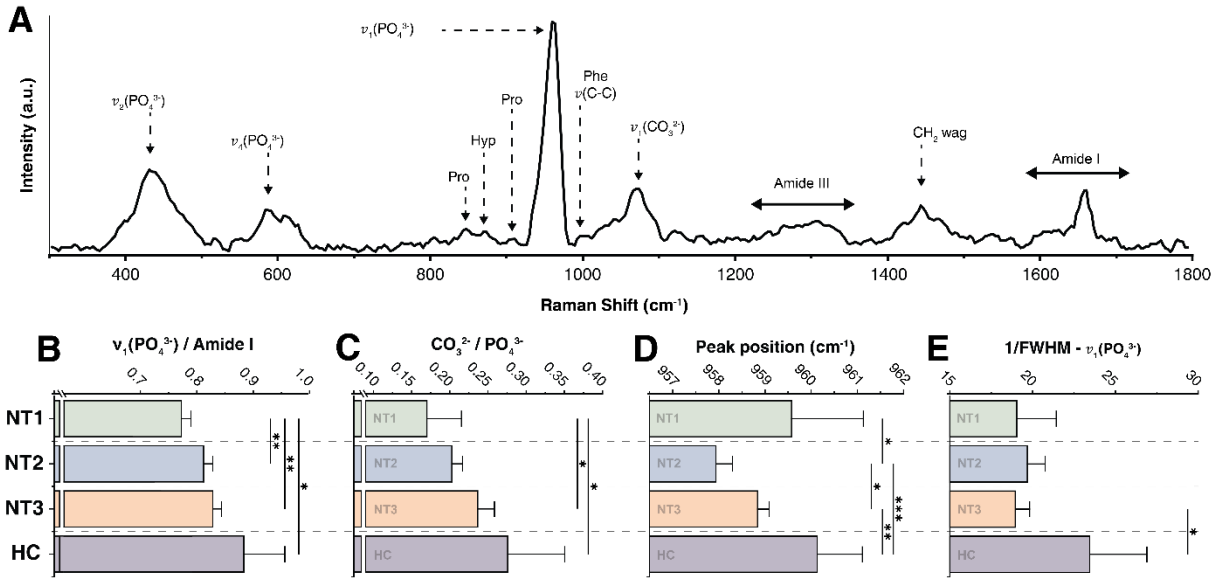


Figure 3-8: Raman spectroscopy of bone nodules

**(A)** Representative Raman spectrum acquired on deposited bone mineral after 28 d of culture. Quantification of physicochemical parameters on nodules deposited on NT1 (n=5), NT2 (n =10), NT3 (n =6) and HC (n =12) surfaces. Mean values with bars representing 95% CI for the **(B)** Mineral-to-matrix ratio, **(C)** Carbonate-to-phosphate ratio, **(D)** Peak position and **(E)** 1/FWHM of the phosphate ($PO_4^{3-}$) v1 band. Statistical significance was defined as *=p < 0.05, **=p < 0.01 and ***=p < 0.001. *Reproduced from Steeves et al. (2020), published by Dove Press under Open Access (CC-BY-NC).*

## 3.4 CONCLUSION

In this work, we created differentially sized nanotubular patterns (NTs) through the rational modulation of the experimental parameters, which also permitted us to create a two-tiered nanotubular architecture (HC). Through the characterization of the complex nanotopographical environment of these surfaces, we delineated important new connections between nanotubes and stem cell response (including proliferation, morphology and deposition of bone mineral). Ultimately, results from this work strengthen the role of direct physicochemical cueing to unlock the potential to affect healing and controlling stem cell fate, paving the way to combine both physical and chemical cues in a synergistic manner for drastically improved, efficient and effective biological

outcomes of implantable materials. In this context, despite the advances made possible by the development of new technologies, the progress of nanoarchitectures for biomedical applications is still restricted by the technical capability of design and fabrication methods, often inadequate to rapidly replicate micro- and nanoscale patterns on relatively large surface areas of medically relevant materials for high-throughput manufacturing.[308] While anodization confers the flexibility of controlling the diameter, we have demonstrated that other morphological parameters are equally important, in particular, the degree of order. The creation of the HC nanoarchitecture could thus become a strategy to vary the order of nanotube arrays without changing their diameter, thereby becoming allowing one extra level of synergistic control of the resulting nanotopography.

## 3.5 ACKNOWLEDGEMENTS

This work was supported by the Natural Sciences and Engineering Research Council of Canada (NSERC) through the Discovery grant, by the Canada Foundation for Innovation (CFI) and the Ontario Ministry of Research and Innovation (MRI) through the Leaders of Opportunity (LOF) fund. FV also acknowledges the IBEC's Severo Ochoa Visiting program for outstanding external researchers. The authors acknowledge the resources and assistance provided by the Cell Biology and Image Acquisition (CBIA) Core, funded in partnership by the University of Ottawa and CFI.

## 3.6 MATERIALS AND METHODS

### 3.6.1 NANOTUBULAR ARRAYS AND TWO-TIERED HONEYCOMB (HC) STRUCTURE

Titanium foil (0.127 mm thick, 99.9+% purity, Alfa Aesar, USA) was cut into 2.5 × 1 cm pieces, ultrasonically cleaned in toluene, rinsed with deionized water (DI) and finally dried in air. Samples were then subject to a two-step anodization procedure in an electrolyte solution containing 0.3 wt% crystalline ammonium fluoride ($NH_4F$, Sigma Aldrich, USA) and 2 wt% DI in anhydrous ethylene glycol ($C_2H_6O_2$, Sigma Aldrich). A two-electrode configuration was used to carry out the anodization treatments with a platinum foil counter electrode (25 × 25 × 0.1 mm, 99.9%, Alfa Aesar). A custom 3D-printed apparatus for reliable electrode alignment (**Figure 3-1A**) was designed in Fusion360 (Autodesk, USA) and printed with 1.75 mm PLA filament (AMZ3D, USA) on an I3 Mega S (ANYCUBIC, China). The apparatus was designed to fit atop of a 50 mL Pyrex beaker, containing exactly 30 mL of the electrolyte solution, and retained a stable distance between the electrodes of 2 cm to ensure consistent results,[81] without contamination of the alligator clips by the solution. After the first step of anodization, samples were rinsed with DI, dried in air and the oxide layer peeled off with tape to expose the newly formed nucleation sites for the subsequent generation of nanotubes during the second anodization step (**Figure 3-1B**). The formation of nucleation sites resulted in the fabrication of nanotubular substrates with a higher degree of order, compared to those obtained by one-step anodization.[309] Samples were thoroughly rinsed in DI and dried prior to being cut into two pieces of 1 × 1 cm. **Table 3-1** contains the applied voltages and times

for the fabrication of nanotubular surfaces characterized with average diameters ≈20, ≈50 and ≈90 nm (hereafter referred to as NT1, NT2 and NT3, respectively) as well as the two-tiered honeycomb surface (hereafter referred to as HC) composed of arrays of smaller nanotubes (s-HC) clustered within larger domains (L-HC).

Table 3-1: Experimental parameters used to create nanotube (NT1–3) and the honeycomb (HC) arrays.

| | Condition | NT1 | NT2 | NT3 | HC |
|---|---|---|---|---|---|
| **Step 1** | **Voltage (V)** | 30 | 40 | 60 | 60 |
| | **Time (Min)** | 60 | 45 | 30 | 30 |
| **Step 2** | **Voltage (V)** | 30 | 40 | 60 | 20 |
| | **Time (Min)** | 5 | 25 | 10 | 20 |

### 3.6.2 MORPHOLOGICAL CHARACTERIZATION

The surface morphology of anodized substrates was investigated by using a Scanning Electron Microscope (6610LV SEM, JEOL, Japan) at 45,000× magnification. SEM images were successively analyzed by the image analysis software Fiji[310] and by a custom CellProfiler pipeline[311] to quantify average nanotube diameter, eccentricity, wall thickness as well as nearest neighbour distance (NND).

The topography of the HC surfaces was characterized by a Dimension AFM instrument (Veeco Instruments, New York, USA) in tapping mode. We employed a rectangular $Si_3N_4$ cantilever characterized by a nominal spring constant (k) of 42 $N \cdot m^{-1}$, resonance frequency (*f*) of 330 kHz and a non-rotated pyramid tip with a nominal radius of 10 nm (PPP-NCH, Nanosensors, Switzerland). Data was subsequently processed and analyzed in WSxM for the step-height between z-structured domains of the HC surface.[312]

### 3.6.3 SPATIAL ANALYSIS AND ENTROPY SIMULATIONS

SEM micrographs were subjected to a custom CellProfiler pipeline, involving the erosion of the nanotube apertures to their respective centroids, followed by 2D Voronoi tessellation to generate the experimental planar tiling for subsequent analysis. Surface Voronoi entropy ($S_v$) was calculated as a metric of systemic order, defined by $S_v = -\sum_n P_n ln\, P_n$, where $P_n$ is the fraction of polygons with *n* sides.[313,314] Data were recorded and processed in OriginPro 2018 software (OriginLab, USA).

Different experimentally observed effects have been reproduced in simulations with Mathematica (Wolfram, USA) to investigate possible simple relations between the nanotubes' geometric distributions and patterns and the collective measure quantified by the entropy. Details are provided in the Supplementary Information.

### 3.6.4 CONTACT ANGLE MEASUREMENTS

The static water contact angle was measured with a VCA Optima Surface Analysis System (AST Products Inc., USA). A 1 µl drop of DI was deposited through a micro-syringe (Hamilton Company, USA) onto the substrates. Manual angular measurement of the droplet was performed to ensure accuracy prior to the automated measurement of the angle. Three droplets per sample were measured, and measurements were carried out on three samples per condition.

### 3.6.5 CELL CULTURES AND IMMUNOFLUORESCENCE IMAGING

#### 3.6.5.1 *BONE-MARROW DERIVED HUMAN MESENCHYMAL CELL (HMSC) CULTURES*

Three sources of bone-marrow-derived human mesenchymal stem cells (hMSCs) were obtained by two distributors (Lonza, USA and RoosterBio, USA) to account for donor variability. hMSCs from RoosterBio (Lot. 00014; Lot. 00082) were expanded in High-Performance Media (RoosterBio) and were thawed in similar media. hMSCs from Lonza (Lot. 603525) were expanded in Mesenchymal Stem Cell Growth Medium BulletKit (MSCGM, Lonza) and were thawed in similar media. Experiments were performed with low-passage hMSCs (≤ P5) cultured in DMEM with 4.5 $g \cdot L^{-1}$ glucose and L-glutamine (Corning, USA), supplemented with 8% fetal bovine serum (FBS, Gibco, USA), 100 $U \cdot mL^{-1}$ penicillin and 100 $\mu g \cdot mL^{-1}$ streptomycin (Gibco). The culture was maintained in a 5% $CO_2$, 37 $^oC$ water-jacketed incubator. Cells were passaged with 1× TrypLE (Gibco) and suspension to be used for experiments were treated with 50 $\mu g \cdot mL^{-1}$ Soybean Trypsin Inhibitor (Sigma-Aldrich) prior to seeding.

Nanotubular substrates were sterilized in 70% EtOH and thoroughly washed in sterile 1× PBS, prior to use in cell culture experiments. They were placed in 24-well plates and 500 ml of the cell suspension was added to each well at a density of 10,000 $cells \cdot cm^{-2}$. Cells for proliferation, morphology, focal adhesions (FAs) and bone mineral deposition studies were cultured on the nanotubular substrates for the experiment-specific time periods, ranging from 6 h to 28 d. Timepoints within the first 48 h were used for morphological analyses as these intervals provide insight into the initial cell-substrate effects, prior to differentiation-induced transformations. These experiments were terminated by cellular fixation with 500 µL of fresh 4%-paraformaldehyde (PFA, Sigma-Aldrich) for 10 minutes at room temperature. Analysis of mineral quality was assessed at 28 d (*i*) for consistency with previous work,[46,236,282] and (*ii*) to provide sufficient time for the mineral to be deposited and to undergo maturation (e.g., the substitution of carbonate in hydroxyapatite).[315] These experiments were terminated by the removal of cell media and incubation within a desiccator to eliminate cell function while preserving the deposited minerals for spectroscopic analysis. All experiments were performed with 3 samples per condition, per time point, and were completed in triplicate.

For fluorescent imaging, cells were permeabilized with 0.25% Triton X-100 (TX-100, Sigma-Aldrich) for 10 min at RT and labelled for nuclei (ReadyProbes NucBlue [DAPI], Thermo Fisher) and actin (Rhodamine Phalloidin, Thermo Fisher). To visualize focal adhesions, samples were blocked in 1%-albumin / 10%-normal goat serum

(Thermo Fisher) for 1h at RT. Vinculin was labelled with a primary 1:400 anti-hVin1 mouse mAb (Sigma-Aldrich) and secondary 1:800 AlexaFluor 488 goat-anti-mouse IgG (Thermo Fisher). Primary antibody was an overnight incubation while blocking and secondary antibody incubations were for 1h each at RT. Samples were washed and mounted on #1.5 VistaVision rectangular cover-glass slides (VWR, USA) with VECTASHIELD Vibrance (Vector Labs, USA) hard-set mounting media.

#### 3.6.5.2 *IMMUNOFLUORESCENCE IMAGING*

Multi-channel images, used in the quantification of nuclei number and cytoskeletal morphological analysis, were captured with an AxioObserver.Z1 inverted microscope (Zeiss, Germany) fitted with an AxioCam MRm CCD (Zeiss). Nuclei were imaged using 5 × 5 tiles visualized through a 10× A-Plan objective (Ph2, NA=0.25, Zeiss). Cytoskeletal elements were observed using 5 × 5 z-stack tiles, visualized through a 20× Plan-Apo objective (Ph2, NA=0.8, Zeiss). Morphological analysis of the nuclei and focal adhesions was observed through at 40× PL APO Oil objective (NA=1.3, Leica) with a Quorum Spinning-disk Confocal setup (Quorum Technologies, Canada) affixed to a Leica BMI16000B inverted microscope (Leica Microsystems, Germany), complemented by a Photometrics Prime BSI sCMOS [95% QE, back illuminated]. The setup was driven by MetaMorph software (Molecular Devices, USA).

Cell count was determined by quantifying the number of DAPI-stained nuclei on each surface with a custom CellProfiler pipeline. Cell count was then normalized against the average cell number per experiment, thereby generating the cell proliferation index (CPI). This was done to reduce inter-experiment variability. Nuclear and actin morphological analysis was achieved by stitching and focus-stacking the panels in Fiji ("Stack Focuser" package) ahead of their processing in a custom pipeline in CellProfiler. Key morphological parameters were the object area, eccentricity, form factor and protrusive index. The index of eccentricity (*e*), an ellipse model of circularity, was measured for both nanotubes and cells. It is calculated by determining the ratio of the distance of the focal length of the ellipse and the major axis length.[311] This entails that a perfectly circular object has an *e*=0 and a line segment *e*=1. Form factor ($F_f$), a measure of shape irregularity, was measured and is defined as $F_f = \frac{4*\pi*A}{P^2}$ where A is the area, P is the perimeter. A perfectly round object has an $F_f$=1 whereas jagged contours yield $F_f$<1. For consistency with previous work,[316] the form factor for the cellular and nuclear morphologies was labelled as the "cell shape index" (CSI) and "nuclear shape index" (NSI), respectively. The measure of "extent" was used as an indicator of protrusion, herein termed the "cell protrusive index" (CPI), and is calculated by the proportion of area in a surrounding bounding rectangle covered by the cell, where perfect coverage would be =1. In the case of elevated protrusiveness, the great number and length of anisotropic protrusions would widen the bounding box without shared isotropic spreading of the cell body, thereby lowering the CPI (i.e., elevated protrusion = lower CPI). Images used for focal adhesion analysis were subjected to a custom macro in Fiji-ImageJ that included focus stacking, background subtraction ("Rolling Ball Background Subtraction") and contrast

enhancement ("Contrast Limited AHE", CLAHE) packages. Peripheral focal adhesion length was then manually measured in FIJI-ImageJ. All resultant data was compiled and processed in GraphPad Prism 8 (GraphPad Software, Inc.) or OriginPro.

### 3.6.6 RAMAN SPECTROSCOPY

Raman spectroscopy was first employed to characterize the crystallinity of the nanotubular layers as well as the physicochemical properties of bone mineral deposited by hMSCs after 4 weeks of culture. To this end, a WITec Alpha 300 Raman microscope was used. The crystallinity was determined by focusing a 542 nm frequency-doubled Nd:YAG laser through a 20× EC EpiPlan objective (NA=0.4, Zeiss) on the surface of the nanotubular substrates, with a 30-second acquisition time. The assignment of Raman bands for anatase and rutile titania peaks is reported in **Figure 3-4A**.[317]

For the analysis of bone mineral, substrates were collected after 28 d of culture directly from the 24-well culture plate and gently rinsed in DI to remove the excess of culture media prior to Raman measurements. Successively, Raman spectra were acquired by using a 100× EC EpiPlan NEOFLUAR objective (NA=0.9, Zeiss) and a 785 nm diode laser with a 240-second integration time and double acquisition to enhance the signal-to-noise ratio. Three different substrates per condition were used, and experiments were carried out by analyzing samples that were derived from two independent cultures. Randomly selected mineral nodules were analyzed *in situ*, directly on each substrate to minimize perturbations associated with the collection of organic/inorganic material from the substrates. The number of mineral nodules analyzed per condition was dictated by the ease at which these could be identified on the substrates by optical microscopy and by the quality of the resulting Raman signature to ensure accurate peak deconvolution. Raman data were compiled and processed in OriginPro.

The assignment of the Raman bands is reported in **Figure 3-8A**.[300,301,318,319] The principal Raman mineral bands used for quantitative analysis include the phosphate ($PO_4^{3-}$) $\nu 1$ band at ≈960 $cm^{-1}$ and the B-type carbonate ($CO_3^{2-}$) $\nu 1$ band at ≈1070 $cm^{-1}$. The positions and heights of these bands provide information about mineral parameters such as crystal structure and deviations from stoichiometry. The most relevant Raman collagen bands to assess bone mineral are the amide I at ≈1660–1680 $cm^{-1}$, the hydroxyproline bands at 855 $cm^{-1}$ and 875 $cm^{-1}$ and the amide III at 1245–1270 $cm^{-1}$. The position, intensity, area and width of these bands are sensitive to changes in protein structure.[320,321] In this study, the surface-induced alterations of the bone mineral were investigated using three metrics: mineral-to-matrix ratio, carbonate-to-phosphate ratio and crystallinity. The analysis of spectral data requires quantification of peak parameters, such as position, the inverse of full width at half maximum (1/FWHM) and peak area. This was achieved by fitting the spectra with Lorentzian functions after background subtraction. Mineral-to-matrix ratio, a measure of the mineral content in bone, was calculated as the ratio of the integrated area of the bands located at 900–1000 and 1590–1720 $cm^{-1}$. Carbonate-to-phosphate ratio, which denotes the carbonate content of the mineral in the bone specimen, was calculated as the intensity

ratio of the carbonate *v*1 (1070 $cm^{-1}$) to phosphate *v*1 (960 $cm^{-1}$) peaks. Mineral crystallinity, which depends on the disorder in the bone structure, was calculated from the 1/FWHM of the phosphate *v*1 band (960 $cm^{-1}$).[302,304,306,322]

### 3.6.7 STATISTICAL ANALYSIS

All experiments in this work were repeated in triplicate with at least three samples/condition. Bar charts are expressed as the mean with a 95% confidence interval (CI). Data sets were tested for normality using the Shapiro-Wilk test. Normal data sets were tested with the parametric Two-Way ANOVA with Tukey's HSD post hoc test for mean comparisons. A difference was considered significant if $p < 0.05$. Statistical significance was defined as *=$p < 0.05$, **=$p < 0.01$ and ***=$p < 0.001$. A comparison of distributions was completed using the non-parametric Kolmogorov-Smirnov (K-S) statistical test,[323] where the deviations between cumulative fraction functions are compared. Quantitative Raman data, which were confirmed for normality, were subsequently tested with Welch's *t*-test which is the recommended statistical method due to the unequal variances (confirmed with Bartlett's test) and unequal sample sizes.[324] Statistical significance was defined *=$p < 0.05$, **=$p < 0.01$ and ***=$p < 0.001$. Analyses were performed with GraphPad Prism and OriginPro.

# 4 DIRECT CUEING BY PULSED-WATERJET TREATED TITANIUM ON FIBROBLAST, OSTEOBLASTIC AND HUMAN STEM CELLS FOR PROSPECTIVE USE IN DENTAL IMPLANTS

*Relevant manuscript*

**Direct cueing by pulsed-waterjet treated titanium on fibroblast, osteoblastic and human stem cells for prospective use in dental implants**

Alexander J. Steeves[1,2], David J. Lomboni[1,2], Mohan Vijay[3], Andrew Tieu[3], Fabio Variola[1,2]

[1] Faculty of Engineering, Department of Mechanical Engineering, University of Ottawa, Ottawa, ON, Canada
[2] Ottawa-Carleton Institute for Biomedical Engineering, Ottawa, Canada
[3] VLN Advanced Technologies Inc., Ottawa, ON, Canada

**Submitted** on **2020–11–16** to **Materials Letters**

**Accepted** on **2021–01–25 | DOI:** 10.1016/j.matlet.2021.129437

## MOTIVATION

This study aims to explore a safer and more cost-effective strategy for preparing titanium surfaces for periodontal implants using Pulsed-Water Jet (PWJ) technology. This innovative method, which uses high-velocity, pulsed water jets to deliver high-velocity water slugs to interact with the surface, aims to provide contaminant-free surface preparation that enhances osseointegration and bone remodelling processes through the application of Saos-2 and NIH/3T3 cell lines, representing bone and gum/mucosa, respectively. The dual application of these cell lines on PWJ-treated titanium surfaces contributes to the interdisciplinary approach of materials science, cellular biology, and clinical dentistry by aiming to comprehensively evaluate the integrative capabilities of treated titanium surfaces within the periodontal milieu.

## RATIONALE, OBJECTIVES AND HYPOTHESES

The advancement of periodontal implant technologies necessitates the development of surface treatments that can promote optimal cell attachment, proliferation, and differentiation. Pulsed-water jet (PWJ) technology offers a promising avenue for creating contaminant-free, bio-compatible titanium surfaces, potentially enhancing periodontal implants' safety, efficacy, and cost-effectiveness.

### OBJECTIVES

1. **Preparation and characterization of surfaces**: To capitalize on the PWJ technology, surfaces of varying morphology properties are generated using variations in the nozzle speed during application

2. P**roliferation analysis of Saos-2 and NIH/3T3 cell models**: To evaluate the biocompatibility of PWJ-treated titanium surfaces, proliferation is assessed using Saos-2 and NIH/3T3 cell lines as models for bone and gum tissue interactions.
3. **Differentiation analysis of hMSCs**: To investigate the differentiation potential of human mesenchymal stem cells (hMSCs) on PWJ-treated titanium surfaces, focusing on the nuclear localization of Osterix (OSX) as a marker for osteogenic differentiation.

## HYPOTHESES

1. The application of PWJ technology in the preparation of titanium surfaces will result in the generation of varied morphological properties, which, in turn, will differentially influence the proliferation of Saos-2 and NIH/3T3 cells, reflecting their respective roles in bone and gum tissue interactions.
2. The differentiation of hMSCs into osteoblasts, as evidenced by the nuclear localization of Osterix (OSX), will be significantly influenced by the specific morphological characteristics of the PWJ-treated titanium surfaces, underscoring the potential of surface engineering to direct stem cell fate towards bone regeneration.

## 4.1 ABSTRACT

Pulsed-waterjet (PWJ) technology holds the potential for the biologically effective surface treatment of dental titanium implants. In addition to the proliferative response of in vitro models for gingiva (NIH/3T3s) and bone (Saos-2) cells, our study investigates the osteogenic potential of PWJ-treated titanium surfaces by employing human mesenchymal stem cells (hMSCs). The most significant proliferation of fibroblast NIH/3T3 and osteoblast-like Saos-2 cells was elicited on $T_{1.76}$ and $T_{4.83}$ treatment conditions, respectively. Morphological traits and the nuclear localization of an osteogenic reporter (OSX) indicate preferential osteogenic differentiation on the $T_{2.43}$ condition. This work demonstrates the potential of PWJ technology for surface modification, supporting its technological translation as a cost-effective, environmentally friendly, and contaminant-free method to incorporate novel bioactive properties into titanium implants.

## 4.2 INTRODUCTION

A fundamental prerequisite in the design of dental implants is the ability to direct osseointegration while limiting the factors that can compromise the therapeutic outcome. Specifically, the quality of the fixation of the screw component into the jawbone is a key determinant of implant success, depending in part on the geometry and surface topography.[325] Traditionally, surface modification of dental screws relies on methods (e.g., acid-etching, sandblasting) which could pose the risk of introducing contaminants (e.g., acid remnants, abrasive particles). These, in turn, may alter the quality of cellular processes at the implant-bone interface.[326] For example, sandblasted, large-grit, acid-etched (SLA) multi-stage protocol employs large/medium particulates (e.g., $Al_2O_3$, $ZrO_2$) to generate micro-rough surfaces via 20–200 µm craters, followed by acid etching (e.g., in a $H_2SO_4$/HCl solution) to superimpose 0.5–2 µm micropores. Suitable process/quality control and/or cleaning may thus be required to mitigate the risk of surface contaminations, adding to fabrication time and manufacturing cost.

This study capitalizes on the Pulsed-Water Jet (PWJ) technology,[113] which has several successful applications (e.g., coating removal, hydro-demolition) to generate surfaces capable of directing cell-specific responses. Specifically, we demonstrate differential effects on the proliferation of osteoblastic and fibroblast cells and on the osteogenic differentiation of human stem cells. Our initial evidence supports the potential of PWJ technology for biologically relevant surface treatments of titanium for applications in dental implant manufacturing. Notably, a viable extension of the PWJ technology is to utilize sterilized water to achieve a single-stage process combining surface texturing and titanium surface sterilization.

## 4.3 RESULTS AND DISCUSSION

### 4.3.1 SURFACE ANALYSIS

Surface topography has a direct influence on several cell functions including the adhesion and proliferation of fibroblasts and osteoblasts and the differentiation of stem cells,[242,327] influencing osseointegration and thereby, implant success.[325]

Microscale roughness ($S_a^{\mu}$) of untreated titanium was 0.51 µm ("$C_{0.51}$") and an inverse relationship with the nozzle speed resulted in $T_{1.76}$, $T_{2.43}$ and $T_{4.83}$ from respective nozzle speeds (**Figure 4-1A,B**). The roughness of $T_{4.83}$ ($S_a^{\mu}$= 4.83 µm, nozzle speed = 450 mm/s) falls within the range of surfaces generated by SLA treatment ($S_a^{\mu}$ =3.97–5.50 µm).[328] SEM and AFM imaging shows treated surfaces with microscale periodic lamellar structures, resulting from the deformative energy of recurrent adjacent water-slugs (**Figure 4-1D,E**). AFM maps provided the quantification of nanoscale roughness ($S_a^n$) and surface area (SA). With respect to CTRL, $S_a^n$ and SA were both significantly increased on all experimental conditions (**Figure 4-1F,G**). Notably, the different treatment did not vary the amorphous nature of the passivation $TiO_2$ layer, as shown by Raman spectroscopy (**Figure 4-2**), thereby indicating no contribution from crystallinity.[329]

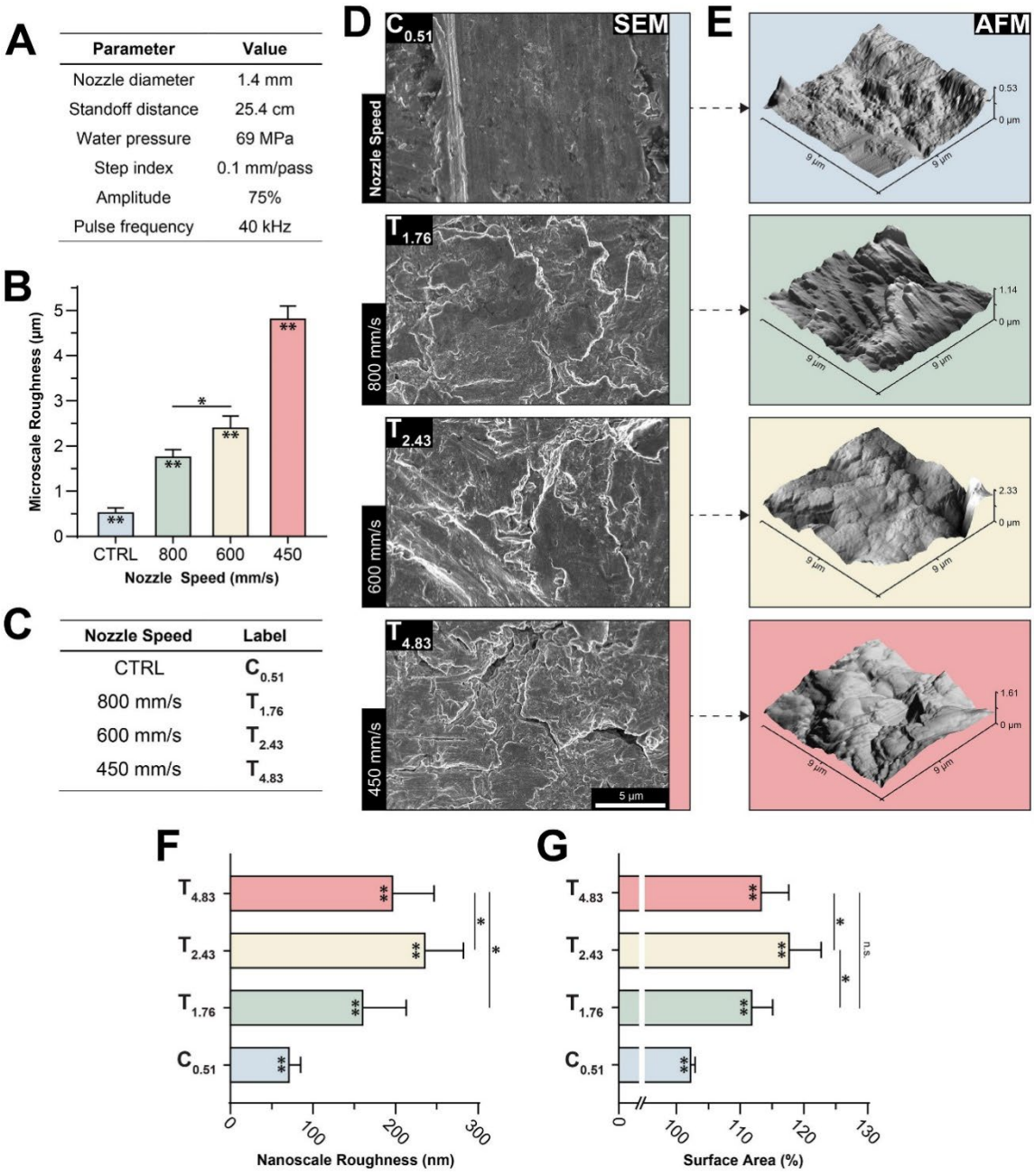


Figure 4-1: Surface analyses results.

**(A)** Pulsed-water jet (PWJ) parameters. **(B)** Micro-roughness and **(C)** resultant condition labels. **(D)** SEM visualization at 5000×. **(E)** 3D projections of non-contact AFM data with quantification of **(F)** nano-roughness and **(G)** surface area. ANOVA: * = $p < 0.05$, ** = $p < 0.01$.

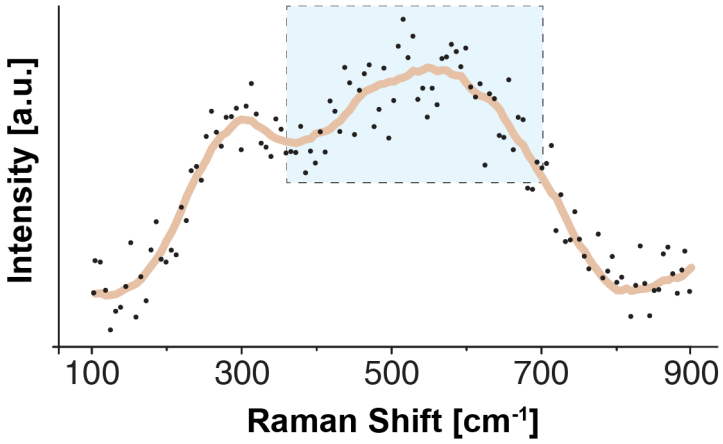


Figure 4-2: Raman analysis of the oxide layer of $T_{2.43}$ as a representative surface.

### 4.3.2 BIOLOGICAL ANALYSES

Differences in multi-scale topographical structures between the surfaces can evoke cell-type-specific responses.[242,327] We investigated the influence of topography-based cueing to proliferation (NIH/3T3, Saos-2), morphology and differentiation (hMSCs).

#### 4.3.2.1 *PROLIFERATION*

Focusing on cell-types generally found at the implantation site, we considered NIH/3T3 fibroblasts and Saos-2 osteoblast-like cells as a model for our in vitro experiments and assessed their proliferation at 72 h (**Figure 4-3A**). Both cell types cultured on $T_{1.76}$ were identical to untreated titanium (CTRL), whereas those cultured on $T_{2.43}$ presented with markedly lower cell counts (NIH/3T3: 54%; Saos-2: 72%; $p < 0.01$). However, cells grown on $T_{4.83}$ exhibited substantial differences in cell-type-specific proliferative response. While the proliferation of NIH/3T3s decreased by -67%, Saos-2 cells showed a decisive enhancement of +26%.

#### 4.3.2.2 *MORPHOLOGY*

Where morphological characteristics of the cell body are a function of cell-biomaterial interactions, analysis of shape-based parameters provides insight on how topographical cues influence cell behaviour.[242] Owing to the potential use of microtextured surfaces to direct stem cells, we focused on assessing the hMSC morphology. Inherently fibroblastic in shape, multipotent hMSCs at 24 h presented a negative relationship between the interfacial area and the nozzle speed: $T_{1.76}$, $T_{2.43}$ and $T_{4.83}$ exhibited area reductions of -11.6%, -31.7% and -37.9%, respectively (**Figure 4-3B**). At 7d, hMSCs grown on $T_{1.76}$ and $T_{4.83}$ experienced a continued decrease in cell area of -41.1% and -62.2%, respectively. Notably, the intermediate $T_{2.43}$ experienced a significantly lesser change of -12.4% in the cell area. At 7d, this dissimilar response on $T_{2.43}$ is accompanied by a significant -40.9% in eccentricity

and +57.7% in form factor (**Figure 4-3C,D**), indicating that the cell body is comparatively round with reduced projections. These attributes are associated with the expression of osteogenic markers.[330]

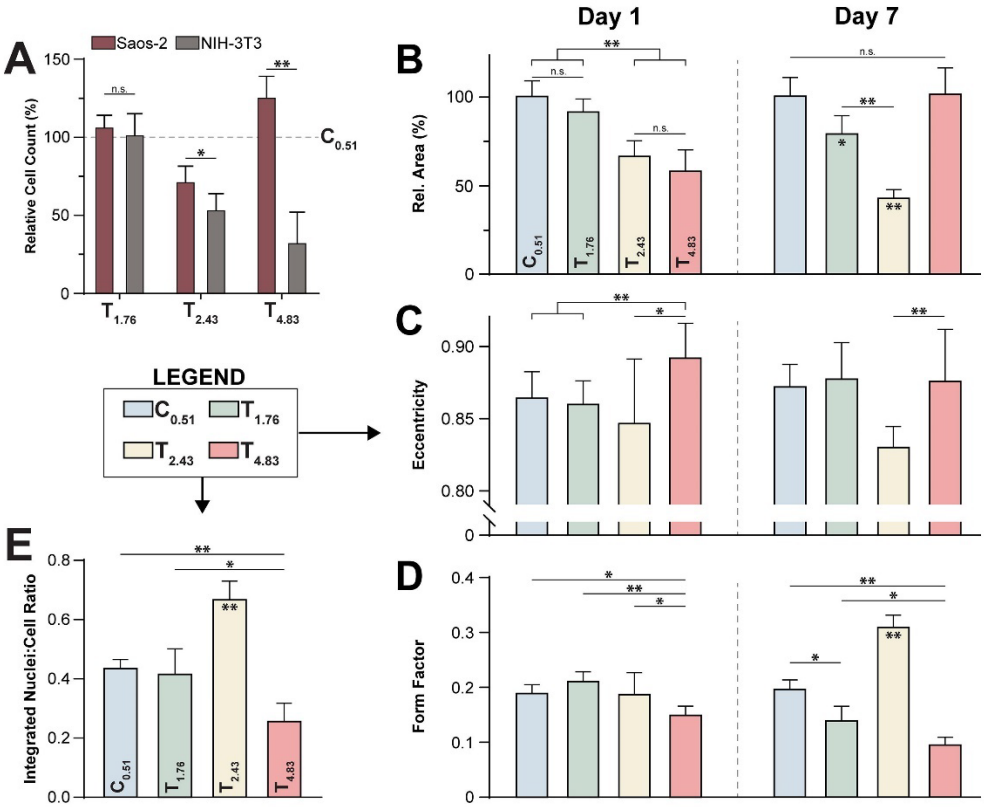


Figure 4-3: Biological testing results.

**(A)** Proliferation of Saos-2 and NIH/3T3s at 72 h. **(B-D)** 1 and 7-day morphological characterization of hMSCs for **(B)** cell area, **(C)** eccentricity and **(D)** form factor with 95%-CI. **(E)** Nuclear localization of OSX with 95%-CI. ANOVA: * = $p < 0.05$, ** = $p < 0.01$.

#### 4.3.2.3 *DIFFERENTIATION*

The positive osteoinductive capabilities of implant material implicates improved osseointegration by forming integrated bone, from local stem cells, at the implant-bone interface. Osterix (OSX), an osteoblast transcription factor, undergoes nuclear localization during osteogenic differentiation.[297] Following a 7-day incubation, hMSCs that were seeded on the $T_{2.43}$ surface presented with 67.3% OSX nuclear localization (**Figure 4-3E**), surpassing all other surfaces including CTRL by significant > 20% ($p < 0.01$). $T_{4.83}$ had the lowest localization (26.2%), indicating the roughness of the surface was non-conducive to differentiation, whereas $T_{1.76}$ (42.1%) was statistically alike to CTRL (44%), likely owing to it being the least transformed of the treatment conditions. The relationship between roughness and osteogenic activity (e.g., osteocalcin levels) for bone-cell models has been previously reported,[331] with a microscale roughness of ≈2.3 µm, resembling $T_{2.43}$. Aside from the greatest nanoscale-

roughness within $T_{2.43}$ microcavities, the spacing between primary features is believed to provide sufficiently large interfacial fields — both of which are influential in osteogenic commitment.[327]

## 4.4 CONCLUSION

In this study, surface preparation of titanium was accomplished with a PWJ setup generally used for material removal applications. Variation of nozzle speed has shown the ability to control roughness at both the micro- and nanoscale, leading to cell-type-specific cueing of proliferation and stem cell differentiation. Since treated surfaces can generate surface roughness similar to the first stage of the SLA procedure, PWJ technology could potentially replace the sand-blasting component, reducing the chances of particulate-based contamination. Considering these results, this work supports the potential PWJ-enabled surface preparation stage in a sterile environment that can, in turn, reduce manufacturing steps and provide a cost-effective and versatile alternative for dental implant fabrication.

## 4.5 ACKNOWLEDGEMENTS

This work was supported by an NSERC Engage Grant and Ontario Centres of Excellence (OCE) VIP I grant in collaboration with VLN Advanced Technologies. The authors thank Mr. Ryan Berthelot for assistance with SEM imaging.

## 4.6 MATERIALS AND METHODS

### 4.6.1 MATERIALS

#### 4.6.1.1 *PREPARATION*

99.2%-pure Titanium foil (Alfa Aesar) was prepared using a pulsed-waterjet process with parameters reported in **Figure 4-1A**. In addition to untreated control samples, four treatment conditions were generated by varying the transverse nozzle speed. Conditions were labelled ("C" = control, "T" = treatment) per their microscale roughness (e.g., "$T_{2.43}$" = RMS of 2.43 µm) with labels reported in **Figure 4-1C**. Surfaces were sterilized by ethanol and UV irradiation.

#### 4.6.1.2 *MORPHOLOGICAL CHARACTERIZATION*

Microscale roughness was measured with a TR200 portable tester (Qualitest). Imaging of surfaces was carried out with a JSM-7500 FESEM (JEOL). Nanoscale 3D-projections were achieved with non-contact atomic force microscopy (NC-AFM) on an alpha300-RSA system (WITec). High-resolution maps (10 × 10 µm; 512 × 512 px) were captured with an 8-nm tip on a RTESPA-300 cantilever ($f_{nom}$ = 300 kHz, $k_{nom}$ = 40 $Nm_{-1}$, Bruker). 3D-reconstruction in Gwyddion provided surface area (SA) and roughness (RMS).[332]

#### 4.6.1.3 *RAMAN CHARACTERIZATION*

Raman spectroscopy was performed on the alpha300-RSA to assess $TiO_2$ crystallinity. Three spectra (6 acc., 10 sec./acc.) were collected from randomly selected regions of each sample (n=9) via a 50× Epiplan-Neofluar objective (NA=0.55, Zeiss), excited by a 632 nm laser (35 mW, Toptica Photonics). The 300–900 $cm^{-1}$ region was analyzed for the characteristic peaks of anatase and rutile.[317]

### 4.6.2 BIOLOGICAL

#### 4.6.2.1 *CELL CULTURE*

NIH/3T3 (ATCC), Saos-2 (ATCC) and human mesenchymal stem cells (hMSCs, Lonza) were cultured in Dulbecco's Modified Eagle Medium (DMEM, Corning) supplemented with 10% (NIH/3T3, Saos-2) or 8% (hMSCs) fetal bovine serum (FBS, Gibco) and 1% Pen-Step (Gibco). Cells were detached with TrypLE (Gibco) and seeded for experiment-specific timepoints. Experiments were completed in triplicate.

#### 4.6.2.2 *MORPHOLOGY ANALYSIS*

Cells were fixed (4% PFA) and permeabilized (0.25% Triton-X100) before labelling of the nuclei (DAPI) and actin (Rhodamine-Phalloidin, ThermoFisher). Z-stacks were captured through a 10× A-Plan (NA = 0.25, cell proliferation) or 20× Plan-Apo (NA = 0.8, morphology). Image analysis for cell morphology was performed in CellProfiler.[311]

#### 4.6.2.3 *OSTEOGENIC DIFFERENTIATION*

At 7 d, hMSCs were fixed, permeabilized and labelled with a primary Osterix (OSX) rabbit pAb (ab22552, Abcam, 1:300) and secondary GAM-Alexa Fluor 488 (ThermoFisher, 1:600). Nuclear localization of OSX, a nuclear osteogenic reporter,[297] was measured as a ratio of nuclear v. cytoplasmic signal in CellProfiler.

# 5 CHARACTERIZATION OF CONCENTRATION-DEPENDENT KINETICS AND PARTICLE FORMATION IN POLYMERS DERIVED FROM DOPAMINE, LEVODOPA, L-NOREPINEPHRINE, AND RACEMIC NOREPINEPHRINE

*Relevant manuscript*

**Characterization of kinetics and particle formation in polymers derived from dopamine, levodopa, L-norepinephrine, and racemic norepinephrine**

Alexander J. Steeves[1,2], Fabio Variola[1-4#]

[1] Faculty of Engineering, Department of Mechanical Engineering, University of Ottawa, Ottawa, ON, Canada
[2] Ottawa-Carleton Institute for Biomedical Engineering, Ottawa, Canada
[3] Faculty of Medicine, Department of Cellular and Molecular Medicine, University of Ottawa, Ottawa, ON, Canada
[4] Children's Hospital of Eastern Ontario (CHEO), Ottawa, ON, Canada

**In preparation**

## 5.1 MOTIVATION

Originating from a similar family of catecholamines, norepinephrine (NE) and levodopa (LD) share an identical base structure with dopamine (DA). The additional hydroxyl groups on the NE and carboxylic acid groups on the LD introduce chirality and have been reported to generate distinct morphologies and chemical surfaces when deposited onto substrates. A defining characteristic is the relative thinness of polynorepinephrine (pLNE) and polylevodopa (pLD) (when used to functionalize 2D substrates) compared to that of polydopamine (pDA), which can preserve nanoscale features more effectively. While the L-enantiomer of DOPA (L-DOPA) is predominantly used in coatings, recent studies have shown the drastic impact of enantioselective polymerization on the kinetics and properties of the resulting polymer. However, there has yet to be any similar work on NE-based coatings, with some studies employing the L-enantiomer, a racemic mixture, or reporting without any reference to chirality. Moreover, some studies have contrasted pDA, pLNE, and pLD substrates, but the influence of precursor concentration on the reaction kinetics and the resulting surfaces remains unexplored. This critical parameter affects the formation of the pDA particles and coatings.

## 5.2 RATIONALE, OBJECTIVES AND HYPOTHESES

The objective of this study was to provide a comparative analysis of how pDA, pLNE, and pLD polymerization and nanoparticle synthesis are influenced by two distinct precursor concentrations: a low concentration (LC) of 0.5 mg/mL and a high concentration (HC) of 2.0 mg/mL. These two concentrations were chosen to capture the

distinct changes in polymer behaviour and properties across a critical threshold. Literature indicates that within the 1.0 to 2.0 mg/mL concentration range, DA exhibits significant shifts in film thickness, particle size, and aggregation kinetics.[136,333] Additionally, we explore the chiral intricacies of NE, examining both the L-enantiomer (L-NE) and the racemic mixture (rac-NE) to elucidate how chirality influences the synthesis process of poly-L-norepinephrine (pLNE) and poly-rac-norepinephrine (pRNE). To this end, an absorbance-based analysis of pCA polymerization was first carried out at two absorbance wavelengths: 450 nm ($\lambda_{abs}^{450}$) and 600 nm ($\lambda_{abs}^{600}$). As both theoretical and experimental studies validate, the $\lambda_{abs}^{450}$ measurements indicate early polymerization stages, where oxidative polymerization yields simpler monomeric and dimeric structures. Conversely, $\lambda_{abs}^{600}$ measurements capture the formation of more advanced oligomers and conjugated structures, characteristic of advanced polymerization. These polymer networks experience a redshift due to the material's structure and energy bandgap changes, reflecting significant electron delocalization due to their extensive donor-acceptor pair interactions. This dual-wavelength approach aims to provide a more comprehensive analysis of the evolving complexity of polymer networks from initial oligomer formation to the development of mature, highly structured polymers.

### *5.2.1* OBJECTIVES

1. **Polymerization absorption analysis:** To investigate the dynamic changes in optical absorbance over time for polymers synthesized using dopamine (DA), levodopa (LD), L-norepinephrine (L-NE), and rac-norepinephrine (R-NE) precursors. The objective of this study was to elucidate the synthesis of polydopamine (pDA), polylevodopa (pLD), poly-L-norepinephrine (pLNE), and poly-rac-norepinephrine (pRNE), including the processing of data into kinetic rates and delineating the impact of a fourfold increase in precursor concentration.
2. **DLS analysis of nanoparticle synthesis:** To present a quantitative examination of particle diameters, detailing the temporal progression of particle size from the initial stages through 24 h of synthesis.
3. **Polymer Dispersion Ratio (PDR):** To introduce PDR as a novel metric and apply it to contextualize the synthesis processes of materials. This multifaceted approach captures not only the rate of formation but also the spatial distribution of particles within the synthesized materials.

### 5.2.2 HYPOTHESES

1. The precursor concentration from low (0.5 mg/mL) to high (2.0 mg/mL) concentrations enhanced the polymerization rate in the early stages. Still, it led to saturation kinetics, resulting in a non-linear enhancement of the peak polymerization rates across both examined wavelengths.
2. Variations in the precursor chemistry and concentration-influenced dynamics lead to distinct particle sizes and temporal profiles in NP/µP synthesis.

3. The chiral differences between pLNE and poly rac-norepinephrine (pRNE) are hypothesized to significantly influence the synthesis kinetics, NP/µP formation, and behaviour. Specifically, incorporating the D-enantiomer may impede the process due to steric hindrance, altering intermolecular interactions.
4. Introducing the Polymer Dispersion Ratio (PDR) as a novel metric will provide insights into polymer aggregates' spatial distribution and temporal dynamics.

## 5.3 ABSTRACT

Polycatecholamines (pCAs), such as polydopamine (pDA), polylevodopa (pLD), and polynorepinephrine (pNE), are pivotal in biomaterials science because of their inherent ability to form versatile and functional coatings. Although pDA has been extensively studied and utilized across various applications due to its robust adhesive properties and bioactivity, pLD and pNE polymers, which potentially offer more suitable physicochemical properties for specific applications, remain less explored. Moreover, despite the interchangeable use or unreported forms of L-norepinephrine (L-NE) and racemic norepinephrine (rac-NE), the impact of chirality on the polymerization process and the resulting polymer properties is still not fully understood. This study aims to address this knowledge gap by providing a comparative analysis of polymerization kinetics and nanoparticle (NP; ≤100 nm)/microparticle (µP; >100 nm) formation within polymers derived from dopamine (DA), levodopa (LD), L-NE, and rac-NE at high and low concentrations. Employing a dual-wavelength absorbance-based approach at 450 and 600 nm, we elucidated how the precursor concentration influenced pDA, pLD, pLNE, and pRNE synthesis dynamics. Our findings indicated that higher concentrations promoted rapid monomer-to-intermediate conversions and introduced complexity owing to potential saturation kinetics.

Furthermore, Dynamic Light Scattering (DLS) analysis elucidated the temporal dynamics of nanoparticle diameters, underscoring the concentration-dependent modulation of nanoparticle size and aggregation behaviour. This relationship was particularly evident in the non-linear response of the particle size distribution to varying precursor concentrations, which significantly influences their physicochemical stability and functional potential in biomedical applications. Introducing the Polymer Dispersion Ratio (PDR) as a novel metric has provided insights into polymer aggregates' spatial distribution and temporal evolution. This study underscored the critical roles of concentration and chirality in designing and applying advanced biomaterials for targeted biomedical uses, highlighting the potential of underexplored pCA polymers.

## 5.4 INTRODUCTION

Catecholamines (CA) are a class of bioactive molecules that function as neurotransmitters within the body and are characterized by a catechol nucleus and an ethylamine side chain. Dopamine (DA) has emerged at the forefront of biomaterials due to its exceptional ability to undergo bioinspired oxidative polymerization into polydopamine (pDA) — one of the most consequential materials in the last two decades.[6] Due to its ability to deposit on a cornucopia of materials of varying properties,[6,334,335] and its intrinsic potential for follow-up functionalization,[336] pDA has been employed in far-reaching applications, including as a functional biomaterial with inherent antibacterial properties [124], a bioactive film for implant surface modification,[125] an immobilization coating for macromolecules (e.g., growth factors),[126] and as a versatile polymeric drug carrier platform.[127] The polymerization and properties of pDA are ascribed to the catecholamine's molecular structure, enabling a rich

tapestry of interactions, including cation-π, anion-π, π-π, covalent, Van der Walls, and hydrogen bonding interactions.[337-341] These interactions endow the material with distinctive adhesive properties, the ability to form cohesive films, and, in turn, influence its interaction with biological systems.

Dopamine (DA) is a member of the catecholamine (CA) family, alongside levodopa (LD) and norepinephrine (NE), both of which are gaining increasing relevance for their ability to polymerize into polylevodopa (pLD) and polynorepinephrine (pNE), respectively. pLD has been employed to modify β-glucan to fabricate novel antibacterial wound dressings capable successively,[342] worked with $TiO_2$ nanoparticles to create a high affinity molecularly imprinted sensor for pesticides,[145] and has been exploited as a coating of capillaries for enhanced enantioseparation in open tubular electrochromatography (OT-CEC).[146] pNE, on the other hand, has garnered attention through its produce ultra-smooth lacquer on several materials (e.g., PCL, PTFE, PDMS, tantalum) and has been reported to support human neural stem cell (hNSC) adhesion and facilitate a 3-fold increase in PC12 neurite length.[140,343-345] Remarkably, a pivotal study by Tan et al. (2021) stands out as the sole systematic comparison that delves into the physicochemical and biological properties of pDA, pNE, and pLD coatings, particularly emphasizing their application in blood-contacting devices.[120] This comprehensive analysis clarifies the distinct characteristics of each polymer and offers insights into their potential biomedical applications.

Distinct from DA, LD and NE molecules possess additional carboxyl (–COOH) and hydroxyl (–OH) functional groups on the β-carbon of their ethylamine side chains. This chirality is notable because it introduces enantioselective polymerization, impacting the physicochemical properties of the resulting polymers. Recent studies on the enzymatic polymerization of L-, D-, and rac- DOPA have revealed that chirality profoundly influences polymer synthesis and the material properties of pLD.[346] These findings underscore the potential of enantiomeric specificity in enhancing the functionality of biomaterials. In this context, the literature reveals a lack of consensus on the enantiomeric composition of polynorepinephrine (pNE); studies have variably utilized the L-enantiomer (L-NE),[140,345,347-349] a racemic mix (R-NE),[343,350-352] or have not reported the chirality at all.[120,150,344,353-355] While factors such as pH, temperature, and solvent are well-documented in their influence on pDA polymerization, the precursor concentration is a pivotal variable in defining the synthesis of coatings and particle formation.[129,130,136,173] This key determinant has not been extensively studied in pNE and pLD synthesis.

In this context, our study aimed to bridge this knowledge gap by providing a comparative analysis of pDA, pNE and pLD polymerization and nanoparticle formation at two distinct concentrations: a low concentration (LC) of 0.5 mg/mL and a high concentration (HC) of 2.0 mg/mL. These concentrations were chosen to capture distinct changes in the polymer behaviour and properties across the critical threshold of 1.0 to 2.0 mg/mL. This range is associated with significant alterations to DA film thickness, particle size, and aggregation kinetics.[136,333] Additionally, we explored the chiral intricacies of NE, examining both the L-enantiomer (L-NE) and the racemic

mixture (rac-NE) to elucidate how chirality influences the synthesis process of poly-L-norepinephrine (pLNE) and poly-rac-norepinephrine (pRNE).

To this end, absorbance-based analysis of pCA polymerization was first carried out, specifically at the absorption wavelengths of 450 nm ($\lambda_{abs}^{450}$) and 600 nm ($\lambda_{abs}^{600}$). The assessment of pCA kinetics via this method is well-established.[346,356,357] Eumelanin-like materials such as those studied herein were noted for broad absorption resulting from the overlapping features of chemically distinct species that progressively assemble through covalent and non-covalent means, contributing to their excitonic effects.[337,358] The selection of $\lambda_{abs}^{450}$, which has been similarly used to measure the formation DA, NE and LD-derived materials,[357] and the comparison of early-to-late-stage products of DA,[153] is underpinned by the evolution of these materials. Specifically, signals in the 400–500 nm range are associated with the formation of less complex oligomers (e.g., DA-DA) as indicated by both theoretical (e.g., density functional theory [DFT]) and experimental reports.[359-361] Higher wavelengths (i.e., $\lambda_{abs}^{600}$), are associated with the more extensively conjugated structures of highly polymerized eumelanin-like materials that extend the absorption spectrum to lower energies.[362,363] These polymer networks experience a redshift due to extensive donor-acceptor pair structures within the microstructure, leading to a decrease in the energy bandgap and enhanced electron delocalization.[358] This transition between absorption bands with increasing network complexity is exemplified by the polymerization of 5,6-dihydroxyindole (DHI), a shared and consequential intermediate in the synthesis and adhesion of pDA, pNE and pLD.[120] Simulated and experimental results indicate that absorption in the 375–500 nm region is associated with DHI monomers and dimers. At the same time, trimers exhibit absorption beyond 500 nm, with hexamers specifically showing an onset at 600 nm.[337,361,364] Additionally, the absorption coefficient at a wavelength of 589 nm was linearly correlated to the thickness of the mature DA-derived coatings, determined through layer-by-layer deposition. The thickening of eumelanin films is associated with an increase in the optical coefficient in the lower energy regions, starting at 600 nm, due to increased Mie scattering.[365,366] This dual-wavelength absorbance-based analysis effectively provides insight into the complex polymerization dynamics and structural evolution of pCA materials during polymerization.

Subsequently, DLS analysis presented a quantitative examination of the microparticle (µP) and nanoparticle (NP) diameters, detailing the temporal progression of particle size from the initial stages through 24 h of synthesis. Finally, we introduced the Polymer Dispersion Ratio (PDR) as a novel metric, applying it to contextualize the materials' synthesis processes. This multifaceted approach captured not only the rate of formation but also the spatial distribution of particles within the synthesized materials.

We sought to establish a more precise link between molecular structure and kinetics by examining the effects of concentration, chirality, and polymerization. Our research focuses on comparative analysis across different catecholamines at two concentration levels, enhancing our knowledge of their polymerization

behaviour and potential for biomedical applications. The findings of this investigation are expected to provide valuable insights into the design and development of advanced biomaterials.

## 5.5 RESULTS AND DISCUSSION

### 5.5.1 POLYMERIZATION ABSORPTION ANALYSIS

#### 5.5.1.1 *POLYDOPAMINE (PDA)*

For both concentrations of DA, $\lambda_{abs}^{450}$ increased rapidly in the initial phase, indicative of the relatively rapid formation of early-stage polymerization intermediates (**Figure 5-1A**). The kinetics rate, peaking within the first half-hour for HC and LC, coincided with DA's noted rapid oxidation character (**Figure 5-1B**).[150] As expected for HC DA, the reaction milieu was more conducive to rapid monomer-to-intermediate conversion in line with the principle that higher reactant concentrations generally resulted in enhanced reaction rates due to the reduced mean free path between reactive species and increased collision probability.[129] However, a 4x increase in DA concentration resulted in only a 2.3–2.4x enhancement in the peak rate at both wavelengths, indicating a non-linear response that suggested saturation kinetics. This behaviour implies that the rate-limiting steps became significant as the monomer concentration increased, echoing the complexities that Salomäki et al. (2018) identified in the interplay of environmental factors affecting polydopamine formation.[159] The system may encounter thermodynamic and kinetic constraints above specific monomer concentrations, involving the transition from monomers to the polymer matrix and, thereby, the overall reaction kinetics.

By 6 h, a sharp decline in the kinetic rate for both HC and LC suggested that the readily polymerizable monomers were becoming depleted. This decline could have been due to the sequestration of dopamine monomers or intermediates, such as DHI, by aggregating particles that impeded film formation, a phenomenon observed when DA concentrations exceeded 1 mg/mL, resulting in thinner films.[136,138] Notably, the reaction kinetics for HC decreased to almost zero after 24 h, while LC maintained approximately 23% of its peak rate for both wavelengths. This difference suggests that lower concentrations might facilitate more regulated and sustained polymerization, potentially reducing the saturation and depletion effects that impact higher-concentration reactions.

In scrutinizing the concentration effects on polymerization, **Figure 5-1C** illustrates how increasing the precursor concentrations differentially impacted the absorbance at the observed wavelengths. Up to approximately 3.5 h post-initiation, the increased precursor significantly affected the species observed at $\lambda_{abs}^{600}$, indicating an accumulation of mature polymer species, likely the formation of aggregates. Over the remaining course, the benefit appeared to flip to the formation of species observed at $\lambda_{abs}^{450}$. These intriguing results might reflect a shift in the polymerization process from forming conjugated mature species to generating more early-

stage intermediates. Furthermore, it could be due to various factors, such as the consumption of specific intermediates, reaction equilibrium shifts, or changes in the chemical environment.

#### 5.5.1.2 *POLYLEVODOPA (PLD)*

In contrast to the behaviour observed with DA polymerization, polylevodopa (pLD) formation appeared to experience an extended lag to its peak formation rate (**Figure 5-1D**). Through similar wavelengths within each concentration, the peak kinetic rate was earlier at HC (6.5 h) than at LC (7.5 h); **Figure 5-1E**. The observed extended lag phase in LD polymerization kinetics, particularly at lower concentrations, could be attributed to multiple physicochemical factors. The inherent hydrophilicity of LD due to its carboxyl group enhanced water dispersibility and solubility, which may have led to a preference for aqueous rather than polymerized states, contributing to the initial delay in polymerization.[342] This hydrophilic nature also implies a lower propensity for LD to participate in hydrophobic interactions, a vital driving force in early-stage polymerization. Following the rapid initial oxidation of levodopa to dopaquinone and subsequently to dopachrome under alkaline conditions,[147] the hydrophilic –COOH group still present on these specific intermediates may have contributed to the slower polymerization and, therefore, the initial lag phase.[147,367] Furthermore, the quinone intermediates may have stabilized through cyclization to form leucodopachrome, which could have temporarily sequestered dopaquinone from further polymerization.[368] Additionally, the presence of the bulky –COOH functional group may have contributed to steric hindrance effects, mirroring observations in glucose-based monomers, that could have hindered the transition from diffusion-limited to kinetically controlled polymerization.[369]

Within the context of the monomer concentration, a marked difference was observed in the lag phase. The LD molecules were dispersed at lower concentrations, leading to reduced collision frequencies and a longer time to achieve the critical concentration necessary for nucleation. Furthermore, the inherent hydrophilicity of LD contributed to its solubility, which, coupled with kinetic constraints (e.g., the probability of overcoming the activation energy for the formation of initial reactive intermediates), hindered the aggregation of monomers into oligomeric nuclei, thereby extending the lag phase. Conversely, higher concentrations of LD fostered a saturation effect, where an increased probability of inter-molecular interactions after the initial complexation or solubility barriers accelerated the polymerization rate to the point of monomer depletion.[370] Additionally, the transition from diffusion-limited to kinetically controlled reactions at higher concentrations contributed to a shorter lag phase, as the reaction rate was less impeded by the slow diffusion of monomers despite the presence of steric hindrance.[369]

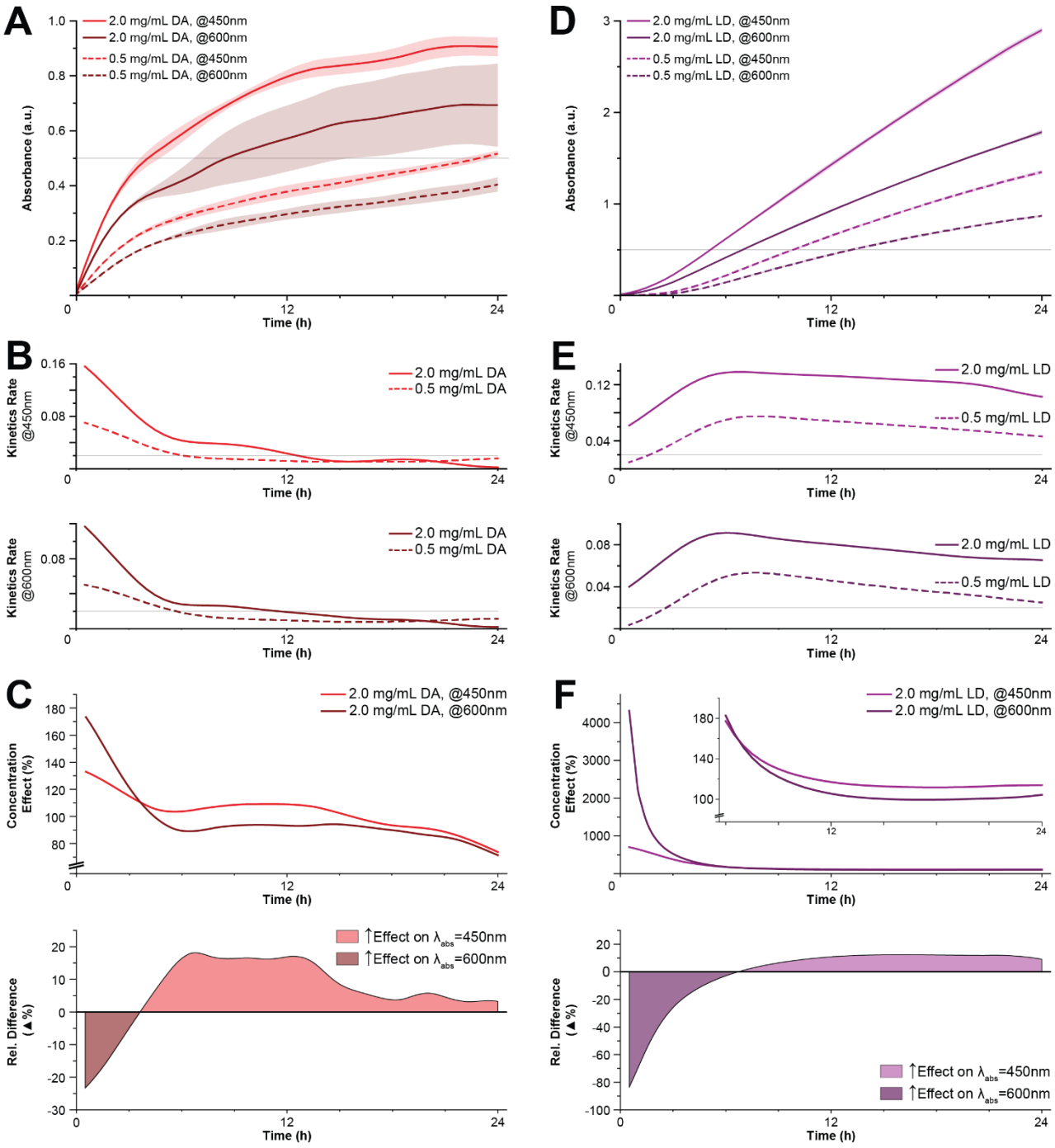


Figure 5-1: Dual-wavelength absorbance analysis of pCA polymerization of DA and LD precursors.

Absorbance analysis of DA (*left*, red) and LD (*right*, purple) polymerizations over 24 h. **(A, C)** Absorption data, represented as mean ± SD, for HC (2.0 mg/mL, –) and LC (0.5 mg/mL, ⁻⁻) measured at $\lambda_{abs}^{450}$ (*lighter*) and $\lambda_{abs}^{600}$ (*darker*). **(B, E)** Kinetics data of HC (–) and LC (⁻⁻) conditions for $\lambda_{abs}^{450}$ (*top*) and $\lambda_{abs}^{600}$ (*bottom*). **(C, F)** Impact of precursor concentration on $\lambda_{abs}^{450}$ and $\lambda_{abs}^{600}$ signals. Elevation effect on per-wavelength absorbance signal (*top*) and relative effect difference between wavelengths (*bottom*).

Quadrupling the precursor concentration led to an 84% increase in peak rate at $\lambda_{abs}^{450}$ and 71% at $\lambda_{abs}^{600}$. Notably, the formation rate was relatively stable compared to the peak rate. At HC, the rate of formation at $\lambda_{abs}^{450}$ and $\lambda_{abs}^{600}$ dropped only 4% and 12% by 12 h (5.5 h after the peak) and 26% and 28% by 24 h, respectively. At LC, the rates dropped by 9% and 14.4% by 12 h (4.5 h after the peak), and 38% and 54% by 24 h. These results suggest that possible rate-limiting steps, such as perturbation of kinetics from product formation affecting thermodynamic equilibrium, did not affect the reaction. The presence of the –COOH group may have improved the stability via similar influences that may have impeded its initiation reaction, including enhanced solubility, pronounced hydrogen bonding capabilities, and distinct steric effects. Solubility and extended hydrogen bonding may stabilize reactive intermediates and reduce the propensity for sudden fluctuations in polymerization rates by maintaining a balance between reactants and products.[369,371] Additionally, the –COOH group introduced steric considerations that could have moderated the polymerization kinetics by tempering the approachability of monomers, avoiding the rapid uncontrolled reactions observed with dopamine.

When exploring the influence of concentration on the polymerization dynamics of LD, it was evident that the initial stages of the reaction were markedly concentration-dependent, exhibiting diffusion-limited behaviour at the outset. The observed >40-fold and >7-fold increases in absorption signals at $\lambda_{abs}^{600}$ and $\lambda_{abs}^{450}$, respectively, at higher concentrations within the first 30 minutes, underscored the accelerated formation of polymerization intermediates or products that selectively absorb at these wavelengths (**Figure 5-1F,** *top*). Such pronounced early differences could be attributed to the heightened collision frequency and reactivity among the monomers at elevated concentrations, facilitating the rapid formation of absorbing species. As the polymerization progresses to 12 h, the absorption signals at higher concentrations ($LD_{2.0}$) only exhibited a 105% and 117% increase over the lower concentration ($LD_{0.5}$) at $\lambda_{abs}^{450}$ and $\lambda_{abs}^{600}$, respectively. This notable decrease in the rate of change suggested a stabilization phase in which the rates of formation and depletion of reactive species approached equilibrium, reducing the differences observed at early time points. The initially more significant concentration effect at $\lambda_{abs}^{600}$, peaking at an 80% higher impact than the $\lambda_{abs}^{450}$, then diminished by 7 h and transitioned to a more pronounced effect on the $\lambda_{abs}^{450}$ signal (**Figure 5-1F,** *bottom*). Notably, the effect-magnitude relationship between the wavelengths was stable for 24 h. This association reflected the evolving polymerization environment, where equilibrium was reached between the production of species, maintaining a 19% higher absorption at $\lambda_{abs}^{450}$ over several h. However, this effect began to wane in the final 2 h, which was attributed to a decline in the kinetics at $\lambda_{abs}^{450}$ while the rate at $\lambda_{abs}^{600}$ remained stable.

#### 5.5.1.3 *POLY-L-NOREPINEPHRINE (PLNE)*

During the first 6 h at HC, pLNE rapidly increased the measured absorbance (**Figure 5-2A**). Within this period, the peak kinetic rate of pLNE was slightly delayed at 2 h post-initiation for both wavelengths (**Figure**

**5-2B**). As expected, the absorbance and kinetics of pLNE at the LC were lower and slower, respectively. However, the peak rate of $\lambda_{abs}^{600}$ at LC was 0.5 h later than that of $\lambda_{abs}^{450}$. This delay contrasted with the HC and HC/LC conditions for pDA and pLD, which matched peak rate time points, suggesting that higher-order complex species were significantly slower to form than pDA or pLD synthesis, particularly under reduced precursor concentrations. Following the oxidation of NE into O-quinone, it might have undergone cyclization to form a secondary amine (–NH) or undergo tautomerization and non-melanogenic breakdown for deaminization into a reactive aldehyde group.[343] The product of the latter reaction, 3,4-dihydroxybenzaldehyde (DHBA), was then capable of a Schiff base reaction with NE to form DHBA-NE. Under similar oxidative conditions, using lower precursor conditions, the formation of these complexes might have been impaired, contributing to the slower formation of conjugated structures.

Significant behaviour differences were observed between wavelengths between 6 and 12 h. Regarding $\lambda_{abs}^{450}$, HC pLNE entered a period of high variability marked by an 86% drop in kinetics, lower than the rate at 24 h, followed by a moderate recovery to 79% of its peak by 12 h. The rate steadily decreased to 84% of its peak after 24 h. In contrast, the $\lambda_{abs}^{600}$ rate experienced a 50% drop from its peak rate after 8 h, followed by a slight plateau until approximately 10 h. It then continued to decline to 43% of its peak rate by 12h and a reduction to nearly zero by 24 h. In contrast, LC experienced no sharp drop in $\lambda_{abs}^{450}$. However, a more significant loss in the rate of $\lambda_{abs}^{600}$ at LC (75% from the peak) than $\lambda_{abs}^{450}$ (59%) was noted after 12 h, further suggesting that the formation of conjugated structures was particularly affected by low NE. The rate reductions continued to be moderate and stable for 24 h.

These results suggested that pLNE had undergone rapid oxidation and formation of DHBA early in the process and quinone could readily form DHBA/DHBA-quinone dimers at a reported ratio of 1:1.[343] Under HC, accelerated DHBA/quinone synthesis would have contributed to the early predominant concentration effect being on $\lambda_{abs}^{450}$ (**Figure 5-2C,** *bottom*). However, these dimers may be unstable due to the abundance of amine-containing NE that compete to react with aldehydes, potentially quinones. As previously reported,[343] these unstable dimers could dissociate to form protonated DHBA units that could undergo Schiff base formation and free quinone, which can polymerize into melanin-like structures. Conceivably, this decomposition phenomenon may have begun to occur around 4 h, marking the beginning of the volatility region of $\lambda_{abs}^{450}$ as the released quinone contributes to the 'rise' component, and its consumption contributes to the 'fall' component (**Figure 5-2A**). The polymerization of quinone into complex structures likely contributed to its sustained growth. $\lambda_{abs}^{600}$ rate during this same period (**Figure 5-2B,** *bottom*). Regarding the $\lambda_{abs}^{450}$ rate, the surplus of protonated DHBA may have resulted in the rapid formation of DHBA-NE structures, sequestering NE and starving the system of free precursor. This dynamic could have led to a sharp drop in the kinetics at $\lambda_{abs}^{450}$ (**Figure 5-2B,** *top*), as NE could not oxidize and form downstream quinone and indole structures. However, Schiff base formation may have

undergone a reversal, mainly through base-catalyzed hydrolysis of the imine linkage under alkaline conditions in our case. In this context, the release of the NE may have corresponded to the rate recovery of $\lambda_{abs}^{450}$, observed between 12 and 15 h. In contrast, the less amine-containing precursor in LC may have led to a more stable synthesis of DHBA/DHBA-quinone and contributed to notably less volatility.

#### 5.5.1.4 *POLY-RAC-NOREPINEPHRINE (PRNE)*

Over the first 6 h, pRNE exhibited a notably more moderate increase in absorbance, with significant delays observed for both LC and HC compared with pLNE (**Figure 5-2D**). A consistent 3 h delay in the kinetics peak rate for both characterized this behaviour $\lambda_{abs}^{450}$ and $\lambda_{abs}^{600}$ relative to pLNE across respective concentrations (**Figure 5-2E**), pinpointing the peak rates at 5 h for HC and between 5.5 and 6 h for LC. This indicated that the presence of the D-enantiomer might have led to delayed reactions, potentially due to more complex intermolecular interactions with NE and its chiral intermediates (e.g., quinone), leading to altered hydrogen bonding and increased steric hindrance. Like pLNE, whereas the peak rate at HC for both wavelengths was matched, at LC, the peak for pRNE at $\lambda_{abs}^{600}$ was 0.5 h later than $\lambda_{abs}^{450}$ and suggested that the concentration-dependent delay in forming conjugated polymers might have been intrinsic to LC pRNE. This behaviour might have been due to the need for free NE to form DHBA-NE complexes, which are considered essential for pNE formation, with their oxidation into quinone impacting this. However, unlike pLNE, which had an increase in concentration that primarily promoted species formation that contributed to $\lambda_{abs}^{450}$, quadrupling the R-NE precursor predominately influenced species formation that absorbed at $\lambda_{abs}^{600}$ throughout (**Figure 5-2F**).

After reaching their peak rates, the LC condition experienced a 40% decrease at 12 h and a 68% decrease by 24 h for $\lambda_{abs}^{450}$, while observing a 52% decrease at 12 h and a 78% decrease by 24 h for absorbance at $\lambda_{abs}^{600}$. In contrast, under the HC condition, there was only a 21% decrease at 12 h and a 44% decrease by 24 h for absorbance for $\lambda_{abs}^{450}$, alongside a 28% decrease at 12 h and a 50% decrease by 24 h for absorbance for $\lambda_{abs}^{600}$. Generally, both D- and L-NE enantiomers might promote a more comprehensive array of initial polymerization reactions and intermediate states, leading to a more sustained polymerization process. At HC, the increased availability of monomers could have facilitated a more continuous and stable polymer formation, buffering against rapid decreases in kinetics and supporting the formation of a conjugated material per the concentration effect we presented.

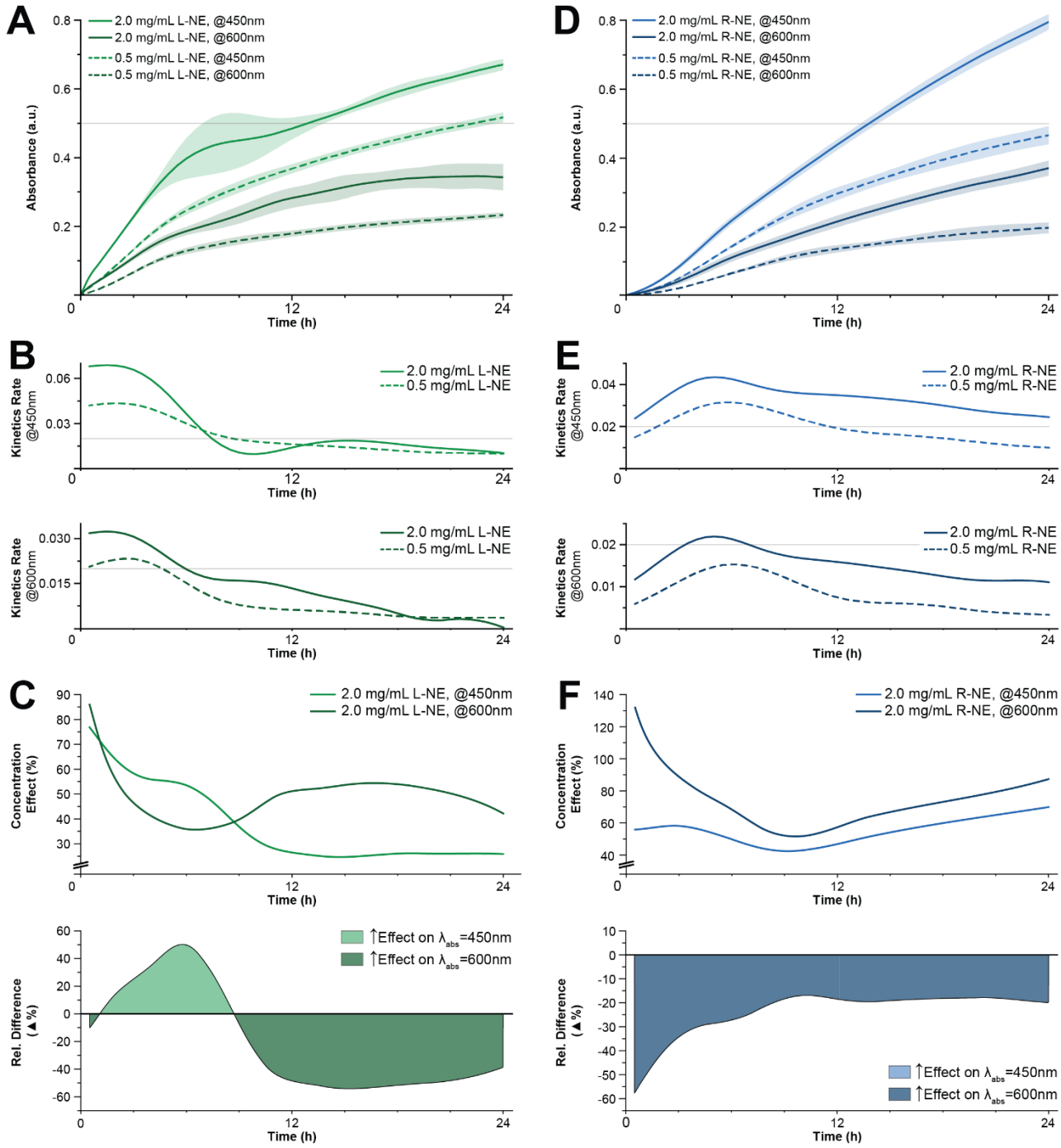


Figure 5-2: Dual-wavelength absorbance analysis of pCA polymerization of L-NE and R-NE precursors.

Absorbance analysis of L-NE (left, green) and R-NE (right, blue) polymerizations over 24 h. **(A, C)** Absorption data, represented as mean ± SD, for HC (2.0 mg/mL, –) and LC (0.5 mg/mL, ⁻⁻) measured at $\lambda_{abs}^{450}$ (*lighter*) and $\lambda_{abs}^{600}$ (*darker*). **(B, E)** Kinetics data of HC (–) and LC (⁻⁻) conditions for $\lambda_{abs}^{450}$ (*top*) and $\lambda_{abs}^{600}$ (*bottom*). **(C, F)** Impact of precursor concentration on $\lambda_{abs}^{450}$ and $\lambda_{abs}^{600}$ signal. Elevation effect on per-wavelength absorbance signal (*top*) and relative effect difference between wavelengths (*bottom*).

### 5.5.2 DLS ANALYSIS OF NANOPARTICLE SYNTHESIS

The formation of pCA particles is a significant area of interest because particle size impacts their biomedical applications. Particle size is a crucial determinant of drug delivery efficiency, cellular internalization, and biocompatibility.[372-376]

In the context of pDA NPs, smaller particles (<100 nm) showed enhanced NIR absorption capacity, which benefited its activity in inhibiting the growth of and ablating tumours,[377] cationic NPs approximately 60 nm in size demonstrated improved penetration in *S. aureus* biofilms with excellent photothermal properties,[378] and 13 nm NPs have proven effective as vehicles for photothermally enhanced gene delivery by supporting high cellular uptake with low toxicity.[379] Although less studied in size-discriminatory applications, pNE and pLD NPs continue to emerge as platforms of interest in growing applications. Regarding pNE, 100 nm NPs have shown promise in their application as drug delivery vehicles,[348] 100 nm NPs were viable as nanoagents for photothermal therapy (PTT) and in their conjugation with drugs for combined chemo-photo-thermal cancer therapy,[354] and 400 nm µP nanospheres could enhance the sensitivity of photoacoustic imaging.[380] Similarly, for pLD, 5–50 nm NPs show promise in the detection of LD for diagnostic purposes,[147] 10–40 nm NPs synthesized into dendritic structure networks are effective biosensing platforms to investigate single-nucleotide polymorphisms and cDNA,[381] NPs of varying sizes exhibited photothermal properties surpassing those of pDA particles for tumour therapy applications,[382] and recently, 125–150 nm µP were employed to treat cellular oxidative stress and acute inflammation.[383] Therefore, enhancing our understanding of the synthesis of these particles by elucidating concentration and temporal effects could deepen insights into the synthesis process and support the tailored production of pCA NPs with a growing range of applications.

Accordingly, this section focuses on the time-resolved synthesis of pCA particles conducted over 8 h with an extended 24 h endpoint to illuminate particle formation and growth kinetics. We aimed to understand how differences in precursor chemistry, mixed with variable concentrations, affected particle size. The aim is to provide a framework for refining the design and application of pCA particles in areas where precise size control is crucial.

#### 5.5.2.1 *PDA*

At LC, pDA-µPs were 316 ± 32 nm at 1 h and rose steadily to a peak of 719 ± 107 nm after 6 h (**Figure 5-3A**). A slight decrease was observed at 618 ± 28 nm at 8 h, with the size remaining stable until the 24 h measurement. This peak corresponded to the inflection point observed in the absorption data, where a nascent plateau was evident (**Figure 5-3A**). Conversely, µPs exhibited a size of 684 ± 26 nm in HC at 1 h, more than double that of the LC, and surged to 1604 ± 46 nm by 4 h. Following a transient decrease at 5 h, the size increased to 1887 ± 341 nm by 8 h, which persisted for 24 h. The initial peak at 4 h and the escalation in standard deviation at subsequent time points for the HC DA particles were notable. An increase in the corresponding error mirrored this variability

in particle size. $\lambda_{abs}^{600}$ data, particularly around the elbow of the curve. A similar, albeit less pronounced, pattern was observed in LC, where increased standard deviation at the 6 h peak aligns with the onset of variability in absorption data. This concurrence in the datasets implies that the 4 and 6 h timepoints for HC and LC may have signified critical concentration-dependent stages in the aggregation of pDA particles, contributing to more significant heterogeneity. The persistence of this heterogeneity through the 24 h timepoint, as manifested in both the absorbance and particle size data, suggested a phase shift in the polymerization process, presumably propelled by interparticle conjugation. These findings underscore the intricate kinetic characteristics of pDA particle polymerization.

#### 5.5.2.2 *PLD*

The formation of pLD particles presented a distinct profile compared with that of pDA, indicating different underlying kinetics and stability mechanisms (**Figure 5-3B**). The pLD µPs at both concentrations exhibited a uniform increase in size, growing from 200–250 nm at 1 h to 380–393 nm after 2 h. These results suggest that this range is the critical size for the initial stability of particles when considering the poor solubility of LD because of its zwitterionic nature at physiological pH levels resulting from its positively charged amino and negatively charged carboxyl groups. However, the subsequent behaviour showed a significant divergence between concentrations. At HC, a notable decrease in particle diameter began at 3 h, with a steep drop to 71 ± 15 nm after 5 h, stabilizing at 35 ± 7 nm for 8 h and remaining consistent for 24 h. In contrast, particles at the LC retained their size until 5 h, after which a sharp decline was seen, reducing to 66 ± 14 nm by 8 h and further to 20 ± 1.3 nm by 24 h.

The similarity in NP size across concentrations of approximately 70 nm, observed 3 h after the initiation of the decline, suggested a process convergence despite initial concentration differences. These sudden drops in size may have represented a new equilibrium state in which the polymeric network's balance between LD monomer availability, solubility, and stability governed the particle size. Moreover, the absorption curves in **Figure 5-1D** suggests a pivotal kinetic transition at 2 h for HC and 5 h for LC. Additionally, the approximate points at which the particle size became stable, 6.5 h at HC and 8 h at LC, corresponded approximately to the pronounced linearization in the absorption data, and the maximum kinetics rate is (**Figure 5-1E**). This observation suggested a significant phase in the reaction kinetics, likely indicating the highest solubilization rate or the peak oxidation of the LD precursor support nucleation, which initiated the polymerization reactions and appeared relatively stable per absorption data.

#### 5.5.2.3 *PLNE*

The kinetic behaviour of pLNE particle formation was like that of pDA but was characterized by notably larger particle size. For the LC of pLNE, the initial particle size at 1 h was 699 ± 25 nm, similar to that of the HC pDA µP,

and reached an early plateau phase with a diameter of 923 ± 130 nm after 2 h (**Figure 5-3C**). A modest increase to 1040 ± 183 nm was observed after 4 h, with the size maintaining relative stability for up to 8 h, followed by a slight rise to an average of 1152 ± 163 nm after 24 h.

In HC, pLNE µPs presented an average diameter of 1303 ± 167 nm at 1 h, increased to 2025 ± 280 nm after 4 h, and began to plateau. However, the diameters fluctuated considerably between 1870 ± 190 and 2384 ± 301 nm up to 8 h. The 4 h timepoint was consistent with the surge in the standard deviation for the $\lambda_{abs}^{450}$ signal (**Figure 5-2A**) marking a period of instability that persisted and stabilized somewhat by 14 h. Furthermore, the latter part of the instability period (t=8–9 h) was matched with the lowest kinetics rate at $\lambda_{abs}^{450}$ (**Figure 5-2B**) the most consistent rate at $\lambda_{abs}^{600}$, and the junction at which the effect of the concentration transitions from being dominant on $\lambda_{abs}^{450}$ to $\lambda_{abs}^{600}$ (**Figure 5-2C**). These trends suggest that the phenomenon was associated with the targeted formation of a more conjugated polymer network at the expense of the particle size. The subsequent decrease in the diameter to 1345 ± 112 nm after 24 h mirrored the LC size more closely. Notably, these particle sizes were significantly greater than those of Lu et al. (2020), who reported an average diameter of 346 and 130 nm for concentrations of approximately 1 and 0.25 mg/mL.[348] However, their methodology used Tris-HCl with 2.8 mM ethanol and with agitation, contributing to a more dispersed solution with disrupted interparticle interactions.

Given the observed trends, several hypotheses can be proposed to elucidate the mechanisms underlying the concentration-dependent stability of pLNE particles. For instance, the increased collision rate between particles at higher concentrations may initially promote aggregation, leading to larger particle sizes.[136,333] However, this aggregation is likely unstable, leading to size fluctuations and potential breakdown into smaller particles owing to repulsive forces between densely packed particles, potential auto-catalytic decomposition of the polymer, or sheer size-related instability that could have resulted in fragmentation or re-dissolution of the aggregates. In contrast, the smaller particles formed in the LC reached a stable state more quickly. This outcome could have been due to a more stable core-shell structure formed early in the process, with a dense core that resisted further change and a shell that moderates environmental interactions.[384] It is also conceivable that the LC limited the extent of particle growth due to less availability of monomers, resulting in a more stable particle population overall.

#### 5.5.2.4 *PRNE*

The pRNE particle formation kinetic profile presented distinctive features compared to the L-enantiomers. In LC, pRNE µPs initially measured 322 ± 58 nm, significantly smaller (less than half) than pLNE particles at the same concentration. The particle size rapidly decreased to 82 ± 7 nm after 4 h. Generally, this narrow size range was maintained, settling at approximately 80 ± 11 nm by 8 h. After 24 h, the average size slightly increased to 103 ± 28 nm, suggesting long-term size stabilization. In our HC condition, pRNE-µPs were reported at 1 h with a

diameter of 212 ± 47 nm, surprisingly more minor than the initial size in the LC condition, and then gradually expanded to 308 ± 15 nm after 6 h. A phase of slight instability was evidenced by a fluctuation of 267 ± 11 nm at 7 h and a rebound to 319 ± 33 nm at 8 h, mirroring the instability observed with the HC pLNE-µPs. However, pRNE-µPs did not experience a substantial size reduction after 24 h, maintaining a size of 335 ± 79 nm, although with increased variability. This pattern suggests that, while pRNE-µPs underwent a degree of instability, it did not lead to a significant collapse in structure, as seen with pLNE-µPs, implying a degree of inherent robustness within the pRNE system.

In the context of previous research, the final diameter of the LC pRNE particles aligned with the 100 nm reported by Liu et al. (2019) at a similar time point (5 h), suggesting their use of rac-NE, whereas it was not reported.[354] However, their method involved a higher precursor concentration of 2 mg/mL, a more alkaline solution (NaOH in DI, pH ≈ 11.9), elevated temperature (50 °C), and agitation. These findings suggest that this diameter range marked a thermodynamically favoured state that supported stability in a dispersed system, achieving a balance between the forces of aggregation and stabilization interactions, as further evidenced by the rapid decrease to a similar size by the 4 h timepoint at a critically lower 0.5 mg/mL. Furthermore, agitation appeared to play a sufficient role in achieving a uniform particle size distribution, countering the trend in pDA systems where agitation typically promotes the formation of larger particles and aggregates.[131,132,173] The mechanical energy introduced by stirring seemed to be a critical factor in overcoming the intrinsic aggregation propensity, forming smaller and more consistently sized particles. Furthermore, including DHBA in the material may have contributed to the manifestation of the critical size and has been reported to suppress pNE particle aggregation.[341,343] Nonetheless, within our static HC environment, the conditions facilitated the sustained formation of µPs over three times larger in the long term. Additionally, at HC, the observed size stability of pRNE particles compared to the instability observed in pLNE suggested that using a racemic mix could have facilitated stronger binding energies and intermolecular forces, potentially conferring a degree of inherent structural robustness. This supposition is supported by Shen et al. (2023), who studied the tyrosine-mediated polymerization of enantiomeric D-, L-, and racemic mixtures of 3,4-dihydroxyphenylalanine (DOPA).[346] It was determined that rac-DOPA resulted in more crystalline heterochiral surfaces that were more tightly packed and presented greater mechanical stability and adhesion.

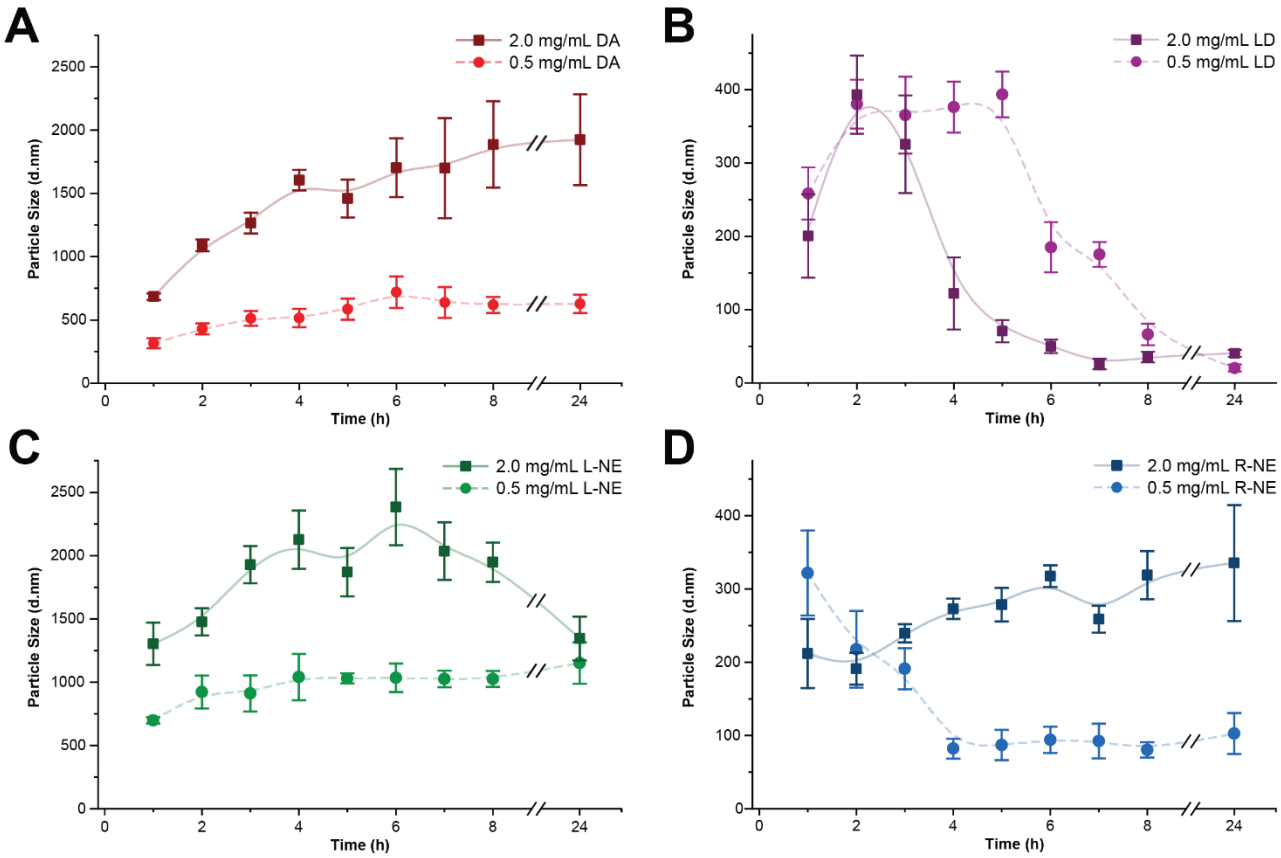


Figure 5-3: Dynamics of particle size evolution in pCA particles under HC and LC conditions.

Dynamic Light Scattering (DLS) results of **(A)** pDA, **(B)** pLD, **(C)** pLNE and **(D)** pRNE taken at LC (0.5 mg/mL, –■–) and HC (2.0 mg/mL, ··●··) precursor concentrations over 24 h. Data points represent the mean particle diameter (d. nm) ± SD.

### 5.5.3 POLYMER DISPERSION RATIO (PDR)

Understanding the dynamics of polymer aggregate formation and dispersion within various media is pivotal for advancing material design and functionality. To address this need, we introduced the Polymer Dispersion Ratio (PDR), a novel and accessible metric designed to elucidate polymer aggregates' spatial distribution and temporal evolution. PDR leveraged the contrast in absorbance signals between the centre and periphery of a well, offering a comprehensive view of the adhesive aggregate behaviour under the influence of hydrodynamic forces, intermolecular interactions, and processing conditions. This method utilized the horizontal motion of a standard plate reader coupled with the sampling of absorbance measurements taken at the centre of each well and two periphery points, effectively capturing the radial distribution of the polymer aggregates (**Figure 5-4A**). The PDR is defined as the ratio of the signal detected at the center ($S_{centre}$) to the average of the signals obtained from the periphery ($\frac{1}{n}\sum_{i=1}^{n} S_{side,i}$). A prototypical PDR curve is illustrated in **Figure 5-4B,** concerning the phases described below (**Figure 5-4C**).

During **Stage A**, the PDR was approximately 1, indicative of a homogeneous phase where the polymerization process was in its initial phase, with aggregates evenly dispersed throughout the well. Transitioning to **Stage B**, where the PDR falls below 1, shear-induced periphery accumulation was observed. This stage resulted from the bidirectional horizontal agitation of the plate reader. This motion differentially impacts the distribution of the polymer aggregates by promoting their movement toward the edges of the well. Instead of vertical or rotational shaking, the unique aspect of horizontal agitation ensures a consistent shear profile across the well, which is critical for PDR measurements. This directed motion intensifies the signal at the periphery relative to the centre, encapsulating the dynamic interplay between the induced shear forces and intrinsic properties of the polymer aggregates. Progressing to **Stage C**, the PDR approaches the equilibrium transition point (ETP) of 1, signifying an aggregate equilibrium distribution. This distribution arises from a delicate balance between hydrodynamic forces and the intrinsic tendency of the aggregates to distribute evenly, facilitated by Brownian motion and a drive toward thermodynamic stability. In **Stage D**, the PDR rose above 1, reflecting a concentration of denser aggregates in the centre of the well. This stage is characterized by increased aggregative convection and interaggregate interaction, working in concert with gravitational settling and adsorption phenomena. **Stage E** is marked by a continued increase in the PDR value, indicative of ongoing sedimentation and aggregate film maturation at the centre of the well.

This methodology facilitated a deeper exploration of polymer aggregation phenomena and optimized polymerization processes for enhanced material properties. By delineating the dispersion and sedimentation behaviours of the polymer aggregates, PDR illuminated the dynamics of pCA aggregation with the potential to shed light on the properties of the underlying substrate.

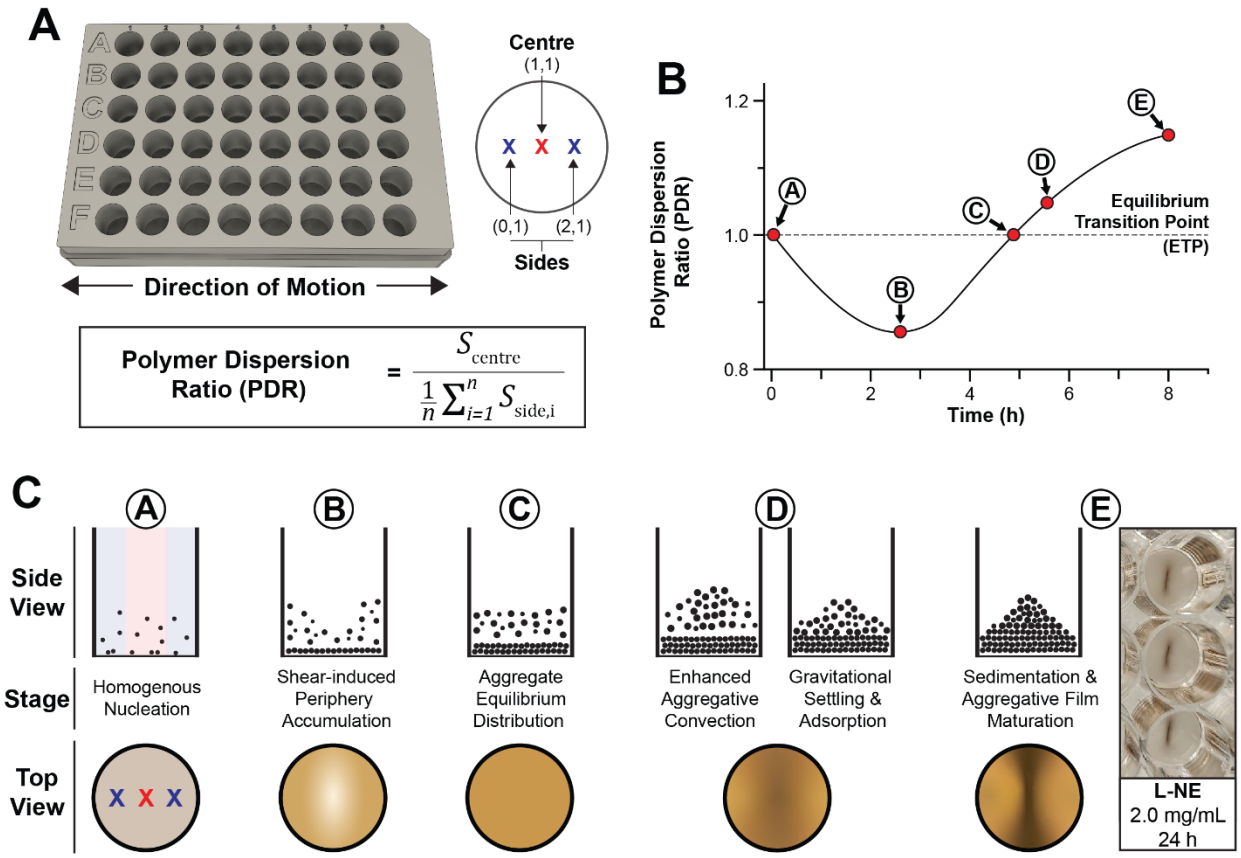


Figure 5-4: Quantitative and visual representation of the Polymer Dispersion Ratio (PDR) assay.

**(A)** Schematic of a multiwell plate, locations of absorbance measurements, and calculation of PDR. **(B)** A prototypical curve displays the temporal evolution of PDR, with distinct stages labelled A through E, demonstrating key phases of polymer aggregate behaviour. The Equilibrium Transition Point (ETP) is the critical threshold at which PDR=1. **(C)** Side and top views for the corresponding stages, illustrating the transition from homogeneous nucleation (*Stage A*), shear-induced periphery accumulation (*B*), through aggregate equilibrium distribution (*C*), enhanced aggregative convection (*D*), to final sedimentation and aggregative film maturation (*E*), with a sample image depicting the actual state of the wells at 24 h for L-NE at HC (2.0 mg/mL).

#### 5.5.3.1 *PDA*

As expected, pDA displayed a concentration-dependent aggregative behaviour. At LC, a uniform minimum PDR value of 0.89 was observed between 1.5 and 2 h across both wavelengths (**Figure 5-5A**). The PDR at $\lambda_{abs}^{600}$ reached the ETP at 3 h, followed by the $\lambda_{abs}^{450}$ PDR crossing at 3.5 h correlates with a µP size of 512 nm. After reaching the ETP, variability significantly increased alongside a gradual rise in aggregation, especially between 5 and 8 h, coinciding with the highest variability in nanoparticle size, fluctuating between 585 and 719 nm in diameter. PDR values started to plateau by 8 h and registered at 1.42 for $\lambda_{abs}^{600}$ and 1.6 for $\lambda_{abs}^{450}$, it slightly decreases by 24 h to 1.37 and 1.54, respectively.

At higher concentrations, the dynamics shifted slightly forward, with the minimum PDR values reaching earlier, at 1.25 h, with values like those at lower concentrations (0.90–0.92). The PDR at $\lambda_{abs}^{600}$ crossed the ETP at 2.5 h, shortly after the $\lambda_{abs}^{450}$ PDR crossed at 2.25 h, corresponding to µP sizes of approximately 1100 nm. The PDR values then plateaued at approximately 4 h, corresponding to a similar plateau in the µP size at 1604 nm. This phase aligned with the concentration effect transitioning to a dominant influence on the $\lambda_{abs}^{450}$ absorbance increase. By 8 h, the PDR for $\lambda_{abs}^{600}$ was 1.15, whereas, for $\lambda_{abs}^{450}$, it reached 1.34. This divergence narrowed by 24 h, with values of 1.96 for $\lambda_{abs}^{600}$ and 1.92 for $\lambda_{abs}^{450}$.

While PDR variability was most pronounced in the $\lambda_{abs}^{450}$ absorbance post-ETP for both concentrations and the film showed considerable variability in the $\lambda_{abs}^{600}$ signal at HC (**Figure 5-5A**), and these results implied that the aggregation and adsorption predominantly involved species that absorbed at $\lambda_{abs}^{450}$. Conversely, aggregates remaining in the free solution, contributing to the noise in the film's measurement, seemed to absorb primarily at $\lambda_{abs}^{600}$.

#### 5.5.3.2 *PLD*

For pLD, PDR measurements across different wavelengths exhibited generally consistent behaviour, signifying a uniform response to the applied hydrodynamic conditions (**Figure 5-5B**). This material contrasted distinctly with the aggregation observed in pDA, as pLD demonstrated a uniquely nonaggregative nature. At LC, the PDR values remained below 1, with a noticeable peak at approximately 3 h near the ETP. This peak suggests an even distribution of particles approximately 365 nm in diameter. The onset of a decline at approximately 4.5 h closely aligned with the commencement of particle size reduction to 66 nm. The PDR reached its minimum, around 0.92, between 6.5 to 7 h, coinciding with observed maximum kinetic rates, and maintained relative stability at 0.94 through to 24 h.

Under HC, the PDR values remained below the ETP until 2 h, exhibiting marked variability, suggesting a stochastic distribution of particles aggregated in the free solution. This increased variability could have stemmed from the particles undergoing aggregation to some extent but failed to achieve a uniform distribution across

samples, likely due to inconsistencies in aggregate formation and dispersion within the highly concentrated environment. Notably, around this time, a slight dip in the $\lambda_{abs}^{600}$ signal correlated with a rapid collapse in nanoparticle size. Subsequently, PDR exhibited relative stability at both wavelengths, with a minor decrease to 0.93 by 8 h, which persisted for 24 h.

The observed dynamics at LC may have reflected the larger aggregates' inherent stability and propensity for even dispersion, leading to a delayed and pronounced peak in the PDR. This result suggests that the more significant, stable aggregates had sufficient time to distribute evenly under less crowded conditions, resulting in a more marked PDR peak. Conversely, a less pronounced peak and more rapid size reduction might have been attributed to accelerated kinetics at HC. These faster kinetics under dense conditions could have driven a swift collapse in particle size, stabilizing PDR values without the pronounced peak observed at lower concentrations.

#### 5.5.3.3 *PLNE*

At LC, the PDR for both wavelengths steadily decreased to approximately 0.92 by 2.5 h (**Figure 5-5C)**, indicative of particles approximately 922 nm in diameter and coinciding with peak kinetic activity. The ETP was subsequently crossed between 3.5 and 4 h, a phase marked by significant variability in nanoparticle diameter, eventually stabilizing at approximately 1030 nm. After this transition, a divergence in wavelength behaviour became apparent; PDR at $\lambda_{abs}^{450}$ increased to 1.24 by 8 h, while PDR at $\lambda_{abs}^{600}$ rose more rapidly to 1.35. This divergence persisted until 24 h, with PDR values settling at 1.21 for $\lambda_{abs}^{450}$ and 1.39 for $\lambda_{abs}^{600}$.

In high-concentration scenarios, the PDR for $\lambda_{abs}^{600}$ absorbance decreased to approximately 0.86 by 2.5 h, delineating a notable plateau in nanoparticle size, around 1928 nm. Conversely, the $\lambda_{abs}^{450}$ absorbance exhibited a slightly earlier minimum at 2 h, with a PDR of 0.89. The ETP was crossed earlier for the $\lambda_{abs}^{450}$ absorbance, around 4.5 h, compared to 5.5 h for the $\lambda_{abs}^{600}$, during a period marked by significant variability in film absorption measurements and nanoparticle sizes. This period hints at the emergence of central aggregates approximately 2000 nm in diameter. Notably, the earlier ETP crossing observed at $\lambda_{abs}^{450}$ absorbance was seemingly influenced by a concentration-induced emphasis on the $\lambda_{abs}^{450}$ signal on the film, which peaked around 6 h, coinciding with the $\lambda_{abs}^{600}$ ETP crossing. By 8 h, PDR values for both wavelengths aligned at approximately 1.27, and they continued to ascend through 24 h, culminating in final values between 1.65 and 1.69 for both wavelengths.

#### 5.5.3.4 *PRNE*

The behaviour of pRNE under hydrodynamic conditions, as quantified by PDR, revealed a surprising concentration-dependent effect on particle aggregation and distribution, with wavelength-specific differences (**Figure 5-5D**). At LC, pRNE displayed consistent behaviour over 8 h, with the PDR remaining below the ETP, indicating no significant central aggregation. This trend persisted for 24 h, where the PDR values approximated those at 8 h, suggesting a stable aggregate distribution was maintained throughout. This stability was like that

observed for the particle diameter, approximately 102 nm. Interestingly, this pattern was observed across the different wavelengths measured, showing no discernible variation in the behaviour.

In contrast, under HC, pRNE exhibited a distinct trend. The PDR value dipped to 0.94 within the first 1.5 h, entering a nascent plateau phase lasting until approximately 2.5 h, a behaviour mirrored by a plateau in nanoparticle size. At 3 h, the PDR began a further decline, reaching a minimum range between 0.86 to 0.88 at around 4.5 h for both wavelengths, coinciding with the nanoparticle diameter stabilizing at approximately 191 nm. Subsequently, a divergence specific to the wavelength emerged. While pLNE maintained a relative similarity between PDR values at $\lambda_{abs}^{450}$ and $\lambda_{abs}^{600}$ wavelengths, the pRNE PDR at $\lambda_{abs}^{600}$ surpassed the ETP at 6.5 h, followed by the $\lambda_{abs}^{450}$ measurement an hour later. Interestingly, the increase from 0.5 mg/ml to 2.0 mg/ml in R-NE precursor concentration predominantly affected the formation of species absorbed at $\lambda_{abs}^{600}$, with the signal at this wavelength persistently about 20% higher than at $\lambda_{abs}^{450}$. This concentration-dependent behaviour likely contributed to the observed divergence at HC for PDR.

Furthermore, this progression was aligned with the observed fluctuations in particle size during the 6–8 h interval. Notably, the slight dip at 7 h could be attributed to the adsorption of conjugated particles of approximately 308 nm in diameter. These trajectories continued to diverge, with the PDR for pRNE at $\lambda_{abs}^{600}$ climbing to 1.18 by 8 h and further to 2.17 by 24 h. Comparatively, the PDR at $\lambda_{abs}^{450}$ ascended more modestly to 1.05 at 8 h, settling at 1.52 by 24 h. This result indicates that for pRNE, the $\lambda_{abs}^{450}$ particles were more evenly distributed, whereas the pRNE aggregation was dominantly absorbent at $\lambda_{abs}^{600}$ (117% higher in the center versus the periphery). This outcome may have been due to the increased phenol content and more ordered polymerization attributed to the racemic mixture, enabling more significant aggregation and adhesion. Remarkably, at the 24 h endpoint, PDR readings for pRNE and pLNE at $\lambda_{abs}^{450}$ converged to similar values between 1.5 and 1.6, while for $\lambda_{abs}^{600}$, pRNE's PDR is 43% higher than that of pLNE. This contrast underscored that pRNE had a significant central localization of aggregates, 28% higher than that of pLNE, despite the pRNE particles being 75% smaller at 24 h. These findings emphasize the influence of the chemical nature of the material on the size of the aggregates in determining the distribution pattern.

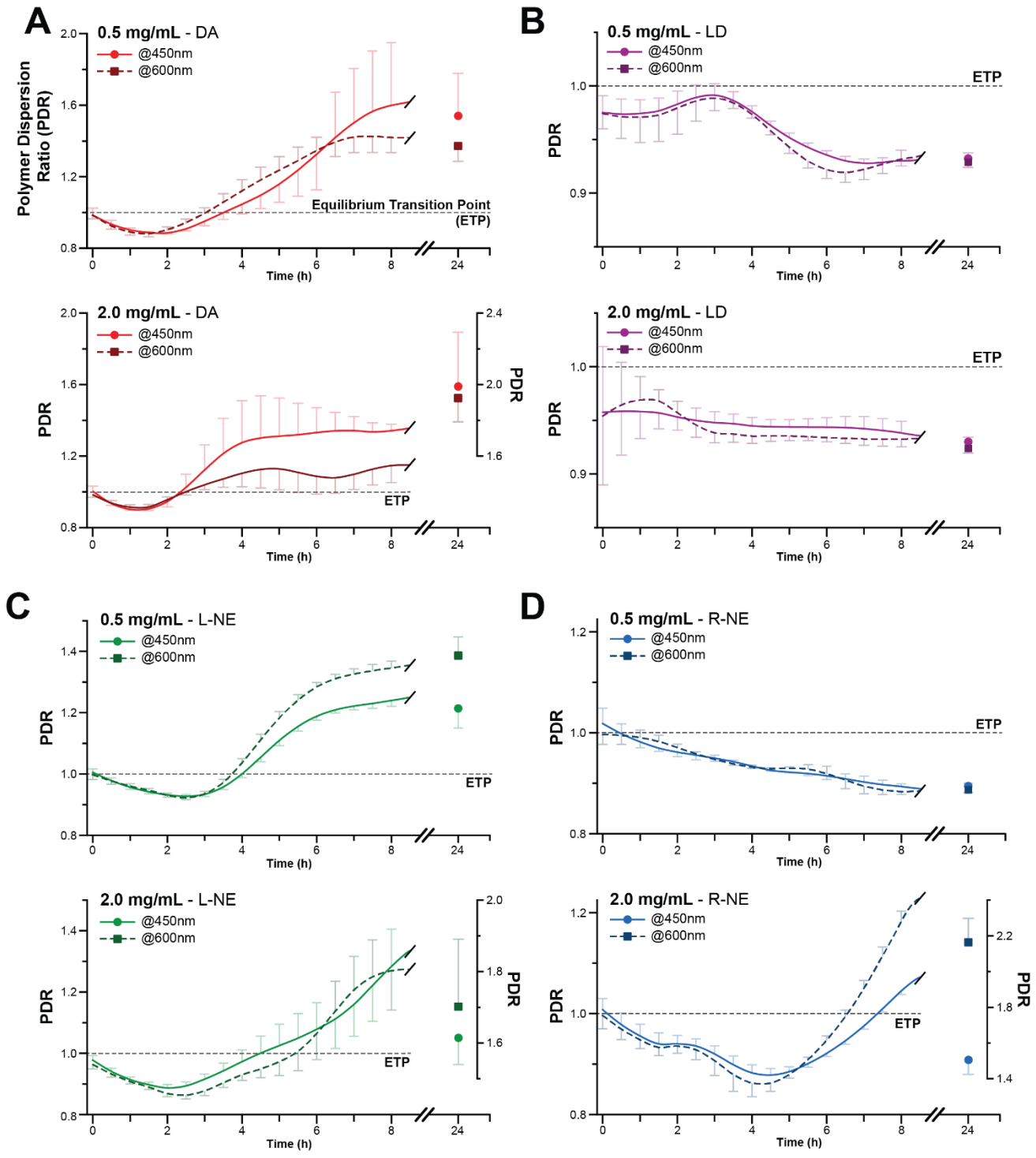


Figure 5-5: Dual-wavelength calculations of polymer dispersion ratio (PDR) dual wavelength calculations.

Time-resolved PDR of **(A)** pDA, **(B)** pLD, **(C)** pLNE, and **(D)** pRNE at LC (*top*) and HC (*bottom*) precursor concentrations for 24 h. Measurements represent the mean ± SD calculated at $\lambda_{abs}^{450}$ (–●–) and $\lambda_{abs}^{600}$ (--■--). The ETP represents the equilibrium transition point.

## 5.6 CONCLUSION

In summary, our study investigated the complex dynamics of polymerization and particle formation in pDA, pLNE, pRNE, and pLD materials, shedding light on the effects of precursor chemistry and concentration. The polymerization kinetics revealed distinct behaviour among the precursors, with concentration-dependent effects markedly influencing the formation of species measured at $\lambda_{abs}^{450}$ and $\lambda_{abs}^{600}$ observed over a high temporal resolution. DLS analysis further highlighted the impact of these variables on particle size, an essential parameter for biomedical applications such as drug delivery and tissue engineering. Chirality plays a pivotal role in the synthesis of pNE. Notably, the racemic mixture in R-NE led to a more stable, albeit delayed, synthesis of pRNE and the formation of significantly smaller particles. The introduction of PDR as a novel metric offered insights into the spatial distribution of polymer aggregates, underlining the influence of hydrodynamic forces and intermolecular interactions on aggregate behaviour during polymerization. This study underscores the potential of precise control over kinetics and synthesis protocols to tailor material properties, significantly contributing to the design and engineering of biomaterials and NP/µP for targeted biomedical applications.

## 5.7 ACKNOWLEDGEMENTS

This work was supported by the Natural Sciences and Engineering Research Council (NSERC) through the Discovery grant, by the Canada Foundation for Innovation (CFI), and the Ontario Ministry of Research and Innovation (MRI) through the Leaders of Opportunity (LOF) fund.

## 5.8 MATERIALS AND METHODS

### 5.8.1 POLYMER SYNTHESIS

The polycatecholamines (pCA) were synthesized from dopamine (DA; Sigma Aldrich), L-norepinephrine (L-NE; Sigma Aldrich, USA), rac-norepinephrine (RNE; VWR, USA) and L-DOPA (LD; Fisher Scientific, USA). Mixtures were comprised of 0.5 (LC) and 2.0 (HC) mg/mL of respective precursor reconstituted in 10 mM Tris-HCl (pH=8.6, Sigma Aldrich).

### 5.8.2 ABSORPTION MEASUREMENTS AND POLYMER DISPERSION RATIO (PDR)

Absorption measurements were performed on a Tecan Infinite 200 Pro at $\lambda_{abs}$=450 nm ± 10 nm and $\lambda_{abs}$=600 nm ± 10 nm at an interval of 30 min over 24 h. The experiments were performed with 0.5 mL/well in a 48-well Cellstar PS multiwell plate (Grenier Bio-One, Germany, Ref# 677102) with a lower well diameter of 11.37 cm. Under the 3 × 3 grid setting, the “centre” of the well was located at position (1,1). The “sides” of the well are located 2.8 cm to the left (position [0,1]) and to the right (position [2,1]) of the centre, as indicated in **Figure 5-4**.

The absorption measurements and kinetics described in **Figure 5-1** and **Figure 5-2** were calculated from per-well averages of the side readings ($S_{side}$). The concentration effect was isolated by the ratio of the respective signal at HC (2.0 mg/mL) to that at LC (0.5 mg/mL) minus 100%.

The polymer dispersion ratio (PDR) was calculated from the ratio of the centre signal ($S_{centre}$) over the mean $S_{side}$ as shown in **Figure 5-4**. The equilibrium transition point (ETP) was defined as PDR=1, representing an even signal across the well.

### 5.8.3 DYNAMIC LIGHT SCATTERING (DLS)

The hydrodynamic diameter of the particles was measured by laser dynamic light scattering (DLS) using a Zetasizer Nano ZS (Malvern Instruments, UK) in a PS cell at 25 °C.

# 6 ENDOMETRIAL AND MYOMETRIAL BIOACTIVITY ANALYSIS OF POLYDOPAMINE, POLY-L-NOREPINEPHRINE AND POLYLEVODOPA COATINGS: FROM PROLIFERATION TO MIGRATION

*Relevant manuscript*

**Endometrial stromal and myometrial bioactivity analysis of polydopamine, poly-L-norepinephrine and polylevodopa coatings: from proliferation to migration**

Alexander J. Steeves[1,2], Fabio Variola[1-4#]

[1] Faculty of Engineering, Department of Mechanical Engineering, University of Ottawa, Ottawa, ON, Canada
[2] Ottawa-Carleton Institute for Biomedical Engineering, Ottawa, Canada
[3] Faculty of Medicine, Department of Cellular and Molecular Medicine, University of Ottawa, Ottawa, ON, Canada
[4] Children's Hospital of Eastern Ontario (CHEO), Ottawa, ON, Canada

**In preparation**

## MOTIVATION

Uterine injury is a prolific cause of distress for women worldwide, with the associated growth of scar tissues and fibroids potentially materializing into debilitating conditions (e.g., Asherman's syndrome). These disorders not only inflict chronic pain and infertility but also significantly impair the quality of life of the affected women. As such, a multifaceted and concerted research effort must be committed. While diverse, current therapeutic strategies reveal a considerable gap in effectively managing these conditions, particularly in fostering endometrial and myometrial tissue regeneration and maintaining physiological integrity post-injury. This study proposes using polycatecholamine (pCA) polymers in the context of female reproductive health and uterine tissue repair, offering a promising avenue for advancing treatment strategies. Drawing upon emerging insights from biomaterials research, this study aims to contribute to biomaterials science and significantly enhance the knowledge base for therapeutic outcomes for women grappling with the ramifications of uterine injuries.

## RATIONALE, OBJECTIVES AND HYPOTHESES

Uterine tissue injury and impaired regeneration significantly impact women's reproductive health. Applying biomaterials like pCA polymers as multifunctional components of novel prospective bioadhesives is expected to enhance cellular- and tissue-level responses essential for uterine repair. This study explores for the first time the effects of polydopamine (pDA), polylevodopa (pLD), and poly-L-norepinephrine (pLNE) on different cell types representing various uterine tissues, specifically of the endometrium (T-HESCs) and myometrium (PHM1-41 cells). Like pDA, pLNE and pLD materials possess amine and catechol groups in varying amounts, resulting in

diverse responses between haematologically relevant cell types and from an immunogenic context.[120] Furthermore, pLNE and pLD are lauded for the smoothness and thinness of their coatings, which is beneficial in therapeutic applications requiring tighter control over these dimensions.[120,343] Lastly, pLD contains carboxyl (–COOH) groups, which introduces functionalization opportunities (e.g., via EDC/NHS). This study aims to advance the understanding of pCA-mediated interactions within the uterine environment by delineating the specific responses of endometrial and myometrial-representing cells. These findings could lead to the development of tailored bioadhesive formulations to optimize material properties (e.g., topographical, mechanical, and grafting capacity) to support healing processes that underpin tissue engineering approaches to treat reproductive health issues.

## OBJECTIVES

1. **Polymer substrate preparation and analysis:** To create surfaces coated with pDA, pLNE, and pLD etched-borosilicate glass, then a detailed characterization of their morphology, wetting, and adhesion.
2. **Cell-material interaction assessment:** To investigate the response of T-HESCs and PHM1-41 cells to the pCA coatings, focusing on proliferation, adhesion, and morphology.
3. **Migration analysis**: To explore how the coated substrates influence the migratory behaviour of T-HESC and PHM1-41 cells, assessing parameters like migration speed, distance, and direction efficiency.

## HYPOTHESES

1. Variations in precursor chemistry will result in distinct surfaces with feature-specific differences in mechanical properties, affecting global measurements characterized by AFM.
2. Lower water contact angles (WCAs), indicating higher hydrophilicity, will inversely correlate with the adhesion strength of materials due to improved surface wettability.
3. The distinct chemical and physical properties of pCA coatings will differentially affect cell proliferation and adhesion dynamics.
4. The characteristics of pCA coatings will influence the dynamics of focal adhesion formation and, thereby, migratory dynamics.

## 6.1 ABSTRACT

Uterine injury is a common cause of distress for women worldwide, with the associated growth of scar tissues and fibroids potentially materializing into debilitating conditions (e.g., Asherman's syndrome). Tissue regeneration and healing within the human body, particularly in complex organs like the uterus, represent intricate biological processes that involve a coordinated interplay of cellular activities, biochemical signals, and structural changes. In the pursuit of solutions for uterine tissue damage, this study probes the application of polycatecholamine (pCA) polymers, namely polydopamine (pDA), polylevodopa (pLD), and poly-L-norepinephrine (pLNE), as potential functionalization avenues for regenerative bioadhesives. To this end, the research presented in this manuscript evaluates the influence of these polymers on two distinct uterine cell types: human endometrial stromal cells (T-HESCs), representing the endometrium, and pregnant human myometrial smooth muscle cells (PHM1-41), representing the myometrium. This dual-cell approach underscores the necessity of addressing the comprehensive cellular environment of the uterus in regenerative strategies. The study first carries out a physicochemical characterization of the pCA coatings by employing NC-AFM and DPFM-AFM for topographical and mechanical analysis, respectively, followed by contact angle goniometry to assess hydrophilicity. Successively, we investigated cell proliferation, morphological adaptations, and migration patterns in response to these pCAs, aiming at revealing how each polymer distinctly affects cell behaviour with significant differences in cell type. The observed differential responses suggest that the polymers' unique properties could be leveraged to design material applications (e.g., bioadhesives, injectable scaffolds) with targeted therapeutic effects, such as enhancing proliferation in specific cell lines while maintaining compatibility across a broader range of cells. These insights contribute to understanding cell-material interactions with pCA-based bioadhesives in the uterine context and open avenues for their inclusion in developing innovative biomaterial-based therapies for uterine tissue engineering.

## 6.2 INTRODUCTION

The growing implementation of bioengineering approaches in treating female infertility resulting from uterine injuries highlights significant therapeutic advancements.[385] These injuries can arise from surgical procedures, such as Cesarean sections (CS), or from disorders like intrauterine adhesions (IUAs), which are bands of fibrous tissue that adhere to each other, affecting a growing number of women worldwide.[386-388]

Following CS, improper wound healing can result in scar tissue formation that may compromise the integrity of the uterine wall, where biomechanical modelling suggests subsequent scar thinning and biomechanical changes may lead to higher regions of stress and, therefore, risk.[210,211] In this context, successful vaginal birth after cesarian (VBAC) occurs at rates between 50 to 85%, with risks including infection, failed trial of labour and an approximate 0.3–1% risk of catastrophic uterine rupture.[212] Additionally, IUAs can form from CS

or other trauma, including dilation and curettage (D&C) after miscarriage or elective termination.[389] Subsequently, IUAs may result in complete or partial closure of the uterus and symptoms, including reproductive concerns such as infertility, miscarriage, and ectopic pregnancies.[213,390] Unfortunately, hysteroscopic treatments to separate the adhered tissue, including D&C, are met with less than desirable post-surgical readhesion rates, ranging from 30 to 62.5%.[214] Consequently, in addition to surgical approaches to minimize trauma to healthy neighbouring tissues, a concerted effort has been made to develop therapeutic biomaterials. These materials are designed to promote myometrial healing, recolonization of the endometrium, and overall uterine fitness while preventing readhesion.[229,391]

To address the multifaceted challenges posed by uterine injuries, tissue engineering (TE) emerges as a promising strategy, leveraging advanced biomaterials and methods such as natural (e.g., collagen) and synthetic (e.g., poly-glycerol sebacate) hydrogel scaffolds, and cell sheets to facilitate tissue regeneration and healing.[221,223,226,229] Among TE approaches, bioadhesive materials are distinguished by the opportunity to design critical properties (e.g., degradability, tuning mechanical and biomimetic properties) and their dual functionality in promoting biological healing and closure of wounds.[392] These materials are vital in clinical settings because they can adapt to complex tissue structures and sustain strong adhesion within internal environments.[393] In particular, polydopamine (pDA), a bioadhesive derived from dopamine (DA) bioadhesive that undergoes autoxidative polymerization in alkaline conditions, enhances tissue adherence due to its exceptional ability to form robust interfaces with various tissue surfaces.[6,165,394]

As indicated by its classification within the catecholamine (CA) family, catechol and amine ($–NH_2$) functional groups are vital for pDA materials, their adhesive properties, and their interactions with biological tissues.[6] Catechol groups feature polar phenolic hydroxyl groups (Ph–OH) that enable the essential oxidation step in the formation of the polymer network and enhance polymer formation and adhesiveness through interactions such as π-π stacking, hydrogen bonding and facilitating intra-/intermolecular crosslinking.[129,151] On the other hand, $–NH_2$ groups serve as critical interfacial sites for effective protein adsorption, contribute to catalytic activity and are crucial in the formation of covalent bonds and interactions with quinone moieties to form pDA; their absence significantly impedes the formation and strength of adhesive films.[152,153,395]

Capitalizing on similarities in base chemistry, other members of the CA family, namely levodopa (LD) and L-norepinephrine (L-NE), can undergo similar polymerization mechanisms to form poly-L-norepinephrine (pLNE) and polylevodopa (pLD).[120,343] These are collectively referred to as polycatecholamine (pCA) materials. It has been observed that each CA precursor generates distinct pCA coatings, with differences in composition and topography, that induce cell-specific reactions.[120] For example, in the context of blood-interfacing devices, human umbilical vascular endothelial cells (HUVECs) proliferation is superior on pLNE-coated 316L stainless steel (SS).[120] In contrast, the proliferation of human umbilical arterial smooth muscle cells (HUASMCs) is best on pDA.

Additionally, each material appears to induce distinct RAW264.7 macrophage cytokine profiles, ranging from anti-inflammatory (pLNE) to neutral (pDA) to inflammatory (pLD).

pDA has been investigated in several restorative contexts, [396] including its ability to reduce pyroptosis-based programmed cell death, improve cardiac function, and reduce fibrosis in myocardial tissues post-infarction.[397] Additionally, the wound healing capacity of *Rattus* skin was found to improve by nearly 14% after 12 d when PLGA polymeric scaffolds were coated with pDA.[398] However, in the uterine context, its use has been mainly limited to drug delivery, while pLNE and pLD remain unexplored.[399] Therefore, the unexplored application of pCA-based materials in the female reproductive environment offers an opportunity to investigate their effects on cell lines representing uterine tissue. To this end, we began with a physicochemical analysis of each pCA material while considering structural differences and similarities. An in vitro bioactivity analysis was performed with transformed human endometrial stromal cells (T-HESCs) and pregnant human myometrial cells (PHM1-41). Subsequently, these cells were assessed for proliferation, morphology, and migration. This research aims to elucidate how uterine cells interact with pCA-based materials, potentially revolutionizing therapeutic approaches for female reproductive health disorders and paving the way for innovative, biomaterial-driven treatments.

## 6.3 RESULTS AND DISCUSSION

### 6.3.1 MATERIAL TOPOGRAPHY

Surface roughness modulates cellular behaviours such as adhesion, proliferation, and differentiation by influencing the topographical interactions between cells and the biomaterial.[331] In this context, the topography of the polymers resulting from their deposition on glass substrates was visualized via non-contact AFM (**Figure 6-1A-C**). The root mean square (RMS; Sq) was calculated as a roughness parameter to quantify the surface texture variations. The RMS values of pDA, pLNE, and pLD surfaces were 10.55 ± 2.09 nm, 4.96 ± 0.93 nm and 1.68 ± 0.22 nm, respectively (**Figure 6-1D**).

The pDA values are lower than the reported values (14.10 ± 0.39 nm) of a similar precursor concentration (1 mg/mL) on 316 L SS.[120] However, the RMS values of our pLNE and PLD surfaces were nearly double (2.46 ± 0.88 nm) and tripe (0.57 ± 0.03 nm), respectively, of those previously reported.[120] These previous results were obtained on a 316 L SS substrate, which impacted the resultant polymeric surface.[334] The increase in the RMS roughness of the pLNE and pLD surfaces may indicate a denser deposition of polymer layers, attributed potentially to the acid etching pre-treatment of the underlying glass substrates. Additionally, the roughness itself may significantly contribute to the lower water contact angles (WCAs), as increased roughness generally enhances the surface energy of polymers and improves wetting properties.[400] From the AFM micrographs, we could visualize two distinct structures on the surface, which we refer to as polymer aggregates and an underlying

film. While the pDA surface was almost entirely covered by a relatively uniform distribution of these granular structures, pLNE was much less covered, with significant variability in coverage (20–50%). In contrast, the pLD surfaces had low coverage, ranging from 0% to 15%, contributing to their low roughness.

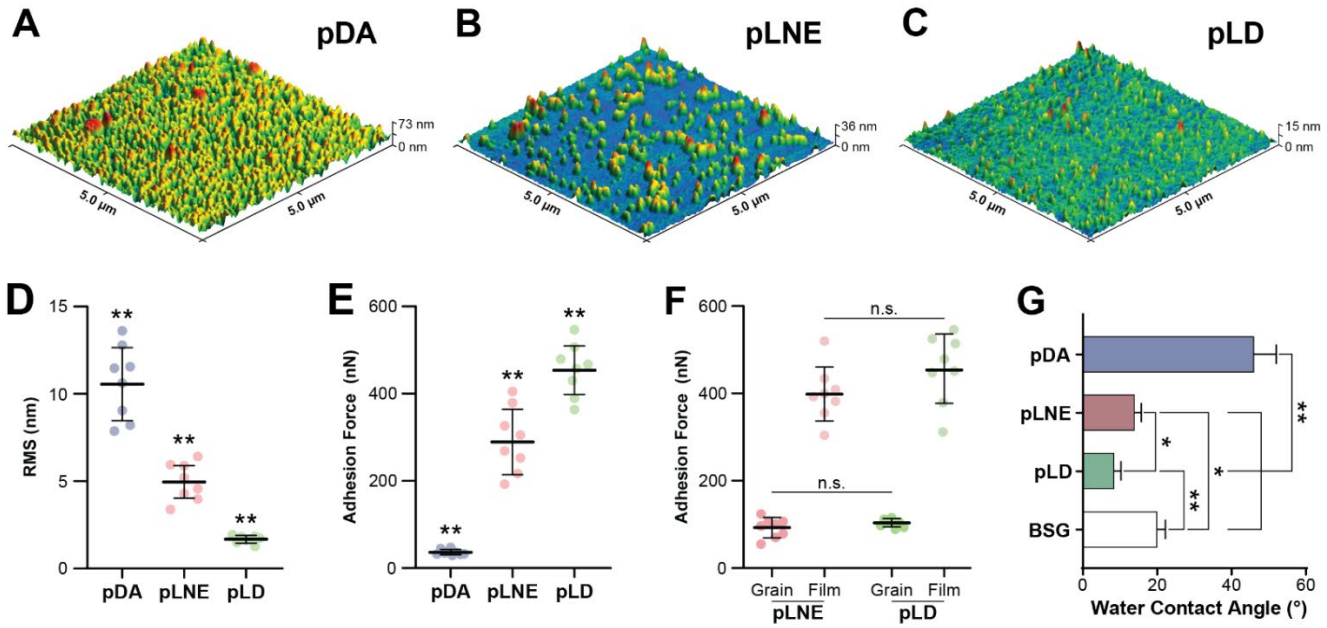


Figure 6-1: Material analysis of pCA coatings.

Non-contact micrographs of the **(A)** pDA, **(B)** pLNE, and **(C)** pLD coatings. **(D)** Root mean square (RMS) roughness was acquired using NC-AFM. **(E)** Global adhesion values acquired from the DPFM-AFM measurements. **(F)** Segmented adhesion values between the aggregates and films. **(G)** Contact angle goniometry. ANOVA: n.s. = not significant; *p < 0.05; **p < 0.01.

### 6.3.2 MATERIAL ADHESION

The adhesion force strongly indicates cell attachment by mediating the adsorption between crucial biomolecules and biomaterials. Cell receptors can detect specific biomolecules (e.g., RGD domains) that activate transmembrane integrin receptors, forming adhesion sites.[401] An intermittent contact method of AFM, the digital pulsed force mode (DPFM), was utilized to determine the adhesive component of these polymeric materials. This method capitalizes on measuring global adhesion and segmenting the data based on adsorbed aggregate and film topographical attributes. This opportunity would have been lost when a colloidal probe was used to sample a wider area per indentation.

Moreover, our lab had previously reported a hierarchical organization of pDA substrates with similar components that were predominantly distinctive based on their adhesion force.[132] In the context of global adhesion, pDA, pLNE and pLD surfaces were determined to be 35.4 ± 5.7 nN, 285.4 ± 79.1 nN and 447.3 ± 55.6 nN, respectively (**Figure 6-1E**). The adhesion forces were calculated upon tiered segmentation based on

topographical height to generate the requisite masks, as shown in **Figure 6-1F**. Because of the inability to segment the pDA effectively, this condition was omitted because the particles entirely covered the surface. Regardless, the adhesion force of the aggregates for pLNE and pLD were determined to be 92.5 ± 23.3 nN and 103.8 ± 9.4 nN, respectively. Concerning the underlying films, the adhesion forces for pLNE and pLD were determined to be 398.4 ± 61.8 nN and 453.8 ± 76.8 nN, respectively.

The observed variations in the global adhesion forces among the pDA, pLNE, and pLD surfaces underscored the significant impact of polymer composition and surface structuring on the material properties. Specifically, there was a marked increase in the global adhesion force from the least adhesive pDA, which was thoroughly blanketed by adsorbed aggregates, to the more adhesive pLNE and pLD surfaces, which had predominant proportions of the surface with an exposed film. Examination of the contributions of aggregates and films on the pLNE and pLD surfaces indicated that the adhesion force was statistically similar, with the film being approximately 4-fold as adhesive as the aggregates. This differential adhesion force between the structures contributed to the global adhesion of pLD owing to the lower incidence of aggregates, thereby exposing a much more substantial underlying adhesive film.

A recent study by Hemmatpour et al. (2023) provided insights into the possible mechanism of these surfaces.[135] The formation of pDA surfaces involves the initial adsorption of DA molecules onto a substrate, followed by their oxidative polymerization into complex structures, such as DA quinone and pCA oligomers. These processes result in a robust adhesive film capable of further complexation and growth through interactions with the additional polymeric aggregates in the surrounding solution. In this case, the adhesive film appeared to interact with the aggregates in the free solution to the point of complete surface coverage, resulting in a rougher pDA surface with little or no exposure to the underlying film.

Similar to DA, NE and LD could have their $–NH_2$ protonated, which could then positively influence the interfacial likelihood with the anionic silanolate groups of BSG and, thereby, the adsorption of early adhesive species, similar to pDA polymerization.[135] In the case of pLNE, it has been noted that the formation of 3,4-dihydroxybenzaldehyde (DHBA) in the reaction mechanism makes the formation of granules and aggregates much less probable.[120,343,349] NE is distinguished from DA by its additional –OH group on the β-carbon of its ethylamine side chain. It may undergo tautomerization and non-melanogenic breakdown into DHBA upon oxidation to quinone.[343] This intermediate interacts with the NE precursor to form DHBA–NE intermediates, contributing to lower steric interactions thereby inhibiting aggregate formation.

In this context, the lower probability of these phenomena likely contributed to the incomplete coverage of pLNE granules. Therefore, the early adhesive molecules that comprise the film were predominant. Moreover, the additional hydroxyl (–OH) group on the ß-carbon may contribute to the adhesive characteristics of pLNE. However, its contribution to polymers' overall composition and characteristics is unclear.

However, a defining characteristic of pLD is the carboxyl (–COOH) group on its ß-carbon.[142] Unlike pLNE, which is less likely to form aggregative structures, pLD readily forms particles in free solution.[147] However, these particles contain an abundance of –COOH groups that are deprotonated into carboxylate anions ($–COO^-$) in the alkaline environment where the polymerization reaction occurs. Subsequently, the anionic charge is believed to repel the pLD particles from each other, conceivably the –COOH-containing surface.[142] Furthermore, its presence introduces steric hindrance that may prevent interfacial bonding. This interaction explains the poor coverage of the pLD surface with adsorbed pLD aggregates, thereby increasing exposure to the film and global adhesion. However, a caveat is present in this study. Surface adhesion was recorded in air to enable the use of DPFM-AFM, whereas, at physiological pH in an aqueous solution, the groups were $–COO^-$ anions. Considering that a primary feature of a performative bioadhesive is the ability of proteins to absorb effectively, be stable, and conform properly, our probing of the surface may not provide an entirely accurate picture of the in situ adhesive nature when assessing the material for use as a biomaterial. However, these results provide valuable insights into the inherent nature of pLD, which can be crucial when considering materials for other applications in which adhesive or cohesive properties are essential.

The last component to discuss is the potential composition of the underlying adhesive film, which appears to be a shared characteristic of these pCA materials. Based on the current understanding, a shared molecule in each reaction mechanism was the presence of the 5,6-dihydroxyindole (DHI) intermediate, considered the main component of pDA.[6,120,343] Recent studies have revealed that, unlike previously thought, DHI, rather than catechol, plays a pivotal role in the adhesion mechanism of mussel-inspired chemistry.[150] However, the study suggested that pDA was uniquely rich in DHI due to its propensity for oxidation and cyclization, suggesting higher adhesion strength than other catechol-based polymers, which was only valid in the context of the first 2 h post-initiation of polymerization per the scope of the study. However, in our previous work, which formed two pDA surfaces, one with fewer aggregates and one with much higher amounts and larger aggregates, Raman spectroscopy suggested that an abundance of DHI was within the aggregates.[132] However, DPFM-AFM determined that the aggregates were significantly less adhesive than the film on those materials, similar to the considerably smaller aggregates mentioned above, suggesting that the adhesive moieties may have been less accessible for interfacial bonding on the apical surface of the adsorbed aggregates. Therefore, in this context, evidence suggests that a shared aspect of pCA polymerization formed a DHI-rich film on the substrate, followed by subsequent interaction, adsorption, and continued polymerization. Depending on the chemistry of the precursor, the coating of the film with polymeric particles can be adsorbed at a high (pDA), medium (pLNE), or low (pLD) degree. Unfortunately, we could not confirm this because of the thinness of the material and the requirement to use borosilicate glass for live-cell microscopy. Raman spectroscopy is typically employed for such analyses; however, this technique is not feasible under these conditions.

This analysis delineated the contrasting attributes and implications of aggregates and films on these pCA materials. The aggregates, while enhancing the surface roughness, potentially augmented cellular interactions owing to the texture and surface area, the latter of which could contribute to a higher adsorptive capacity. Despite these benefits, aggregates exhibit comparatively poor adhesion properties, which might limit their utility in specific applications (e.g. material binding). However, this increased adhesion seems to be achieved at the expense of nanoscale texture, potentially reducing the effectiveness of the material in applications where topographical cues are crucial. Furthermore, while adhesion could serve as a proxy for the material's ability to adsorb proteins, the overall cellular response is considered a multifactorial reaction to the panoply of cues in this context, topography, and adhesion. Moreover, other factors of the material, including chemical composition and surface charge, may have contributed to the interfacial outcome of the material. For instance, the surface charge and its distribution could affect the adsorption of charged biomolecules, potentially influencing their orientation and stability on the surface.[66,401,402] This influence on the adsorbed species might affect the likelihood that these molecules would bind to and activate cellular receptors, such as integrins. This juxtaposition highlights a trade-off between the structural potential facilitated by the adsorbed aggregates and the adhesive capabilities of the smoother films. Understanding these interactions is crucial for tailoring the material design to specific application needs and balancing the surface texture, adhesion, and other properties (e.g. surface energy) to optimize the performance.

### 6.3.3 WATER CONTACT ANGLE (WCA) GONIOMETRY

Before coating, borosilicate glass (BSG) coverslips were subjected to acid etching (4 h, 1N HCl) to clean and increase surface hydrophilicity. This modification was primarily attributed to increased silanol (Si–OH) groups on the glass, which enhanced the availability of hydroxide (–OH) groups and drastically influenced the interaction dynamics of subsequent polymer coatings.[403,404] The etching effect was confirmed by the decrease in the WCA from 72° to 20°, establishing our BSG control condition as the base substrate for pCA coatings (**Figure 6-1G**).

In the case of pDA coatings, the WCA was 46.4° ± 5.6 and was comparable with previously reported values, both on unetched glass and different materials, including 316L stainless steel (45°), titanium (51°) and silicon (54°).[6,120,132] This regularity suggested that the etching did not significantly perturb the surface adsorption of early oxidized intermediates and later-stage oligo-DA micro- and nano-particles.[135] Notably, Zhang et al. (2017) reported that pDA has the poorest interfacial adhesion to –OH functionalized Au substrate of similar wettability to our BSG (22.8°) when compared to increasingly hydrophobic –OH/$CH_3$ and –$CH_3$ terminated surfaces.[334] However, these experiments were performed using end-stage pDA and KCl solutions.

In contrast to the consistency of pDA, the WCA observed for pLNE (14.3° ± 1.4°) coatings on BSG was less than half of that reported for 316 L stainless steel (38° ± 3°) despite similar reaction conditions.[120] Additionally, pLNE coated on a Si wafer was reported with a WCA of 8.6°, much lower than our result (15.2°).[343] However,

their approach used twice the amount of precursor. A common factor between the silicon wafer and our BSG is the silanol mentioned above groups, typically found as silicon dioxide ($SiO_2$) on the silicon surface but transformed into reactive silanol groups when exposed to water.[405] In both instances, the alkaline environment would induce deprotonation into reactive silanolate groups, which may explain the significantly higher hydrophilicity than that reported on 316 L SS.[120] In this context, silanolate may have a greater chance of interacting with the Ph–OH as NE oxidizes more slowly into quinone intermediates than DA.

Furthermore, unlike pDA, which is renowned for its granular surface roughness and aggregate formation, pLNE possesses a highly smooth surface owing to the inclusion of DHBA.[343] Its aldehyde group (–CH=O) could act as an electrophile, resulting from transforming the ß-carbon –OH group. This characteristic facilitates its potential involvement in nucleophilic addition reactions when attacked by an oxide anion of the silanolate, strengthening cell-substrate interactions. Taken together, these additional interactions enabled by the structure of the NE precursor may contribute to the generation of a pLNE coating that takes advantage of the deprotonated siloxide groups on the BSG under alkaline conditions, resulting in a more uniform and stable polymer network integrated with the glass substrate. This integration enhances the hydrophilic nature of the pLNE coating and promotes effective crosslinking at the interface.

Regarding pLD, the WCA was 8.7° ± 1.5, which, like pLNE, was less than half that reported when coated on 316 L SS (29° ± 2°).[120] As previously mentioned, the structure of LD further diverges from that of the other precursors as its ß-carbon possesses a –COOH instead of the –OH group seen on NE or no functional group with DA. In a neutral environment,–COOH enhances the density of polar sites on the polymer surface, contributing to extensive hydrogen bonding with water molecules and, therefore, greater hydrophilicity.[406] However, depending on the composition of the resulting pLD coating and alkaline conditions,–$COO^-$undergoes deprotonation to form highly reactive–$COO^-$groups. This transformation facilitated coordination bonding with silanolate on the BSG. Such bonding enhances the pLD and, therefore, the density of its polar –COOH content and other hydrophilic groups in LD, contributing to its notably superior hydrophilicity.

### 6.3.4 CELL PROLIFERATION

The impact on the proliferation process is a critical metric for understanding the long-term suitability of biomaterials, with cell-specific responses being exciting in the design of therapeutics for use in multicellular environments.[407] We conducted PrestoBlue-based measurements at 1, 3, 5, and 7 days to assess the proliferation of T-HESC and PHM1-41 cells. Additionally, we evaluated the positivity rate and intra-nuclear morphology of the proliferative marker Ki-67 at D 1 and 3.[408]

#### 6.3.4.1 *RESULTS*

**T-HESCs**: PrestoBlue indicates substrate differences on Day 1. Normalized elevations of T-HESCs on pLNE and pDA were significant ($p>0.05$), being 7.8% ± 3.5% and 4.4% ± 2.1% greater, respectively, than those on BSG (**Figure 6-2A**). In contrast, pLD showed no tangible benefit. Notably, while Ki67 positivity was similar between pDA and pLNE, both were significantly higher than that of BSG, whereas pLD was lower (**Figure 6-2B**). These differences were diminished by Day 2. By Day 3, divergence between pLNE and pDA was observed, with pLNE showing 15.8% ± 2.4% greater fluorescence than BSG, whereas pDA was 9.7% ± 3.2% higher. Notably, a benefit to pLD emerged with 5.4% ± 2.2% greater signal than BSG. Although the differences between pDA and pLD were not statistically significant, the trend of pDA>pLD was sustained throughout the full-time course and was present in all trials. Similar relationships were observed on Day 5. pLNE increased its signal to 20.9% ± 5.2% over BSG, followed by pDA (14.6% ± 5%) and pLD (10.4% ± 3.2%). By Day 7, owing to the rapid proliferation of T-HESCs, confluence was reached on all the substrates, resulting in fewer differences.

**PHM1-41:** The PHM1-41 response to all three pCA substrates appeared more favourable than T-HESCs. On Day 1, pLNE and pDA presented similar increased signals of 17.9% ± 3.3% and 17.1% ± 2.6%, respectively (**Figure 6-2C**). Compared to T-HESCs, PHM1-41 cells on pLD presented a significantly higher signal (8.4% ± 1.7%). No discernible differences in Ki67 positivity between any conditions were observed on Day 1 or 2 (**Figure 6-2D**). Similar relationships were observed on Day 3, with pLNE and pDA increasing their normalized signals to 27.6% ± 3.6% and 24.2% ± 3.7%, respectively, over BSG. The pLD showed a slight increase to 10.5% ± 1.4%. On Day 5, significant divergence was observed between pLNE and pDA, being 42.9% ± 5.6% and 29.2% ± 4.1%, respectively, with pLD further increasing to 14.6% ± 5.0%. These trends continued through Day 7, with normalized fluorescence of pLNE, pDA, and pLD being 55.9% ± 4.9%, 37.5% ± 5.5%, and 16.8% ± 3.3% over BSG, respectively.

#### 6.3.4.2 *DISCUSSION*

To elucidate the intrinsic effects of the pCA coatings on cellular proliferation, highlighting distinct interactions between these materials and different cell types, we assessed PrestoBlue signals for T-HESCs and PHM1-41 cells over a week. Initially, on Day 1, T-HESCs cultured on surfaces coated with pDA and pLNE exhibited a 4–8% higher proliferation rate than the BSG surface. However, the difference between the pDA and pLNE groups was not statistically significant. Conversely, pLD cells displayed proliferation rates similar to those observed in BSG. By Day 3, the proliferation on pLNE surfaces notably surpassed that on pDA by 6%, while pLD showed a modest increase to approximately 5% above BSG. This trend persisted until Day 5. By Day 7, rapid proliferation rates across the substrates began to converge.

In contrast, PHM1-41 cells cultured on pDA and pLNE on Day 1 showed an 18% increase in proliferation over BSG, more than double the rate observed with pLD, which exhibited an 8% increase over BSG. This pattern continued until Day 3, with proliferation on pDA and pLNE significantly outpacing that on pLD, reaching a 26%

increase over BSG. The divergence in cell responses between the pDA and pLNE coatings became apparent by Day 5, with pLNE maintaining an 11% higher proliferation rate than pDA, which increased to 14% by Day 7. Throughout this period, pLD continued to show a slight yet statistically significant increase in cell proliferation.

Previous research has documented the efficacy of pDA in promoting cellular proliferation across various cell types, including endothelial, neural stem, and pluripotent stem cells.[193,409,410] This was mainly attributed to its chemistry, which contains vital functional groups, including catechol and quinone molecules. These enhance the immobilization of biomolecules (e.g., protein adsorption) to contribute to a microenvironment that mimics the ECM, supporting cellular adhesion and growth.[156] Similarly, pLNE coatings have been reported to enhance the proliferation of skeletal muscle cells and PC12 neuron-like on PCL and PLCL electrospun fibres, respectively.[344,411] Comparatively, pLD has been less studied in the context of cell-facing biomaterial applications. However, adding pLD to β-glucan hydrogels significantly enhanced their suitability as wound dressings by improving their physicochemical stability, enabling effective drug delivery, and ensuring biocompatibility and antibacterial efficacy.[342]

However, the effectiveness of these materials in promoting adhesion appears to be cell-specific. When coated on 316 L SS, both pDA and pLNE have been reported to promote the growth of HUVECs but inhibit the growth of HUASMCs.[120,412] Moreover, when coated with tissue culture plastic (TCP), the proliferation of human induced pluripotent stem cell-derived mesenchymal stem cells (hiPS-MSCs) benefited significantly from pLNE coatings, compared to pDA.[413] In contrast, no tangible benefit was observed for human mesenchymal stem cells (hMSCs).

The differential effects observed with pDA, pLNE, and pLD coatings in promoting proliferation highlight the complexity of cell-material interactions. Considering our findings, the superior performance of pLNE, despite the well-documented advantages of pDA, suggests an alternative or complementary mechanism that influences cell behaviour. This concept is crucial, as the reported content of crucial amine and Ph–OH groups, considered primary mediators of adsorption and cell-substrate interactions, are reduced in pLNE versus pDA.[120] In this context, considering the proliferative responses across different cell types, it is imperative to examine the role of adhesion in mediating these effects. The adhesive properties of biomaterials, influenced by their chemical functional groups and surface topography, are central to cell attachment and proliferation.

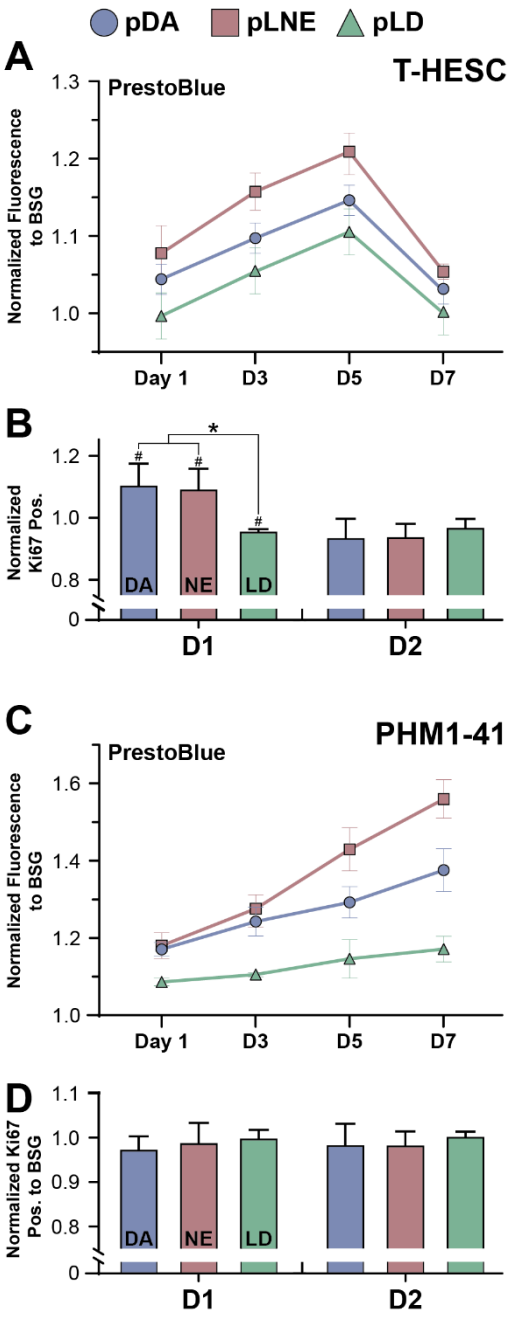


Figure 6-2: Cellular proliferation metrics for T-HESCs and PHM1-41 cells.

Includes data for T-HESCs (*top*) and PHM1-41 cells (b*ottom*). **(A, C)** PrestoBlue proliferation assay was performed over seven days. **(B, D)** Ki-67 positivity rates were normalized against the BSG control on Days 1 and 2 post-seeding. ANOVA: n.s. = not significant; *p < 0.05; **p < 0.01. # indicates significance (p < 0.05) compared to BSG.

### 6.3.5 CELL ADHESION

Morphological investigation is fundamental to studying cell-material interactions and provides insight into how cells perceive and adapt to their underlying substrates. To comprehensively analyze how each biomaterial uniquely influenced T-HESCs and PHM1-41 cells and how these interactions changed over time from early (2–6 h) to late (24 h) time points, we quantified the parameters of cell area, eccentricity (*ecc*), which represents elongation with *ecc*=0 as a perfect circle, and form factor (FF), which means shape irregularity that is indicative of protrusiveness.

#### 6.3.5.1 *RESULTS*

**T-HESCs:** At the initial 2 h interval, T-HESCs seeded on pLNE and pDA presented 271% ± 41% and 180% ± 34% more interfacial area than BSG, respectively (**Figure 6-3A**). Although the cells on pLNE were 32% larger than those on pDA, they were similar in *ecc* and FF. T-HESCs on pLD had similar ecc and FF characteristics; therefore, the cells exhibited a 15.6% ± 3.3% greater area. Relationships changed by 6 h, when cells on pDA were the largest and displayed a 269% ± 17% higher surface area than those on BSG, whereas pLNE supported a substantially lower 109% ± 13% greater area (**Figure 6-3B**). Cell cultured on pDA were markedly more elongated than all other cells, maintaining a similar FF value to that observed at 2 h. Cells on pLNE became much less elongated, although still more significant than those on BSG and pLD, with their protrusiveness approaching that of BSG ($p>0.05$). Throughout this period, cells on pLD consistently mirrored BSG with an insignificant 7.1% ± 13% difference in area and similar *ecc* and FF metrics. After 24 h, cells across all substrates converged to similar areas and roundness (**Figure 6-3C**). However, pDA was statistically more protrusive than pLD was.

**PHM1-41s:** During the first 6 h, although PHM1-41 cells exhibited a markedly similar response to pLNE and pDA, a much more significant effect was observed with pLD treatment. Starting at 2 h, cells on pDA and pLNE were 197% ± 34% and 267% ± 46% greater than those on BSG (**Figure 6-4A**). Similar to T-HESCs, cells on pDA and pLNE were elongated and irregular in shape according to their *e* and FF. However, unlike T-HESCs, PHM1-41 cells on pLD responded more intensely to the coating, with cells having a 101% ± 31% greater area. Reflecting an intermediate phenotype, cells on pLD were statistically like all other conditions in circularity, although pDA and pLNE were significantly more elongated than BSG. This phenotype was characterized by protrusiveness but was statistically different from all other conditions. By 6 h, the area rankings switched, with cells on pDA becoming larger than those on pLNE, with areas 230% ± 39% and 129% ± 41% more spread than those on BSG (**Figure 6-4B**). Cells on pDA had similar elongation and protrusiveness as those at 2 h. PHM1-41 cells continued to benefit from pLD and were determined to be 79% ± 15% larger than BSG and statistically like pLNE in all parameters. Notably, the cells in the pLD varied more in shape metrics per standard deviation. At the 24 h mark and dissimilar to T-HESCs, the PHM1-41 cells on pDA and pLNE retained 42–45% greater area than BSG and pLD (**Figure 6-4C**).

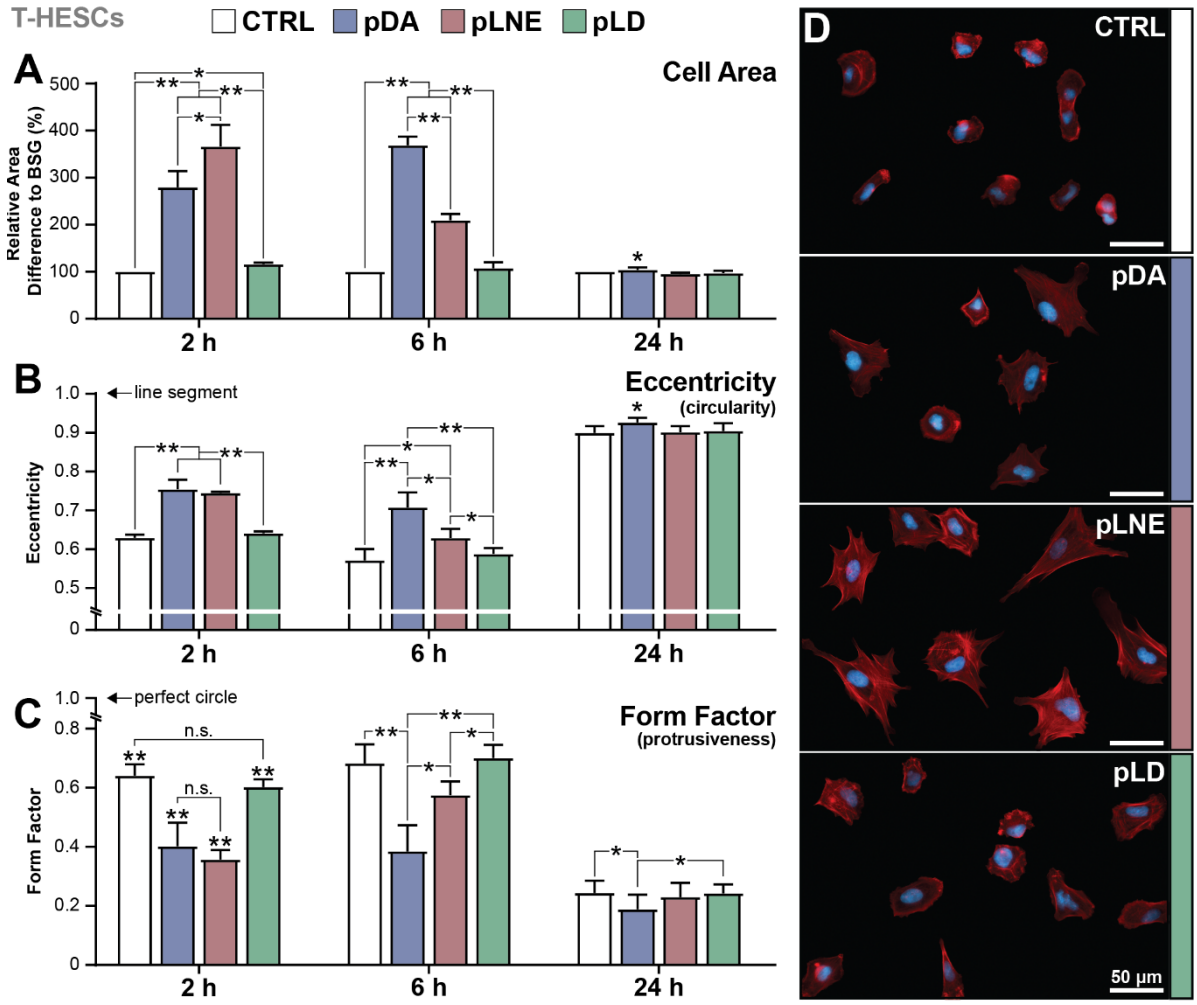


Figure 6-3: Morphometric analysis of T-HESCs at 2, 6, and 24 h.

Metrics included **(A)** percentage change in cell area relative to the BSG control, **(B)** eccentricity reflecting cell circularity, and **(C)** form factor reflecting cellular shape irregularity. ANOVA: n.s. = not significant; *p < 0.05; **p < 0.01. The two asterisks (**) above the data indicate statistical significance compared to all other conditions unless indicated otherwise. **(D)** Fluorescence microscopy images of T-HESCs with nuclei (*blue*) and actin filaments (*red*) at 2 h. Scale bar = 50 µm.

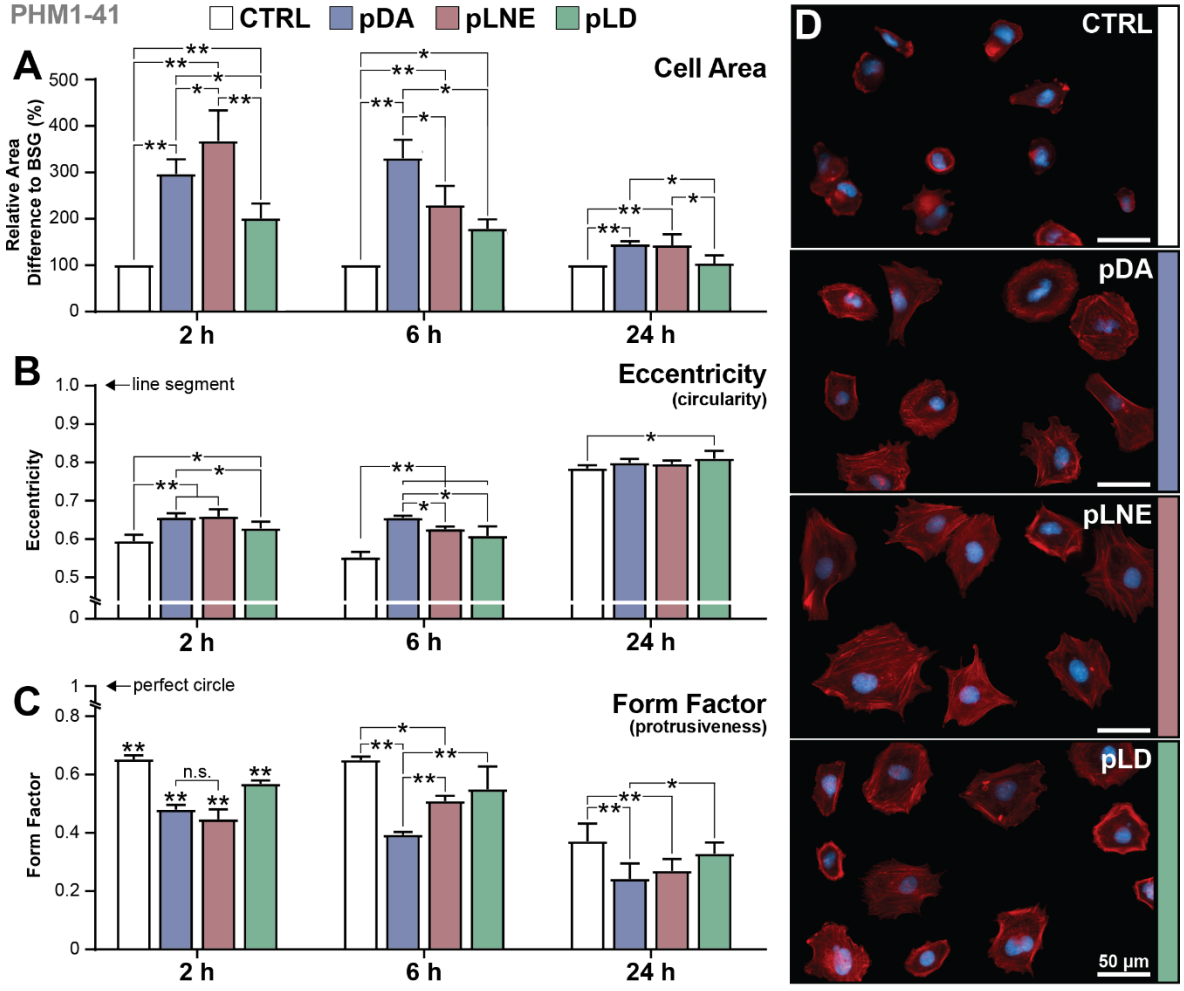


Figure 6-4: Morphometric analysis of PHM1-41 cells at 2, 6, and 24 h.

Metrics include **(A)** percentage change in cell area relative to the BSG control, **(B)** eccentricity, and **(C)** form factor. ANOVA: n.s. = not significant; *p < 0.05; **p < 0.01. The two asterisks (**) above the data indicate statistical significance compared to all other conditions unless indicated otherwise. **(D)** Fluorescence microscopy images of PHM1-41 cells with nuclei (*blue*) and actin filaments (*red*) at 2 h. Scale bar = 50 µm.

#### 6.3.5.2 *POLYDOPAMINE (PDA) AND POLY-L-NOREPINEPHRINE (PLNE)*

A possible explanation begins when contrasting the proliferation results with morphometric analysis, particularly at earlier times. As early as 2 h, significant differences were observed between the two cell lines. At this point, pLNE promoted more significant cell spreading than pDA did. These differences, pronounced across cell lines, showed that cell areas on pLNE were 265–270% larger than those on BSG, whereas those influenced by pDA were 180–197% larger. Consequently, T-HESCs and PHM1-41 cells cultured on pLNE exhibited approximately 33% and 24% greater spreading than those cultured on pDA. Additional metrics indicated that both cell types on pDA and pLNE presented significantly more elongated and protrusive morphologies than those on BSG. Although we previously reported that cells might directly interact with pDA aggregates, the similarity in shape metrics, despite the advantage in cell area for pLNE, suggests that these structures did not influence early adhesion mechanisms. By 6 h, the ranks shifted, with T-HESCs and PHM1-41 cells showing 75% and 63% greater spread on pDA than on pLNE. Additionally, cells cultured on pDA were notably more elongated and protrusive than those cultured on pLNE were. These results suggest that this ranking transition resulted from the accelerated initiation of cell spreading on pLNE compared to pDA. By 24 h, T-HESCs on pLNE had normalized in area and shape to those on BSG and pLD. Those on pDA maintained a slightly yet significantly larger, more elongated, and more protrusive morphology. In contrast, PHM1-41 cells responded similarly to pDA and pLNE, with cells on both being approximately 40% more spread than BSG and having significant displays of protrusiveness. The increase in cell area and protrusiveness of pDA likely resulted from direct interfacing with pDA aggregates, a phenomenon previously demonstrated by our group, showing that cells could and did form membrane envelopes over these structures.[132] However, the difference in morphometrics between cell lines for pLNE signalled that PHM1-41 cells were more responsive to pLNE than T-HESCs at later time points, which may translate into functional differences.

Both pDA and pLNE have been reported as being able to coat various substrates with diverse wettability and chemistries, generally increasing their hydrophilicity.[6,334,343,345] This benefit was directly tied to the rich tapestry of catechol and amine-reactive grouping of the resultant polymers. These functional groups facilitated electrostatic, hydrogen bonding and covalent interactions with a host of biomolecules.[116,414] pDA had been well described to take advantage of these promising pairings to immobilize growth factors (e.g., IGF-1), peptides (e.g., RGD-containing) and proteins (e.g., BSA) that result in enhancements in biocompatibility, drug delivery and anti-fouling.[168,415,416] Similarly, pLNE has also been effective in immobilizing molecules, including enzymes (e.g., catalase) and molecules (e.g., NO).[343,355] In this context, the shared immobilization advantage of these materials contributed to improved protein adsorption, a hallmark characteristic of bioadhesives that can enhance the cell response, including adhesion, spreading and proliferation.[61,417,418]

However, during early cell spreading, a clear and consistent differential response between pDA and pLNE was observed between cell lines. We hypothesized that the accelerated spreading initiation might be due to the increased accessibility of the adsorbed protein. A defining characteristic that sets pLNE apart from pDA is its staggering flatness, which supports its utilization in use cases that require precise topography management, including biosensors and fibrous biomaterials.[350,352,411,419] The aggregative nature of pDA contributes to the roughness of the thin film and the formation of aggregates dispersed across the resultant surface. As previously mentioned, the pDA aggregates were significantly less adhesive than the underlying film, suggesting a polymeric network that sequestered reactive functional groups within its internal structure and contributed to the reduced adhesion of the material. This effect could increase with polymerization time and maturation.[132,150] Additionally, this aggregative nature contributes to the rougher surface texture of pDA, which is considered an advantage of the material and could potentially enhance the adsorption capacity.[420] However, owing to their rough topology, proteins adsorbed on pDA may be less accessible, reducing their probability of interfacing with cell surface receptors and structures. This impeded interaction was ascribed to the reduced activity of enzymes immobilized on pDA compared with those immobilized on pLNE.[355] In this case, the exceedingly flat surface of pLNE may have allowed for more optimal accessibility, distribution, or orientation of adsorbed proteins, thereby facilitating more immediate and effective cell spreading.

#### 6.3.5.3 *POLYLEVODOPA (PLD)*

In stark contrast to pDA and pLNE, the behaviour of T-HESCs and PHM1-41 cells on pLD presented cell-specific adhesion responses. In the assessment of T-HESCs, no significant changes in cell area or other morphometric parameters were observed when compared with BSG. These results were surprising given the prior performance of the other pCA materials and the documented variable, but significant, positive (HUVECs) and negative (HUASMCs) adhesion results at a similar 2 h post-seeding.[120] This BSG-like behaviour of T-HESCs to pLD was maintained for 24 h.

Conversely, PHM1-41 cells responded dramatically to pLD and presented cell areas more than two times that of cells on BSG by 2 h. Additionally, the cells were elongated and protrusive. Notably, at 6 h, through the relationships continued, PHM1-41 cells on the surface exhibited a significantly higher deviation than other surfaces in eccentricity and form factor. This variation may indicate more effective yet heterogeneous interactions with the substrate, such as regions of polymeric discontinuity or affected protein adsorption. However, after 24 h, PHM1-41 cells on pLD resembled those on BSG. These findings underscored the cell-specific interactions with substrates, where T-HESCs did not markedly recognize the pLD surface, in contrast to PHM1-41 cells, which exhibited a robust response. To explain these cell-specific responses, we suggested two possible contributing factors: suboptimal adsorption dynamics attributed to the presence of –COOH and cell-specific enhanced substrate mechanosensing of PHM1-41 cells.

As previously mentioned, the –COOH groups on pLD surfaces present unique challenges for cell-substrate interactions due to their structural and electrostatic properties. These –COOH groups in the pLD polymer were attributed to dihydroxyindole-carboxylic acid (DHICA), which retained the functional group during the oxidation and rearrangement of L-dopachrome.[346] In contrast, its molecularly similar counterpart, DHI, results from a pathway in which the –COOH is lost during the cyclization process of L-dopachrome. In the case of DHICA, the proximity of the α–COOH group to the secondary amine within the pyrrole ring introduces potential steric hindrance. This spatial arrangement could obstruct the access of protein side chains or active sites, which might typically interact with the secondary amine group, as observed with the decarboxylated DHI constituent. This imposition reduces the binding affinity for protein adsorption, which is crucial for cellular recognition and adhesion.

Moreover, these –COOH groups are deprotonated at physiological pH to form $–COO^-$ anions, which impart a negative charge to the surface. Because the charge distribution of cationic and anionic charges can benefit long-range electrostatic interactions, repulsive forces between the negatively charged $–COO^-$ groups and similarly charged regions on proteins may significantly hinder effective protein adsorption, whether by leading to insufficient or inconsistent adsorption or by causing deleterious orientation of proteins on the surface.[402,417,421] Different cellular responses to adsorbed proteins and bioactive factors underscore the complexity of substrate-mediated cell behaviour.[401,422] In this context, the insufficient quality and quantity of adsorption on pLD may not have created an inadequate milieu for enhancing the adhesion and spreading of T-HESCs, which remained broadly consistent with the BSG condition, which serves as the underlying substrate. Conversely, for PHM1-41 cells, the species that did not adsorb onto the pLD may have been adequate to activate the specific integrins expressed by these cells, thereby supporting some level of cellular activation and adhesion. However, because of other contributing factors, such as the heterogeneity of the adsorbed layer, which may explain the higher variability per standard deviation or the overall biomolecular residue milieu on the pLD, the response of PHM1-41 cells did not reach the efficacy observed with substrates such as pDA or pLNE.

Another contributing factor that may have contributed to the adsorption limitations is related to the mechanical factors that span the polymer-substrate interface. pLD coatings on 316 L SS are reportedly exceedingly thin (approximately 8 nm) and much thinner than those of pDA and pLNE, with indications of incomplete coverage.[120] Furthermore, the etching process on the BSG substrate increased the concentration of Si–OH groups, potentially enhancing the interface between the pLD coating and the BSG substrate. This enhanced interfacial interaction could influence the mechanical properties of the thin polymer films, particularly leading to matrix stiffening.[423]

During early adhesion events, T-HESCs may respond unfavourably to the combination of low-quality protein adsorption and mechanical properties of the pLD condition. However, for PHM1-41 cells, an important

characteristic is that the line was derived from an elective Cesarean section at 39 weeks, one week after a full term.[243] During pregnancy, the myometrium is maintained in a quiescent state through progesterone receptor dynamics to ensure the relaxation of the myometrial walls, supporting fetal development.[207] As parturition approaches, receptor dynamics shift to promote increased contractility in labour preparation, enhancing smooth muscle cells' plasticity.[206] This plasticity is characterized by the upregulated expression and activation of proteins critical for mechanosensing and mechanotransduction, such as FAK and paxillin, generally reversed shortly after parturition.[424] Given the provenance of the PHM1-41 line, this elevated sensitivity to substrate mechanical properties may have contributed to the positive response in cell spreading at earlier time points, regardless of less effective protein adsorption. This hypothesis is partially corroborated by observations in aortic smooth muscle cells, which have shown more extensive spreading on substrates that better match their internal stiffness, with glass providing the most favourable results during initial adhesion stages.[425]

### 6.3.6 FOCAL ADHESIONS (FA) AND CELL MIGRATION

#### 6.3.6.1 *FA RESULTS*

Focal adhesions (FAs) are pivotal components in cellular biology and act as critical mediators in the connection between cells and the extracellular matrix (ECM) and regulating processes, including proliferation, migration, and differentiation.[426-428] These adhesions are remodelled in response to various external stimuli, including the physical and chemical properties of the substrate to which cells adhere.[427,429] This dynamic nature makes them critical targets in studying cell-material interactions, particularly in tissue engineering and regenerative medicine. In this context, we assessed FAs at 24 h concerning the number per cell, length and area, coverage per cell, and geometrical aspects, such as the aspect ratio (AR) and form factor (FF). These metrics collectively provide a comprehensive view of how substrates influence FAs and reflect cellular responses regarding adhesion, morphology, and signalling.

**T-HESCs**: The most significant number of FAs per cell was observed in BSG, with 43 ± 16 FAs per cell (**Figure 6-5A**). In contrast, these numbers were significantly lower than those of pDA, pLNE, and pLD, yielding 34 ± 15, 28 ± 13, and 33 ± 14 FAs per cell, respectively. Statistical analysis revealed significant differences across all surfaces, except between pDA and pLD (p=0.49). The FA length also varied significantly across different substrates. Cells on BSG exhibited the longest FAs, measuring 3.98 ± 1.42 µm (**Figure 6-5B**). Comparatively, lengths on pCA substrate were 3.07 ± 0.97 µm for pDA, 3.03 ± 1.00 µm for pLNE, and 3.32 ± 1.21 µm for pLD. Similar to the FA numbers, the differences were statistically significant, except for pDA and pLNE (p=0.22). The FAs followed similar trends, with T-HESCs on BSG presenting the most considerable area (2.90 ± 1.19 $\mu m^2$), as shown in **Figure 6-5C**. This result contrasted with the pCA substrate, where areas were 1.82 ± 0.76 $\mu m^2$ for pDA, 1.87 ± 0.81 $\mu m^2$ for pLNE, and 1.99 ± 0.90 $\mu m^2$ for pLD. Notably, although all pCA substrates were statistically lower than the BSG, the measurements between the pCA substrates were similar. Regarding FA coverage per

cell, the relationships were identical to the FA length, with T-HESCs on BSG having a coverage of 9.87 ± 2.35% (**Figure 6-5D**). Coverage was notably lower on pDA and pLNE, with 5.17 ± 1.94% and 5.13 ± 2.08%, respectively. The coverage on the pLD surface was slightly higher at 5.66 ± 2.1%. In terms of shape and geometrical parameters, the AR of FAs was significantly higher on BSG (3.74 ± 1.51) and pLD (3.84 ± 1.55) than on pDA (3.30 ± 1.20) and pLNE (3.17 ± 1.12); (**Figure 6-5E**). Finally, the FF was the lowest on BSG compared to all other substrates at a value of 0.47 ± 0.18 (**Figure 6-5F**). Measurements on the pCA substrate were similar, with 0.55 ± 0.19 for pDA and pLNE and 0.53 ± 0.19 for pLD.

**PHM1-41s:** The number of FAs per cell was highest on pDA, averaging 52 ± 21 adhesions per cell, like that on pLD at 49 ± 21 (**Figure 6-6A**). These numbers contrasted with PHM1-41s on BSG (42 ± 17) and pLNE (43 ± 19). Statistical analysis indicated a similarity between pDA and pLD (p=0.39) and BSG and pLNE (p=0.98). The FA length shown in **Figure 6-6B** was determined to be longest on BSG (3.34 ± 1.27 μm) and pLD (3.23 ± 1.15 μm) in comparison to pDA (3.05 ± 1.04 μm) and pLNE (3.09 ± 1.10 μm);). FAs on BSG presented with the most significant area (2.22 ± 1.11) compared to the pCA substrate (pDA: 1.75 ± 0.72 $\mu m^2$; pLNE: 1.82 ± 0.78 $\mu m^2$; pLD: 1.90 ± 0.84 $\mu m^2$), as illustrated in **Figure 6-6C**. Like the length and area, FA coverage was the highest on BSG (6.70% ± 1.87%) (**Figure 6-6D**). Notably, the coverage on pLNE was markedly lower, 3.67% ± 1.18%) than that on pDA (4.04% ± 1.12%) and pLD (4.65% ± 1.48%). Regarding the shape and geometry of the FAs, the AR was more significant in pDA (3.47 ± 1.28) and pLD (3.54 ± 1.35) than in BSG (3.24 ± 1.15) and pLNE (3.34 ± 1.21) (**Figure 6-6E**). Additionally, the FF was highest on pLNE (0.57 ± 0.19) and pDA (0.56 ± 0.18) when compared to BSG (0.54 ± 0.19) and pLD (0.54 ± 0.18), as shown in **Figure 6-6F**.

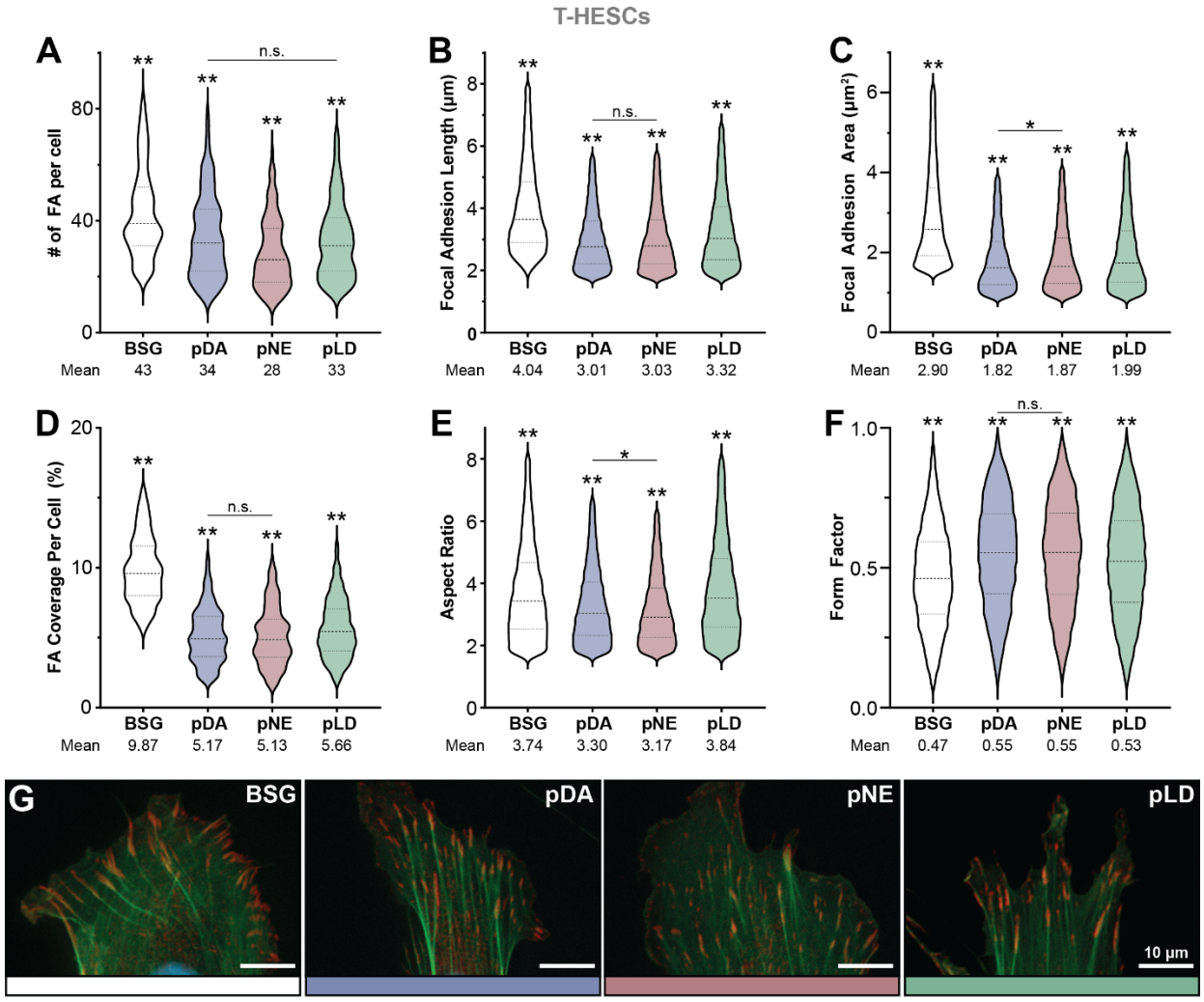


Figure 6-5: Quantitative vinculin-mediated FA analysis of T-HESCs 24 h post-seeding.

The metrics included **(A)** the number of FAs per cell, **(B)** length (µm), **(C)** area (µm²), **(D)** the percentage of cell interfacial area covered by FAs, **(E)** FA aspect ratio, and **(F)** form factor. ANOVA: *p < 0.05; **p < 0.01. The two asterisks (**) above the data indicate statistical significance compared to all other conditions unless indicated otherwise. **(G)** Fluorescence microscopy images of T-HESCs with vinculin-stained focal adhesions (*red*) and actin filaments (*green*) at 24 h. Scale bar = 10 µm.

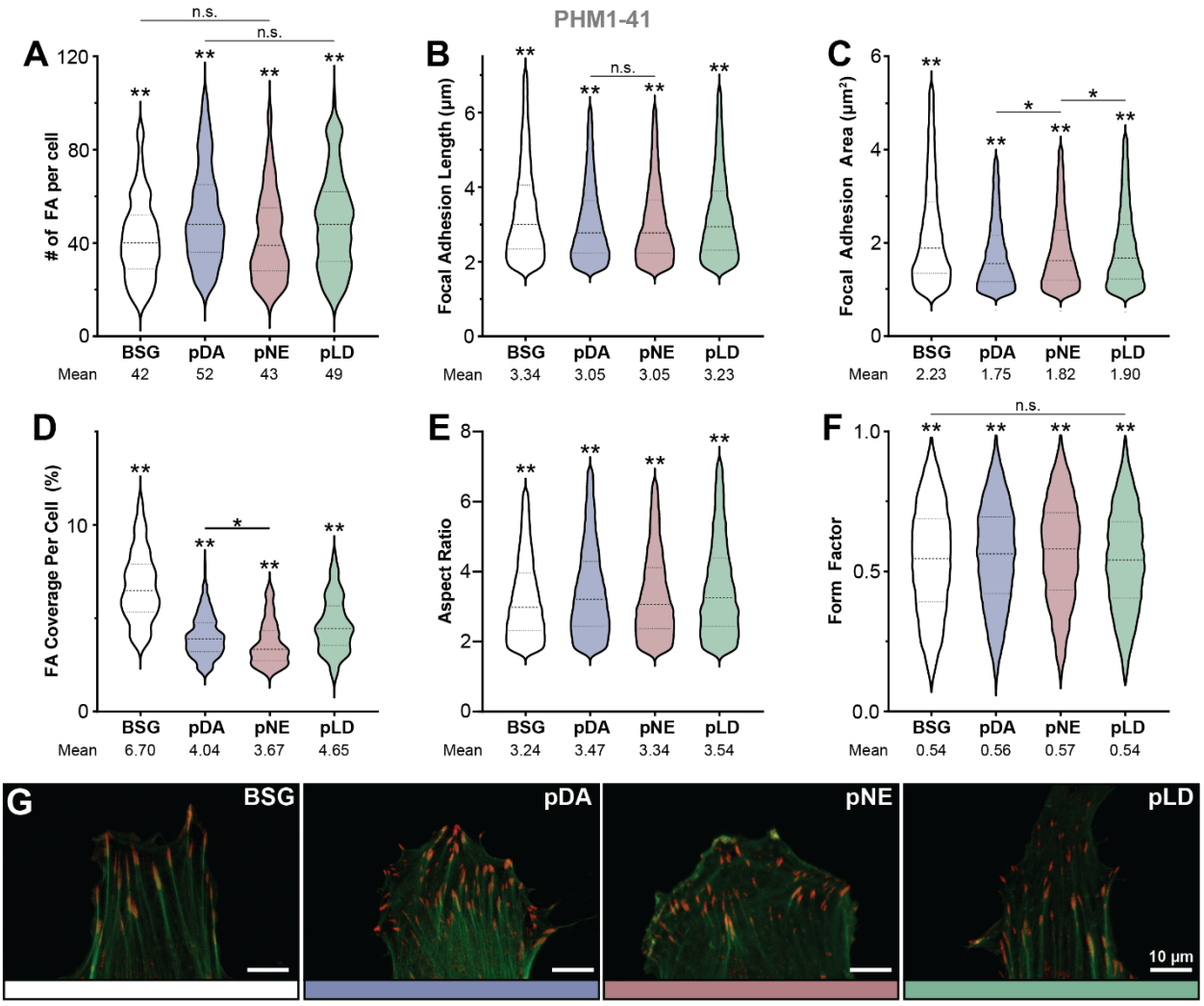


Figure 6-6: Quantitative vinculin-mediated FA analysis of PHM1-41 cells 24 h post-seeding.

The metrics included **(A)** the number of FAs per cell, **(B)** length (µm), **(C)** area (µm²), **(D)** the percentage of cell interfacial area covered by FAs, **(E)** FA aspect ratio, and **(F)** form factor. ANOVA: *$p < 0.05$; **$p < 0.01$. The two asterisks (**) above the data indicate statistical significance compared to all other conditions unless indicated otherwise. **(G)** Fluorescence microscopy images of T-HESCs with vinculin-stained focal adhesions (*red*) and actin filaments (*green*) at 24 h. Scale bar = 10 µm.

#### 6.3.6.2 *MIGRATION RESULTS*

Cell migration is a critical process in numerous physiological and pathological contexts, and understanding how different substrates affect this behaviour is essential in fields ranging from tissue engineering to cancer research.[426,430-432] The investigation focused on how T-HESCs navigate these different surfaces, which play a crucial role in endometrial function and regeneration. Understanding their movement revealed insights into how endometrial cells interact with various materials, an essential aspect for implantation and wound healing applications.[433] Similarly, the migration of PHM1-41 cells, representing myometrial cells, was studied to understand their behaviour in pregnancy and labour, as myometrial contractility and cellular dynamics are critical factors in these processes.[434] Three critical parameters from the cell tracks were analyzed to provide a comprehensive view of the migratory patterns: average speed, displacement from the original position, and linear forward progression index (LFPI).

**T-HESCs:** In examining the cell tracks of T-HESCs, notable results were obtained (**Figure 6-7A**). The average speed was highest on pDA and pLNE, recording 5.6 ± 1.6 nm/s and 5.4 ± 1.5 nm/s, respectively, with both significantly surpassing the speeds on BSG at 4.8 ± 1.4 nm/s and pLD at ± 1.5 nm/s (**Figure 6-7B**). The speeds of pLNE and pDA were statistically similar to those of BSG and pLD, respectively. Regarding displacement (**Figure 6-7C**), T-HESCs on pDA exhibited the most significant displacement from the starting position (168 ± 75 µm), which was significantly higher than those on pLNE (156 ± 71 µm), pLD (149 ± 66 µm), and BSG (117 ± 56 µm). The LFPI (**Figure 6-7D**), a measure of the directness of cell migration, was lowest on BSG (0.54 ± 0.23), whereas the pCA surfaces were 0.64 ± 0.24, 0.65 ± 0.23 and 0.67 ± 0.22 for pDA, pLNE and pLD, respectively. Although pLNE was statistically similar to pDA and pLD, pLD was higher than pDA.

**PHM1-41s:** Analysis of the PHM1-41 cell tracks (**Figure 6-8A**) determined that the average speed of PHM1-41 cells was the lowest on BSG, with an average speed of 2.99 ± 1.25 nm/s. In contrast, cells moved quickest on pLNE and pLD, with averages of 4.38 ± 1.47 nm/s, followed closely by pLD at 4.32 ± 1.78 nm/s and pDA at 4.21 ± 1.58 nm/s. pLNE was significantly faster than pDA, whereas pLNE and pLD showed similar speeds (**Figure 6-8B**). Notably, pLD exhibited significant variability in distribution. Regarding the displacement from the starting position (**Figure 6-8C**), PHM1-41 cells on pLNE achieved the highest displacement (121 µm ± 57), which was significantly higher than that of both pDA (107 ± 59 µm) and pLD (108 ± 59 µm). The pDA and pLD values were similar between groups. Again, the displacements of all three polymer materials were significantly greater than that of BSG (83 ± 51 µm). The LFPI (**Figure 6-8D**) indicated that cells on pLNE, pLD, and pDA migrated more directly per their values of 0.63 ± 0.23, 0.61 ± 0.24, and 0.62 ± 0.12, respectively, when compared to those on BSG (0.54 ± 0.23).

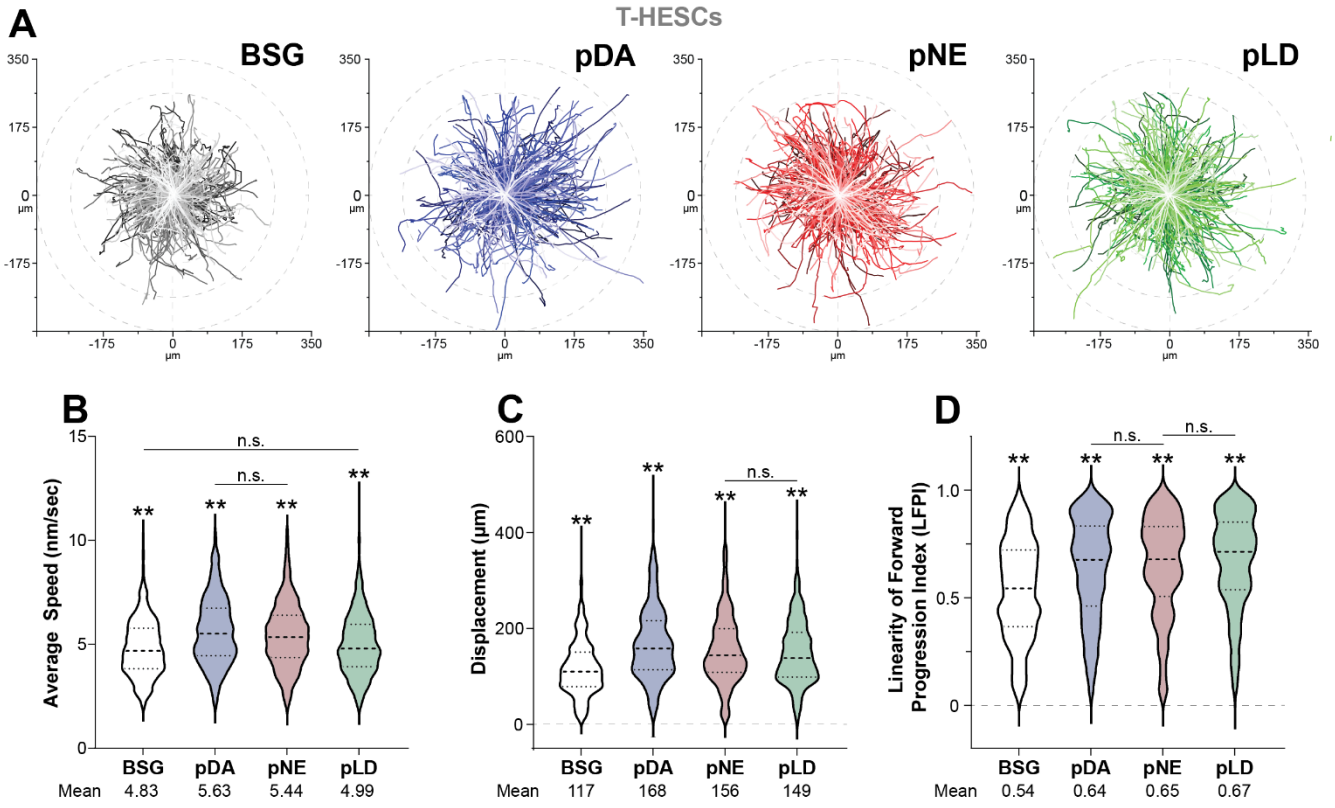


Figure 6-7: Single-cell migration dynamics of T-HESCs over 16 h.

**(A)** Trajectory plots depicting the individual cell paths. **(B)** Quantification of the average cell velocity. **(C)** Analysis of net displacement from initial position. **(D)** Evaluation of cell migration directness using the linear forward progression index (LFPI). ANOVA: *p < 0.05; **p < 0.01. The two asterisks (**) above the data indicate statistical significance compared to all other conditions unless indicated otherwise.

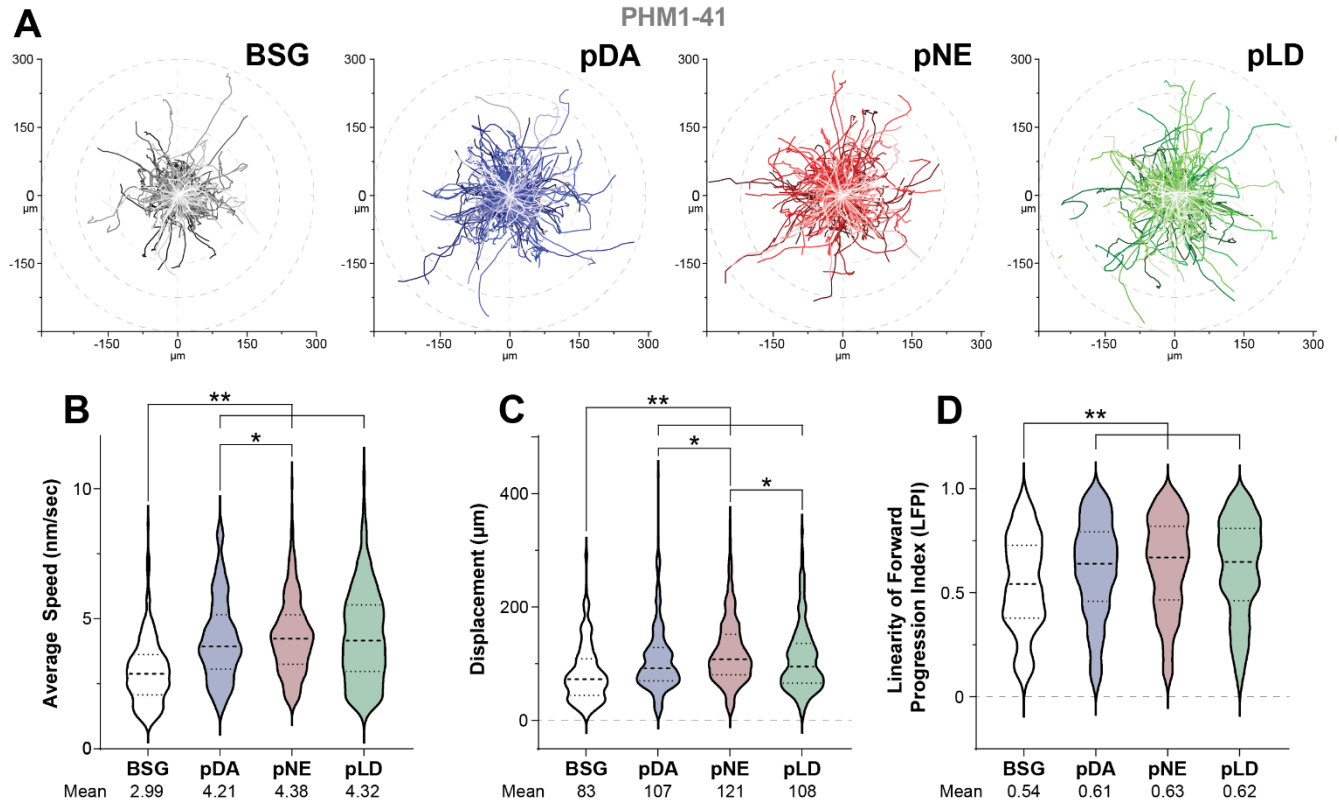


Figure 6-8: Single-cell migration dynamics of PHM1-41 cells over 16 h.

**(A)** Trajectory plots depicting the individual cell paths. **(B)** Quantification of the average cell velocity. **(C)** Analysis of net displacement from initial position. **(D)** Evaluation of cell migration directness using the linear forward progression index (LFPI). ANOVA: *p < 0.05; **p < 0.01. The two asterisks (**) above the data indicate statistical significance compared to all other conditions unless indicated otherwise.

#### 6.3.6.3 *DISCUSSION*

The divergent responses of T-HESCs and PHM1-41 cells to pLD, influenced by a complex interplay of biochemical and mechanical cues, along with the temporally matched adhesion rates observed for pDA and pLNE, underscores the necessity for a deeper examination of the underlying molecular mechanisms. FAs, acting as multimeric protein hubs, integrate signals from the extracellular environment and mediate cell adhesion and mechanotransduction, thus directing cell behaviour. Therefore, a detailed FA analysis further elucidated the specific interactions at the cell-substrate interface. Additionally, we assessed the migratory patterns of the cells by exploring the pCA substrate to understand how migration was influenced by the different biochemical and mechanical cues presented by the coatings. Examining FAs and cellular migration provides insights into the mechanisms governing cell behaviour on these substrates and can inform the design of biomaterials optimized for specific cellular responses.

Regarding the BSG condition, a consistent relationship was observed between T-HESC and PHM1-41 cell lines. For FA length, FA area, and FA coverage per cell, the cells cultured on BSG were longer and more extensive, with a higher 2D coverage than on the pCA substrate. Notably, while aspects including length and area were within 5% between cell lines for the pCA material, T-HESC length and area were 20% and 30% greater than the PHM1-41 cells when cultured on BSG. In the migratory analysis, both cell lines were least motile on BSG. They presented the lowest displacement and least efficient migration based on the Linearity of Forward Progression Index (LFPI). Additionally, T-HESCs were over 60% faster with 40% less displacement than PHM1-41 cells despite having a similar LFPI. The results for T-HESCs and PHM1-41 cells on BSG appear to be predominantly due to the rigidity of the substrate, as when compared to gels of different stiffnesses, very stiff materials like glass resulted in more significant FAs in similar size (length, area) and shape (FF) metrics.[58] In turn, these more numerous larger FAs, which result from increased mechanical resistance along the cell-substrate axis, can exert greater traction forces.[59] However, these FAs may also be more likely to exhibit stable traction (less dynamic tugging), which could hinder cells' ability to quickly adjust their dynamic traction via their adhesion points, potentially slowing their migration.[435] Additionally, in response to various stimuli (e.g., integrin engagement, growth factors, mechanical stress), tyrosine-mediated phosphorylation of paxillin, facilitated by focal adhesion kinase (FAK), promoted FA turnover.[436] With FAK inhibition predominantly impeding FA disassembly, its absence resulted in more stable and larger FAs with reduced cell migration.[437,438] In this context, while the stiffness of BSG supports the formation of large and numerous FAs, a lack of stimuli, such as limited adsorbed protein, may impair integrin activation and downstream FAK activity, resulting in large FA and lower turnover. Therefore, this contributes to the lower measured velocity, displacement, and efficiency in migration patterns for T-HESC and PHM1-41 cells under the BSG condition.

Material-dependent and cell-specific responses were observed when comparing pLNE and pDA conditions. In the context of FA attributes, the relationships between pDA and pLNE were consistent between cell types concerning the number of FAs per cell, FA length, FA area, and aspect ratio. pDA consistently had more FAs per cell, which were smaller in area and had a higher aspect ratio than pLNE. In contrast, the lengths of the FAs were statistically similar, suggesting that the stimuli that drove FA length were consistent in intensity between the substrates. However, we observed differences between cell types concerning cell coverage, where T-HESCs had equivalent coverage between pDA and pLNE, whereas PHM1-41 cells had a lower coverage of pLNE than pDA.

Interestingly, this mirrored the differences in the migration velocity. While T-HESCs had equivalent migration velocities between pDA and pLNE, PHM1-41 cells were faster on pLNE than on pDA. These results suggested that the PHM1-41 cells' lower coverage of FAs might be associated with a faster velocity, indicative of more transient and dynamic FAs. This comparison indicated that the best migration was not directly correlated with the highest density of FAs but, instead, an optimal amount based on a spatiotemporal feedback system.[439] Another notable difference was that T-HESCs were observed to displace significantly further on pDA than on pLNE and pLD. As pLNE and pLD are notably much smoother than pDA, this indicates that the texture of the surface has a more considerable influence on the migration distance, but not the speed, of T-HESCs. In contrast, PHM1-41 cells benefited more from the properties of pLNE, as both the velocity and displacement were more remarkable than those of pDA. Regardless, the benefits of pLNE were almost definitely underpinned by the similar ability of pDA to activate critical integrins, such as α5β1, whose activation was indicated in pDA coatings to benefit endothelial adhesion and hMSC migration through the activation of FAK signalling.[187,440,441]

In the context of pLD, unlike cell morphometrics, FA morphometrics and prevalence in both T-HESCs and PHM1-41 cells were similar across pCA substrates. Specifically, cells on pLD consistently presented FA counts identical to those observed on pDA, and these FAs were 6–10% longer and 9% larger in area. These results indicate that while the initiation and early reinforcement of cell adhesions on pLD were cell-specific, by steady state (24 h), both cell lines could equally form stable adhesions. Despite these similarities in FA morphometrics, the average speed of T-HESCs on pLD mirrored the slow velocities observed in BSG. This muted response of T-HESCs on pLD could be attributed to the specific interactions between cell integrins and their unique surface chemistry, particularly the–COOH groups, which may result in compromised protein adsorption, affecting integrin engagement and downstream signalling pathways, similar to those observed on BSG. While T-HESCs may have generated adequate and stable traction forces, limited integrin activation and the activity of critical mediators (e.g., FAK) likely influenced the observed larger FA length and area compared to pDA and pLNE.[437,438] Although these pathways supported a robust cell-substrate interaction, evident from the 18% lower length and 31% smaller area of FAs on pLD versus BSG, the subsequent stimuli necessary for FA turnover and effective

migration were insufficient, leading to a reduced velocity. [436] However, T-HESCs migrating on pLD demonstrated a 27% increase in displacement over BSG, aligning with pLNE, and with an LFPI 24% higher than BSG, comparable to other pCA surfaces. Conversely, PHM1-41 cells on pLD showed a 45% faster velocity than BSG, similar to pLNE yet faster than pDA. Nevertheless, the pLNE exhibited a more significant displacement than the pLD. This enhanced linearity efficiency could be attributed to the flat and uniform properties of the pLD, which might facilitate consistent cellular orientation and movement unaffected by the variability in substrate stiffness or texture, which could otherwise disrupt cell polarity. These results suggest that the mechanisms that drive initial adhesion are shared by those that potentiate velocity and are impaired in T-HESCs on pLD. In contrast, the factors influencing migration efficacy, measured by displacement and velocity consistency, were not compromised.

## 6.4 CONCLUSION

Functional polymeric substrates were successfully generated when pCA substrates were developed on acid-etched borosilicate glass. The pDA substrates displayed a relatively unremarkable topography and contact angle, which was in line with expectations and was characterized by a complete coverage of pDA aggregates. In contrast, substrates of pLNE and pLD demonstrated significant reductions in hydrophilicity and featured incomplete coverage, thereby exposing a super-adhesive underlying film. Common across all substrates, this film is likely driven by forming DHI, a shared intermediate or product of the reaction mechanisms involved, recently identified as a critical adhesive driver in pDA systems.[150] Our analysis confirmed that the exposure of this adhesive layer primarily contributed to the global adhesion differences observed between pLNE and pLD substrates, as variations in aggregates and film adhesion were not significantly different between substrates when assessed by AFM. This determination supported the concept that an initial thin adhesive film, likely DHI-based, is crucial for initial pCA adhesion coatings, subsequently attracting more complex oligomers during the maturation of the substrate.[135,150] pLNE substrates, influenced by the presence of DHBA, exhibited reduced aggregate formation, which led to less aggregate adsorption and enhanced exposure of the adhesive film. However, this also implied a trade-off between adhesiveness (due to the film) and texture/roughness (due to aggregates), but to what degree and how this may be tuned remains to be determined. Meanwhile, pLD substrates that can readily form particles in free solution also appeared to produce a DHI-based film.[147] However, the –COOH groups on these particles, whether through steric or electrostatic effects, inhibited their particle adsorption onto the surface. Moreover, the film appears enriched with –COOH groups, which can reduce the adsorption of negatively charged residues or larger residues that depend on interactions with the amine group in the pyrrole ring of pLD substituents (e.g., dopachrome). This character resulted in a thin pLD film that offered high adhesion and potential for functionalization but demonstrated poor protein adsorption — attributes that may make it a great functional candidate for cohesive bonding with anti-fouling capabilities.

In exploring pCA surfaces for cell interactions, distinct behaviours were observed between T-HESCs of the endometrium and PHM1-41 cells of the myometrium. Both cell types exhibited a more rapid cell spreading on pDA and pLNE, with pLNE surfaces facilitating the quickest initiation response. This fast spreading on pLNE was attributed to its superior adhesive characteristics, which may enhance protein adsorption, which is crucial for integrin-mediated cell attachment and spreading. Despite pDA's increased roughness providing a larger surface area, its textural complexity might not significantly improve biomolecule interactions to the same degree as the adhesive character of pLNE. This difference in the initiation of cell spreading is particularly noteworthy in T-HESCs, suggesting that the differences in proliferation between pDA and pLNE surfaces may be the result of the speed to which the cells can reach a basal state and reinitiate cell proliferation and with the material properties after that minimally affecting proliferation rates. The similarity in migration data between pLNE and pDA surfaces points to a possible equivalent activation of critical pathways such as FAK/PI3K/AKT and RhoGTPase, which are essential for migration and proliferation.[28,283,442]

For PHM1-41 cells, smooth muscle cells with a slower division rate, differences between pDA and pLNE became apparent only after five d. This delay in observable differences might be due to the slower nature of PHM1-41 cells responding to environmental stimuli or perhaps stimuli that can increase in effect with increased cell number (e.g., confinement). However, they are pronounced once differences manifest, with PHM1-41 cells showing higher migration speeds and more significant displacement on pLNE than on pDA. This difference suggests a more robust activation of the migration and proliferation pathways on pLNE, which could drive the observed differences in proliferation rates.

Interestingly, T-HESCs were relatively unresponsive to pLD regarding initial adhesion and migration speed. However, they still managed to generate well-formed FAs, indicative of adequate traction and potential for reinforcement. This ability to form consistent FAs despite poor initial adhesion suggests a unique compensatory mechanism in T-HESCs, possibly driven by FA stability rather than the immediate adhesive environment. Both T-HESCs and PHM1-41 cells showed a proliferation increase of about 10% by Day 5 on pLD, suggesting that the stability of FAs may play a significant role in supporting cell proliferation, independent of initial adhesion or migration dynamics.

In conclusion, this investigation into the interaction of T-HESC and PHM1-41 cells with pCA polymers, namely pDA, pLNE, and pLD, has revealed critical insights into their material properties and biocompatibility. Through detailed examinations of the surface properties, including topography and structurally segmented adhesion characteristics, these findings support the strategic design of biomaterials based on optimizing features, including hydrophilicity, roughness, and biochemical functionality. Subsequently, we have shown that these properties can induce uterine cell-specific and non-specific responses in cellular behaviour, including adhesion, proliferation, FA morphodynamics, and migration. By harnessing these determined attributes, we may

better tailor material surfaces of future pCA materials to meet the precise needs of uterine tissue engineering, potentially improving therapeutic outcomes in reproductive health applications.

## 6.5 ACKNOWLEDGEMENTS

This work was supported by the Natural Sciences and Engineering Research Council (NSERC) through the Discovery grant, by the Canada Foundation for Innovation (CFI) and the Ontario Ministry of Research and Innovation (MRI) through the Leaders of Opportunity (LOF) fund.

## 6.6 MATERIALS AND METHODS

### 6.6.1 SAMPLE PREPARATION

12 mm borosilicate glass coverslips (#1.5, Fisher Scientific, USA) were ultrasonically cleaned in toluene and rinsed three times with distilled water (DI). Coverslips were then etched in 1N HCl at 60 °C for 4 h to generate a hydrophilic control surface with improved wettability and adsorptive capacity and washed three times in DI. Unmodified etched coverslips were used as the base borosilicate substrate (BSG). All samples were sterilized in 70%-EtOH for 30 minutes.

The polycatecholamine (pCA) substrate to be used is based on the following precursors: dopamine (DA; Sigma Aldrich), L-norepinephrine (L-NE; Sigma Aldrich, USA), and L-DOPA (LD; Fisher Scientific, USA). Fabrication of pCA substrate, denoted as pDA, pLNE and pLD, precursor concentrations were 1 mg/mL of precursor in 10 mM Tris-HCl (pH=8.6, Sigma Aldrich). Samples were covered from light during the 24 h coating period at RT (25 °C); surfaces were immediately washed with DI and sterilized three times. Washing with DI first is necessary, as subsequent immediate use of EtOH was observed to produce stochastically rougher substrates. This effect is likely due to the polar nature of ethanol, which generates repulsive forces between the pDA aggregates and the solvent, promoting uneven adherence and potential embedding of the aggregates into the underlying substrate.

### 6.6.2 ATOMIC FORCE MICROSCOPY

Atomic force microscopy (AFM) analysis was performed on an alpha300 RSA system (WITec, Germany) that is capable of non-resonant, intermittent-contact Digital Pulsed Force Mode (DPFM) and Non-Contact (NC) modes. Topographical imaging was performed with NC-AFM, and adhesion was measured in DPFM mode.

NC-AFM mode was employed to collect high resolution (256 × 256) 5 × 5 µm maps using the rectangular $Si_3N_4$ cantilever of the RTESPA-300 chip (Bruker) characterized by a pyramidal tip with a nominal radius ($r_{nom}$) of 8 nm, spring constant ($k_{nom}$) of 40 N/m and nominal frequency ($f_{nom}$) of 300 kHz. In addition, 3D reconstruction and analysis of morphological characteristics, including roughness (RMS), is performed in Gwyddion.[332]

DPFM acquisition utilizes the rectangular $Si_3N_4$ cantilever of the MLCT chip (Bruker, USA) characterized by a rotated pyramidal tip with a nominal radius ($r_{nom}$) of 20 nm, spring constant ($k_{nom}$) 0.6 N/m and nominal

frequency ($f_{nom}$) of 125 kHz. 5 × 2 µm high-resolution maps (256 × $10^5$) was collected to provide upwards of 2.69 × $10^4$ force-distance curves to be analyzed. Processing and analysis were performed in WITec Project 4 (WITec, Germany). Global adhesion was determined following slope background subtraction and error (scar) correction. Subsequent segmentation between the adsorbed aggregates and film was done manually using the topography channel to isolate the film and produce drawfield masks. The inverse field was used to make the aggregate drawfield masks. Those masks were used to isolate the requisite DPFM curves to calculate the average adhesion per component per image.

### 6.6.3 WATER CONTACT ANGLE (WCA) GONIOMETRY

The static water contact angle (WCA) was measured with a VCA Optima Surface Analysis System (AST Products Inc., USA) after samples were rinsed and vacuum-dried for 16 h. A (1 µL) drop of deionized water was ejected from a micro syringe (Hamilton Company, USA), a picture was taken, and a manual outline of critical points of the droplet was performed to ensure accuracy before automated measurement of the angle. Three droplets were measured per sample, three samples per experiment. Experiments were carried out in triplicate.

### 6.6.4 CELL CULTURES

All cell cultures were maintained in a 5% $CO_2$, 37 °C water-jacketed incubator. Charcoal-dextran (C/D) filtered FBS (C/D-FBS, Corning) was used for both T-HESC and PHM1-41 cell culture as C/D filtration removes any free hormones or hormone-protein complexes, particularly estrogen. Chemical dissociation from the substrate was achieved using the recombinant enzyme TrypLE (ThermoFisher, 12604021) to reduce unintentional enzymatic degradation and retain the integrity of cell surface antigens when compared to Trypsin-EDTA. All media and dissociation products were free of phenol-red (phenolsulfonphthalein), as it acts as a weak analogue to estrogen[443] and can mimic estradiol in both *in vitro* and *in vivo* conditions.[444]

T-HESC cells were cultured in a 50:50 mixture of phenol-red free DMEM and Ham's F-12 (DMEM/F12, ThermoFisher), ITS+ premix supplement (1%, Corning), 1 mM additional GlutaMAX (ThermoFisher), 10% C/D-FBS, and the selection antibiotic puromycin (500 ng/mL, ThermoFisher). The ITS+ premix contains **i**nsulin, human **t**ransferrin, **s**elenous acid, bovine serum albumin (BSA) and linoleic acid to support defined culture media. Specific formulation details of the complete culture media are described in **Table A-1**.

PHM1-41 cells were cultured in phenol-red free DMEM with 4.5 g/L glucose (ThermoFisher) with the addition of GlutaMAX (6mM), sodium pyruvate (1 mM, ThermoFisher), 10% C/D-BS and the selection antibiotic Geneticin (G418, Gibco). Specific formulation details of the complete culture media are described in **Table A-2**.

### 6.6.5 PRESTOBLUE PROLIFERATION ANALYSIS

PrestoBlue (PB) was employed as a non-destructive resazurin-based microplate assay to determine cell viability at study-specific time points. Tetrazolium-based assays (e.g., MTT) were avoided due to their propensity to

provide inaccurate results when used with pDA surfaces.[445] In cell-specific culture media, 400 µL of fresh 10% PrestoBlue (ThermoFisher, A13262) was prewarmed to 37 °C and administered to each well in a 24-well plate. Plates were incubated at 37 °C for 120min after gently mixing the media, and 3 × 100 µL samples were transferred to a 96-well F-bottom plate. Absorbance was read on a BioTek Synergy H1 microplate reader (Agilent, USA) at $\lambda_{ex}$=570 nm and $\lambda_{em}$=600 nm.

### 6.6.6 FIXED IMAGING

After specific experimental intervals, cells were fixed at room temperature with 4%-PFA for 10 minutes, washed with 1× PBS three times and permeabilized with 0.2% Triton-X100 (Sigma-Aldrich) for 10 minutes. Nuclei were stained with a 1:1000 dilution of 1 mg/mL Hoechst 33342 (ThermoFisher), and the actin cytoskeleton was stained with manufacturer-suggested concentrations of via Alexa Fluor 568 conjugated to Phalloidin (ThermoFisher). To visualize the focal adhesions (FAs), we labelled Vinculin with a 1:400 mouse monoclonal Anti-hVIN1 (Sigma Aldrich, V9131) as the primary antibody and 1:600 Goat anti-Mouse IgG conjugated to Alexa Fluor 488 (ThermoFisher, A11001) as the secondary antibody. The proliferative marker Ki67 was stained using the primary antibody was a 1:300 rabbit monoclonal recombinant Anti-Ki67 antibody (Abcam, ab16667) with a 1:600 Donkey anti-Rabbit conjugated to Alexa Fluor 647 (ThermoFisher, A31573) as the secondary.

Multi-channel images were captured with an AxioObserver.Z1 inverted microscope (Zeiss) fitted with the Zeiss Filter Set 49 ($^{365}/_{445}$, Hoechst 33342), Zeiss Filter Set 38 HE ($^{470}/_{525}$, Alexa Fluor 488), Filter Set 64 HE ($^{585}/_{647}$, Alexa Fluor 568) and Zeiss Filter Set 50 ($^{640}/_{690}$, Alexa Fluor 647). Mid-magnification tiles of the surfaces were imaged with a 20× LD Plan-Neofluar Objective (NA = 0.4, Zeiss) to assess Ki67 and actin-based morphology. High-magnification tiles of the surface were imaged with a 40× EC Plan-Neofluar Objective (NA = 0.8, Zeiss) for high-resolution imaging of advanced cell structure and FAs. Image collections were collected and stitched with the Zen 2 software (Zeiss).

The quantification of cell morphology (i.e., area, eccentricity, form factor) was performed with custom pipelines in CellProfiler.[311] Cell area was calculated by counting the scaled number of pixels within the measured cells, and values were normalized to the area of the BSG condition. The eccentricity index (*ecc*), an ellipse model of circularity, was measured for cells. It is calculated by determining the distance ratio between the ellipse's focal length and the primary axis length. A perfectly circular object has an *ecc*=0 and a line segment, *ecc*=1. The form factor (FF) is a measure of shape irregularity, was measured and is defined as "$4 \times \pi \times (\text{area}/\text{perimeter}^2)$". A perfectly round object has an FF=1, whereas one with jagged contours has an FF<1.

Regarding cell morphology, a lower FF represents increased protrusiveness. Quantification of FAs was achieved using a custom pipeline in CellProfiler that enabled individual FA analysis (e.g., length, area, aspect ratio) and between-cell comparisons (e.g., number of FAs per cell, FA coverage per cell). Data sets were tested with the parametric two-way ANOVA with Tukey's HSD post hoc test for mean comparisons, and statistical

significance is defined as * = $p < 0.05$ and ** = $p < 0.01$. Analyses are performed with GraphPad Prism 8 (GraphPad Software, Inc.) and OriginPro.

### 6.6.7 SINGLE-CELL MIGRATION

Live cell imaging for single-cell migration and wound healing assays were performed on an AxioObserver.Z1 with a live-cell apparatus to maintain 37 °C and 5% $CO_2$. Images were captured through a 10× EC Plan-Neofluar Objective (NA = 0.3, Zeiss). Before imaging, the system was preheated for 3 h to ensure thermal stability and mitigate effects, including thermal drift. Visualization of T-HESC and PHM1-41 cells was achieved with CellTracker Red CMTPX dye (CT[Red], $^{577}/_{602}$, Invitrogen) and Zeiss Filter Set 43 ($^{545}/_{605}$). 10 mM stock solution was diluted to 1.5µM in respective serum-free media (SFM). Following 24 h after seeding on experimental surfaces (T-HESC: $1 \times 10^4$ cells/cm$^2$; PHM1-41: $0.8 \times 10^4$ cells/cm$^2$), cells were rinsed and incubated with prewarmed SFM-CT(Red) and incubated at 37 °C for 30 min. SFM-CT(Red) was removed, cells rinsed, fresh complete media added, and cells were left to equilibrate on the microscope stage for 60 min before imaging. Automatic tracking was performed using the TrackMate 7.10.0 in FIJI,[446] using the LoG spot detector and Simple Lap tracker. Tracks were processed in OriginPro.

# 7 SUMMARY AND FUTURE DIRECTIONS

This thesis explores the interactions between human cells and various biomaterials, ranging from nanotubular titanium structures to polycatecholamine polymers. This research investigates how these materials influence cellular responses, emphasizing the significance of material properties such as micro/nanostructure, composition, topographical, and mechanical properties. Detailed studies first demonstrate how Ti substrates can be modified by (*i*) fabricating spatially structured nanotubes to enhance stem cell adhesion, proliferation, and differentiation, highlighting the critical role of nanotopographical cues in directing cell fate, and (*ii*) applying pulsed-water jet technology to titanium surfaces to reveal osteogenic potential and biocompatibility enhancements suitable for dental implants. Subsequently, we focused on the unique chemistry of CA precursors by (*iii*) further investigating the concentration-influenced temporal dynamics of pCA polymerization and (*iv*) assessing their biological activity in the uterine context, with assessments ranging from proliferation to migration. This comprehensive research advances our understanding of material synthesis, cell-material interactions, and their application to biomaterials to be tailored for specific therapeutic applications, aiming to optimize outcomes in tissue engineering and regenerative strategies. A more detailed summary of each study is as follows.

In **Chapter 3**, our paper titled "**The implication of spatial statistics in human mesenchymal stem cell response to nanotubular architectures**" takes a unique approach to exploring the interaction of human mesenchymal stem cells (hMSCs) with $TiO_2$ NT architectures. This study introduces a novel application of spatial statistical analysis to systematically characterize the geometric and structural parameters of NTs, such as diameter, wall thickness, nearest neighbour distance, and surface entropy and correlates these parameters with cellular responses. The key findings demonstrate that the detailed architecture of the nanotubes significantly affected hMSC adhesion, proliferation, and osteogenic differentiation. Notably, this study highlights how specific nanotubular dimensions influence the nuclear localization of osteogenic markers, pointing to a direct relationship between nanotopographical cues and stem cell fate. Furthermore, using two-tiered nanostructures introduces a hierarchical complexity that mimics the natural bone architecture more closely, thus enhancing the biological efficacy of the implant surfaces.

In **Chapter 4**, our paper called "**Direct cueing by pulsed-waterjet treated titanium on fibroblast, osteoblastic and human stem cells for prospective use in dental implants**" assesses the application of Pulsed-Water Jet (PWJ) technology for preparing titanium surfaces for dental implants, offering a contaminant-free method that enhances osseointegration. This study investigated the biocompatibility and osteogenic potential of PWJ-treated titanium using Saos-2 cells, NIH/3T3 cells, and hMSCs. Key findings include differential proliferation effects on Saos-2 and NIH/3T3 cells depending on the treatment conditions, with significant enhancement in osteoblast-like cell proliferation under specific surface roughness parameters. Furthermore, the

nuclear localization of osterix in hMSCs highlights the osteogenic potential of specific Ti topographies. This study highlights the efficacy of PWJ technology in creating bioactive, cost-effective, and environmentally friendly surfaces for dental implants, supporting its potential application in supporting periodontal health through accessible and sustainable manufacturing.

In **Chapter 5**, our study entitled "**Characterization of kinetics and particle formation in polymers derived from dopamine, levodopa, L-norepinephrine, and racemic norepinephrine**" examines the polymerization and particle formation dynamics of CA-derived polymers, pDA, pLD, pLNE, and pRNE, at varying concentrations. Utilizing dual-wavelength absorbance-based analysis, our research elucidates the significant differences in the kinetics and behaviour of these materials under different conditions, highlighting the influence of chirality and precursor concentration on the properties of the resulting polymers. Notable findings include the distinct polymerization behaviours of pLD owing to its hydrophilic nature and the complex interplay of concentration and chiral effects in pLNE and pRNE systems. Additionally, this study introduces the Polymer Dispersion Ratio (PDR) as a novel metric for understanding polymer aggregate dynamics, further contributing to the synthesis of these materials and their potential biomedical applications. This study provides valuable insights into the design of advanced catecholamine-based biomaterials through detailed kinetic analysis and particle characterization for various therapeutic purposes.

In **Chapter 6**, our study dubbed "**Endometrial stromal and myometrial bioactivity analysis of polydopamine, poly-L-norepinephrine and polylevodopa coatings: from proliferation to migration**" investigates the bioactivity of pCA polymers, specifically pDA, pLNE and pLD, within a uterine context using human endometrial stromal cells (T-HESCs), which represent the endometrium, and pregnant human myometrial smooth muscle cells (PHM1-41), which represent the myometrium. This research focuses on the cellular responses to these biomaterials, examining aspects such as cell proliferation, morphology, and migration on polymer-coated substrates. Significant findings demonstrate that these polymers distinctly influence cell behaviours: pDA and pLNE promote notable enhancements in proliferation and migration, particularly for PHM1-41 cells, whereas pLD showed a divergent effect, supporting cell adhesion, morphological changes and migration more significantly in PHM1-41 cells than in T-HESCs. Additionally, this study explores the material properties of the polymers, highlighting discoveries such as the structure-based adhesion characteristics and mechanical properties of pDA, which exhibit a complex interplay of adhesion forces influenced by its surface roughness and microstructure. These material-specific responses and differential cellular interactions underscore the potential of pCA polymers to be tailored for specific therapeutic applications in uterine tissue engineering to optimize regenerative outcomes by leveraging the distinct properties of each polymer to cater to the intricate requirements of different uterine cell environments.

**IN SUMMARY**, this thesis elucidates not only the intricate relationships between biomaterials and cellular responses but also pioneers novel approaches to manufacturing (e.g., multi-hierarchical NTs, PWJ-based surface preparation) and design (e.g., concentration-based high temporal resolution kinetics of pCA synthesis) that can significantly advance biomaterials science and engineering. The research presented collectively enhances our understanding of how tailored material properties, from ceramic nanostructures to polymer chemistry, can be strategically leveraged to direct cell behaviour in predictable and beneficial ways. Future endeavours will focus on refining the integration of these biomaterials into complex biological systems. These opportunities include enabling and pursuing the study of higher-order phenomena to uncover discrete mechanisms and behaviours that will inform future designs and potential applications in multi-tissue contexts for healing and regeneration. To this end, the following section will outline four primary directions: (*i*) protein adsorption studies to better understand the adsorptive character of the pCA materials for not only overall adsorption but also specificity; (*ii*) DPFM-AFM in aqueous solutions on adhesive polymers to improve our nanoscale topomechanical analysis to better represent in vitro conditions; (*iii*) wound healing methodologies for soft polymers, to expand our understanding of collective wound closure when delicate materials are employed, and classical methods are inadequate; and (*iv*) the development of polycatecholamine copolymers, utilizing base CA precursors or specific derivatives to manufacture bespoke 2D/3D materials with potential for scaled functionalization and topomechanical properties.

## 7.1 FUTURE DIRECTIONS

### 7.1.1 PROTEIN ADSORPTION STUDIES

Protein adsorption is crucial for cellular adhesion, spreading, and differentiation.[60] It creates a biological interface on material surfaces that mediates interactions between cells and biomaterials, essential for tissue regeneration and implant integration. Chapter 6 discusses cell-specific responses to pCA materials synthesized from chemically distinct precursors. Evaluating how these surfaces compare their adsorptive character is essential, especially if the aim is to delineate the impact of physical properties (e.g., topography) on chemical properties. Notably, the pLD substrate features –COOH groups that become anionic –$COO^-$groups at physiological pH, likely influencing the adsorption dynamics. Therefore, knowing that there are impacts on surface charge and distribution, studying protein adsorption from cationic (e.g., VEGF) and anionic (e.g., fibronectin, albumin) perspectives is advisable. Furthermore, it has been documented that variations in surface roughness alone elicit differential increases in biomolecule adsorption.[420] Specifically, augmenting the roughness from 2 nm to 32.9 nm resulted in a 20% enhancement in bovine serum albumin (BSA) adsorption. Conversely, fibronectin adsorption exhibited a more pronounced increase of 70%, prompting the consideration of protein anisotropy in complex biomolecules. Consequently, considering both the charge and molecular complexity, a comprehensive approach is essential to

elucidate how these surfaces influence the adsorption of various model proteins. The four possible methods with increasing complexity are as follows.

1. **Adsorption with fluorescently tagged protein:**[447] An accessible method is fluorophore-tagged protein (e.g., FITC-conjugated BSA). Following incubation and rinsing, microscopic images were taken at the appropriate channel to ensure that the exposure times and distance to the substrate were consistent. The fluorescence intensity was then integrated into the measurements. Limitations include the fact that this method is semi-quantitative and subject to concerns, including the maintenance of exact and consistent sample distances and the thickness of the focal plane, which limits accurate readings of a sample with an irregular morphology (e.g., aggregates). Additionally, adding a conjugate fluorochrome may affect the adsorption behaviour, particularly in cases where steric hindrance impedes access to the adsorptive functional groups. For example, in pLD, the carbonyl group on the β-carbon may sterically hinder the accessibility of the amine group.
2. **Fluorescamine assay:**[448] This experiment exploits fluorescamine, a molecule that reacts with primary amines in the protein, forming a fluorescent product with an $^{ex}/_{em}$ of $^{385}/_{465nm}$. A solution with a known target protein concentration (BSA) was incubated with the material to be studied. The supernatant was then recovered, the solution was reacted with fluorescamine, and the protein concentration was compared with the concentration without the material. These limitations include their potential to interact with secondary amines. In addition, variations between proteins may lead to confounding results when testing the adsorption of multiple model proteins. For instance, those with a higher lysine content may exhibit increased fluorescence, potentially leading to an overestimation of protein concentration.
3. **Surface plasmon resonance (SPR) sensor:**[449] SPR is a sensitive technique for real-time monitoring of biomolecular interactions. When light hits a thin metal under total internal reflection, it excites the electrons at the surface to oscillate, creating a surface plasmon. When biomolecules adsorb onto the chip surface, the local refractive index (RI) changes, altering the resonance of the surface plasmons. The SPR sensor measured this difference. One advantage of this method is that it can be used without any labels (e.g., antibodies) and monitored in real-time, providing quantitative data on the rate of adsorption and protein binding capacity. A significant limitation is the potential inaccuracies caused by uneven or non-uniform coatings, particularly on surfaces with aggregates (e.g., pDA). The cost of the equipment and SPR chips is also a concern.
4. **Liquid chromatography-mass spectrometry (LC-MS):**[5] LC-MS combines the physical separation capabilities of liquid chromatography and mass spectrometry. In this context, protein adsorption can be quantified by comparing the protein concentrations in a solution before and after contact with the substrate. In this approach, a known volume of the protein solution is incubated with the surface,

allowing proteins to be adsorbed. The solution was analyzed using LC-MS to detect and quantify proteins not adsorbed onto the surface. The differences in protein concentration relative to the control solution directly measured the amount of adsorbed protein. One advantage of LC-MS is its high specificity and sensitivity, which allows for precise identification and quantification of a wide range of biomolecules. However, the limitations include the potential for protein degradation during analysis and the requirement for extensive sample preparation.

### 7.1.2 DPFM-AFM IN AQUEOUS ENVIRONMENTS

The material analysis in Chapter 6 revealed distinct mechanical properties among the pCA polymers, particularly the roughness and adhesion. Crucially, these experiments highlighted the uncovered hierarchical structures that exhibit specific adhesive characteristics. Digital pulsed force mode (DPFM)-AFM (tapping mode) was used to capture the topography and mechanical properties to elucidate these structure-specific differences. However, these measurements were conducted in the air owing to cantilever oscillation from detachment inducing destructive noise in liquid environments. In the limited trials conducted in liquid, the notably strong adhesion of the pLNE and pLD substrates resulted in more forceful detachments, which generated significant noise and hindered the acquisition of high-quality images. Notably, the WITec RSA300 system used in this study was predominantly used in non-aqueous settings. Other AFM setups, such as JPK NanoWizard, are more commonly used in aqueous environments for cells and would be more appropriate for this use case. Considerations include:

1. **Environmental**: The liquid parameters used for the experiment are of particular concern, particularly the dissolved gases, pH, and temperature. Degassing the liquid before use in AFM experiments is crucial for minimizing the presence of air bubbles, which can interfere with the movement and oscillation of the cantilever, leading to noise and artifacts in the data. The pH of the liquid should be as close to physiological as possible while remaining stable, as it can influence the ionic character of the substrate, which the use of HEPES can assist. The temperature must also be stable, as it can cause thermal drift and alter the properties of the cantilever, affecting the sensitivity and accuracy of force measurements.
2. **Electrostatic interactions**: Long-range electrostatic forces can significantly impact the quality and reliability of AFM measurements. Adding KCl (500 mM) can be beneficial for increasing the ionic strength of the liquid, which can help screen these electrostatic interactions.
3. **Cantilever selection:** The most consequential consideration is the selection of the cantilever, precisely, aspects such as its spring constant ($k$), resonance frequency ($f$), and tip shape/size.

   Like imaging soft polymers in air, a lower spring constant is advisable to reduce destructive forces and increase sensitivity. However, the lower the spring constant ($k$), the more susceptible it is to

environmental noise, often preventing detachment from an exceedingly adhesive substrate. Our experience required a value of 0.6 N/m; a typical suggested range is 0.3–0.06 N/m in this context.

Regarding the resonance frequency, a lower frequency reduces the hydrodynamic drag, which can lead to a lower force sensitivity and increased noise. Additionally, immersion in the liquid dampens the frequency, an effect that must be considered when selecting an ideal resonance frequency (*f*). Our work utilized *f*=125 kHz, although the typical range can be 30–90 kHz in air.

A sharper tip is preferable for dimensional accuracy regarding the tip shape and size. However, sharper tips are more prone to variations in wear and tear. Pyramidal tips are commonly used; however, the tip angle (front, back, side) is essential in considering the penetration potential of the tip and is vital in estimating the contact area for contact-mechanics-based calculations of material properties. Tall circular symmetric tips are an excellent choice. While spherical and colloid tips help measure bulk interactions, this can reduce dimensional sensitivity, particularly in the tapping mode, where the correlation between topography and mechanical properties is desired. In addition, these tips are prone to contamination. Moreover, the size (e.g., 5–20 µm) and material (e.g., PS and BSG) can introduce substantial weight on the tip end and additional hydrodynamic drag and noise.

### 7.1.3 WOUND HEALING ON SOFT POLYMERS

To effectively recapitulate the *in vivo* wound healing process, it is imperative to transition from studying single cell to collective cell morphology. Collective cell migration, a crucial aspect of development and tissue repair, involves the coordinated movement of cell groups and fundamentally differs from single-cell migration.[429] This coordinated behaviour is influenced by environmental mechanical and biochemical cues, which affect cellular processes such as adhesion, migration, and mechanosensing.

Traditional methods, such as the scratch assay, which involves creating a wound, typically around 500 µm, in a cell monolayer using a pipette tip (e.g., 200 µL pipette tip) or a blunted needle (e.g., 25g), are not suitable for soft polymers used in our experiments, because they damage the material. An alternative method is to use PDMS-based barriers.[450] To this end, we investigated the design and fabrication of 3D-printed moulds to allow the casting of custom PDMS barriers that permit the closure and expansion of collective cell migration. Notably, we wanted to expand upon cutting a PDMS block for rectangular barriers and enable high-content imaging by producing inserts for use in 24-well and 96-well plates. These attempts used different 3D fabrication methods (FDM and SLA) and fixation methods (pressure and magnetic), as described below.

1. **3D-printed moulds, fused deposition modelling (FDM)**: Initial attempts involved using FDM to create PLA-based moulds intended for PDMS casting, thereby facilitating wounding assays (**Figure B-1**). However, the horizontal striations inherent to layer-by-layer filament deposition complicate the PDMS

extraction process (**Figure B-2**). Additionally, the mould's inability to form a perfectly flat base resulted in irregular sides on the PDMS inserts, compromising their capacity to maintain a watertight seal when positioned in a multi-well plate. A method with better dimensional accuracy is required.

2. **3D-printed moulds, stereolithography (SLA)**: A strategic pivot to stereolithography (SLA) facilitated the production of resin-based moulds, achieving higher dimensional accuracy and surface smoothness. This improvement significantly enhanced the quality of inserts for 24-well and 96-well plates, which were designed to generate pores (**Figure B-3**). Despite these advancements, maintaining sufficient pressure to achieve a watertight seal remains challenging. Additionally, controlling the pressure to normalize the compressive force on the substrate was not possible. A method other than pressure fitting is required.
3. **Magnetic cell culture inserts:** Another pivot involves the development of magnetic inserts incorporating magnetite into PDMS. To facilitate a stable and consistent magnetic field application, holders of 24-well and 96-well plates were designed and fabricated (**Figure B-4**). The subsequent testing of these magnetite-PDMS inserts is shown in **Figure B-5**. However, concerns regarding adequate sealing, magnetite leaching, and overall stability resulted in the abandonment of this approach, which favoured focusing on research studies rather than methodological development.

Whether through the continuation or design of a different approach, the fabrication of PDMS inserts would enable the study of wound healing on soft substrates, such as the pCA polymers investigated in this thesis. Future studies should focus on preventing leaching, improving the insert/substrate interface, and optimizing the magnetite concentration to modulate the compressive force.

### 7.1.4 POLYCATECHOLAMINE COPOLYMERS

Advanced biomaterials require a proper design to ensure biocompatibility, functional versatility, and mechanical stability. Capitalizing on the chemical similarities of precursor molecules and shared intermediates, there exists a future opportunity to incorporate three different catecholamines (NE, LD, and DA) into a single, multifunctional surface coating. The approach would use molar ratios, indicated as a polyNLD coating with the ratios expressed as NE:LD:DA precursors (e.g., 1:2:1). Furthermore, enzyme-mediated polymerization, particularly with **tyrosinase**, improves the control over the reaction rate and subsequent products.[346] The reasoning for the inclusion of the components is as follows:

1. **NE (base)**: Provides a stable, flat substrate, enhancing the uniformity and integrity of the coating.
2. **LD (functionalization)**: The Inclusion of –COOH-containing pLD intermediates (e.g., dopachrome) enables functionalization for targeted biological interactions, including conjugation of proteins (e.g., RGD-containing peptides), drugs (e.g., dexamethasone), and other bioactive molecules (e.g., carbon nanodots).

3. **DA (surface morphology modifier)**: Modifies surface topography to enhance cellular adhesion and integration within biological systems through controlled roughness. Additionally, DA rapidly oxidizes and may act as an initiator or modulator of reaction kinetics.

Optimizing the molar ratios and kinetics can enhance our understanding of the polymerization processes governing pCA materials. This approach can potentially facilitate the development of coatings that improve the functionality and performance of medical devices for various applications, including cardiovascular and orthopedic devices, wound care, and biosensors.

Precursor substitution is an option for better-controlled and more predictable reactions and materials. Each precursor undergoes oxidization followed by cyclization, with different rates between precursors.[150] Substituting precursors with already cyclized products reduces the variability in reaction mechanisms and improves uniformity. The suggested substitutions are detailed below and visualized in **Figure 7-1**.

1. **DA** with **5,6-dihydroxyindole (DHI)**: This intermediate is believed to be integral for adhesion and may be the backbone of the initial adhesive film.
2. **NE** with **3,4-Dihydroxybenzaldehyde (DHBA)**: The intermediate responsible for reducing the aggregate formation and enabling the "ultra smoothness" of pNE. However, a monomer component may be required to form the DHBA-NE complexes. NE is preferred as it is slower to oxidize than DA and is, therefore, more likely to be integrated into these dimers.
3. **LD** with **5,6-dihydroxyindole-2-carboxylic acid (DHICA):** The intermediate similar to DHI in structure but with –COOH group on its β-carbon, allowing for functionalization (e.g., EDC/NHS)

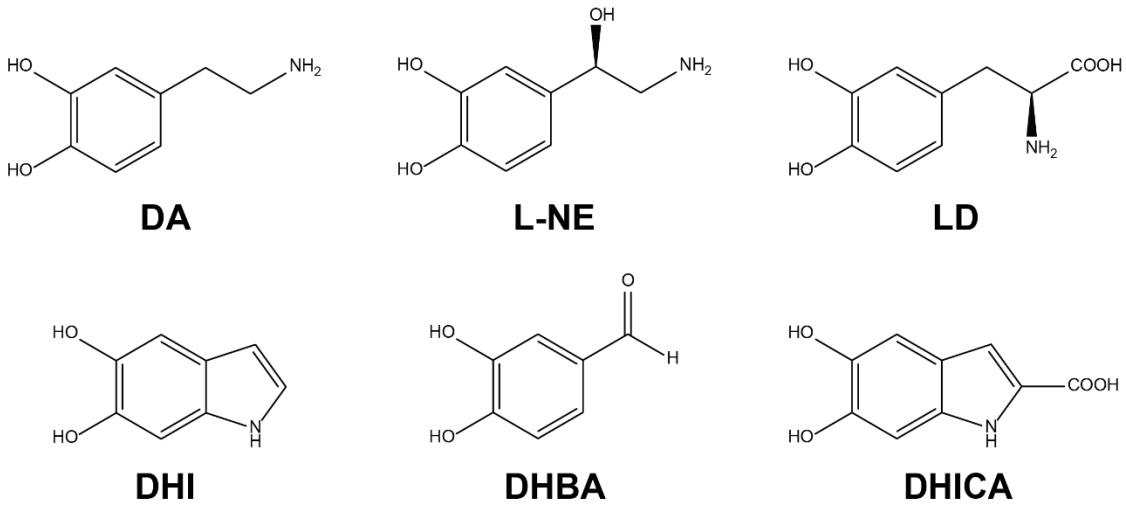


Figure 7-1: Proposed molecules for potential use in polycatecholamine copolymers.

# 8 REFERENCES


1 Park, J., Kim, D. H. & Levchenko, A. Topotaxis: A New Mechanism of Directed Cell Migration in Topographic ECM Gradients. *Biophys J* **114**, 1257-1263 (2018). https://doi.org:10.1016/j.bpj.2017.11.3813

2 Espina, J. A., Marchant, C. L. & Barriga, E. H. Durotaxis: the mechanical control of directed cell migration. *FEBS J* **289**, 2736-2754 (2022). https://doi.org:10.1111/febs.15862

3 Wen, J. H. *et al.* Haptotaxis is cell type specific and limited by substrate adhesiveness. *Cell Mol Bioeng* **8**, 530-542 (2015). https://doi.org:10.1007/s12195-015-0398-3

4 Insall, R. The interaction between pseudopods and extracellular signalling during chemotaxis and directed migration. *Curr Opin Cell Biol* **25**, 526-531 (2013). https://doi.org:10.1016/j.ceb.2013.04.009

5 Steeves, A. J., Atwal, A., Schock, S. C. & Variola, F. Evaluation of the direct effects of poly(dopamine) on the in vitro response of human osteoblastic cells. *J Mater Chem B* **4**, 3145-3156 (2016). https://doi.org:10.1039/c5tb02510a

6 Lee, H., Dellatore, S. M., Miller, W. M. & Messersmith, P. B. Mussel-inspired surface chemistry for multifunctional coatings. *Science* **318**, 426-430 (2007). https://doi.org:10.1126/science.1147241

7 Sun, M. *et al.* Effects of Matrix Stiffness on the Morphology, Adhesion, Proliferation and Osteogenic Differentiation of Mesenchymal Stem Cells. *Int J Med Sci* **15**, 257-268 (2018). https://doi.org:10.7150/ijms.21620

8 Niu, H. *et al.* Surface Topography Regulates Osteogenic Differentiation of MSCs via Crosstalk between FAK/MAPK and ILK/beta-Catenin Pathways in a Hierarchically Porous Environment. *ACS Biomater Sci Eng* **3**, 3161-3175 (2017). https://doi.org:10.1021/acsbiomaterials.7b00315

9 Kulangara, K., Yang, Y., Yang, J. & Leong, K. W. Nanotopography as modulator of human mesenchymal stem cell function. *Biomaterials* **33**, 4998-5003 (2012). https://doi.org:10.1016/j.biomaterials.2012.03.053

10 Ermis, M., Antmen, E. & Hasirci, V. Micro and Nanofabrication methods to control cell-substrate interactions and cell behavior: A review from the tissue engineering perspective. *Bioact Mater* **3**, 355-369 (2018). https://doi.org:10.1016/j.bioactmat.2018.05.005

11 Putra, V. D. L., Kilian, K. A. & Knothe Tate, M. L. Biomechanical, biophysical and biochemical modulators of cytoskeletal remodelling and emergent stem cell lineage commitment. *Commun Biol* **6**, 75 (2023). https://doi.org:10.1038/s42003-022-04320-w

12 Sit, S. T. & Manser, E. Rho GTPases and their role in organizing the actin cytoskeleton. *J Cell Sci* **124**, 679-683 (2011). https://doi.org:10.1242/jcs.064964

13 Leijnse, N., Oddershede, L. B. & Bendix, P. M. Helical buckling of actin inside filopodia generates traction. *Proc Natl Acad Sci U S A* **112**, 136-141 (2015). https://doi.org:10.1073/pnas.1411761112

14 McNamara, L. E. *et al.* Investigation of the limits of nanoscale filopodial interactions. *J Tissue Eng* **5**, 2041731414536177 (2014). https://doi.org:10.1177/2041731414536177

15 Barczyk, M., Carracedo, S. & Gullberg, D. Integrins. *Cell Tissue Res* **339**, 269-280 (2010). https://doi.org:10.1007/s00441-009-0834-6

16 Schumacher, S. *et al.* Structural insights into integrin alpha(5)beta(1) opening by fibronectin ligand. *Sci Adv* **7** (2021). https://doi.org:10.1126/sciadv.abe9716

17 Gardel, M. L., Schneider, I. C., Aratyn-Schaus, Y. & Waterman, C. M. Mechanical integration of actin and adhesion dynamics in cell migration. *Annu Rev Cell Dev Biol* **26**, 315-333 (2010). https://doi.org:10.1146/annurev.cellbio.011209.122036

18 Andreu, I. *et al.* The force loading rate drives cell mechanosensing through both reinforcement and cytoskeletal softening. *Nat Commun* **12**, 4229 (2021). https://doi.org:10.1038/s41467-021-24383-3

19 Kanchanawong, P. *et al.* Nanoscale architecture of integrin-based cell adhesions. *Nature* **468**, 580-584 (2010). https://doi.org:10.1038/nature09621

20 Theodosiou, M. *et al.* Kindlin-2 cooperates with talin to activate integrins and induces cell spreading by directly binding paxillin. *Elife* **5**, e10130 (2016). https://doi.org:10.7554/eLife.10130

21 Klapholz, B. & Brown, N. H. Talin - the master of integrin adhesions. *J Cell Sci* **130**, 2435-2446 (2017). https://doi.org:10.1242/jcs.190991
22 Calderwood, D. A. Talin controls integrin activation. *Biochem Soc Trans* **32**, 434-437 (2004). https://doi.org:10.1042/BST0320434
23 Sun, Z., Costell, M. & Fassler, R. Integrin activation by talin, kindlin and mechanical forces. *Nat Cell Biol* **21**, 25-31 (2019). https://doi.org:10.1038/s41556-018-0234-9
24 Carisey, A. *et al.* Vinculin regulates the recruitment and release of core focal adhesion proteins in a force-dependent manner. *Curr Biol* **23**, 271-281 (2013). https://doi.org:10.1016/j.cub.2013.01.009
25 Bays, J. L. & DeMali, K. A. Vinculin in cell-cell and cell-matrix adhesions. *Cell Mol Life Sci* **74**, 2999-3009 (2017). https://doi.org:10.1007/s00018-017-2511-3
26 Zhao, Y., Lykov, N. & Tzeng, C. Talin-1 interaction network in cellular mechanotransduction (Review). *Int J Mol Med* **49** (2022). https://doi.org:10.3892/ijmm.2022.5116
27 Zhang, H. *et al.* Proliferation of preosteoblasts on TiO(2) nanotubes is FAK/RhoA related. *RSC Adv* **5**, 38117-38124 (2015). https://doi.org:10.1039/C4RA16803H
28 Gilmore, A. P. & Romer, L. H. Inhibition of focal adhesion kinase (FAK) signaling in focal adhesions decreases cell motility and proliferation. *Mol Biol Cell* **7**, 1209-1224 (1996). https://doi.org:10.1091/mbc.7.8.1209
29 Partridge, M. A. & Marcantonio, E. E. Initiation of attachment and generation of mature focal adhesions by integrin-containing filopodia in cell spreading. *Mol Biol Cell* **17**, 4237-4248 (2006). https://doi.org:10.1091/mbc.e06-06-0496
30 Cavalcanti-Adam, E. A. *et al.* Cell spreading and focal adhesion dynamics are regulated by spacing of integrin ligands. *Biophys J* **92**, 2964-2974 (2007). https://doi.org:10.1529/biophysj.106.089730
31 Paluch, E. K., Aspalter, I. M. & Sixt, M. Focal Adhesion-Independent Cell Migration. *Annu Rev Cell Dev Biol* **32**, 469-490 (2016). https://doi.org:10.1146/annurev-cellbio-111315-125341
32 Cipitria, A. & Salmeron-Sanchez, M. Mechanotransduction and Growth Factor Signalling to Engineer Cellular Microenvironments. *Adv Healthc Mater* **6** (2017). https://doi.org:10.1002/adhm.201700052
33 Das, R. K. & Zouani, O. F. A review of the effects of the cell environment physicochemical nanoarchitecture on stem cell commitment. *Biomaterials* **35**, 5278-5293 (2014). https://doi.org:10.1016/j.biomaterials.2014.03.044
34 Kim, D. H., Provenzano, P. P., Smith, C. L. & Levchenko, A. Matrix nanotopography as a regulator of cell function. *J Cell Biol* **197**, 351-360 (2012). https://doi.org:10.1083/jcb.201108062
35 Kassianidou, E. *et al.* Extracellular Matrix Geometry and Initial Adhesive Position Determine Stress Fiber Network Organization during Cell Spreading. *Cell Rep* **27**, 1897-1909 e1894 (2019). https://doi.org:10.1016/j.celrep.2019.04.035
36 Di Cio, S. & Gautrot, J. E. Cell sensing of physical properties at the nanoscale: Mechanisms and control of cell adhesion and phenotype. *Acta Biomater* **30**, 26-48 (2016). https://doi.org:10.1016/j.actbio.2015.11.027
37 Schvartzman, M. *et al.* Nanolithographic control of the spatial organization of cellular adhesion receptors at the single-molecule level. *Nano Lett* **11**, 1306-1312 (2011). https://doi.org:10.1021/nl104378f
38 Guilak, F. *et al.* Control of stem cell fate by physical interactions with the extracellular matrix. *Cell Stem Cell* **5**, 17-26 (2009). https://doi.org:10.1016/j.stem.2009.06.016
39 Punzon-Quijorna, E. *et al.* Nanostructured porous silicon micropatterns as a tool for substrate-conditioned cell research. *Nanoscale Res Lett* **7**, 396 (2012). https://doi.org:10.1186/1556-276X-7-396
40 Bell, S. & Terentjev, E. M. Focal Adhesion Kinase: The Reversible Molecular Mechanosensor. *Biophys J* **112**, 2439-2450 (2017). https://doi.org:10.1016/j.bpj.2017.04.048
41 Nguyen, A. T., Sathe, S. R. & Yim, E. K. From nano to micro: topographical scale and its impact on cell adhesion, morphology and contact guidance. *J Phys Condens Matter* **28**, 183001 (2016). https://doi.org:10.1088/0953-8984/28/18/183001
42 Park, J. *et al.* TiO2 nanotube surfaces: 15 nm--an optimal length scale of surface topography for cell adhesion and differentiation. *Small* **5**, 666-671 (2009). https://doi.org:10.1002/smll.200801476

43 Park, J., Bauer, S., von der Mark, K. & Schmuki, P. Nanosize and vitality: TiO2 nanotube diameter directs cell fate. *Nano Lett* **7**, 1686-1691 (2007). https://doi.org:10.1021/nl070678d

44 Cowden, K., Dias-Netipanyj, M. F. & Popat, K. C. Effects of titania nanotube surfaces on osteogenic differentiation of human adipose-derived stem cells. *Nanomedicine* **17**, 380-390 (2019). https://doi.org:10.1016/j.nano.2019.01.008

45 Lv, L. *et al.* The nanoscale geometry of TiO2 nanotubes influences the osteogenic differentiation of human adipose-derived stem cells by modulating H3K4 trimethylation. *Biomaterials* **39**, 193-205 (2015). https://doi.org:10.1016/j.biomaterials.2014.11.002

46 Oh, S. *et al.* Stem cell fate dictated solely by altered nanotube dimension. *Proc Natl Acad Sci U S A* **106**, 2130-2135 (2009). https://doi.org:10.1073/pnas.0813200106

47 Wang, J. *et al.* Nanostructured titanium regulates osseointegration via influencing macrophage polarization in the osteogenic environment. *Int J Nanomedicine* **13**, 4029-4043 (2018). https://doi.org:10.2147/IJN.S163956

48 Cooper, A., Jana, S., Bhattarai, N. & Zhang, M. Aligned chitosan-based nanofibers for enhanced myogenesis. *Journal of Materials Chemistry* **20** (2010). https://doi.org:10.1039/c0jm01841d

49 D'Amato, A. R. *et al.* Exploring the effects of electrospun fiber surface nanotopography on neurite outgrowth and branching in neuron cultures. *PLoS One* **14**, e0211731 (2019). https://doi.org:10.1371/journal.pone.0211731

50 Xie, J., Liu, W., MacEwan, M. R., Bridgman, P. C. & Xia, Y. Neurite outgrowth on electrospun nanofibers with uniaxial alignment: the effects of fiber density, surface coating, and supporting substrate. *ACS Nano* **8**, 1878-1885 (2014). https://doi.org:10.1021/nn406363j

51 Paul, C. D. *et al.* Probing cellular response to topography in three dimensions. *Biomaterials* **197**, 101-118 (2019). https://doi.org:10.1016/j.biomaterials.2019.01.009

52 Yang, L. *et al.* Disordered Topography Mediates Filopodial Extension and Morphology of Cells on Stiff Materials. *Advanced Functional Materials* **27** (2017). https://doi.org:10.1002/adfm.201702689

53 Steeves, A. J. *et al.* The Implication of Spatial Statistics in Human Mesenchymal Stem Cell Response to Nanotubular Architectures. *Int J Nanomedicine* **15**, 2151-2169 (2020). https://doi.org:10.2147/IJN.S238280

54 Bennett, M. *et al.* Molecular clutch drives cell response to surface viscosity. *Proc Natl Acad Sci U S A* **115**, 1192-1197 (2018). https://doi.org:10.1073/pnas.1710653115

55 Krishna, L. *et al.* Nanostructured scaffold as a determinant of stem cell fate. *Stem Cell Res Ther* **7**, 188 (2016). https://doi.org:10.1186/s13287-016-0440-y

56 Yi, B., Xu, Q. & Liu, W. An overview of substrate stiffness guided cellular response and its applications in tissue regeneration. *Bioact Mater* **15**, 82-102 (2022). https://doi.org:10.1016/j.bioactmat.2021.12.005

57 Bangasser, B. L. *et al.* Shifting the optimal stiffness for cell migration. *Nat Commun* **8**, 15313 (2017). https://doi.org:10.1038/ncomms15313

58 Kim, D. H. & Wirtz, D. Focal adhesion size uniquely predicts cell migration. *FASEB J* **27**, 1351-1361 (2013). https://doi.org:10.1096/fj.12-220160

59 Vazquez, K., Saraswathibhatla, A. & Notbohm, J. Effect of substrate stiffness on friction in collective cell migration. *Sci Rep* **12**, 2474 (2022). https://doi.org:10.1038/s41598-022-06504-0

60 Ngandu Mpoyi, E. *et al.* Protein Adsorption as a Key Mediator in the Nanotopographical Control of Cell Behavior. *ACS Nano* **10**, 6638-6647 (2016). https://doi.org:10.1021/acsnano.6b01649

61 Wu, S. *et al.* Adsorption of serum proteins on titania nanotubes and its role on regulating adhesion and migration of mesenchymal stem cells. *J Biomed Mater Res A* **108**, 2305-2318 (2020). https://doi.org:10.1002/jbm.a.36987

62 Metwally, S. & Stachewicz, U. Surface potential and charges impact on cell responses on biomaterials interfaces for medical applications. *Mater Sci Eng C Mater Biol Appl* **104**, 109883 (2019). https://doi.org:10.1016/j.msec.2019.109883

63 Bacakova, L., Filova, E., Parizek, M., Ruml, T. & Svorcik, V. Modulation of cell adhesion, proliferation and differentiation on materials designed for body implants. *Biotechnol Adv* **29**, 739-767 (2011). https://doi.org:10.1016/j.biotechadv.2011.06.004

64 De Luca, I. *et al.* Positively charged polymers modulate the fate of human mesenchymal stromal cells via ephrinB2/EphB4 signaling. *Stem Cell Res* **17**, 248-255 (2016). https://doi.org:10.1016/j.scr.2016.07.005

65 Felgueiras, H. P., Antunes, J. C., Martins, M. C. L. & Barbosa, M. A. in *Peptides and Proteins as Biomaterials for Tissue Regeneration and Repair* 1-27 (2018).

66 Arima, Y. & Iwata, H. Effects of surface functional groups on protein adsorption and subsequent cell adhesion using self-assembled monolayers. *Journal of Materials Chemistry* **17** (2007). https://doi.org:10.1039/b708099a

67 Cao, B., Peng, Y., Liu, X. & Ding, J. Effects of Functional Groups of Materials on Nonspecific Adhesion and Chondrogenic Induction of Mesenchymal Stem Cells on Free and Micropatterned Surfaces. *ACS Appl Mater Interfaces* **9**, 23574-23585 (2017). https://doi.org:10.1021/acsami.7b08339

68 Cernochova, P. *et al.* Cell type specific adhesion to surfaces functionalised by amine plasma polymers. *Sci Rep* **10**, 9357 (2020). https://doi.org:10.1038/s41598-020-65889-y

69 Jiang, B. *et al.* Investigation on the effect of functional groups on the wettability of coal dust: Experiments and theoretical validation. *Fuel* **351** (2023). https://doi.org:10.1016/j.fuel.2023.128987

70 Guo, S. *et al.* Parallel Control over Surface Charge and Wettability Using Polyelectrolyte Architecture: Effect on Protein Adsorption and Cell Adhesion. *ACS Appl Mater Interfaces* **8**, 30552-30563 (2016). https://doi.org:10.1021/acsami.6b09481

71 Hartvig, R. A., van de Weert, M., Ostergaard, J., Jorgensen, L. & Jensen, H. Protein adsorption at charged surfaces: the role of electrostatic interactions and interfacial charge regulation. *Langmuir* **27**, 2634-2643 (2011). https://doi.org:10.1021/la104720n

72 Keselowsky, B. G., Collard, D. M. & Garcia, A. J. Surface chemistry modulates fibronectin conformation and directs integrin binding and specificity to control cell adhesion. *J Biomed Mater Res A* **66**, 247-259 (2003). https://doi.org:10.1002/jbm.a.10537

73 Ballet, T., Boulange, L., Brechet, Y., Bruckert, F. & Weidenhaupt, M. Protein conformational changes induced by adsorption onto material surfaces: an important issue for biomedical applications of material science. *Bulletin of the Polish Academy of Sciences: Technical Sciences* **58** (2010). https://doi.org:10.2478/v10175-010-0028-0

74 Fu, Y. & Mo, A. A Review on the Electrochemically Self-organized Titania Nanotube Arrays: Synthesis, Modifications, and Biomedical Applications. *Nanoscale Res Lett* **13**, 187 (2018). https://doi.org:10.1186/s11671-018-2597-z

75 Indira, K., Mudali, U. K., Nishimura, T. & Rajendran, N. A Review on TiO2 Nanotubes: Influence of Anodization Parameters, Formation Mechanism, Properties, Corrosion Behavior, and Biomedical Applications. *Journal of Bio- and Tribo-Corrosion* **1** (2015). https://doi.org:10.1007/s40735-015-0024-x

76 Jafari, S. *et al.* Biomedical Applications of TiO(2) Nanostructures: Recent Advances. *Int J Nanomedicine* **15**, 3447-3470 (2020). https://doi.org:10.2147/IJN.S249441

77 Wang, Q. *et al.* TiO(2) nanotube platforms for smart drug delivery: a review. *Int J Nanomedicine* **11**, 4819-4834 (2016). https://doi.org:10.2147/IJN.S108847

78 Brammer, K. S., Frandsen, C. J. & Jin, S. TiO2 nanotubes for bone regeneration. *Trends Biotechnol* **30**, 315-322 (2012). https://doi.org:10.1016/j.tibtech.2012.02.005

79 Zhao, P. *et al.* 3D printed titanium scaffolds with ordered TiO2 nanotubular surface and mesoporous bioactive glass for bone repair. *Progress in Natural Science: Materials International* **30**, 502-509 (2020). https://doi.org:10.1016/j.pnsc.2020.08.009

80 Durdu, S., Cihan, G., Yalcin, E. & Altinkok, A. Characterization and mechanical properties of TiO2 nanotubes formed on titanium by anodic oxidation. *Ceramics International* **47**, 10972-10979 (2021). https://doi.org:10.1016/j.ceramint.2020.12.218

81 Fan, R. & Wan, J. Electrode distance regulates the anodic growth of titanium dioxide (TiO(2)) nanotubes. *Nanotechnology* **28**, 25LT01 (2017). https://doi.org:10.1088/1361-6528/aa703d

82 Mansoorianfar, M. *et al.* Scalable fabrication of tunable titanium nanotubes via sonoelectrochemical process for biomedical applications. *Ultrason Sonochem* **64**, 104783 (2020). https://doi.org:10.1016/j.ultsonch.2019.104783
83 Yao, L., Chen, J., Wang, Z. & Sham, T.-K. TiO2 Nanotubes: Morphology, Size, Crystallinity, and Phase-Dependent Properties from Synchrotron-Spectroscopy Studies. *The Journal of Physical Chemistry C* **126**, 3265-3275 (2022). https://doi.org:10.1021/acs.jpcc.1c10577
84 Alkanad, K. *et al.* One-Step Hydrothermal Synthesis of Anatase TiO(2) Nanotubes for Efficient Photocatalytic CO(2) Reduction. *ACS Omega* **7**, 38686-38699 (2022). https://doi.org:10.1021/acsomega.2c04211
85 Obregón, S. & Rodríguez-González, V. Photocatalytic TiO2 thin films and coatings prepared by sol–gel processing: a brief review. *Journal of Sol-Gel Science and Technology* **102**, 125-141 (2021). https://doi.org:10.1007/s10971-021-05628-5
86 Chernozem, R. V., Surmeneva, M. A. & Surmenev, R. A. Influence of Anodization Time and Voltage on the Parameters of TiO2Nanotubes. *IOP Conference Series: Materials Science and Engineering* **116** (2016). https://doi.org:10.1088/1757-899x/116/1/012025
87 Yu, H. *et al.* Effects of electrolyte composition on the growth and properties of titanium oxide nanotubes. *Electrochemistry Communications* **135** (2022). https://doi.org:10.1016/j.elecom.2022.107217
88 Suhadolnik, L. *et al.* Influence of Anodization-Electrolyte Aging on the Photocatalytic Activity of TiO(2) Nanotube Arrays. *J Phys Chem C Nanomater Interfaces* **124**, 4073-4080 (2020). https://doi.org:10.1021/acs.jpcc.9b09522
89 Yan, S. *et al.* Essential distinction between one-step anodization and two-step anodization of Ti. *Materials Research Bulletin* **95**, 444-450 (2017). https://doi.org:10.1016/j.materresbull.2017.08.025
90 Sitler, S. J. & Raja, K. S. Self-ordering dual-layered honeycomb nanotubular titania: a study in formation mechanisms. *RSC Advances* **6**, 11991-12002 (2016). https://doi.org:10.1039/c5ra24667a
91 Wei, J. *et al.* Research on the Electrochemical Performance of Rutile and Anatase Composite TiO2 Nanotube Arrays in Lithium-Ion Batteries. *J Nanosci Nanotechnol* **15**, 5013-5019 (2015). https://doi.org:10.1166/jnn.2015.9847
92 Talla, A. *et al.* Effect of annealing temperature and atmosphere on the structural, morphological and luminescent properties of TiO2 nanotubes. *Physica B: Condensed Matter* **640** (2022). https://doi.org:10.1016/j.physb.2022.414026
93 De Matteis, V., Cascione, M., Brunetti, V., Toma, C. C. & Rinaldi, R. Toxicity assessment of anatase and rutile titanium dioxide nanoparticles: The role of degradation in different pH conditions and light exposure. *Toxicol In Vitro* **37**, 201-210 (2016). https://doi.org:10.1016/j.tiv.2016.09.010
94 Sampath, J., Kullman, A., Gebhart, R., Drobny, G. & Pfaendtner, J. Molecular recognition and specificity of biomolecules to titanium dioxide from molecular dynamics simulations. *npj Computational Materials* **6** (2020). https://doi.org:10.1038/s41524-020-0288-7
95 Zhao, L. *et al.* Protein adsorption on TiO2 nanostructures and its effects on surface topography and bactericidal performance. *Applied Surface Science* **576** (2022). https://doi.org:10.1016/j.apsusc.2021.151779
96 Ribeiro, B. *et al.* On Growth and Morphology of TiO(2) Nanotubes on Ti6Al4V by Anodic Oxidation in Ethylene Glycol Electrolyte: Influence of Microstructure and Anodization Parameters. *Materials (Basel)* **14** (2021). https://doi.org:10.3390/ma14102540
97 Poddar, S., Bit, A. & Sinha, S. K. A study on influence of anodization on the morphology of titania nanotubes over Ti6Al4V alloy in correlation to hard tissue engineering application. *Materials Chemistry and Physics* **254** (2020). https://doi.org:10.1016/j.matchemphys.2020.123457
98 Mutreja, I., Kumar, D., Boyd, A. R. & Meenan, B. J. Titania nanotube porosity controls dissolution rate of sputter deposited calcium phosphate (CaP) thin film coatings. *RSC Advances* **3** (2013). https://doi.org:10.1039/c3ra40898a
99 Lu, B., Zhu, C., Zhang, Z., Lan, W. & Xie, E. Preparation of highly porous TiO2nanotubes and their catalytic applications. *J. Mater. Chem.* **22**, 1375-1379 (2012). https://doi.org:10.1039/c1jm15242d

100 Stassi, S. *et al.* Evolution of nanomechanical properties and crystallinity of individual titanium dioxide nanotube resonators. *Nanotechnology* **29**, 085702 (2018). https://doi.org:10.1088/1361-6528/aaa46c
101 Radtke, A., Ehlert, M., Jedrzejewski, T. & Bartmanski, M. The Morphology, Structure, Mechanical Properties and Biocompatibility of Nanotubular Titania Coatings before and after Autoclaving Process. *J Clin Med* **8** (2019). https://doi.org:10.3390/jcm8020272
102 Gusmao, S. B. S. *et al.* Nanohydroxyapatite/Titanate Nanotube Composites for Bone Tissue Regeneration. *J Funct Biomater* **13** (2022). https://doi.org:10.3390/jfb13040306
103 Khrunyk, Y. Y. *et al.* Surface-Dependent Osteoblasts Response to TiO(2) Nanotubes of Different Crystallinity. *Nanomaterials (Basel)* **10** (2020). https://doi.org:10.3390/nano10020320
104 Junkar, I. *et al.* Titanium Dioxide Nanotube Arrays for Cardiovascular Stent Applications. *ACS Omega* **5**, 7280-7289 (2020). https://doi.org:10.1021/acsomega.9b04118
105 Pan, C. *et al.* Improved Blood Compatibility and Endothelialization of Titanium Oxide Nanotube Arrays on Titanium Surface by Zinc Doping. *ACS Biomater Sci Eng* **6**, 2072-2083 (2020). https://doi.org:10.1021/acsbiomaterials.0c00187
106 Stolzoff, M. *et al.* Decreased bacterial growth on titanium nanoscale topographies created by ion beam assisted evaporation. *Int J Nanomedicine* **12**, 1161-1169 (2017). https://doi.org:10.2147/IJN.S119750
107 Li, H. *et al.* Antibacterial activity of TiO2 nanotubes: Influence of crystal phase, morphology and Ag deposition. *Applied Surface Science* **284**, 179-183 (2013). https://doi.org:10.1016/j.apsusc.2013.07.076
108 Bilek, O. *et al.* Antibacterial activity of AgNPs-TiO(2) nanotubes: influence of different nanoparticle stabilizers. *RSC Adv* **10**, 44601-44610 (2020). https://doi.org:10.1039/d0ra07305a
109 Ketabchi, A., Komm, K., Miles-Rossouw, M., Cassani, D. A. & Variola, F. Nanoporous titanium surfaces for sustained elution of proteins and antibiotics. *PLoS One* **9**, e92080 (2014). https://doi.org:10.1371/journal.pone.0092080
110 Park, J., Cimpean, A., Tesler, A. B. & Mazare, A. Anodic TiO(2) Nanotubes: Tailoring Osteoinduction via Drug Delivery. *Nanomaterials (Basel)* **11** (2021). https://doi.org:10.3390/nano11092359
111 Yang, M. *et al.* Incorporation of copper and strontium ions in TiO2 nanotubes via dopamine to enhance hemocompatibility and cytocompatibility. *Nanotechnology Reviews* **11**, 1450-1463 (2022). https://doi.org:10.1515/ntrev-2022-0090
112 Lai, M. *et al.* The controlled naringin release from TiO(2) nanotubes to regulate osteoblast differentiation. *J Biomater Appl* **33**, 673-680 (2018). https://doi.org:10.1177/0885328218809239
113 M.M. Vijay, A. H. T., Y. Wenzhuo, B.R. Daniels. Method and apparatus for prepping surfaces with a high-frequency forced pulsed waterjet. (2009).
114 Steeves, A. J., Vijay, M., Tieu, A., Yan, W. & Xu, M. in *WJTA-IMCA Conference & Expo.*
115 Han, Z. *et al.* Biomimetic multifunctional surfaces inspired from animals. *Adv Colloid Interface Sci* **234**, 27-50 (2016). https://doi.org:10.1016/j.cis.2016.03.004
116 Alfieri, M. L., Weil, T., Ng, D. Y. W. & Ball, V. Polydopamine at biological interfaces. *Adv Colloid Interface Sci* **305**, 102689 (2022). https://doi.org:10.1016/j.cis.2022.102689
117 Li, H. *et al.* Polydopamine-based nanomaterials and their potentials in advanced drug delivery and therapy. *Colloids Surf B Biointerfaces* **199**, 111502 (2021). https://doi.org:10.1016/j.colsurfb.2020.111502
118 Lim, C. *et al.* Nanomechanics of Poly(catecholamine) Coatings in Aqueous Solutions. *Angew Chem Int Ed Engl* **55**, 3342-3346 (2016). https://doi.org:10.1002/anie.201510319
119 Maier, G. P., Rapp, M. V., Waite, J. H., Israelachvili, J. N. & Butler, A. BIOLOGICAL ADHESIVES. Adaptive synergy between catechol and lysine promotes wet adhesion by surface salt displacement. *Science* **349**, 628-632 (2015). https://doi.org:10.1126/science.aab0556
120 Tan, X. *et al.* Poly-dopamine, poly-levodopa, and poly-norepinephrine coatings: Comparison of physico-chemical and biological properties with focus on the application for blood-contacting devices. *Bioact Mater* **6**, 285-296 (2021). https://doi.org:10.1016/j.bioactmat.2020.06.024
121 Waite, J. H. & Qin, X. Polyphosphoprotein from the adhesive pads of Mytilus edulis. *Biochemistry* **40**, 2887-2893 (2001). https://doi.org:10.1021/bi002718x

122 Lee, H., Scherer, N. F. & Messersmith, P. B. Single-molecule mechanics of mussel adhesion. *Proc Natl Acad Sci U S A* **103**, 12999-13003 (2006). https://doi.org:10.1073/pnas.0605552103
123 Liu, Y., Ai, K. & Lu, L. Polydopamine and its derivative materials: synthesis and promising applications in energy, environmental, and biomedical fields. *Chem Rev* **114**, 5057-5115 (2014). https://doi.org:10.1021/cr400407a
124 Fu, Y. *et al.* Polydopamine antibacterial materials. *Mater Horiz* **8**, 1618-1633 (2021). https://doi.org:10.1039/d0mh01985b
125 Jia, L. *et al.* Polydopamine-assisted surface modification for orthopaedic implants. *J Orthop Translat* **17**, 82-95 (2019). https://doi.org:10.1016/j.jot.2019.04.001
126 Godoy-Gallardo, M., Portoles-Gil, N., Lopez-Periago, A. M., Domingo, C. & Hosta-Rigau, L. Multi-layered polydopamine coatings for the immobilization of growth factors onto highly-interconnected and bimodal PCL/HA-based scaffolds. *Mater Sci Eng C Mater Biol Appl* **117**, 111245 (2020). https://doi.org:10.1016/j.msec.2020.111245
127 Jin, A., Wang, Y., Lin, K. & Jiang, L. Nanoparticles modified by polydopamine: Working as "drug" carriers. *Bioact Mater* **5**, 522-541 (2020). https://doi.org:10.1016/j.bioactmat.2020.04.003
128 Liebscher, J. Chemistry of Polydopamine – Scope, Variation, and Limitation. *European Journal of Organic Chemistry* **2019**, 4976-4994 (2019). https://doi.org:10.1002/ejoc.201900445
129 Ball, V., Del Frari, D., Toniazzo, V. & Ruch, D. Kinetics of polydopamine film deposition as a function of pH and dopamine concentration: insights in the polydopamine deposition mechanism. *J Colloid Interface Sci* **386**, 366-372 (2012). https://doi.org:10.1016/j.jcis.2012.07.030
130 Patel, K. *et al.* Polydopamine films change their physicochemical and antimicrobial properties with a change in reaction conditions. *Phys Chem Chem Phys* **20**, 5744-5755 (2018). https://doi.org:10.1039/c7cp08406d
131 Su, L., Yu, Y., Zhao, Y., Liang, F. & Zhang, X. Strong Antibacterial Polydopamine Coatings Prepared by a Shaking-assisted Method. *Sci Rep* **6**, 24420 (2016). https://doi.org:10.1038/srep24420
132 Steeves, A. J. & Variola, F. Elucidating structure-function relationships governing the interfacial response of human mesenchymal stem cells to polydopamine coatings. *J Mater Chem B* **8**, 199-215 (2020). https://doi.org:10.1039/c9tb02188d
133 Delparastan, P., Malollari, K. G., Lee, H. & Messersmith, P. B. Direct Evidence for the Polymeric Nature of Polydopamine. *Angew Chem Int Ed Engl* **58**, 1077-1082 (2019). https://doi.org:10.1002/anie.201811763
134 Ryu, J. H., Messersmith, P. B. & Lee, H. Polydopamine Surface Chemistry: A Decade of Discovery. *ACS Appl Mater Interfaces* **10**, 7523-7540 (2018). https://doi.org:10.1021/acsami.7b19865
135 Hemmatpour, H. *et al.* New insights in polydopamine formation via surface adsorption. *Nat Commun* **14**, 664 (2023). https://doi.org:10.1038/s41467-023-36303-8
136 Ding, Y. *et al.* Insights into the aggregation/deposition and structure of a polydopamine film. *Langmuir* **30**, 12258-12269 (2014). https://doi.org:10.1021/la5026608
137 Liebscher, J. *et al.* Structure of polydopamine: a never-ending story? *Langmuir* **29**, 10539-10548 (2013). https://doi.org:10.1021/la4020288
138 Lyu, Q., Hsueh, N. & Chai, C. L. L. Direct Evidence for the Critical Role of 5,6-Dihydroxyindole in Polydopamine Deposition and Aggregation. *Langmuir* **35**, 5191-5201 (2019). https://doi.org:10.1021/acs.langmuir.9b00392
139 Nakatsuka, N. & Andrews, A. M. Differentiating Siblings: The Case of Dopamine and Norepinephrine. *ACS Chem Neurosci* **8**, 218-220 (2017). https://doi.org:10.1021/acschemneuro.7b00056
140 Park, M. *et al.* The Promotion of Human Neural Stem Cells Adhesion Using Bioinspired Poly(norepinephrine) Nanoscale Coating. *Journal of Nanomaterials* **2014**, 1-10 (2014). https://doi.org:10.1155/2014/793052
141 Chen, Y. *et al.* Bioadhesive anisotropic nanogrooved microfibers directing three-dimensional neurite extension. *Biomater Sci* **7**, 2165-2173 (2019). https://doi.org:10.1039/c8bm01603h

142 Huang, Q. *et al.* Facile synthesis and characterization of poly(levodopa)-modified silica nanocomposites via self-polymerization of levodopa and their adsorption behavior toward Cu2+. *Journal of Materials Science* **51**, 9625-9637 (2016). https://doi.org:10.1007/s10853-016-0178-z
143 Tarhan, T., Dündar, A., Okumuş, V. & Çulha, M. Synthesis and Characterization of Bionanomaterials and Evaluation of Their Antioxidant, Antibacterial, and DNA Cleavage Activities. *ChemistrySelect* **6**, 4217-4223 (2021). https://doi.org:10.1002/slct.202004773
144 Kuziel, A. *et al.* Biomimetically Inspired Highly Homogeneous Hydrophilization of Graphene with Poly(l-DOPA): Toward Electroconductive Coatings from Water-Processable Paints. *ACS Sustain Chem Eng* **10**, 6596-6608 (2022). https://doi.org:10.1021/acssuschemeng.2c00226
145 Ghodsi, J. & Rafati, A. A. A novel molecularly imprinted sensor for imidacloprid pesticide based on poly(levodopa) electro-polymerized/TiO(2) nanoparticles composite. *Anal Bioanal Chem* **410**, 7621-7633 (2018). https://doi.org:10.1007/s00216-018-1372-4
146 Guo, H. *et al.* The preparation of poly-levodopa coated capillary column for capillary electrochromatography enantioseparation. *J Chromatogr A* **1578**, 91-98 (2018). https://doi.org:10.1016/j.chroma.2018.10.007
147 Hormozi-Nezhad, M. R., Moslehipour, A. & Bigdeli, A. Simple and rapid detection of l-dopa based on in situ formation of polylevodopa nanoparticles. *Sensors and Actuators B: Chemical* **243**, 715-720 (2017). https://doi.org:10.1016/j.snb.2016.12.059
148 Kishida, R., Saputro, A. G. & Kasai, H. Mechanism of dopachrome tautomerization into 5,6-dihydroxyindole-2-carboxylic acid catalyzed by Cu(II) based on quantum chemical calculations. *Biochim Biophys Acta* **1850**, 281-286 (2015). https://doi.org:10.1016/j.bbagen.2014.10.024
149 Panzella, L., Napolitano, A. & d'Ischia, M. Is DHICA the key to dopachrome tautomerase and melanocyte functions? *Pigment Cell Melanoma Res* **24**, 248-249 (2011). https://doi.org:10.1111/j.1755-148X.2010.00771.x
150 Zhang, C. *et al.* Revisiting the adhesion mechanism of mussel-inspired chemistry. *Chem Sci* **13**, 1698-1705 (2022). https://doi.org:10.1039/d1sc05512g
151 Cheng, B. *et al.* Ultrastrong underwater adhesion on diverse substrates using non-canonical phenolic groups. *Nat Commun* **13**, 1892 (2022). https://doi.org:10.1038/s41467-022-29427-w
152 Della Vecchia, N. F. *et al.* Building‐Block Diversity in Polydopamine Underpins a Multifunctional Eumelanin‐Type Platform Tunable Through a Quinone Control Point. *Advanced Functional Materials* **23**, 1331-1340 (2012). https://doi.org:10.1002/adfm.201202127
153 Alfieri, M. L. *et al.* The Chemistry of Polydopamine Film Formation: The Amine-Quinone Interplay. *Biomimetics (Basel)* **3** (2018). https://doi.org:10.3390/biomimetics3030026
154 Stöckle, B. *et al.* Precise Control of Polydopamine Film Formation by Electropolymerization. *Macromolecular Symposia* **346**, 73-81 (2014). https://doi.org:10.1002/masy.201400130
155 Nirasay, S., Badia, A., Leclair, G., Claverie, J. & Marcotte, I. Polydopamine-Supported Lipid Bilayers. *Materials* **5**, 2621-2636 (2012). https://doi.org:10.3390/ma5122621
156 Harati, J. *et al.* Polydopamine-Mediated Protein Adsorption Alters the Epigenetic Status and Differentiation of Primary Human Adipose-Derived Stem Cells (hASCs). *Front Bioeng Biotechnol* **10**, 934179 (2022). https://doi.org:10.3389/fbioe.2022.934179
157 Li, H., Xi, J., Zhao, Y. & Ren, F. Mechanical properties of polydopamine (PDA) thin films. *MRS Advances* **4**, 405-412 (2019). https://doi.org:10.1557/adv.2019.52
158 Zangmeister, R. A., Morris, T. A. & Tarlov, M. J. Characterization of polydopamine thin films deposited at short times by autoxidation of dopamine. *Langmuir* **29**, 8619-8628 (2013). https://doi.org:10.1021/la400587j
159 Salomaki, M., Marttila, L., Kivela, H., Ouvinen, T. & Lukkari, J. Effects of pH and Oxidants on the First Steps of Polydopamine Formation: A Thermodynamic Approach. *J Phys Chem B* **122**, 6314-6327 (2018). https://doi.org:10.1021/acs.jpcb.8b02304

160 Saiz-Poseu, J., Mancebo-Aracil, J., Nador, F., Busque, F. & Ruiz-Molina, D. The Chemistry behind Catechol-Based Adhesion. *Angew Chem Int Ed Engl* **58**, 696-714 (2019). https://doi.org:10.1002/anie.201801063
161 Davidsen, M. B. *et al.* Post-treatments of polydopamine coatings influence cellular response. *Colloids Surf B Biointerfaces* **207**, 111972 (2021). https://doi.org:10.1016/j.colsurfb.2021.111972
162 Schaap-Oziemlak, A. M., Kühn, P. T., van Kooten, T. G. & van Rijn, P. Biomaterial–stem cell interactions and their impact on stem cell response. *RSC Adv.* **4**, 53307-53320 (2014). https://doi.org:10.1039/c4ra07915a
163 Morais, J. M., Papadimitrakopoulos, F. & Burgess, D. J. Biomaterials/tissue interactions: possible solutions to overcome foreign body response. *AAPS J* **12**, 188-196 (2010). https://doi.org:10.1208/s12248-010-9175-3
164 Andalib, M. N., Dzenis, Y., Donahue, H. J. & Lim, J. Y. Biomimetic substrate control of cellular mechanotransduction. *Biomater Res* **20**, 11 (2016). https://doi.org:10.1186/s40824-016-0059-1
165 Kord Forooshani, P. & Lee, B. P. Recent approaches in designing bioadhesive materials inspired by mussel adhesive protein. *J Polym Sci A Polym Chem* **55**, 9-33 (2017). https://doi.org:10.1002/pola.28368
166 Xu, J. *et al.* Polydopamine coatings embedded with silver nanoparticles on nanostructured titania for long-lasting antibacterial effect. *Surface and Coatings Technology* **320**, 608-613 (2017). https://doi.org:10.1016/j.surfcoat.2016.10.065
167 Li, P. *et al.* High-performance multilayer composite membranes with mussel-inspired polydopamine as a versatile molecular bridge for CO2 separation. *ACS Appl Mater Interfaces* **7**, 15481-15493 (2015). https://doi.org:10.1021/acsami.5b03786
168 Sileika, T. S., Kim, H. D., Maniak, P. & Messersmith, P. B. Antibacterial performance of polydopamine-modified polymer surfaces containing passive and active components. *ACS Appl Mater Interfaces* **3**, 4602-4610 (2011). https://doi.org:10.1021/am200978h
169 Ku, S. H., Ryu, J., Hong, S. K., Lee, H. & Park, C. B. General functionalization route for cell adhesion on non-wetting surfaces. *Biomaterials* **31**, 2535-2541 (2010). https://doi.org:10.1016/j.biomaterials.2009.12.020
170 Lord, M. S., Foss, M. & Besenbacher, F. Influence of nanoscale surface topography on protein adsorption and cellular response. *Nano Today* **5**, 66-78 (2010). https://doi.org:10.1016/j.nantod.2010.01.001
171 Wei, X. *et al.* Mesenchymal stem cells: a new trend for cell therapy. *Acta Pharmacol Sin* **34**, 747-754 (2013). https://doi.org:10.1038/aps.2013.50
172 Boyan, B. D., Lotz, E. M. & Schwartz, Z. Roughness and Hydrophilicity as Osteogenic Biomimetic Surface Properties. *Tissue Eng Part A* **23**, 1479-1489 (2017). https://doi.org:10.1089/ten.TEA.2017.0048
173 Zhou, P. *et al.* Rapidly-deposited polydopamine coating via high temperature and vigorous stirring: formation, characterization and biofunctional evaluation. *PLoS One* **9**, e113087 (2014). https://doi.org:10.1371/journal.pone.0113087
174 Della Vecchia, N. F. *et al.* Tris buffer modulates polydopamine growth, aggregation, and paramagnetic properties. *Langmuir* **30**, 9811-9818 (2014). https://doi.org:10.1021/la501560z
175 Kavousanakis, M. E., Chamakos, N. T. & Papathanasiou, A. G. Connection of Intrinsic Wettability and Surface Topography with the Apparent Wetting Behavior and Adhesion Properties. *The Journal of Physical Chemistry C* **119**, 15056-15066 (2015). https://doi.org:10.1021/acs.jpcc.5b00718
176 Jiang, J., Zhu, L., Zhu, L., Zhu, B. & Xu, Y. Surface characteristics of a self-polymerized dopamine coating deposited on hydrophobic polymer films. *Langmuir* **27**, 14180-14187 (2011). https://doi.org:10.1021/la202877k
177 Lo, C. M., Wang, H. B., Dembo, M. & Wang, Y. L. Cell movement is guided by the rigidity of the substrate. *Biophys J* **79**, 144-152 (2000). https://doi.org:10.1016/S0006-3495(00)76279-5
178 Dubin-Thaler, B. J., Giannone, G., Dobereiner, H. G. & Sheetz, M. P. Nanometer analysis of cell spreading on matrix-coated surfaces reveals two distinct cell states and STEPs. *Biophys J* **86**, 1794-1806 (2004). https://doi.org:10.1016/S0006-3495(04)74246-0
179 Reinhart-King, C. A., Dembo, M. & Hammer, D. A. The dynamics and mechanics of endothelial cell spreading. *Biophys J* **89**, 676-689 (2005). https://doi.org:10.1529/biophysj.104.054320

180 Livne, A. & Geiger, B. The inner workings of stress fibers - from contractile machinery to focal adhesions and back. *J Cell Sci* **129**, 1293-1304 (2016). https://doi.org:10.1242/jcs.180927
181 Pasapera, A. M. *et al.* Rac1-dependent phosphorylation and focal adhesion recruitment of myosin IIA regulates migration and mechanosensing. *Curr Biol* **25**, 175-186 (2015). https://doi.org:10.1016/j.cub.2014.11.043
182 Wakatsuki, T., Wysolmerski, R. B. & Elson, E. L. Mechanics of cell spreading: role of myosin II. *J Cell Sci* **116**, 1617-1625 (2003). https://doi.org:10.1242/jcs.00340
183 Kuo, J. C. Mechanotransduction at focal adhesions: integrating cytoskeletal mechanics in migrating cells. *J Cell Mol Med* **17**, 704-712 (2013). https://doi.org:10.1111/jcmm.12054
184 Smith, L., Cho, S. & Discher, D. E. Mechanosensing of matrix by stem cells: From matrix heterogeneity, contractility, and the nucleus in pore-migration to cardiogenesis and muscle stem cells in vivo. *Semin Cell Dev Biol* **71**, 84-98 (2017). https://doi.org:10.1016/j.semcdb.2017.05.025
185 Watts, K. L., Cottrell, E., Hoban, P. R. & Spiteri, M. A. RhoA signaling modulates cyclin D1 expression in human lung fibroblasts; implications for idiopathic pulmonary fibrosis. *Respir Res* **7**, 88 (2006). https://doi.org:10.1186/1465-9921-7-88
186 McNamara, L. E. *et al.* The role of microtopography in cellular mechanotransduction. *Biomaterials* **33**, 2835-2847 (2012). https://doi.org:10.1016/j.biomaterials.2011.11.047
187 Wang, J. L. *et al.* Direct adhesion of endothelial cells to bioinspired poly(dopamine) coating through endogenous fibronectin and integrin alpha5 beta1. *Macromol Biosci* **13**, 483-493 (2013). https://doi.org:10.1002/mabi.201200390
188 Wolfenson, H., Iskratsch, T. & Sheetz, M. P. Early events in cell spreading as a model for quantitative analysis of biomechanical events. *Biophys J* **107**, 2508-2514 (2014). https://doi.org:10.1016/j.bpj.2014.10.041
189 Schiller, H. B. & Fassler, R. Mechanosensitivity and compositional dynamics of cell-matrix adhesions. *EMBO Rep* **14**, 509-519 (2013). https://doi.org:10.1038/embor.2013.49
190 Zimmer, C. C. *et al.* F-Actin reassembly during focal adhesion impacts single cell mechanics and nanoscale membrane structure. *Science China Chemistry* **55**, 1922-1930 (2012). https://doi.org:10.1007/s11426-012-4535-8
191 Tsai, W. B., Chen, W. T., Chien, H. W., Kuo, W. H. & Wang, M. J. Poly(dopamine) coating of scaffolds for articular cartilage tissue engineering. *Acta Biomater* **7**, 4187-4194 (2011). https://doi.org:10.1016/j.actbio.2011.07.024
192 Zhou, W., Xiao, X., Cai, M. & Yang, L. Polydopamine-coated, nitrogen-doped, hollow carbon-sulfur double-layered core-shell structure for improving lithium-sulfur batteries. *Nano Lett* **14**, 5250-5256 (2014). https://doi.org:10.1021/nl502238b
193 Luo, R. *et al.* In vitro investigation of enhanced hemocompatibility and endothelial cell proliferation associated with quinone-rich polydopamine coating. *ACS Appl Mater Interfaces* **5**, 1704-1714 (2013). https://doi.org:10.1021/am3027635
194 Lee, J.-J. *et al.* Effects of polydopamine coating on the bioactivity of titanium for dental implants. *International Journal of Precision Engineering and Manufacturing* **15**, 1647-1655 (2014). https://doi.org:10.1007/s12541-014-0515-6
195 Salasznyk, R. M., Klees, R. F., Williams, W. A., Boskey, A. & Plopper, G. E. Focal adhesion kinase signaling pathways regulate the osteogenic differentiation of human mesenchymal stem cells. *Exp Cell Res* **313**, 22-37 (2007). https://doi.org:10.1016/j.yexcr.2006.09.013
196 Ruijtenberg, S. & van den Heuvel, S. Coordinating cell proliferation and differentiation: Antagonism between cell cycle regulators and cell type-specific gene expression. *Cell Cycle* **15**, 196-212 (2016). https://doi.org:10.1080/15384101.2015.1120925
197 Mao, H., Kim, S. M., Ueki, M. & Ito, Y. Serum-free culturing of human mesenchymal stem cells with immobilized growth factors. *J Mater Chem B* **5**, 928-934 (2017). https://doi.org:10.1039/c6tb02867e
198 Bergmann, S., Schindler, M., Munger, C., Penfold, C. A. & Boroviak, T. E. Building a stem cell-based primate uterus. *Commun Biol* **4**, 749 (2021). https://doi.org:10.1038/s42003-021-02233-8

199 Martyn, F., McAuliffe, F. M. & Wingfield, M. The role of the cervix in fertility: is it time for a reappraisal? *Hum Reprod* **29**, 2092-2098 (2014). https://doi.org:10.1093/humrep/deu195
200 Yamaguchi, M. *et al.* Three-dimensional understanding of the morphological complexity of the human uterine endometrium. *iScience* **24**, 102258 (2021). https://doi.org:10.1016/j.isci.2021.102258
201 Masuda, H. *et al.* Endometrial side population cells: potential adult stem/progenitor cells in endometrium. *Biol Reprod* **93**, 84 (2015). https://doi.org:10.1095/biolreprod.115.131490
202 Masuda, A. *et al.* An improved method for isolation of epithelial and stromal cells from the human endometrium. *J Reprod Dev* **62**, 213-218 (2016). https://doi.org:10.1262/jrd.2015-137
203 Winuthayanon, W. *et al.* Juxtacrine Activity of Estrogen Receptor alpha in Uterine Stromal Cells is Necessary for Estrogen-Induced Epithelial Cell Proliferation. *Sci Rep* **7**, 8377 (2017). https://doi.org:10.1038/s41598-017-07728-1
204 Ueshima, C. *et al.* Decidualization of Stromal Cells Promotes Involvement of Mast Cells in Successful Human Pregnancy by Increasing Stem Cell Factor Expression. *Front Immunol* **13**, 779574 (2022). https://doi.org:10.3389/fimmu.2022.779574
205 Kagami, K. *et al.* A novel third mesh-like myometrial layer connects the longitudinal and circular muscle fibers -A potential stratum to coordinate uterine contractions. *Sci Rep* **10**, 8274 (2020). https://doi.org:10.1038/s41598-020-65299-0
206 Mendelson, C. R., Gao, L. & Montalbano, A. P. Multifactorial Regulation of Myometrial Contractility During Pregnancy and Parturition. *Front Endocrinol (Lausanne)* **10**, 714 (2019). https://doi.org:10.3389/fendo.2019.00714
207 Wilson, R. A. & Mesiano, S. A. Progesterone signaling in myometrial cells: role in human pregnancy and parturition. *Current Opinion in Physiology* **13**, 117-122 (2020). https://doi.org:10.1016/j.cophys.2019.09.007
208 Hanuman, S., Pande, G. & Nune, M. Current status and challenges in uterine myometrial tissue engineering. *Bioengineered* **14**, 2251847 (2023). https://doi.org:10.1080/21655979.2023.2251847
209 Pique-Regi, R. *et al.* A single-cell atlas of the myometrium in human parturition. *JCI Insight* **7** (2022). https://doi.org:10.1172/jci.insight.153921
210 Wang, P. H., Yuan, C. C., Chao, H. T., Yang, M. J. & Ng, H. T. Posterior uterine wall rupture during labour. *Hum Reprod* **15**, 1198-1199 (2000). https://doi.org:10.1093/humrep/15.5.1198
211 Scott, A. K., Louwagie, E. M., Myers, K. M. & Oyen, M. L. Biomechanical Modeling of Cesarean Section Scars and Scar Defects. *bioRxiv* (2024). https://doi.org:10.1101/2023.11.03.565565
212 Dy, J., DeMeester, S., Lipworth, H. & Barrett, J. No. 382-Trial of Labour After Caesarean. *J Obstet Gynaecol Can* **41**, 992-1011 (2019). https://doi.org:10.1016/j.jogc.2018.11.008
213 Dreisler, E. & Kjer, J. J. Asherman's syndrome: current perspectives on diagnosis and management. *Int J Womens Health* **11**, 191-198 (2019). https://doi.org:10.2147/IJWH.S165474
214 Chen, Y. *et al.* Effects of Aspirin and Intrauterine Balloon on Endometrial Repair and Reproductive Prognosis in Patients with Severe Intrauterine Adhesion: A Prospective Cohort Study. *Biomed Res Int* **2017**, 8526104 (2017). https://doi.org:10.1155/2017/8526104
215 Bhandari, S., Bhave, P., Ganguly, I., Baxi, A. & Agarwal, P. Reproductive Outcome of Patients with Asherman's Syndrome: A SAIMS Experience. *J Reprod Infertil* **16**, 229-235 (2015).
216 Baradwan, S., Baradwan, A., Bashir, M. & Al-Jaroudi, D. The birth weight in pregnant women with Asherman syndrome compared to normal intrauterine cavity: A case-control study. *Medicine (Baltimore)* **97**, e11797 (2018). https://doi.org:10.1097/MD.0000000000011797
217 Wang, J. *et al.* Injectable collagen hydrogel combines human umbilical cord mesenchymal stem cells to promote endometrial regeneration in rats with thin endometrium. *Int J Biol Macromol* **254**, 127591 (2024). https://doi.org:10.1016/j.ijbiomac.2023.127591
218 Chen, L. *et al.* An injectable gelatin/sericin hydrogel loaded with human umbilical cord mesenchymal stem cells for the treatment of uterine injury. *Bioeng Transl Med* **8**, e10328 (2023). https://doi.org:10.1002/btm2.10328

219 Lopez-Martinez, S. *et al.* Bioengineered endometrial hydrogels with growth factors promote tissue regeneration and restore fertility in murine models. *Acta Biomater* **135**, 113-125 (2021). https://doi.org:10.1016/j.actbio.2021.08.025
220 Deng, Q. *et al.* PF-127 hydrogel plus sodium ascorbyl phosphate improves Wharton's jelly mesenchymal stem cell-mediated skin wound healing in mice. *Stem Cell Res Ther* **11**, 143 (2020). https://doi.org:10.1186/s13287-020-01638-2
221 Xiao, B. *et al.* PGS Scaffolds Promote the In Vivo Survival and Directional Differentiation of Bone Marrow Mesenchymal Stem Cells Restoring the Morphology and Function of Wounded Rat Uterus. *Adv Healthc Mater* **8**, e1801455 (2019). https://doi.org:10.1002/adhm.201801455
222 Lin, Y. *et al.* Application of Hydrogel-Based Delivery System in Endometrial Repair. *ACS Appl Bio Mater* **3**, 7278-7290 (2020). https://doi.org:10.1021/acsabm.0c00971
223 Kuramoto, G. *et al.* Human Mesenchymal Stem Cell Sheets Improve Uterine Incision Repair in a Rodent Hysterotomy Model. *Am J Perinatol* **39**, 1212-1222 (2022). https://doi.org:10.1055/s-0040-1721718
224 Xing, Q. *et al.* Decellularization of fibroblast cell sheets for natural extracellular matrix scaffold preparation. *Tissue Eng Part C Methods* **21**, 77-87 (2015). https://doi.org:10.1089/ten.tec.2013.0666
225 Jahanbani, Y., Davaran, S., Ghahremani-Nasab, M., Aghebati-Maleki, L. & Yousefi, M. Scaffold-based tissue engineering approaches in treating infertility. *Life Sci* **240**, 117066 (2020). https://doi.org:10.1016/j.lfs.2019.117066
226 Xin, L. *et al.* A collagen scaffold loaded with human umbilical cord-derived mesenchymal stem cells facilitates endometrial regeneration and restores fertility. *Acta Biomater* **92**, 160-171 (2019). https://doi.org:10.1016/j.actbio.2019.05.012
227 Park, J. Y. *et al.* A microphysiological model of human trophoblast invasion during implantation. *Nat Commun* **13**, 1252 (2022). https://doi.org:10.1038/s41467-022-28663-4
228 Fitzgerald, H. C., Schust, D. J. & Spencer, T. E. In vitro models of the human endometrium: evolution and application for women's health. *Biol Reprod* **104**, 282-293 (2021). https://doi.org:10.1093/biolre/ioaa183
229 Han, Q. & Du, Y. Advances in the Application of Biomimetic Endometrium Interfaces for Uterine Bioengineering in Female Infertility. *Front Bioeng Biotechnol* **8**, 153 (2020). https://doi.org:10.3389/fbioe.2020.00153
230 Fitzgerald, H. C., Dhakal, P., Behura, S. K., Schust, D. J. & Spencer, T. E. Self-renewing endometrial epithelial organoids of the human uterus. *Proc Natl Acad Sci U S A* **116**, 23132-23142 (2019). https://doi.org:10.1073/pnas.1915389116
231 Heidari Kani, M. *et al.* 3D Cell Culturing and Possibilities for Myometrial Tissue Engineering. *Ann Biomed Eng* **45**, 1746-1757 (2017). https://doi.org:10.1007/s10439-016-1749-5
232 Friedenstein, A. J., Chailakhjan, R. K. & Lalykina, K. S. The development of fibroblast colonies in monolayer cultures of guinea-pig bone marrow and spleen cells. *Cell Tissue Kinet* **3**, 393-403 (1970). https://doi.org:10.1111/j.1365-2184.1970.tb00347.x
233 Charbord, P. Bone marrow mesenchymal stem cells: historical overview and concepts. *Hum Gene Ther* **21**, 1045-1056 (2010). https://doi.org:10.1089/hum.2010.115
234 Chen, T., Yang, T., Zhang, W. & Shao, J. The therapeutic potential of mesenchymal stem cells in treating osteoporosis. *Biol Res* **54**, 42 (2021). https://doi.org:10.1186/s40659-021-00366-y
235 Song, N., Scholtemeijer, M. & Shah, K. Mesenchymal Stem Cell Immunomodulation: Mechanisms and Therapeutic Potential. *Trends Pharmacol Sci* **41**, 653-664 (2020). https://doi.org:10.1016/j.tips.2020.06.009
236 Cowden, K., Dias-Netipanyj, M. F. & Popat, K. C. Adhesion and Proliferation of Human Adipose-Derived Stem Cells on Titania Nanotube Surfaces. *Regenerative Engineering and Translational Medicine* **5**, 435-445 (2019). https://doi.org:10.1007/s40883-019-00091-9
237 Khaw, J. S., Bowen, C. R. & Cartmell, S. H. Effect of TiO(2) Nanotube Pore Diameter on Human Mesenchymal Stem Cells and Human Osteoblasts. *Nanomaterials (Basel)* **10** (2020). https://doi.org:10.3390/nano10112117

238 Kong, K. *et al.* TiO(2) Nanotubes Promote Osteogenic Differentiation Through Regulation of Yap and Piezo1. *Front Bioeng Biotechnol* **10**, 872088 (2022). https://doi.org:10.3389/fbioe.2022.872088
239 Du, L., Fan, Q., Tu, B., Yan, W. & Tang, T. Establishment and characterization of a new highly metastatic human osteosarcoma cell line derived from Saos2. *Int J Clin Exp Pathol* **7**, 2871-2882 (2014).
240 Czekanska, E. M., Stoddart, M. J., Richards, R. G. & Hayes, J. S. In search of an osteoblast cell model for in vitro research. *Eur Cell Mater* **24**, 1-17 (2012). https://doi.org:10.22203/ecm.v024a01
241 Todaro, G. J. & Green, H. Quantitative studies of the growth of mouse embryo cells in culture and their development into established lines. *J Cell Biol* **17**, 299-313 (1963). https://doi.org:10.1083/jcb.17.2.299
242 Teng, F. Y. *et al.* A comparison of epithelial cells, fibroblasts, and osteoblasts in dental implant titanium topographies. *Bioinorg Chem Appl* **2012**, 687291 (2012). https://doi.org:10.1155/2012/687291
243 Monga, M., Ku, C. Y., Dodge, K. & Sanborn, B. M. Oxytocin-stimulated responses in a pregnant human immortalized myometrial cell line. *Biol Reprod* **55**, 427-432 (1996). https://doi.org:10.1095/biolreprod55.2.427
244 Rajagopal, S. P., Hutchinson, J. L., Dorward, D. A., Rossi, A. G. & Norman, J. E. Crosstalk between monocytes and myometrial smooth muscle in culture generates synergistic pro-inflammatory cytokine production and enhances myocyte contraction, with effects opposed by progesterone. *Mol Hum Reprod* **21**, 672-686 (2015). https://doi.org:10.1093/molehr/gav027
245 Makieva, S. *et al.* Androgen-Induced Relaxation of Uterine Myocytes Is Mediated by Blockade of Both Ca(2+) Flux and MLC Phosphorylation. *J Clin Endocrinol Metab* **101**, 1055-1065 (2016). https://doi.org:10.1210/jc.2015-2851
246 Siricilla, S. *et al.* Comparative analysis of myometrial and vascular smooth muscle cells to determine optimal cells for use in drug discovery. *Pharmacol Res* **146**, 104268 (2019). https://doi.org:10.1016/j.phrs.2019.104268
247 Jeon, H., Simon, C. G., Jr. & Kim, G. A mini-review: Cell response to microscale, nanoscale, and hierarchical patterning of surface structure. *J Biomed Mater Res B Appl Biomater* **102**, 1580-1594 (2014). https://doi.org:10.1002/jbm.b.33158
248 Zhang, Y., Gordon, A., Qian, W. & Chen, W. Engineering nanoscale stem cell niche: direct stem cell behavior at cell-matrix interface. *Adv Healthc Mater* **4**, 1900-1914 (2015). https://doi.org:10.1002/adhm.201500351
249 Zhukova, Y. & Skorb, E. V. Cell Guidance on Nanostructured Metal Based Surfaces. *Adv Healthc Mater* **6** (2017). https://doi.org:10.1002/adhm.201600914
250 Hogrebe, N. J., Reinhardt, J. W. & Gooch, K. J. Biomaterial microarchitecture: a potent regulator of individual cell behavior and multicellular organization. *J Biomed Mater Res A* **105**, 640-661 (2017). https://doi.org:10.1002/jbm.a.35914
251 Wang, S., Li, J., Zhou, Z., Zhou, S. & Hu, Z. Micro-/Nano-Scales Direct Cell Behavior on Biomaterial Surfaces. *Molecules* **24**, 1-13 (2018). https://doi.org:10.3390/molecules24010075
252 Limongi, T. *et al.* Fabrication and Applications of Micro/Nanostructured Devices for Tissue Engineering. *Nanomicro Lett* **9**, 1 (2017). https://doi.org:10.1007/s40820-016-0103-7
253 Simitzi, C., Ranella, A. & Stratakis, E. Controlling the morphology and outgrowth of nerve and neuroglial cells: The effect of surface topography. *Acta Biomater* **51**, 21-52 (2017). https://doi.org:10.1016/j.actbio.2017.01.023
254 Chen, Z. *et al.* Nanotopography-based strategy for the precise manipulation of osteoimmunomodulation in bone regeneration. *Nanoscale* **9**, 18129-18152 (2017). https://doi.org:10.1039/c7nr05913b
255 Chen, S. *et al.* Tuning surface properties of bone biomaterials to manipulate osteoblastic cell adhesion and the signaling pathways for the enhancement of early osseointegration. *Colloids Surf B Biointerfaces* **164**, 58-69 (2018). https://doi.org:10.1016/j.colsurfb.2018.01.022
256 Greiner, A. M. *et al.* Nano- and microstructured materials for in vitro studies of the physiology of vascular cells. *Beilstein J Nanotechnol* **7**, 1620-1641 (2016). https://doi.org:10.3762/bjnano.7.155

257 Dobbenga, S., Fratila-Apachitei, L. E. & Zadpoor, A. A. Nanopattern-induced osteogenic differentiation of stem cells - A systematic review. *Acta Biomater* **46**, 3-14 (2016). https://doi.org:10.1016/j.actbio.2016.09.031

258 Park, J. *et al.* Synergistic control of mesenchymal stem cell differentiation by nanoscale surface geometry and immobilized growth factors on TiO2 nanotubes. *Small* **8**, 98-107 (2012). https://doi.org:10.1002/smll.201100790

259 Tan, A. W., Pingguan-Murphy, B., Ahmad, R. & Akbar, S. A. Review of titania nanotubes: Fabrication and cellular response. *Ceramics International* **38**, 4421-4435 (2012). https://doi.org:10.1016/j.ceramint.2012.03.002

260 Minagar, S., Wang, J., Berndt, C. C., Ivanova, E. P. & Wen, C. Cell response of anodized nanotubes on titanium and titanium alloys. *J Biomed Mater Res A* **101**, 2726-2739 (2013). https://doi.org:10.1002/jbm.a.34575

261 Khudhair, D. *et al.* Anodization parameters influencing the morphology and electrical properties of TiO2 nanotubes for living cell interfacing and investigations. *Mater Sci Eng C Mater Biol Appl* **59**, 1125-1142 (2016). https://doi.org:10.1016/j.msec.2015.10.042

262 Bai, L. *et al.* The effects of TiO(2) nanotube arrays with different diameters on macrophage/endothelial cell response and ex vivo hemocompatibility. *J Mater Chem B* **6**, 6322-6333 (2018). https://doi.org:10.1039/c8tb01675e

263 von der Mark, K., Bauer, S., Park, J. & Schmuki, P. Another look at "Stem cell fate dictated solely by altered nanotube dimension". *Proc Natl Acad Sci U S A* **106**, E60; author reply E61 (2009). https://doi.org:10.1073/pnas.0903663106

264 Oh, S. *et al.* Reply to von der Mark et al.: Looking further into the effects of nanotube dimension on stem cell fate. *Proc Natl Acad Sci U S A* **106** (2009). https://doi.org:10.1073/pnas.0904869106

265 Li, M. & Yang, Y. Nanoscale TiO(2) nanotubes as a basis for governing cell behaviors and application challenges. *Int J Nanomedicine* **12**, 575-576 (2017). https://doi.org:10.2147/IJN.S128749

266 Yu, W., Qian, C., Jiang, X., Zhang, F. & Weng, W. Mechanisms of stem cell osteogenic differentiation on TiO2 nanotubes. *Colloids Surf B Biointerfaces* **136**, 779-785 (2015). https://doi.org:10.1016/j.colsurfb.2015.10.019

267 Biggs, M. J., Richards, R. G., Gadegaard, N., Wilkinson, C. D. & Dalby, M. J. The effects of nanoscale pits on primary human osteoblast adhesion formation and cellular spreading. *J Mater Sci Mater Med* **18**, 399-404 (2007). https://doi.org:10.1007/s10856-006-0705-6

268 Dalby, M. J. *et al.* The control of human mesenchymal cell differentiation using nanoscale symmetry and disorder. *Nat Mater* **6**, 997-1003 (2007). https://doi.org:10.1038/nmat2013

269 Li, S., Zhang, G., Guo, D., Yu, L. & Zhang, W. Anodization Fabrication of Highly Ordered TiO2Nanotubes. *The Journal of Physical Chemistry C* **113**, 12759-12765 (2009). https://doi.org:10.1021/jp903037f

270 Yu, D., Song, Y., Zhu, X., Yang, R. & Han, A. Morphological evolution of TiO2 nanotube arrays with lotus-root-shaped nanostructure. *Applied Surface Science* **276**, 711-716 (2013). https://doi.org:10.1016/j.apsusc.2013.03.158

271 Jin, R. *et al.* Formation Mechanism of Lotus-root-shaped Nanostructure during Two-step Anodization. *Electrochimica Acta* **188**, 421-427 (2016). https://doi.org:10.1016/j.electacta.2015.12.027

272 Paterlini, T. T. *et al.* The role played by modified bioinspired surfaces in interfacial properties of biomaterials. *Biophys Rev* **9**, 683-698 (2017). https://doi.org:10.1007/s12551-017-0306-2

273 Liu, X. *et al.* Subcellular cell geometry on micropillars regulates stem cell differentiation. *Biomaterials* **111**, 27-39 (2016). https://doi.org:10.1016/j.biomaterials.2016.09.023

274 Biggs, M. J., Richards, R. G. & Dalby, M. J. Nanotopographical modification: a regulator of cellular function through focal adhesions. *Nanomedicine* **6**, 619-633 (2010). https://doi.org:10.1016/j.nano.2010.01.009

275 Huang, J. *et al.* Impact of order and disorder in RGD nanopatterns on cell adhesion. *Nano Lett* **9**, 1111-1116 (2009). https://doi.org:10.1021/nl803548b

276 Yu, W. Q., Jiang, X. Q., Zhang, F. Q. & Xu, L. The effect of anatase TiO2 nanotube layers on MC3T3-E1 preosteoblast adhesion, proliferation, and differentiation. *J Biomed Mater Res A* **94**, 1012-1022 (2010). https://doi.org:10.1002/jbm.a.32687
277 Tsuchiya, H. *et al.* Hydroxyapatite growth on anodic TiO2 nanotubes. *J Biomed Mater Res A* **77**, 534-541 (2006). https://doi.org:10.1002/jbm.a.30677
278 Su, Z., Zhang, L., Jiang, F. & Hong, M. Formation of crystalline TiO2 by anodic oxidation of titanium. *Progress in Natural Science: Materials International* **23**, 294-301 (2013). https://doi.org:10.1016/j.pnsc.2013.04.004
279 Gui, N. *et al.* The effect of ordered and partially ordered surface topography on bone cell responses: a review. *Biomater Sci* **6**, 250-264 (2018). https://doi.org:10.1039/c7bm01016h
280 Yi, J.-H. *et al.* Characterization of a bioactive nanotextured surface created by controlled chemical oxidation of titanium. *Surface Science* **600**, 4613-4621 (2006). https://doi.org:10.1016/j.susc.2006.07.053
281 Wang, X. *et al.* Mechanical stability of the cell nucleus - roles played by the cytoskeleton in nuclear deformation and strain recovery. *J Cell Sci* **131** (2018). https://doi.org:10.1242/jcs.209627
282 Brammer, K. S. *et al.* Improved bone-forming functionality on diameter-controlled TiO(2) nanotube surface. *Acta Biomater* **5**, 3215-3223 (2009). https://doi.org:10.1016/j.actbio.2009.05.008
283 Tomakidi, P., Schulz, S., Proksch, S., Weber, W. & Steinberg, T. Focal adhesion kinase (FAK) perspectives in mechanobiology: implications for cell behaviour. *Cell Tissue Res* **357**, 515-526 (2014). https://doi.org:10.1007/s00441-014-1945-2
284 Biggs, M. J. & Dalby, M. J. Focal adhesions in osteoneogenesis. *Proc Inst Mech Eng H* **224**, 1441-1453 (2010). https://doi.org:10.1243/09544119JEIM775
285 Nagano, M., Hoshino, D., Koshikawa, N., Akizawa, T. & Seiki, M. Turnover of focal adhesions and cancer cell migration. *Int J Cell Biol* **2012**, 310616 (2012). https://doi.org:10.1155/2012/310616
286 Tsimbouri, P. *et al.* Nanotopographical effects on mesenchymal stem cell morphology and phenotype. *J Cell Biochem* **115**, 380-390 (2014). https://doi.org:10.1002/jcb.24673
287 Schlie, S., Gruene, M., Dittmar, H. & Chichkov, B. N. Dynamics of cell attachment: adhesion time and force. *Tissue Eng Part C Methods* **18**, 688-696 (2012). https://doi.org:10.1089/ten.TEC.2011.0635
288 Cao, X. *et al.* Multiscale model predicts increasing focal adhesion size with decreasing stiffness in fibrous matrices. *Proc Natl Acad Sci U S A* **114**, E4549-E4555 (2017). https://doi.org:10.1073/pnas.1620486114
289 Legerstee, K., Geverts, B., Slotman, J. A. & Houtsmuller, A. B. Dynamics and distribution of paxillin, vinculin, zyxin and VASP depend on focal adhesion location and orientation. *Sci Rep* **9**, 10460 (2019). https://doi.org:10.1038/s41598-019-46905-2
290 Liu, J. *et al.* Talin determines the nanoscale architecture of focal adhesions. *Proc Natl Acad Sci U S A* **112**, E4864-4873 (2015). https://doi.org:10.1073/pnas.1512025112
291 Humphries, J. D. *et al.* Vinculin controls focal adhesion formation by direct interactions with talin and actin. *J Cell Biol* **179**, 1043-1057 (2007). https://doi.org:10.1083/jcb.200703036
292 Bauer, S., Park, J., von der Mark, K. & Schmuki, P. Improved attachment of mesenchymal stem cells on super-hydrophobic TiO2 nanotubes. *Acta Biomater* **4**, 1576-1582 (2008). https://doi.org:10.1016/j.actbio.2008.04.004
293 Teo, B. K. *et al.* Nanotopography modulates mechanotransduction of stem cells and induces differentiation through focal adhesion kinase. *ACS Nano* **7**, 4785-4798 (2013). https://doi.org:10.1021/nn304966z
294 Lai, M., Cai, K., Hu, Y., Yang, X. & Liu, Q. Regulation of the behaviors of mesenchymal stem cells by surface nanostructured titanium. *Colloids Surf B Biointerfaces* **97**, 211-220 (2012). https://doi.org:10.1016/j.colsurfb.2012.04.029
295 Lavenus, S. *et al.* Adhesion and osteogenic differentiation of human mesenchymal stem cells on titanium nanopores. *Eur Cell Mater* **22**, 84-96 (2011). https://doi.org:10.22203/ecm.v022a07

296 Shin, Y. C. *et al.* Enhanced osteogenic differentiation of human mesenchymal stem cells on Ti surfaces with electrochemical nanopattern formation. *Mater Sci Eng C Mater Biol Appl* **99**, 1174-1181 (2019). https://doi.org:10.1016/j.msec.2019.02.039
297 Nakashima, K. *et al.* The novel zinc finger-containing transcription factor osterix is required for osteoblast differentiation and bone formation. *Cell* **108**, 17-29 (2002). https://doi.org:10.1016/s0092-8674(01)00622-5
298 Nishio, Y. *et al.* Runx2-mediated regulation of the zinc finger Osterix/Sp7 gene. *Gene* **372**, 62-70 (2006). https://doi.org:10.1016/j.gene.2005.12.022
299 Artigas, N., Urena, C., Rodriguez-Carballo, E., Rosa, J. L. & Ventura, F. Mitogen-activated protein kinase (MAPK)-regulated interactions between Osterix and Runx2 are critical for the transcriptional osteogenic program. *J Biol Chem* **289**, 27105-27117 (2014). https://doi.org:10.1074/jbc.M114.576793
300 Mandair, G. S. & Morris, M. D. Contributions of Raman spectroscopy to the understanding of bone strength. *Bonekey Rep* **4**, 620 (2015). https://doi.org:10.1038/bonekey.2014.115
301 Morris, M. D. & Mandair, G. S. Raman assessment of bone quality. *Clin Orthop Relat Res* **469**, 2160-2169 (2011). https://doi.org:10.1007/s11999-010-1692-y
302 Stewart, S. *et al.* Trends in early mineralization of murine calvarial osteoblastic cultures: a Raman microscopic study. *Journal of Raman Spectroscopy* **33**, 536-543 (2002). https://doi.org:10.1002/jrs.892
303 Stammeier, J. A., Purgstaller, B., Hippler, D., Mavromatis, V. & Dietzel, M. In-situ Raman spectroscopy of amorphous calcium phosphate to crystalline hydroxyapatite transformation. *MethodsX* **5**, 1241-1250 (2018). https://doi.org:10.1016/j.mex.2018.09.015
304 Crane, N. J., Popescu, V., Morris, M. D., Steenhuis, P. & Ignelzi, M. A., Jr. Raman spectroscopic evidence for octacalcium phosphate and other transient mineral species deposited during intramembranous mineralization. *Bone* **39**, 434-442 (2006). https://doi.org:10.1016/j.bone.2006.02.059
305 Yerramshetty, J. S., Lind, C. & Akkus, O. The compositional and physicochemical homogeneity of male femoral cortex increases after the sixth decade. *Bone* **39**, 1236-1243 (2006). https://doi.org:10.1016/j.bone.2006.06.002
306 Alakpa, E. V. *et al.* Nacre Topography Produces Higher Crystallinity in Bone than Chemically Induced Osteogenesis. *ACS Nano* **11**, 6717-6727 (2017). https://doi.org:10.1021/acsnano.7b01044
307 Marklein, R. A. *et al.* High Content Imaging of Early Morphological Signatures Predicts Long Term Mineralization Capacity of Human Mesenchymal Stem Cells upon Osteogenic Induction. *Stem Cells* **34**, 935-947 (2016). https://doi.org:10.1002/stem.2322
308 Magin, C. M., Alge, D. L. & Anseth, K. S. Bio-inspired 3D microenvironments: a new dimension in tissue engineering. *Biomed Mater* **11**, 022001 (2016). https://doi.org:10.1088/1748-6041/11/2/022001
309 Wang, D., Yu, B., Wang, C., Zhou, F. & Liu, W. A Novel Protocol Toward Perfect Alignment of Anodized TiO2 Nanotubes. *Advanced Materials* **21**, 1964-1967 (2009). https://doi.org:10.1002/adma.200801996
310 Schneider, C. A., Rasband, W. S. & Eliceiri, K. W. NIH Image to ImageJ: 25 years of image analysis. *Nat Methods* **9**, 671-675 (2012). https://doi.org:10.1038/nmeth.2089
311 Carpenter, A. E. *et al.* CellProfiler: image analysis software for identifying and quantifying cell phenotypes. *Genome Biol* **7**, R100 (2006). https://doi.org:10.1186/gb-2006-7-10-r100
312 Horcas, I. *et al.* WSXM: a software for scanning probe microscopy and a tool for nanotechnology. *Rev Sci Instrum* **78**, 013705 (2007). https://doi.org:10.1063/1.2432410
313 Bormashenko, E. *et al.* Characterization of Self-Assembled 2D Patterns with Voronoi Entropy. *Entropy (Basel)* **20**, 1-18 (2018). https://doi.org:10.3390/e20120956
314 Steyer, A., Guenoun, P., Beysens, D. & Knobler, C. M. Two-dimensional ordering during droplet growth on a liquid surface. *Phys Rev B Condens Matter* **42**, 1086-1089 (1990). https://doi.org:10.1103/physrevb.42.1086
315 Farlay, D., Panczer, G., Rey, C., Delmas, P. D. & Boivin, G. Mineral maturity and crystallinity index are distinct characteristics of bone mineral. *J Bone Miner Metab* **28**, 433-445 (2010). https://doi.org:10.1007/s00774-009-0146-7

316 Versaevel, M., Grevesse, T. & Gabriele, S. Spatial coordination between cell and nuclear shape within micropatterned endothelial cells. *Nat Commun* **3**, 671 (2012). https://doi.org:10.1038/ncomms1668
317 Hardcastle, F. D., Ishihara, H., Sharma, R. & Biris, A. S. Photoelectroactivity and Raman spectroscopy of anodized titania (TiO2) photoactive water-splitting catalysts as a function of oxygen-annealing temperature. *Journal of Materials Chemistry* **21**, 6337-6345 (2011). https://doi.org:10.1039/c0jm03106b
318 Penel, G., Leroy, G., Rey, C. & Bres, E. MicroRaman spectral study of the PO4 and CO3 vibrational modes in synthetic and biological apatites. *Calcif Tissue Int* **63**, 475-481 (1998). https://doi.org:10.1007/s002239900561
319 Awonusi, A., Morris, M. D. & Tecklenburg, M. M. Carbonate assignment and calibration in the Raman spectrum of apatite. *Calcif Tissue Int* **81**, 46-52 (2007). https://doi.org:10.1007/s00223-007-9034-0
320 Carden, A. & Morris, M. D. Application of vibrational spectroscopy to the study of mineralized tissues (review). *J Biomed Opt* **5**, 259-268 (2000). https://doi.org:10.1117/1.429994
321 Morris, M. D. & Finney, W. F. Recent developments in Raman and infrared spectroscopy and imaging of bone tissue. *J. Spectrosc.* **18**, 155-159 (2004). https://doi.org:10.1155/2004/765753
322 Wopenka, B. & Pasteris, J. D. A mineralogical perspective on the apatite in bone. *Materials Science and Engineering: C* **25**, 131-143 (2005). https://doi.org:10.1016/j.msec.2005.01.008
323 Massey, F. J. The Kolmogorov-Smirnov Test for Goodness of Fit. *Journal of the American Statistical Association* **46**, 68-78 (1951). https://doi.org:10.1080/01621459.1951.10500769
324 Ruxton, G. D. The unequal variance t-test is an underused alternative to Student's t-test and the Mann–Whitney U test. *Behavioral Ecology* **17**, 688-690 (2006). https://doi.org:10.1093/beheco/ark016
325 von Wilmowsky, C., Moest, T., Nkenke, E., Stelzle, F. & Schlegel, K. A. Implants in bone: part I. A current overview about tissue response, surface modifications and future perspectives. *Oral Maxillofac Surg* **18**, 243-257 (2014). https://doi.org:10.1007/s10006-013-0398-1
326 Jurczak, P., Witkowska, J., Rodziewicz-Motowidlo, S. & Lach, S. Proteins, peptides and peptidomimetics as active agents in implant surface functionalization. *Adv Colloid Interface Sci* **276**, 102083 (2020). https://doi.org:10.1016/j.cis.2019.102083
327 Faia-Torres, A. B. *et al.* Osteogenic differentiation of human mesenchymal stem cells in the absence of osteogenic supplements: A surface-roughness gradient study. *Acta Biomater* **28**, 64-75 (2015). https://doi.org:10.1016/j.actbio.2015.09.028
328 Lossdorfer, S. *et al.* Microrough implant surface topographies increase osteogenesis by reducing osteoclast formation and activity. *J Biomed Mater Res A* **70**, 361-369 (2004). https://doi.org:10.1002/jbm.a.30025
329 Barthes, J. *et al.* Review: the potential impact of surface crystalline states of titanium for biomedical applications. *Crit Rev Biotechnol* **38**, 423-437 (2018). https://doi.org:10.1080/07388551.2017.1363707
330 Kino-Oka, M. *et al.* Morphological evaluation of chondrogenic potency in passaged cell populations. *J Biosci Bioeng* **107**, 544-551 (2009). https://doi.org:10.1016/j.jbiosc.2008.12.018
331 Andrukhov, O. *et al.* Proliferation, behavior, and differentiation of osteoblasts on surfaces of different microroughness. *Dent Mater* **32**, 1374-1384 (2016). https://doi.org:10.1016/j.dental.2016.08.217
332 Nečas, D. & Klapetek, P. Gwyddion: an open-source software for SPM data analysis. *Open Physics* **10**, 181-188 (2012). https://doi.org:10.2478/s11534-011-0096-2
333 Ball, V. Physicochemical perspective on "polydopamine" and "poly(catecholamine)" films for their applications in biomaterial coatings. *Biointerphases* **9**, 030801 (2014). https://doi.org:10.1116/1.4875115
334 Zhang, C. *et al.* Deposition and Adhesion of Polydopamine on the Surfaces of Varying Wettability. *ACS Appl Mater Interfaces* **9**, 30943-30950 (2017). https://doi.org:10.1021/acsami.7b09774
335 Lee, H. A., Ma, Y., Zhou, F., Hong, S. & Lee, H. Material-Independent Surface Chemistry beyond Polydopamine Coating. *Acc Chem Res* **52**, 704-713 (2019). https://doi.org:10.1021/acs.accounts.8b00583
336 Ding, Y. H., Floren, M. & Tan, W. Mussel-inspired polydopamine for bio-surface functionalization. *Biosurf Biotribol* **2**, 121-136 (2016). https://doi.org:10.1016/j.bsbt.2016.11.001

337 Hong, S., Wang, Y., Park, S. Y. & Lee, H. Progressive fuzzy cation-pi assembly of biological catecholamines. *Sci Adv* **4**, eaat7457 (2018). https://doi.org:10.1126/sciadv.aat7457
338 Chen, F. *et al.* Nanoscale Polydopamine (PDA) Meets pi-pi Interactions: An Interface-Directed Coassembly Approach for Mesoporous Nanoparticles. *Langmuir* **32**, 12119-12128 (2016). https://doi.org:10.1021/acs.langmuir.6b03294
339 Svoboda, J., Kral, M., Dendisova, M., Matejka, P. & Pop-Georgievski, O. Unraveling the influence of substrate on the growth rate, morphology and covalent structure of surface adherent polydopamine films. *Colloids Surf B Biointerfaces* **205**, 111897 (2021). https://doi.org:10.1016/j.colsurfb.2021.111897
340 Chan, W. Investigation of the chemical structure and formation mechanism of polydopamine from self-assembly of dopamine by liquid chromatography/mass spectrometry coupled with isotope-labelling techniques. *Rapid Commun Mass Spectrom* **33**, 429-436 (2019). https://doi.org:10.1002/rcm.8373
341 Hong, S. *et al.* Non ‐ Covalent Self ‐ Assembly and Covalent Polymerization Co ‐ Contribute to Polydopamine Formation. *Advanced Functional Materials* **22**, 4711-4717 (2012). https://doi.org:10.1002/adfm.201201156
342 Michalicha, A., Roguska, A., Przekora, A., Budzynska, B. & Belcarz, A. Poly(levodopa)-modified beta-glucan as a candidate for wound dressings. *Carbohydr Polym* **272**, 118485 (2021). https://doi.org:10.1016/j.carbpol.2021.118485
343 Hong, S. *et al.* Poly(norepinephrine): ultrasmooth material-independent surface chemistry and nanodepot for nitric oxide. *Angew Chem Int Ed Engl* **52**, 9187-9191 (2013). https://doi.org:10.1002/anie.201301646
344 Taskin, M. B. *et al.* Poly(norepinephrine) as a functional bio-interface for neuronal differentiation on electrospun fibers. *Phys Chem Chem Phys* **17**, 9446-9453 (2015). https://doi.org:10.1039/c5cp00413f
345 Kang, S. M., Rho, J., Choi, I. S., Messersmith, P. B. & Lee, H. Norepinephrine: material-independent, multifunctional surface modification reagent. *J Am Chem Soc* **131**, 13224-13225 (2009). https://doi.org:10.1021/ja905183k
346 Shen, Y. *et al.* Enzymatic polymerization of enantiomeric (L)-3,4-dihydroxyphenylalanine into films with enhanced rigidity and stability. *Nat Commun* **14**, 3054 (2023). https://doi.org:10.1038/s41467-023-38845-3
347 Lu, Z., Acter, S., Teo, B. M. & Tabor, R. F. Synthesis and characterisation of polynorepinephrine-shelled microcapsules via an oil-in-water emulsion templating route. *J Mater Chem B* **9**, 9575-9582 (2021). https://doi.org:10.1039/d1tb01786a
348 Lu, Z. *et al.* Bioinspired polynorepinephrine nanoparticles as an efficient vehicle for enhanced drug delivery. *J Mater Chem B* **8**, 961-968 (2020). https://doi.org:10.1039/c9tb02375e
349 Lu, Z. *et al.* Polynorepinephrine as an Efficient Antifouling-Coating Material and Its Application as a Bacterial Killing Photothermal Agent. *ACS Appl Bio Mater* **3**, 5880-5886 (2020). https://doi.org:10.1021/acsabm.0c00578
350 Baldoneschi, V., Palladino, P., Banchini, M., Minunni, M. & Scarano, S. Norepinephrine as new functional monomer for molecular imprinting: An applicative study for the optical sensing of cardiac biomarkers. *Biosens Bioelectron* **157**, 112161 (2020). https://doi.org:10.1016/j.bios.2020.112161
351 Kang, S. M. & Lee, H. Surface Modification of Highly Ordered Pyrolytic Graphite (HOPG) by a Mussel-Inspired Poly(norepinephrine) Coating: Characterizations and Cell Adhesion Test. *Bulletin of the Korean Chemical Society* **34**, 960-962 (2013). https://doi.org:10.5012/bkcs.2013.34.3.960
352 Liu, Y. *et al.* A glucose biosensor based on the immobilization of glucose oxidase and Au nanocomposites with polynorepinephrine. *RSC Adv* **9**, 16439-16446 (2019). https://doi.org:10.1039/c9ra02054c
353 Liang, R. P., Xiang, C. Y., Wang, J. W. & Qiu, J. D. Preparation of polynorepinephrine adhesive coating via one-step self-polymerization for enantioselective capillary electrochromatography coupled with electrogenerated chemiluminesense detection. *J Chromatogr A* **1284**, 194-201 (2013). https://doi.org:10.1016/j.chroma.2013.02.007

354 Liu, X. *et al.* Polynorepinephrine Nanoparticles: A Novel Photothermal Nanoagent for Chemo-Photothermal Cancer Therapy. *ACS Appl Mater Interfaces* **11**, 19763-19773 (2019). https://doi.org:10.1021/acsami.9b03458
355 Yang, D., Wang, X., Ai, Q., Shi, J. & Jiang, Z. Performance comparison of immobilized enzyme on the titanate nanotube surfaces modified by poly(dopamine) and poly(norepinephrine). *RSC Advances* **5**, 42461-42467 (2015). https://doi.org:10.1039/c5ra02420j
356 Zhang, C. *et al.* CuSO4/H2O2-Induced Rapid Deposition of Polydopamine Coatings with High Uniformity and Enhanced Stability. *Angew Chem Int Ed Engl* **55**, 3054-3057 (2016). https://doi.org:10.1002/anie.201510724
357 Ha, D. & Kang, K. Nucleophilic Regulation of the Formation of Melanin-like Species by Amyloid Fibers. *ACS Omega* **7**, 773-779 (2022). https://doi.org:10.1021/acsomega.1c05399
358 Zou, Y. *et al.* Regulating the absorption spectrum of polydopamine. *Sci Adv* **6** (2020). https://doi.org:10.1126/sciadv.abb4696
359 Stark, K. B., Gallas, J. M., Zajac, G. W., Eisner, M. & Golab, J. T. Spectroscopic Study and Simulation from Recent Structural Models for Eumelanin: II. Oligomers. *The Journal of Physical Chemistry B* **107**, 11558-11562 (2003). https://doi.org:10.1021/jp034965r
360 Gauden, M. *et al.* Ultrafast excited state dynamics of 5,6-dihydroxyindole, a key eumelanin building block: nonradiative decay mechanism. *J Phys Chem B* **113**, 12575-12580 (2009). https://doi.org:10.1021/jp903190k
361 d'Ischia, M. *et al.* Structural effects on the electronic absorption properties of 5,6-dihydroxyindole oligomers: the potential of an integrated experimental and DFT approach to model eumelanin optical properties. *Photochem Photobiol* **84**, 600-607 (2008). https://doi.org:10.1111/j.1751-1097.2007.00249.x
362 Nofsinger, J. B., Forest, S. E., Eibest, L. M., Gold, K. A. & Simon, J. D. Probing the building blocks of eumelanins using scanning electron microscopy. *Pigment Cell Res* **13**, 179-184 (2000). https://doi.org:10.1034/j.1600-0749.2000.130310.x
363 Winterwerber, P., Harvey, S., Ng, D. Y. W. & Weil, T. Photocontrolled Dopamine Polymerization on DNA Origami with Nanometer Resolution. *Angew Chem Int Ed Engl* **59**, 6144-6149 (2020). https://doi.org:10.1002/anie.201911249
364 Stark, K. B. *et al.* Effect of stacking and redox state on optical absorption spectra of melanins -- comparison of theoretical and experimental results. *J Phys Chem B* **109**, 1970-1977 (2005). https://doi.org:10.1021/jp046710z
365 Bernsmann, F. *et al.* Melanin-containing films: growth from dopamine solutions versus layer-by-layer deposition. *Chemphyschem* **11**, 3299-3305 (2010). https://doi.org:10.1002/cphc.201000384
366 Abbas, M. *et al.* Structural, electrical, electronic and optical properties of melanin films. *Eur Phys J E Soft Matter* **28**, 285-291 (2009). https://doi.org:10.1140/epje/i2008-10437-9
367 Lv, Y. *et al.* The synthesis and adhesive performance of the poly(N-benzyloxycarbonyl-3,4-dihydroxyphenylalanine) derived from 3,4-dihydroxyphenylalanine. *Journal of Adhesion Science and Technology* **27**, 81-89 (2013). https://doi.org:10.1080/01694243.2012.701508
368 Thompson, A., Land, E. J., Chedekel, M. R., Subbarao, K. V. & Truscott, T. G. A pulse radiolysis investigation of the oxidation of the melanin precursors 3,4-dihydroxyphenylalanine (dopa) and the cysteinyldopas. *Biochim Biophys Acta* **843**, 49-57 (1985). https://doi.org:10.1016/0304-4165(85)90048-0
369 Sharma, S. K., Durand, G. & Pucci, B. Synthesis and Determination of Polymerization Rate Constants of Glucose-Based Monomers. *Designed Monomers and Polymers* **14**, 499-513 (2012). https://doi.org:10.1163/138577211x587690
370 Oral, E. & Peppas, N. A. Dynamic studies of molecular imprinting polymerizations. *Polymer* **45**, 6163-6173 (2004). https://doi.org:10.1016/j.polymer.2004.06.059
371 Elroby, S. A. K., Makki, M. S. I., Sobahi, T. R. & Hilal, R. H. Toward the understanding of the metabolism of levodopa I. DFT investigation of the equilibrium geometries, acid-base properties and levodopa-water complexes. *Int J Mol Sci* **13**, 4321-4339 (2012). https://doi.org:10.3390/ijms13044321

372 Nieto, C., Vega, M. A., Enrique, J., Marcelo, G. & Martin Del Valle, E. M. Size Matters in the Cytotoxicity of Polydopamine Nanoparticles in Different Types of Tumors. *Cancers (Basel)* **11** (2019). https://doi.org:10.3390/cancers11111679
373 Mitchell, M. J. *et al.* Engineering precision nanoparticles for drug delivery. *Nat Rev Drug Discov* **20**, 101-124 (2021). https://doi.org:10.1038/s41573-020-0090-8
374 Patra, J. K. *et al.* Nano based drug delivery systems: recent developments and future prospects. *J Nanobiotechnology* **16**, 71 (2018). https://doi.org:10.1186/s12951-018-0392-8
375 Behzadi, S. *et al.* Cellular uptake of nanoparticles: journey inside the cell. *Chem Soc Rev* **46**, 4218-4244 (2017). https://doi.org:10.1039/c6cs00636a
376 Rennick, J. J., Johnston, A. P. R. & Parton, R. G. Key principles and methods for studying the endocytosis of biological and nanoparticle therapeutics. *Nat Nanotechnol* **16**, 266-276 (2021). https://doi.org:10.1038/s41565-021-00858-8
377 He, Y. *et al.* Pyrrole-Doped Polydopamine-Pyrrole (PDA-nPY) Nanoparticles with Tunable Size and Improved NIR Absorption for Photothermal Therapy. *Pharmaceuticals (Basel)* **16** (2023). https://doi.org:10.3390/ph16121642
378 Yuan, X., Zhao, X., Lin, Y. & Su, Z. Polydopamine-Based Nanoparticles for an Antibiofilm Platform: Influence of Size and Surface Charge on Their Penetration and Accumulation in S. aureus Biofilms. *Langmuir* **38**, 10662-10671 (2022). https://doi.org:10.1021/acs.langmuir.2c01650
379 Zhang, P., Xu, Q., Du, J. & Wang, Y. Polydopamine-based nanoparticles with excellent biocompatibility for photothermally enhanced gene delivery. *RSC Adv* **8**, 34596-34602 (2018). https://doi.org:10.1039/c8ra06916f
380 Lu, Z. *et al.* Mesoporous, anisotropic nanostructures from bioinspired polymeric catecholamine neurotransmitters and their potential application as photoacoustic imaging agents. *J Mater Chem B* **10**, 9662-9670 (2022). https://doi.org:10.1039/d2tb01756c
381 Liu, J. *et al.* Topochemical assembly of levodopa nanoparticles network as a high-performance biosensing platform coupling with pi-pi stacking and electrostatic repulsion interactions. *Talanta* **219**, 121285 (2020). https://doi.org:10.1016/j.talanta.2020.121285
382 Wang, X. *et al.* Quaternary Ammonium Assisted Synthesis of Melanin-like Poly(l-DOPA) Nanoparticles with a Boosted Photothermal Effect. *ACS Appl Mater Interfaces* **16**, 22493-22503 (2024). https://doi.org:10.1021/acsami.4c01513
383 Wang, X. *et al.* Eumelanin-like Poly(levodopa) Nanoscavengers for Inflammation Disease Therapy. *Biomacromolecules* **25**, 2563-2573 (2024). https://doi.org:10.1021/acs.biomac.4c00092
384 Eom, T., Barat, V., Khan, A. & Stuparu, M. C. Aggregation-free and high stability core-shell polymer nanoparticles with high fullerene loading capacity, variable fullerene type, and compatibility towards biological conditions. *Chem Sci* **12**, 4949-4957 (2021). https://doi.org:10.1039/d1sc00602a
385 Kuo, C. Y. *et al.* Bioengineering Strategies to Treat Female Infertility. *Tissue Eng Part B Rev* **23**, 294-306 (2017). https://doi.org:10.1089/ten.TEB.2016.0385
386 Bi, B. *et al.* Analysis on clinical association of uterine scar diverticulum with subsequent infertility in patients underwent cesarean section. *Medicine (Baltimore)* **100**, e27531 (2021). https://doi.org:10.1097/MD.0000000000027531
387 Vikhareva Osser, O. & Valentin, L. Risk factors for incomplete healing of the uterine incision after caesarean section. *BJOG* **117**, 1119-1126 (2010). https://doi.org:10.1111/j.1471-0528.2010.02631.x
388 Betran, A. P., Ye, J., Moller, A. B., Souza, J. P. & Zhang, J. Trends and projections of caesarean section rates: global and regional estimates. *BMJ Glob Health* **6** (2021). https://doi.org:10.1136/bmjgh-2021-005671
389 Lyell, D. J. Adhesions and perioperative complications of repeat cesarean delivery. *Am J Obstet Gynecol* **205**, S11-18 (2011). https://doi.org:10.1016/j.ajog.2011.09.029
390 Hooker, A. B. *et al.* Systematic review and meta-analysis of intrauterine adhesions after miscarriage: prevalence, risk factors and long-term reproductive outcome. *Hum Reprod Update* **20**, 262-278 (2014). https://doi.org:10.1093/humupd/dmt045

391 Ma, J. *et al.* Recent trends in therapeutic strategies for repairing endometrial tissue in intrauterine adhesion. *Biomater Res* **25**, 40 (2021). https://doi.org:10.1186/s40824-021-00242-6
392 Li, X. *et al.* Designing Regenerative Bioadhesives for Tissue Repair and Regeneration. *Advanced Therapeutics* **7** (2023). https://doi.org:10.1002/adtp.202300139
393 Zhu, W., Chuah, Y. J. & Wang, D. A. Bioadhesives for internal medical applications: A review. *Acta Biomater* **74**, 1-16 (2018). https://doi.org:10.1016/j.actbio.2018.04.034
394 Costa, P. M. *et al.* Mussel-Inspired Catechol Functionalisation as a Strategy to Enhance Biomaterial Adhesion: A Systematic Review. *Polymers (Basel)* **13** (2021). https://doi.org:10.3390/polym13193317
395 Pawar, S. A., Chand, A. N. & Kumar, A. V. Polydopamine: An Amine Oxidase Mimicking Sustainable Catalyst for the Synthesis of Nitrogen Heterocycles under Aqueous Conditions. *ACS Sustainable Chemistry & Engineering* **7**, 8274-8286 (2019). https://doi.org:10.1021/acssuschemeng.8b06677
396 Yazdi, M. K. *et al.* Polydopamine Biomaterials for Skin Regeneration. *ACS Biomater Sci Eng* **8**, 2196-2219 (2022). https://doi.org:10.1021/acsbiomaterials.1c01436
397 Wei, Y. *et al.* Engineered Biomimetic Nanoplatform Protects the Myocardium Against Ischemia/Reperfusion Injury by Inhibiting Pyroptosis. *ACS Appl Mater Interfaces* **13**, 33756-33766 (2021). https://doi.org:10.1021/acsami.1c03421
398 Zhao, J. *et al.* Toward improved wound dressings: effects of polydopamine-decorated poly(lactic-co-glycolic acid) electrospinning incorporating basic fibroblast growth factor and ponericin G1. *RSC Adv* **9**, 33038-33051 (2019). https://doi.org:10.1039/c9ra05030b
399 Xu, G. *et al.* Robust aptamer-polydopamine-functionalized M-PLGA-TPGS nanoparticles for targeted delivery of docetaxel and enhanced cervical cancer therapy. *Int J Nanomedicine* **11**, 2953-2965 (2016). https://doi.org:10.2147/IJN.S103513
400 Encinas, N., Pantoja, M., Abenojar, J. & Martínez, M. A. Control of Wettability of Polymers by Surface Roughness Modification. *Journal of Adhesion Science and Technology* **24**, 1869-1883 (2010). https://doi.org:10.1163/016942410x511042
401 Allen, L. T. *et al.* Surface-induced changes in protein adsorption and implications for cellular phenotypic responses to surface interaction. *Biomaterials* **27**, 3096-3108 (2006). https://doi.org:10.1016/j.biomaterials.2006.01.019
402 Thyparambil, A. A., Wei, Y. & Latour, R. A. Experimental characterization of adsorbed protein orientation, conformation, and bioactivity. *Biointerphases* **10**, 019002 (2015). https://doi.org:10.1116/1.4906485
403 González-Benito, J., Baselga, J. & Aznar, A. J. Microstructural and wettability study of surface pretreated glass fibres. *Journal of Materials Processing Technology* **92-93**, 129-134 (1999). https://doi.org:10.1016/s0924-0136(99)00212-5
404 Singh, J., Banerjee, R. & Adhikari, B. Poly(aniline-co-m-aminobenzoic acid): A Novel Ester Vapor Sensor and its Thin Film Deposition on Silane Functionalized SAM Glass Surface. *Advanced Materials Research* **1123**, 92-95 (2015). https://doi.org:10.4028/www.scientific.net/AMR.1123.92
405 Dalstein, L., Potapova, E. & Tyrode, E. The elusive silica/water interface: isolated silanols under water as revealed by vibrational sum frequency spectroscopy. *Phys Chem Chem Phys* **19**, 10343-10349 (2017). https://doi.org:10.1039/c7cp01507k
406 Xi, Z.-Y., Xu, Y.-Y., Zhu, L.-P., Wang, Y. & Zhu, B.-K. A facile method of surface modification for hydrophobic polymer membranes based on the adhesive behavior of poly(DOPA) and poly(dopamine). *Journal of Membrane Science* **327**, 244-253 (2009). https://doi.org:10.1016/j.memsci.2008.11.037
407 Przekora, A. The summary of the most important cell-biomaterial interactions that need to be considered during in vitro biocompatibility testing of bone scaffolds for tissue engineering applications. *Mater Sci Eng C Mater Biol Appl* **97**, 1036-1051 (2019). https://doi.org:10.1016/j.msec.2019.01.061
408 Sun, X. & Kaufman, P. D. Ki-67: more than a proliferation marker. *Chromosoma* **127**, 175-186 (2018). https://doi.org:10.1007/s00412-018-0659-8
409 Yang, K. *et al.* Polydopamine-mediated surface modification of scaffold materials for human neural stem cell engineering. *Biomaterials* **33**, 6952-6964 (2012). https://doi.org:10.1016/j.biomaterials.2012.06.067

410 Yan, N. *et al.* Polydopamine-mediated Surface Modification Promotes the Adhesion and Proliferation of Human Induced Pluripotent Stem Cells. *MRS Advances* **5**, 591-599 (2020). https://doi.org:10.1557/adv.2019.405
411 Liu, Y. *et al.* Mussel Inspired Polynorepinephrine Functionalized Electrospun Polycaprolactone Microfibers for Muscle Regeneration. *Sci Rep* **7**, 8197 (2017). https://doi.org:10.1038/s41598-017-08572-z
412 Yang, Z. *et al.* Mussel-inspired coating of polydopamine directs endothelial and smooth muscle cell fate for re-endothelialization of vascular devices. *Adv Healthc Mater* **1**, 548-559 (2012). https://doi.org:10.1002/adhm.201200073
413 Jiang, X., Li, Y., Liu, Y., Chen, C. & Chen, M. Selective enhancement of human stem cell proliferation by mussel inspired surface coating. *RSC Advances* **6**, 60206-60214 (2016). https://doi.org:10.1039/c6ra11173d
414 Ma, T., Wang, C. X., Ge, X. Y. & Zhang, Y. Applications of Polydopamine in Implant Surface Modification. *Macromol Biosci* **23**, e2300067 (2023). https://doi.org:10.1002/mabi.202300067
415 Lee, Y. B. *et al.* Polydopamine-mediated immobilization of multiple bioactive molecules for the development of functional vascular graft materials. *Biomaterials* **33**, 8343-8352 (2012). https://doi.org:10.1016/j.biomaterials.2012.08.011
416 Gao, T. *et al.* Biodegradable Microcarriers of Poly(Lactide-co-Glycolide) and Nano-Hydroxyapatite Decorated with IGF-1 via Polydopamine Coating for Enhancing Cell Proliferation and Osteogenic Differentiation. *Macromol Biosci* **15**, 1070-1080 (2015). https://doi.org:10.1002/mabi.201500069
417 Hoshiba, T., Yoshikawa, C. & Sakakibara, K. Characterization of Initial Cell Adhesion on Charged Polymer Substrates in Serum-Containing and Serum-Free Media. *Langmuir* **34**, 4043-4051 (2018). https://doi.org:10.1021/acs.langmuir.8b00233
418 Assfalg, M. Protein Adsorption and Conformational Changes. *Molecules* **26** (2021). https://doi.org:10.3390/molecules26237079
419 Torrini, F., Palladino, P., Baldoneschi, V., Scarano, S. & Minunni, M. Sensitive 'two-steps' competitive assay for gonadotropin-releasing hormone detection via SPR biosensing and polynorepinephrine-based molecularly imprinted polymer. *Anal Chim Acta* **1161**, 338481 (2021). https://doi.org:10.1016/j.aca.2021.338481
420 Rechendorff, K., Hovgaard, M. B., Foss, M., Zhdanov, V. P. & Besenbacher, F. Enhancement of protein adsorption induced by surface roughness. *Langmuir* **22**, 10885-10888 (2006). https://doi.org:10.1021/la0621923
421 Toledano, M., Carrasco-Carmona, A., Medina-Castillo, A. L., Toledano-Osorio, M. & Osorio, R. Protein adsorption and bioactivity of functionalized electrospun membranes for bone regeneration. *J Dent* **102**, 103473 (2020). https://doi.org:10.1016/j.jdent.2020.103473
422 Ricoult, S. G., Thompson-Steckel, G., Correia, J. P., Kennedy, T. E. & Juncker, D. Tuning cell-surface affinity to direct cell specific responses to patterned proteins. *Biomaterials* **35**, 727-736 (2014). https://doi.org:10.1016/j.biomaterials.2013.10.023
423 Xia, W. & Keten, S. Interfacial stiffening of polymer thin films under nanoconfinement. *Extreme Mechanics Letters* **4**, 89-95 (2015). https://doi.org:10.1016/j.eml.2015.05.001
424 Wu, X., Morgan, K. G., Jones, C. J., Tribe, R. M. & Taggart, M. J. Myometrial mechanoadaptation during pregnancy: implications for smooth muscle plasticity and remodelling. *J Cell Mol Med* **12**, 1360-1373 (2008). https://doi.org:10.1111/j.1582-4934.2008.00306.x
425 Engler, A. *et al.* Substrate compliance versus ligand density in cell on gel responses. *Biophys J* **86**, 617-628 (2004). https://doi.org:10.1016/S0006-3495(04)74140-5
426 Yamada, K. M. *et al.* Extracellular matrix dynamics in cell migration, invasion and tissue morphogenesis. *Int J Exp Pathol* **100**, 144-152 (2019). https://doi.org:10.1111/iep.12329
427 Puleo, J. I. *et al.* Mechanosensing during directed cell migration requires dynamic actin polymerization at focal adhesions. *J Cell Biol* **218**, 4215-4235 (2019). https://doi.org:10.1083/jcb.201902101

428 Burridge, K. & Guilluy, C. Focal adhesions, stress fibers and mechanical tension. *Exp Cell Res* **343**, 14-20 (2016). https://doi.org:10.1016/j.yexcr.2015.10.029
429 De Pascalis, C. & Etienne-Manneville, S. Single and collective cell migration: the mechanics of adhesions. *Mol Biol Cell* **28**, 1833-1846 (2017). https://doi.org:10.1091/mbc.E17-03-0134
430 Friedl, P. & Gilmour, D. Collective cell migration in morphogenesis, regeneration and cancer. *Nature Reviews Molecular Cell Biology* **10**, 445-457 (2009). https://doi.org:doi.org/10.1038/nrm2720
431 Mierke, C. T. The matrix environmental and cell mechanical properties regulate cell migration and contribute to the invasive phenotype of cancer cells. *Rep Prog Phys* **82**, 064602 (2019). https://doi.org:10.1088/1361-6633/ab1628
432 Lintz, M., Munoz, A. & Reinhart-King, C. A. The Mechanics of Single Cell and Collective Migration of Tumor Cells. *J Biomech Eng* **139**, 0210051-0210059 (2017). https://doi.org:doi.org/10.1115/1.4035121
433 Berkhout, R. P. *et al.* High-quality human preimplantation embryos actively influence endometrial stromal cell migration. *J Assist Reprod Genet* **35**, 659-667 (2018). https://doi.org:10.1007/s10815-017-1107-z
434 Ciarmela, P. *et al.* Growth factors and myometrium: biological effects in uterine fibroid and possible clinical implications. *Hum Reprod Update* **17**, 772-790 (2011). https://doi.org:10.1093/humupd/dmr031
435 Plotnikov, S. V., Pasapera, A. M., Sabass, B. & Waterman, C. M. Force fluctuations within focal adhesions mediate ECM-rigidity sensing to guide directed cell migration. *Cell* **151**, 1513-1527 (2012). https://doi.org:10.1016/j.cell.2012.11.034
436 Lopez-Colome, A. M., Lee-Rivera, I., Benavides-Hidalgo, R. & Lopez, E. Paxillin: a crossroad in pathological cell migration. *J Hematol Oncol* **10**, 50 (2017). https://doi.org:10.1186/s13045-017-0418-y
437 Webb, D. J. *et al.* FAK-Src signalling through paxillin, ERK and MLCK regulates adhesion disassembly. *Nat Cell Biol* **6**, 154-161 (2004). https://doi.org:10.1038/ncb1094
438 Zaidel-Bar, R., Milo, R., Kam, Z. & Geiger, B. A paxillin tyrosine phosphorylation switch regulates the assembly and form of cell-matrix adhesions. *J Cell Sci* **120**, 137-148 (2007). https://doi.org:10.1242/jcs.03314
439 Gupton, S. L. & Waterman-Storer, C. M. Spatiotemporal feedback between actomyosin and focal-adhesion systems optimizes rapid cell migration. *Cell* **125**, 1361-1374 (2006). https://doi.org:10.1016/j.cell.2006.05.029
440 Veevers-Lowe, J., Ball, S. G., Shuttleworth, A. & Kielty, C. M. Mesenchymal stem cell migration is regulated by fibronectin through alpha5beta1-integrin-mediated activation of PDGFR-beta and potentiation of growth factor signals. *J Cell Sci* **124**, 1288-1300 (2011). https://doi.org:10.1242/jcs.076935
441 Deng, Z., Wang, W., Xu, X., Ma, N. & Lendlein, A. Polydopamine-based biofunctional substrate coating promotes mesenchymal stem cell migration. *MRS Advances* **6**, 739-744 (2021). https://doi.org:10.1557/s43580-021-00091-4
442 Meng, X. N. *et al.* Characterisation of fibronectin-mediated FAK signalling pathways in lung cancer cell migration and invasion. *Br J Cancer* **101**, 327-334 (2009). https://doi.org:10.1038/sj.bjc.6605154
443 Berthois, Y., Katzenellenbogen, J. A. & Katzenellenbogen, B. S. Phenol red in tissue culture media is a weak estrogen: implications concerning the study of estrogen-responsive cells in culture. *Proc Natl Acad Sci U S A* **83**, 2496-2500 (1986). https://doi.org:10.1073/pnas.83.8.2496
444 Ernst, M., Schmid, C. & Froesch, E. R. Phenol red mimics biological actions of estradiol: enhancement of osteoblast proliferation in vitro and of type I collagen gene expression in bone and uterus of rats in vivo. *J Steroid Biochem* **33**, 907-914 (1989). https://doi.org:10.1016/0022-4731(89)90239-2
445 Awasthi, A. K., Gupta, S., Namdev, K. R., Banerjee, A. & Srivastava, A. Polydopamine and dopamine interfere with tetrazolium-based cytotoxicity assays and produce exaggerated cytocompatibility inferences. *Biomater Sci* **9**, 3300-3305 (2021). https://doi.org:10.1039/d1bm00140j
446 Tinevez, J. Y. *et al.* TrackMate: An open and extensible platform for single-particle tracking. *Methods* **115**, 80-90 (2017). https://doi.org:10.1016/j.ymeth.2016.09.016

447 Ponzio, F. *et al.* Oxidant Control of Polydopamine Surface Chemistry in Acids: A Mechanism-Based Entry to Superhydrophilic-Superoleophobic Coatings. *Chemistry of Materials* **28**, 4697-4705 (2016). https://doi.org:10.1021/acs.chemmater.6b01587

448 Horejs, C. M. *et al.* Preventing tissue fibrosis by local biomaterials interfacing of specific cryptic extracellular matrix information. *Nat Commun* **8**, 15509 (2017). https://doi.org:10.1038/ncomms15509

449 Shumaker-Parry, J. S. & Campbell, C. T. Quantitative methods for spatially resolved adsorption/desorption measurements in real time by surface plasmon resonance microscopy. *Anal Chem* **76**, 907-917 (2004). https://doi.org:10.1021/ac034962a

450 Comelles, J. *et al.* Epithelial colonies in vitro elongate through collective effects. *Elife* **10** (2021). https://doi.org:10.7554/eLife.57730

# APPENDIX A: Culturing media for T-HESCs and PHM1-41 cells

Table A-1: T-HESC media formulation

| Component | Working Concentration | Supplier (Product Code) | Notes |
|---|---|---|---|
| DMEM/F-12<br>No phenol red | 90%† | ThermoFisher<br>(11054020) | 50/50 mix of DMEM and F-12 nutrient mixture<br>Low glucose, without glutamine<br>Formulation available here |
| Glucose | 3.15 g/L<br>(17.5 mM) | included in DMEM/F12 | |
| L-glutamine | 0.37 g/L<br>(2.5 mM) | | *Not* GlutaMAX |
| Sodium Pyruvate | 0.11 g/L<br>(1 mM) | | |
| Additions | | | |
| GlutaMAX‡<br>(200 mM) | 0.217 g/L<br>(1 mM) | ThermoFisher<br>(35050061) | Shelf-stable form of L-glutamine<br>**250 µL** per 50 mL tube |
| Puromycin | 500 ng/mL<br>(18.4 pM) | Corning<br>(91-385) | Selection antibiotic<br>**100 µL** per 50 mL tube |
| ITS+ premix (100x) with:<br>Human recombinant insulin (I)<br>Human transferrin (T)<br>Selenious acid (S)<br>BSA (+)<br>Linoleic acid (+) | 1:100 dil.<br>6.25 µg/mL<br>6.25 µg/mL<br>6.25 ng/mL<br>1.25 mg/mL<br>5.35 ng/mL | Corning<br>(354352) | **500 µL** per 50 mL tube |
| Fetal bovine serum,<br>US Origin<br>(*Charcoal-Dextran stripped*) | 10% | Corning<br>(35-072-CV) | **5 mL** per 50 mL tube |
| Suggested Subculturing Ratio<br>*Media renewal frequency* | | | 1:3 to 1:6<br>*E2D to E3D* |

†Mandatory additions pooled before the addition of DMEM/F12; actual DMEM/F12 is approximately 88.3%
‡An additional 1 mM of GlutaMAX (L-alanyl-L-glutamine) was added for stable L-glutamine levels

Table A-2: PHM1-41 media formulation

| Component | Working Concentration | Supplier (Product Code) | Notes |
|---|---|---|---|
| DMEM<br>No phenol red | 90%† | ThermoFisher<br>(31053028) | High glucose, w/o glutamine and $Na^+$ pyruvate<br>Formulation available here |
| Glucose | 4.5 g/L<br>(25.2 mM) | included in DMEM | |
| Additions | | | |
| GlutaMAX<br>(200 mM) | 1.29 g/L<br>(6 mM) | ThermoFisher<br>(35050061) | **1.5 mL** per 50 mL tube |
| Sodium Pyruvate<br>(100 mM) | 1 mM | ThermoFisher<br>(11360070) | **500 µL** per 50 mL tube |
| Geneticin (G-418) | 0.1 g/L<br>(200 mM) | VWR<br>(97064-358) | **100 µL** per 50 mL tube |
| Fetal bovine serum,<br>US Origin<br>(*Charcoal-Dextran stripped*) | 10% | Corning<br>(35-072-CV | **5 mL** per 50 mL tube |
| Suggested Subculturing Ratio<br>*Media renewal frequency* | | | 1:2 to 1:3<br>*E2D to E3D* |

†Mandatory additions pooled before the addition of DMEM; actual DMEM is approximately 85.8%

# APPENDIX B: 3D-printed wounding assay insert fabrication

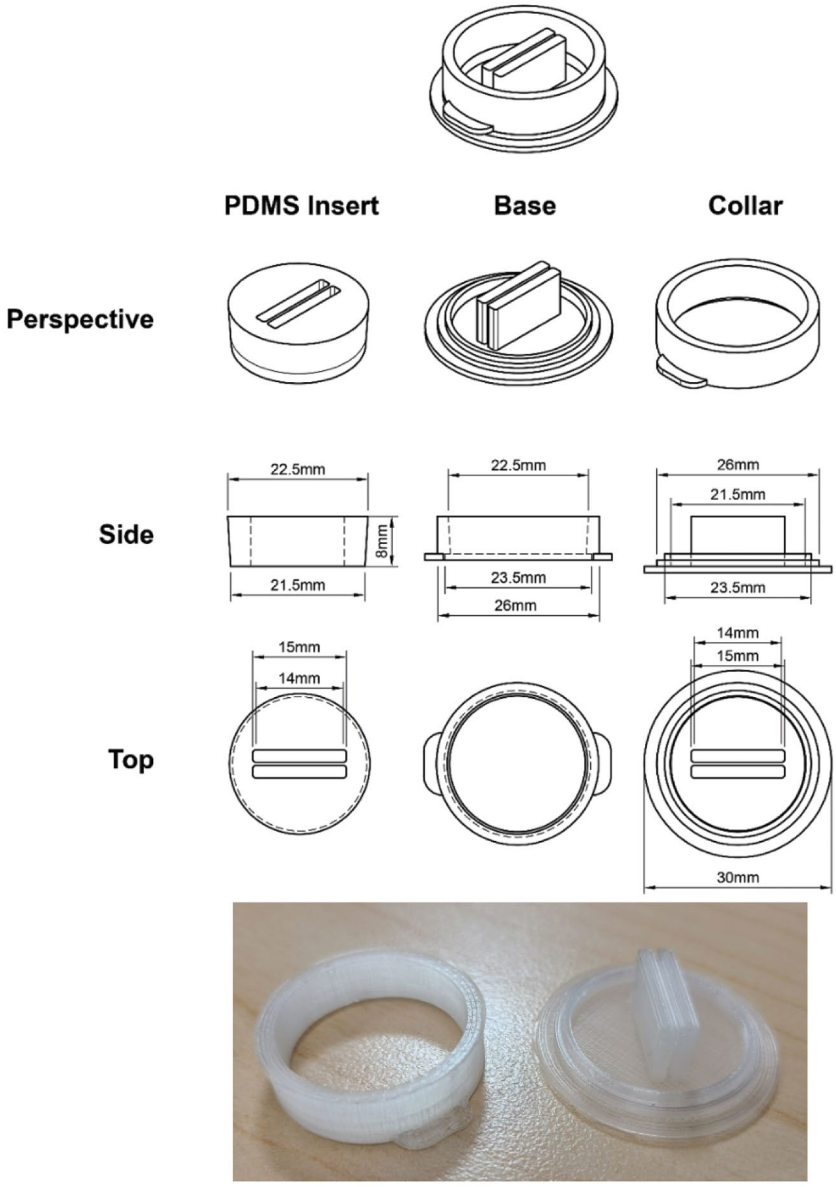


Figure B-1: FDM-3D printed moulds.

Schematic visualization and photograph of a 2-part 3D-printed mould to fabricate custom PDMS inserts for wound healing assays in multi-well plates.

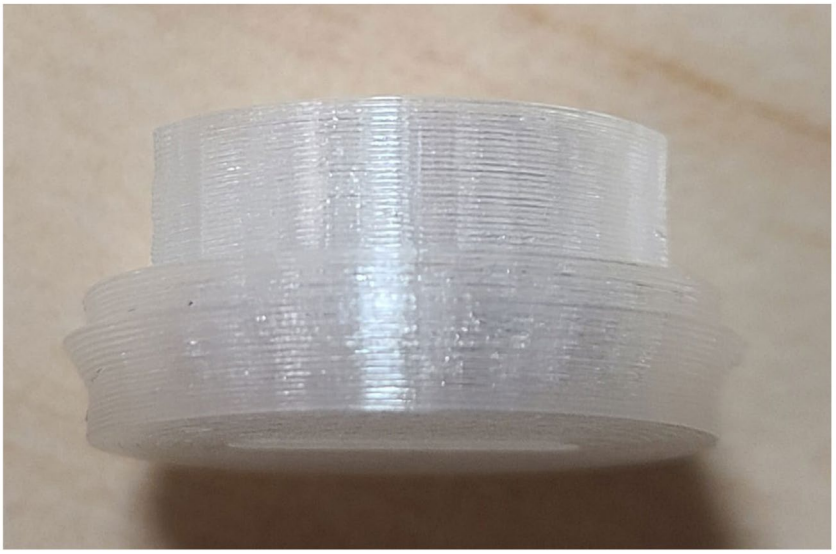

Figure B-2: Visualization of horizontal striations of FDM-3D printed moulds.

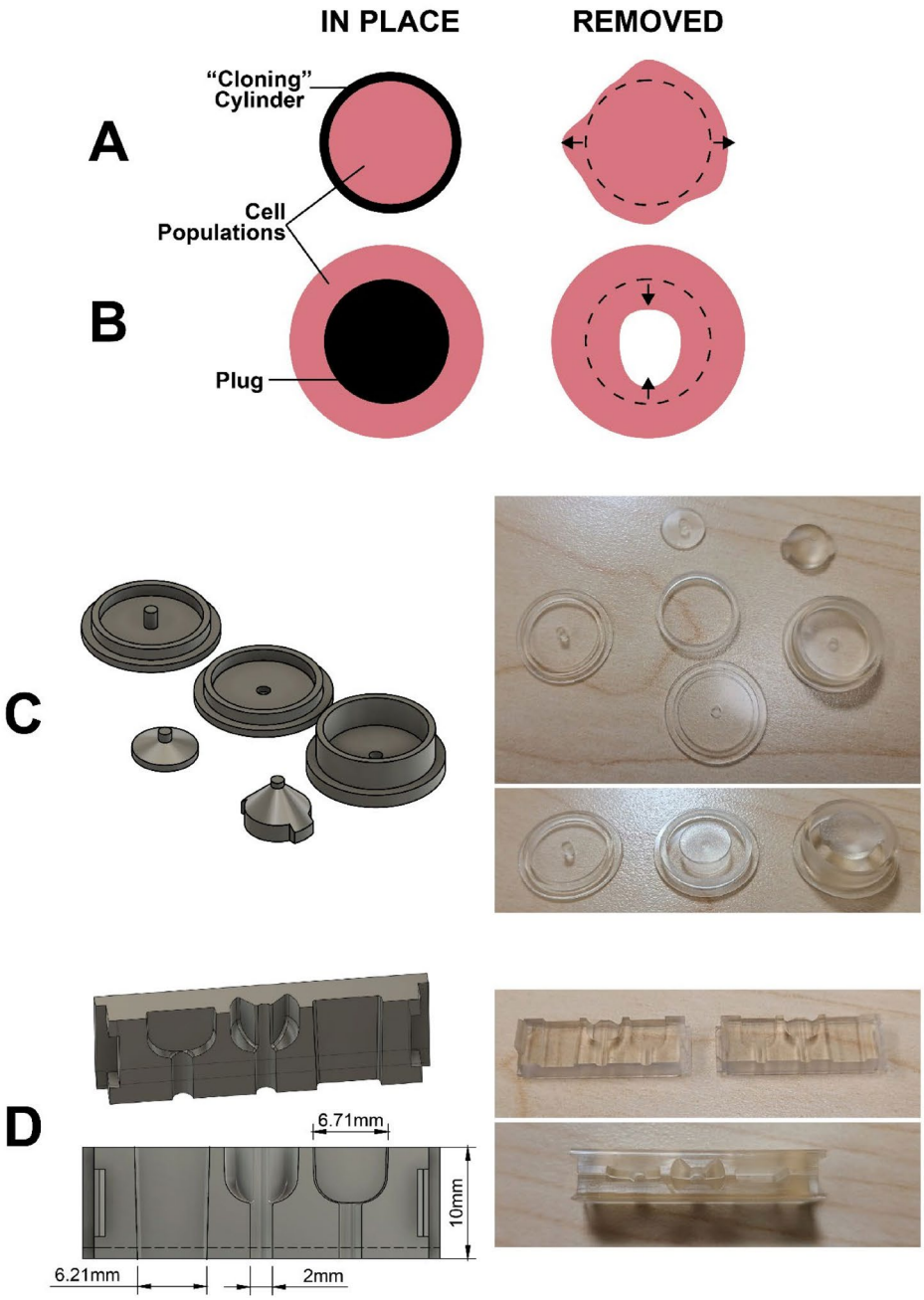


Figure B-3: Design and fabrication of SLA-3D printed moulds.

Schematics of **(A)** expansion and **(B)** contraction wounding assays. **(C)** Renderings and pictures of 1-piece and 2-piece moulds for PDMS inserts sized for a 24-well plate. **(D)** Pinch mould rendering and photographs for several PDMS inserts for 96-well plates.

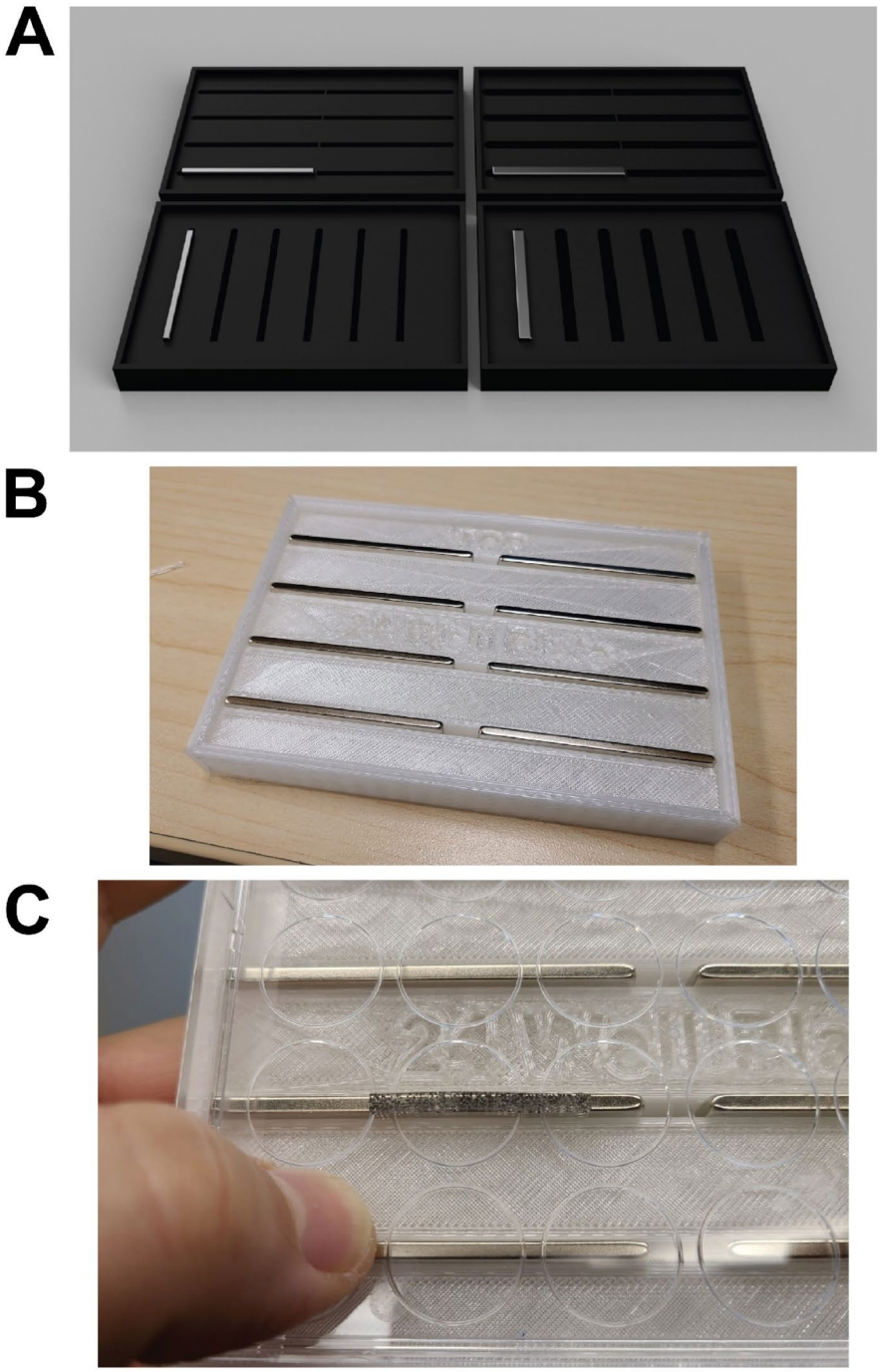


Figure B-4: Magnetic holder plates for 24 and 96-multiwell plates.

**(A)** Rendering and **(B)** a picture of FDM-3D printed holders to hold magnetics to apply a magnetic field across 24-well and 96-well multiwell plates. **(C)** Proof of concept with a piece of PDMS that contains iron powder.

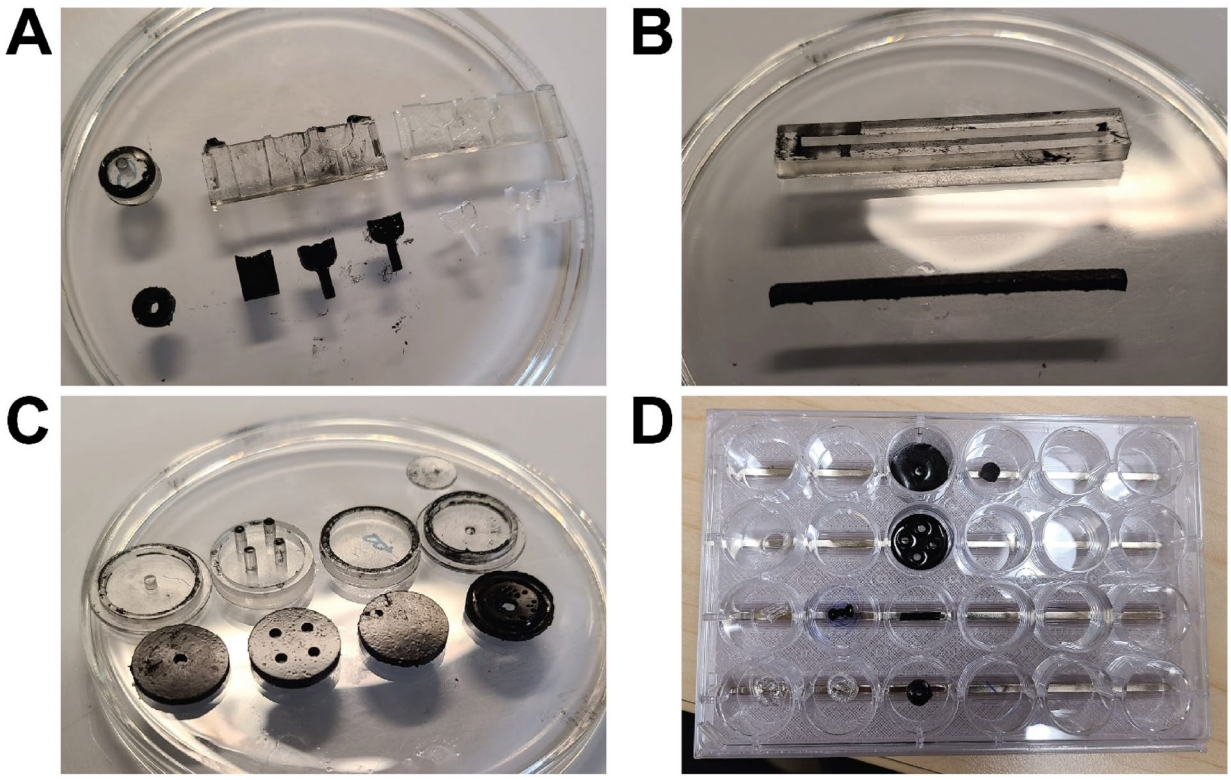


Figure B-5: Magnetic PDMS insert examples.

**(A)** Inserts for use in 96-well plates. **(B)** Rectangular barriers for general use. **(C)** Inserts for use in 24-well plates. **(D)** Example application of inserts in a 24-well plate.